FORSCHUNGSZENTRUM ROSSENDORF
Mitglied der Wissenschaftsgemeinschaft Gottfried Wilhelm Leibniz

WISSENSCHAFTLICH-TECHNISCHE BERICHTE
FZR-372
May 2003

Annual Report 2002

Institute of Nuclear and Hadron Physics

Editors:

F. Dönau, W. Enghardt, K. Fahmy,
E. Grosse, B. Kämpfer, C. Schneidereit

Explanation of special symbols:

The letters given in parentheses in the following text and used as appendix in the titles of the scientific contributions do express our grateful acknowledgement to the funding, sponsoring or grants provided by several institutions.

Research projects were funded by the Federal Ministry of Education and Research BMBF (B), by the Saxon Ministry of Education and Arts SMWK (S), by the German Research Community DFG (D), by the German Academic Exchange Service DAAD (A), by the European Commission (E), by the GSI Darmstadt (G), by the FZ Jülich (J), and by the special program HSP III (H) or were sponsored within Scientific agreements with eastern European countries (W).

Contents

PAGE

Preface 1

Structure of Matter: Nuclear and Hadron Physics 3

The Dilepton Spectrometer HADES at SIS/GSI Darmstadt in Operation 5

Sub-Threshold Phi Meson Production in the Reaction Ni (1.93 A·GeV) + Ni 7

Inclusive K-meson and Pion Production in Proton-Nucleus Collisions at SIS Energies 8

Hyperon-Nucleon Bound States and the Electroproduction of Strangeness on $^{3,4}He$ 10

In-Medium Spectral Change of ω Mesons as a Probe of Four-Quark Condensate 11

Modifications of the Di-Electron Spectra from ϕ Meson Decays 12

Tagging the $pn \to d\phi$ Reaction by Backward Protons in $pd \to d\phi p_{sp}$ Processes 13

Measuring the Effect of ϕ Meson Life Time in Proton-Nucleus Collsions 14

Nucleon-K^+ Correlations in Deuteron Induced Collisions with Nuclei at Intermediate Energies 15

Strangeness Saturation: Dependence on System-Size, Centrality and Energy within the Thermal Model 16

Energy Loss of Charm Quarks by Gluon Radiation 17

Relativistic Effects in Deuteron Break-Up Reactions 18

Exclusive Charge-Exchange Reaction $pD \to n(pp)$ within the Bethe-Salpeter Formalism 19

From QCD Lattice Calculations to the Equation of State of Quark Matter 20

Quality Assessment for Monitoring of HADES DST Production 21

A Method for Separation of Faulty Wire Connections in the HADES Drift Chambers 22

Examination of the Wire Deflections for the HADES Drift Chambers MDC III 23

Momentum-Reconstruction System for ANKE Side Detectors 25

ELBE-n-TOF: Comparison to other Neutron Sources and Experiments 26

Detector Setup for Nuclear-Resonance-Fluorescence Experiments at ELBE 27

Collimators for the BGO Escape-Suppression Shields 29

Radiator for the Production of Bremsstrahlung at ELBE 30

Steering Magnets for the Production of Polarized Bremsstrahlung at ELBE 31

Beam Separation Magnet of the Bremsstrahlung Facility at ELBE 33

Dipole Excitations in ^{98}Mo 34

Nuclear Resonance Fluorescence Experiments on ^{100}Mo 35

Simulations for a Double Time-of-Flight Spectrometer for Fission Fragments 36

A Time Coincidence Test Setup for an MCP Detector 37

Secondary Electron Trajectories for an Electrostatic Mirror 38

Measuring Foil Thicknesses for a Time-of-Flight Spectrometer 39

Probing the Gateway to Superheavy Nuclei in Cranked Relativistic Hartree-Bogoliubov Theory 40

Proton-Neutron Pairing in Rotating $N \approx Z$ Nuclei 41

Beta-Decay Studies of Neutron-Deficient Tin Isotopes 42

Beta Decay of ^{103}Sn 43

Gamma-Ray Spectroscopy of Fission Fragments with Super Clover Ge Detectors 44

Study of the Neutron-Rich Isotopes ^{91}Sr and ^{92}Sr in a Fusion-Fission Experiment 45

Life Sciences: Biostructures and Radiation 47

Installation of Biochemical and Biophysical Working Facilities at the IKH 49

Whole Cell Characterisation by Second-Derivative FTIR Spectroscopy for the Detection of Radiation Damage 50

Analysis of Structural Flexibility in S-Layer Proteins from *Bacillus Sphaericus* 51

Investigation of Structure and Function of the Visual Photoreceptor Rhodopsin 52

Analysis of Dye DNA Interactions 53

Experimental Set-Up for IR Measurements of Dynamics of Water-Lipid Interaction 54

Infrared Characterization of Environmental Samples by Pulsed Photo-Thermal Spectroscopy 55

Using Pulsed Photo-Thermal Spectroscopy for Microspectroscopy in the Infrared Region. A First Approach 56

Temperature Stabilization of the Out-Coupling Mirror Wheel 57

A Four Pole Magnetic Chicane for Phase Matching 58

New Elements of the GPT Code to Simulate a Resonator Free-Electron Laser 59

Start-Up Simulations of the Spectral and Spatial Evolution of the ELBE FEL 60

Simulation of Limit Cycle Oscillations in the U27 FEL 61

Dynamics of Matrix–Isolated Molecules 62

Clonogenic Survival of Mammary Epithelial Cells MCF-12A after Irradiation with 200 kV X-Rays 64

Influence of the Handling Procedure During Irradiation on Cell Survival and Micronucleus Test Results 65

Measurements of Spectral Dose Distributions of a Soft X-Ray Tube 66

Changing the Dose Range of TSEE Dosimeters 67

An X-Ray Monochromator for the Channeling Source at ELBE 68

The Influence of Electron Scattering in the Target on the Beam Transmission 69

Background at the Radiation Physics Beam Line 70

Shielding Calculations for an X-Ray Laboratory 71

Comparison of Bremsstrahlung Distributions with Results from Monte-Carlo Codes 72

Calculation of Photon-Induced Auger Transitions in Tc and Re 73

Auger Electron Emission in Tc: Photon Induced versus Radioactive Decay 74

Dose Distributions of Photon-Induced Secondary Electrons in Tc 75

Scatter Correction for In-Beam PET Monitoring of Heavy Ion Therapy 76

The Time Dependence of the γ-Ray Intensity Seen by an In-Beam PET Monitor 77

The Quantification of the Mechanical Deformation of the Rotating Double Head PET Scanner at the ^{12}C Ion Therapy Facility at GSI Darmstadt 78

Nuclear Reaction Cross Sections for the Assessment of Positron Emitter Generation by Therapeutic Irradiations with ^{4}He Beams 79

Hamamatsu S8550 APD Arrays for High-Resolution Scintillator Matrices Readout 80

Position Sensitive Photon Detectors of Lutetium Oxyorthosilicate Crystals Coupled to Avalanche Photodiode Arrays 81

A CAMAC Data Acquisition System for Multi Parameter Measurements 82

A Technical Feasibility Study for a PET Therapy Monitor Combined with a Rotating Ion Beam Delivery 83

Author Index 85

Publications and Talks 87

Publications 89

Proceedings and Reports 98

Theses 101

Talks at Conferences and other Institutes 102

Talks at Rossendorf 107

Talks of Visitors 108

Meetings organized by the IKH 110

Personnel 111

Personnel of the Institute for Nuclear and Hadron Physics 113

Guest Scientists 114

Preface

The Forschungszentrum Rossendorf (FZR) at Dresden is a research centre within the Wissenschaftsgemeinschaft Gottfried Wilhelm Leibniz (WGL), one of the German national institutions responsible for extra-unversity research. Using radiation and radioactivity the centre is active in investigations on the structure of matter as well as in the life sciences and in environmental research. The **Institute of Nuclear and Hadron Physics (IKH)** *in the FZR is engaged in fundamental research on the structure of subatomic systems and it strongly pursues the transfer of knowledge to other fields of science. It especially investigates and exploits the possibilities for introducing experimental and theoretical techniques from particle and nuclear physics to the life sciences.*

Experimental and theoretical physicists closely work together in various fields related to research at accelerators and secondary radiation as produced by accelerator beams. With these tools sub-nuclear degrees of freedom, the dynamics of nuclei and their collisions as well as complex biological systems on much larger scales are investigated together with their absorption or emission of electromagnetic radiation. An important advantage of connecting studies in seemingly unconnected fields is due to the fact that theoretical procedures as well as experimental techniques as applied to objects of such different size and structure nonetheless show large similarities. The coupling to radiation together with the importance of many-particle aspects or medium effects establish an important link in theoretical studies. A remarkable example of interdisciplinary transfer is the institute's work on the Radiation Source ELBE at the FZR. This instrument is centered around a superconducting electron linac; thus nuclear physicists could contribute with their experience gained at accelerators outside of Rossendorf. From the electron beam of 1 mA at up to 40 MeV intense secondary radiation is produced: for the medium and far infrared (IR) the free electron laser (FEL) principle will be used, whereas keV-X-rays can be produced via electron channeling or Compton backscattering. Bremsstrahlung photons in the MeV range are a very interesting probe for investigations in nuclear spectroscopy and astrophysics and they allow for the generation of fast neutrons, of interest for many applications.

The interaction between the different areas of research at IKH is especially important with respect to soft- and hardware for running and analyzing the experimental investigations; here the transfer of information from the large international particle and nuclear physics community to the life sciences already has led to considerable synergy effects. Thus there are ample interconnections between the various research projects of the institute -reaching from laboratory studies related to cosmic processes all the way to the interactions of various types of radiation with bio-molecules and cells.

The following R & D projects of the FZR are directed by the institute's research groups. Those indicated by (*) are pursued in collaboration with other FZR institutes under the direction of scientists from the IKH:

Structure of Matter - Nuclear and Hadron Physics

- *Nuclear structure*
- *Nuclear astrophysics*
- *A pulsed source of fast neutrons**
- *Rare hadronic processes*

Life Sciences - Biostructures and Radiation

- *Radiation induced cell damage*
- *Photon activation therapy**
- *Structural dynamics of biomolecules*
- *Tomography and tumour-conform radiotherapy*

In this Scientific Report of the Institute of Nuclear and Hadron Physics these projects are presented by several articles. Other contributions describe the progress made in the production of the different kinds of secondary radiation at ELBE, and on the experimental equipment to be installed for their use. The conceptual design studies for the IR-FEL and the detailed work on a magnetic undulator constitute a very important contribution to the FEL aspect of ELBE,

which very likely will be attractive to many outside users. Similarly, the numerical simulations performed for the optimization of the X-ray and the MeV-photon production stations and the experimental areas indicate that in both fields ELBE is apt to allow experiments with high sensitivity and favourable background conditions.

Nuclear and Hadron Physics at the IKH - as described in the first part of this report - deals with the strong (nuclear) interaction as such and also within the hadronic medium. Experiments related to such questions were performed at the heavy-ion synchrotron SIS at Darmstadt. Theoretical studies refer to these experiments and to data obtained at higher energy accelerators where a phase transition to a quark gluon plasma has been predicted to occur. Understanding the high density phases of hadronic matter is an important step towards understanding the Big Bang and the evolution of the universe. Experimental and theoretical research on low energy electromagnetic processes in nuclei plays an important role in the simulation of processes occuring during the stellar synthesis of the elements. Photon or electron induced fission will be of interest as the source of neutron rich nuclei whose properties are of special importance for the detailed understanding of the stellar element cooking; here neutron beams in the MeV range play a role as well. They and especially the bremsstrahlung photons from ELBE will also allow investigations on specific nuclear structure problems, and they pave the way to many interesting analytical studies, e.g. in the life sciences and materials research.

In its second section this Report comprises research on biomedical problems, mainly performed by using nuclear technology. In the past the main contribution of the institute to this field came from Positron Emission Tomography (PET) and the outstanding achievement here is the successful operation of a PET scanner simultaneously to the irradiation of tumors with heavy ion beams. A significant number of patients was treated at GSI in the last years and the reliability and reproducibility of such radiation therapy had been improved considerably by in-situ PET, as developed at the IKH. In the upcoming years biomedical research will be performed increasingly with the beams coming from ELBE: The quasi-monochromatic X-rays of easily variable energy as produced in electron channeling will be used as a probe for the elementary processes responsible for radiation damage in tissue and for first experiments related to photon activation therapy (PAT). For such studies a cell laboratory is installed at ELBE, which will also be used for investigating the interactions of cells with the tunable FEL-radiation in the infrared - as available at ELBE. Interesting research in biophysics and biochemistry will become possible; here the rather low damage caused by IR combined with its sensitivity to selected bio-molecular bonds will play an increasing role.

The scientific activities of the institute have benefitted from generous support from various sources. First of all, we gratefully acknowledge the close and fruitful collaboration with the Technical University (TU) Dresden and many other scientific institutions in Germany and abroad; such contacts are of vital importance for our institute. Specific projects were subsidized by the Federal Ministry for Education and Research (BMBF), the Saxon State Ministry for Science and Art (SMWK), Forschungszentrum Jülich and GSI Darmstadt. We express our gratitude to all these as well as to the Deutsche Forschungsgemeinschaft (DFG) and to the European Union (EU) for the support of several research projects initiated by the institute.

E. Grosse

Structure of Matter:
Nuclear and Hadron Physics

In this section the Scientific Report deals with nuclei, their excitations and their constituents, the hadrons. It thus contains work exploring details of the excitation spectrum of finite, strongly interacting systems as represented by the atomic nucleus and investigations probing strongly interacting matter and its hadronic constituents as produced in collisions between nuclei. Thus various facets of matter in the universe and the processes governing its development in time are investigated.

One milestone in our research was the start of the physics program of the HADES[1] *detector system. The HADES experiments at the SIS accelerator focus on studying the in-medium behaviour of hadrons. The most prevalent hadron, the nucleon, is the building block of nuclei, which constitute nearly all the mass of matter surrounding us. The origin of the masses of hadrons has been proposed to be a key to understand the phenomenon "mass": When embedded in strongly interacting matter vector mesons are expected to undergo alterations in their basic properties like lifetimes, decay widths, and especially masses. HADES offers the unique opportunity to explore such in-medium changes. In the fall of 2002 HADES has taken data out of 200 million events of the reaction C(1.95 AGeV)+C. In this measurement all the components of the detector were used: ring imaging Cerenkov counter, multi-wire drift chambers, time-of-flight wall and shower wall. The forthcoming analysis and interpretation of the data allows to acces fundamental properties of particles with far reaching consequences down to the absolute ground state (vacuum), where strongly interacting particles emerge as excitations. This aspect of our research with supplementary experimental and theoretical investigations on strangeness degrees of freedom in dense matter is reported in the first part of the this Report.*

A second milestone of the nuclear physics research at Rossendorf in 2002 was the start of operation of the radiation source ELBE. ELBE delivered a primary electron beam which produced Bremsstrahlung photons. These photons are ideally suited to excite selected states of nuclei to study their properties, e.g. in nuclear resonance fluorescence (NRF) experiments. The details of this research and the accompanying theoretical investigations are described in the second part of this report. The very first experiment are devoted to the test of the Bremsstrahlung facility at ELBE. In preparing the NRF experiments on $^{98,100}Mo$ *to be performed at ELBE two measurements at the DYNAMITRON in Stuttgart, were carried out in cooperation with other NRF groups. As a rather surprising result the deexcitation from a dipole state to low lying intruder states was observed. Progress was also achieved in developing a novel time-of-flight spectrometer for the detection of fission fragments. This instrument will allow the study and spectroscopy of fission fragments at ELBE delivering information strongly related to the r-process in the "element cooking" in the universe, leading to the production of the heavy elements. As another astrophysically relevant nuclear reaction we plan to observe the energy dependence of the nuclear photo-effect and thus the behaviour of nuclei in a photon bath, as present e.g. in the early universe or high temperature stellar scenarios. Thus mimicing the various cosmic nuclear processes in the laboratory our research contributes to a comprehensive understanding of where, when and how individual isotopes of the chemical elements are formed. In this field we also want to exploit a pulsed source of fast neutrons, driven by primary electrons from ELBE; this set-up which is developed jointly with IfS of FZR and IKTP of TU Dresden.*

[1] The **H**igh-**A**cceptance **D**i **E**lectron **S**pectrometer HADES is installed at the heavy-ion synchrotron SIS in GSI/Darmstadt. In 2002 the manufacturing of the six sectors of the multi-wire drift chambers of plane III has been completed in the FZ Rossendorf.

The results decsribed in this Report are obtained in the following collaborations:

ANKE: Univ. Münster, FZ Jülich, Univ. Giessen, Univ. Bonn, Univ. Köln, Univ. Erlangen-Nürnberg, Fachhochschule München, FZ Rossendorf, JINR Dubna (Russia), Univ. Tbilisi (Georgia), Petersburg Nuclear Physics Institute (Russia), ITEP Moscow (Russia), Russian Academy of Science Moscow (Russia), ECN-Nuclear Energy (Netherlands), Jagellonian Univ. Cracow (Poland), Moscow State University (Russia), Univ. College London (England), Soltan Institute for Nuclear Studies (Poland).

FOPI: Univ. Heidelberg, GSI Darmstadt, FZ Rossendorf, IPNE Bucharest (Romania), KFKI Budapest (Hungary), LPC and Univ. Blaise Pascal Clermont (France), ITEP Moscow (Russia), Kurchatov Institute Moscow (Russia), Korea Univ. Seoul (South Korea), IreS Strasbourg (France), Univ. Warsaw (Poland), RBI Zagreb (Croatia).

HADES: Univ. Frankfurt, TU München, Univ. Giessen, GSI Darmstadt, FZ Rossendorf, Institute of Physics Bratislava (Slovakia), LNS Catania (Italy), LPC and Univ. Blaise Pascal Clermont (France), Jagellonian Univ. Cracow (Poland), JINR Dubna (Russia), Univ. degli Studi di Milano (Italy), ITEP Moscow (Russia), INR Moscow (Russia), MEPhI Moscow (Russia), Univ. of Cyprus (Cyprus), Institute de Physique Nucleaire d'Orsay (France), Nuclear Physics Institute Rez (Czechia), Univ. of Santiago de Compostela (Spain), Univ. of Valencia (Spain).

JLab E 91916: JLAB E91-016: Argonne National Laboratory, Argonne (USA), California Institute of Technology, Pasadena (USA), College of William and Mary, Williamsburg (USA), Duke University, Durham (USA), Florida International University, Miami (USA), FZ Rossendorf, Juniata College, Huntingdon (U0SA), Kent State University, Kent (USA), North Carolina A&T State University, Greensboro (USA), Northwestern University, Evanston (USA), Ohio University, Athens (USA), Southern University at New Orleans, New Orleans (USA), The George Washington University, Washington DC (USA), Thomas Jefferson National Accelerator Facility, Newport News (USA), Tohoku University, Sendai (Japan), University of Houston, Houston, (USA), University of Maryland, College Park (USA), University of Minnesota, Minneapolis (USA), University of Virginia, Charlottesville (USA), Yerevan Physics Institute, Yerevan, (Armenia).

KaoS: TU Darmstadt, Univ. Frankfurt, Univ. Marburg, GSI Darmstadt, Jagellonian Univ. Cracow (Poland), FZ Rossendorf.

TOF: Univ. Bochum, FZ Jülich, Univ. Bonn, TU Dresden, Fachhochschule Jülich, Univ. Tübingen, Univ. Erlangen-Nürnberg, FZ Rossendorf, IUCF Bloomington (USA), INFN Torino (Italy), SINS Warsaw (Poland).

NRF: As in previous years the NRF project was substantially benefitting from the successfull cooperation with the spectroscopy groups from the German universities at Stuttgart, Cologne and Darmstadt as well as with the GSI Darmstadt. We acknowledge also the fruitful collaboration with the colleagues from INRE and the University of Sofia. Furthermore, we are grateful to the cooperation with our colleagues at the Universities of Tennessee and of Notre Dame, USA and with the Joint Institute of Nuclear Research at Dubna.

The Dilepton Spectrometer HADES at SIS/GSI Darmstadt in Operation [B,G]

F. Dohrmann, W. Enghardt, E. Grosse, K. Heidel, J. Hutsch, B. Kämpfer, K. Kanaki, R. Kotte, L. Naumann, A. Sadovski, J. Seibert, M. Sobiella and the HADES collaboration

The High Acceptance Di-Electron Spectrometer (HADES) aimes at measuring in-medium modifications of light vector mesons (ρ,ω,ϕ) in nuclear matter. Such modifications of hadron properties are predicted by various models based on fundamental principles like chiral symmetry and QCD.

The HADES setup is nearly complete; it includes the most detector units, read-out, data-acquisition and trigger electronics. The ring imaging Cherenkov counters (RICH), the inner multiwire drift chambers (MDC-I, MDC-II), the time of flight scintillation hodoscopes (TOF, TOFINO) and the pre-shower modules were completely installed. The performance of the drift chambers as well as all other detectors were monitored online.

Up to now four large-area drift chamber modules of MDC-III, produced at FZ Rossendorf, and two MDC-IV modules,prepared at IPN Orsay, for the outer tracking planes were installed. All six modules of MDC-IIIwere produced at the Rossendorf detector workshop. Thus, two sectors of the spectrometer are fully equipped. The angular acceptance of each segment amounts to $\phi = 0° - 60°$ and $\theta = 18° - 85°$.

The HADES collaboration [1] performed three measuring periods in the year 2002 (see Tab. 1).

Reaction	E/A [GeV]	Events	Remarks
C+C	0.6; 0.8	10^9	DAQ commisioning
Mg+C	1.0	10^8	benchmark beamtime
C+C	2.0	10^9	production beamtime

Tab. 1 *HADES beamtime at 2002.*

First physics studies, aimed at measuring electron-positron pairs produced in relativistic collisions of C+C started in 2001 and have been continued extensively in 2002.

In the November/December 2002 beam time a 2 GeV/nucleon carbon beam with an averaged intensity of $1. \times 10^7$ particles per spill hit a carbon target. The spill length amounted to 9.5 s. The target was 3 mm in diameter and had a length of 2×3 mm. A fast twofold hardware selection was implemented with the first level and the second level triggers. These triggers reduced the data by more than one order of magnitude. Using these triggers, most of the detected reaction products were protons and pions. Tab. 2. shows the accumulated statistics for different trigger levels.

HADES proposal

avg beam curr. pps	beam days	duty cycle %	total beam part.	target int. length %	useful target collisions	Trig2 fraction	physics events
5.00E+06	5	50	1.08E+12	1	1.08E+10	0.1	1.08E+09
2.00E+06	5	50	4.32E+11	1	4.32E+09	0.1	4.32E+08
1.00E+06	5	50	2.16E+11	1	2.16E+09	0.1	2.16E+08

Effective beam data

total stored events	Trig2 fraction	Downscaling fraction	Trig2'ed evts	primary collisions	≈ target collision efficiency	useful target collisions
2.13.E+08	0.073	0.094	9.31.E+07	1.28.E+09	0.8	1.02.E+09

N. of events accumulated through the beam time	The fraction of accepted lvl1 triggers accepted by lvl2	The fraction of accepted lvl1 triggers stored but with no leptons	lvl2 accepted events	N. of events examined by lvl2	Fraction of events coming from the real target	N. of beam - target interactions
	The fraction of accepted lvl1 triggers stored to disk					

useful target collisions	Stored physics events
1.08E+10	1.08E+09
4.32E+09	4.32E+08
2.16E+09	2.16E+08

useful target collisions	Stored physics events
1.02.E+09	7.45.E+07

N. of beam - target interactions	Real "clean" events from target filtered by lvl2

Tab. 2 *Amount of data accumulated during the production beamtime under various trigger conditions in Nov./Dec. 2002.*

Future runs, especially for heavier collision systems require therefore a threefold trigger which is able to reduce the event rate up to a factor of 10^{-4} by preselecting lepton pair candidates to about 100 events/sec. The first level trigger selects central events via the multiplicity information from the TOF scintillators. The second level trigger selects events with dilepton pairs within a given invariant mass range. Pattern recognition units detect electron or positron signatures from Cherenkov rings and electromagnetic showers as well as appropriate time of flight candidates in the TOF wall. In the third level trigger, tracking information from the MDC will be used to reduce the number of fake leptons.
During the beam time we stored 2.13×10^8 events at high magnetic field generated by a current of $I = 2500$ A. A few files were taken without magnetic field for calibration purposes.
A restricted data analysis is available already during the data collection stage and can be used for the monitoring of different parameters to check the detector performance.
As an example of the monitoring process the vertex distribution along the beam axis around the target region is shown in Fig. 1. The reconstruction has been performed only with a drift cell combination. The insert of Fig. 1 shows, that the vertex reconstruction with this cluster finding algorithm is able to identify the two carbon target discs separated by a distance of $\Delta Z = 20$ mm along the beam axis.

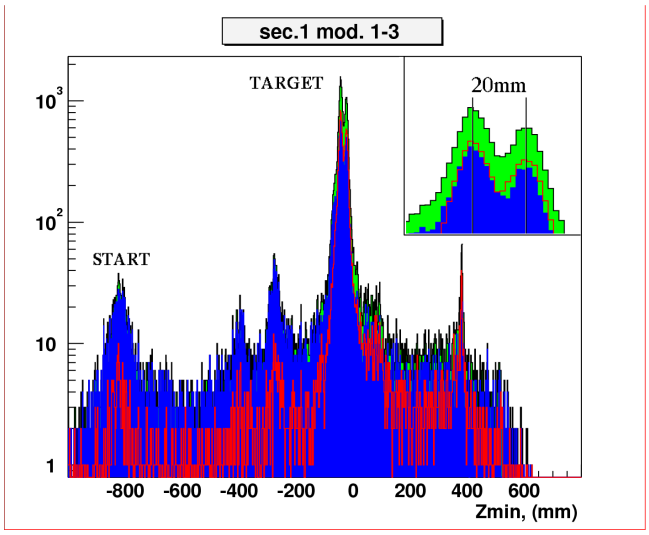

Fig. 1 *Vertex reconstruction with the smallest MDC–I and a large MDC–III in one HADES sector. The cluster finding method requires that the magnet is off to get straight flight pathes. The insert is explained in the text.*

The HADES spectrometer is designed to allow a measurement of the dilepton mass spectrum with an invariant mass resolution of about one percent. Fig. 2 shows the result of the simulated dilepton mass spectrum for the HADES spectrometer. Only conventional sources have been included in the simulation.
The present measurement can determine the e^+e^- yield in the invariant mass region around 500 MeV/c^2. In this region the the DLS collaboration reported [2] a puzzling large yield. The excess of the dileptons in the same invariant mass region, observed by the CERES collaboration [3], can be explained by a strong reshaping of the ρ meson strength. It is therefore important to have sufficiently rich statistics to resolve the ρ and ω peaks to address this issue in more detail.

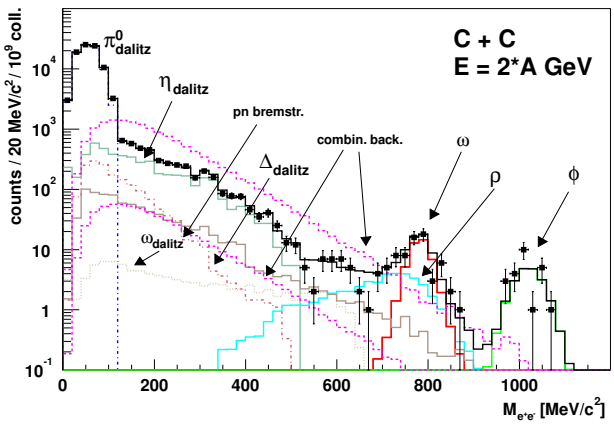

Fig. 2 *Expected frequency of e^+e^- pairs generated in C+C collisions at 2 AGeV versus invariant dilepton mass. The spectra are obtained under realistic assumptions for detector properties. The low (high) combinatorial background is obtained with the best (worst) spatial drift chamber resolution. An amount of 9×10^4 e^+e^- pairs is generated in 2×10^9 target collisions.*

In 2003 one of the main foci of the collaboration is the analysis of the data taken in 2002; this includes the optimization of the analysis software.
Moreover we plan to improve the reliability of the the detector components. For this case one important point is the understanding of the drift chamber aging.
New measurements with proton and pion beams are foreseen for the second half of 2003.

[1] http://www-hades.gsi.de
[2] H. S. Matis et al. (DLS collaboration), Nucl. Phys. A583 (1995) 617c
[3] G. Agakichiev et al. (CERES collaboration), Phys. Rev. Lett. 75 (1995) 1272

Sub-Threshold Phi Meson Production in the Reaction Ni (1.93 A·GeV) + Ni [B,D]

R. Kotte for the FOPI collaboration

Previous exploratory studies of sub-threshold $\phi(1020)$ meson production in central Ni+Ni reactions at 1.93A·GeV have been improved by systematic reanalyses and cross checks. Scanning through $4.7 \cdot 10^6$ central events which comprise about 10% of the total cross section, within the CDC/Barrel acceptance acceptance ($K^{\pm}$ momentum and angular ranges: $p_{t,K} > 100$ MeV/c, $p_{lab,K} < 600$ MeV/c, $40^o < \theta_K < 140^o$) of the FOPI detector setup [1] a number of $23 \pm 7 \pm 2$ correlated K^+K^- meson pairs have been identified (cf. fig. 1). Within this acceptance, the analysis delivers a multiplicity of

$$P_{\phi}^{CDC/Bar} = (1.9 \pm 0.6 \pm 0.95) \cdot 10^{-5}$$

of ϕ mesons per central collision [2]. As a prerequisite, $K^{\pm}$ pair detection efficiencies have been determined performing a complete GEANT simulation.

Assuming an isotropic thermal ϕ source of temperature $T \simeq 90$ MeV, this yield can be extrapolated to a 4π production probability per central collision of

$$P_{\phi} = (2.3 \pm 0.7 \pm 1.1) \cdot 10^{-3}$$

which increases (decreases) by a factor of 2 if the inverse slope parameter T is decreased (increased) to 70 (130) MeV. Comparing the total ϕ yield with the total K^- production probabilities as deduced from FOPI [3] and KaoS [4, 5] experiments (rescaled according to beam energy and centrality differences), we find a surprisingly large ϕ/K^- ratio of at least 0.4. This observation gives rise to the conjecture that presently the K^- production is underestimated due to extrapolations based on rather restricted experimental acceptances. Especially at low c.m. kinetic energies the spectra [4] exhibit hints to an antikaon enhancement on top of the usually observed exponentially declining distribution. Note that such a surplus of low-energy yield may be caused by the decay of intermediate ϕ mesons. (The decay of thermal ϕ mesons with typical inverse slopes of 70-130 MeV would result in daughter $K^{\pm}$ mesons with inverse slopes of only 50% - 60% of that value.) Therefore, future experiments devoted to strangeness production in heavy-ion collisions at sub-threshold energies should aim at sufficient acceptance at low transverse momenta around midrapidity.

The measured yields of correlated K^+K^- pairs as well as the total ϕ production probability have been compared with the output of different transport approaches. The IQMD transport code underestimates the yields in the CDC/Barrel acceptance region by more than an order of magnitude [6]. However, a remarkable step is reached with the most recent BUU approach which includes channels involving intermediate ρ mesons [7]. Within the experimental uncertainties, this code is the first one being able to reproduce the ϕ yield within the FOPI acceptance.

If - in further experiments with statistical more significant results - the unexpectedly high ϕ production [2] will be reconfirmed, then the channel $\phi \rightarrow K^+K^-$ would play a comparably important role for K^- meson production in heavy-ion reactions at subthreshold energies as in near-threshold proton-proton collisions where about 50 % of the antikaons stem from intermediate ϕ mesons [8].

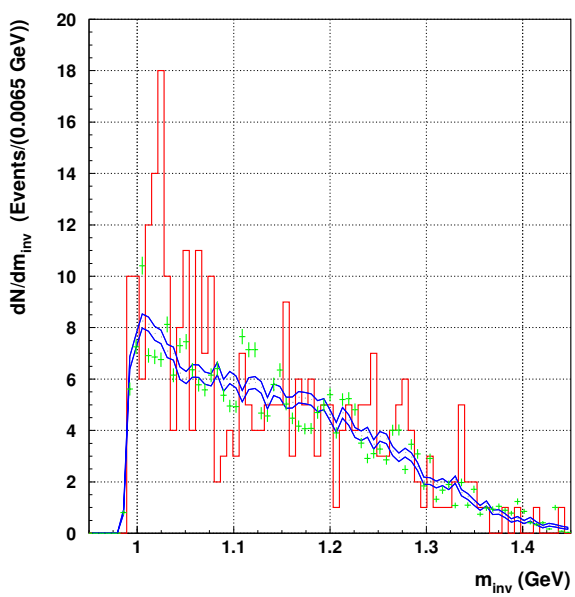

Fig. 1 *The invariant mass distribution of K^+K^- pairs ideintified within the CDC/Barrel acceptance (histogram). The two smooth lines and the error bars show the uncorrelated background obtained via event mixing techniques under different conditions [2].*

[1] A. Gobbi et al. (FOPI collaboration), Nucl. Instr. Meth. A 325 (1993) 156;
J. Ritman for the FOPI collaboration, Nucl. Phys. (Proc. Suppl.) B 44 (1995) 708
[2] A. Mangiarotti and the FOPI collaboration, Nucl. Phys. A 714 (2003) 89
[3] K. Wiśniewski et al. (FOPI collaboration), Eur. Phys. J. A 9 (2000) 515
[4] R. Barth et al. (KaoS collaboration), Phys. Rev. Lett. 78 (1997) 4007
[5] M. Menzel et al. (KaoS collaboration), Phys. Lett. B 495 (2000) 26
[6] C. Hartnack and J. Aichelin, private communication
[7] H. W. Barz, M. Zétényi, G. Wolf, B. Kämpfer, Nucl. Phys. A 705 (2002) 223
[8] F. Balestra et al. (DISTO collaboration), Phys. Lett. B 468 (1999) 7

Inclusive K-meson and Pion Production in Proton-Nucleus Collisions at SIS Energies[B, G]

W. Scheinast and L. Naumann for the KaoS Collaboration:
I. Böttcher[3], M. Dębowski, F. Dohrmann, A. Förster[2], E. Grosse, B. Kamys[5], P. Koczoń[1], B. Kohlmeyer[3], F. Laue[1], M. Menzel[3], L. Naumann, H. Oeschler[2], F. Pühlhofer[3], W. Scheinast, Ch. Schneider, E. Schwab[1], P. Senger[1], Y. Shin[4], H. Ströbele[4], Ch. Sturm[2], G. Surówka[5], F. Uhlig[2], A. Wagner, W. Waluś[5] and H.W. Barz

In 1998 the KaoS collaboration carried out an experiment to investigate the production of kaons and antikaons in proton-nucleus collisions. The Kaon Spectrometer KaoS [1] at the heavy-ion synchrotron SIS at GSI Darmstadt was used to observe charged mesons emitted from a C or Au target struck by the first proton beam at GSI. The kinetic beam energies $T_{\rm kin}$ (1.6, 2.5, and 3.5 GeV) were close to the production threshold of K^+ (1.58 GeV) and K^- (2.5 GeV) in nucleon-nucleon collisions. The whole set of K^+ and K^- spectra, covering four observation angles (32°, 40°, 48°, 56°), was presented in [2].

In addition to these measurements there were also collected data on π^+ and π^- production for a subset of the aforementioned parameters. Their recent analysis opened a new aspect of the interpretation of the $p + A$ reaction dynamics.

To estimate the total cross sections we adjusted to both K- and π-mesons a Maxwell-Boltzmann distribution. For each inclusive reaction (*one* particle species, target nucleus, bombarding energy) all available spectra, i. e. the entire angular distribution, were described by a single function

$$\frac{d^3\sigma}{dp^3} = A \cdot \exp\left(-\frac{E'}{E_0}\right) ,$$

where E' is the total energy of the particle in the frame of maximun isotropic emission moving with velocity $\beta_{\rm em}$. Because there is no a priori reason to choose a particular emission frame, $\beta_{\rm em}$ varied freely together with A and E_0. So, we obtained for each reaction three parameters $(A, E_0, \beta_{\rm em})$, two of which are presented in Fig. 1 (c, d). Fig. 1a shows the total cross section $\sigma_{\rm tot}$ obtained from integrating the Maxwell-Boltzmann distribution.

The energy dependence of $\sigma_{\rm tot}$ and E_0 is much smaller for $\pi^\pm$ than for $K^\pm$ because the pions are produced far above their threshold energy of about $T_{\rm kin} = 0.29$ GeV. In Fig. 1b the cross section is normalized to the geometrical one, yielding the multiplicity

$$M = \frac{\sigma_{\rm tot}}{\sigma_{geo}} \quad \text{with} \quad \sigma_{geo} = \pi\left(1.9\,\text{fm} + \text{A}^{1/3} \cdot 1.2\,\text{fm}\right)^2 .$$

If the target nucleus was an opaque object for the impinging proton, the multiplicity would be equal for

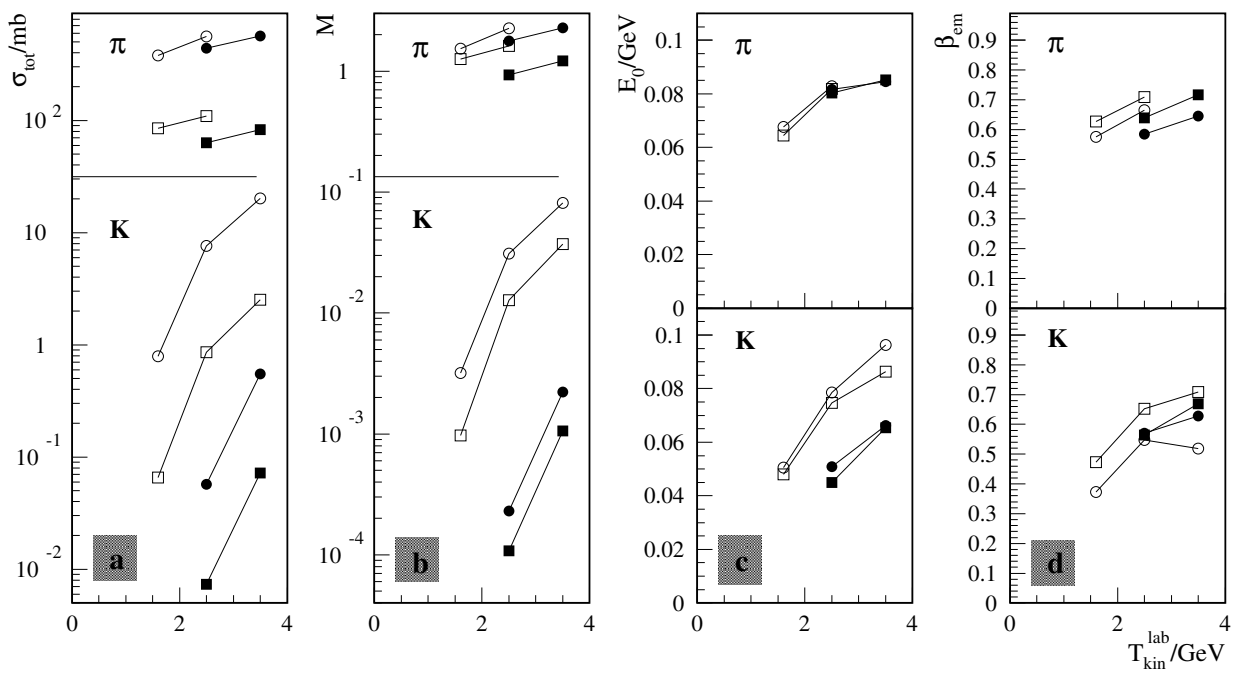

Fig. 1 *Total cross sections (a), multiplicities (b) and fit parameters (c,d) resulting from the adjustment of a Maxwell-Boltzmann distribution to the measured spectra. Open symbols denote* K^+, π^+, *closed symbols* K^-, π^-. *The circles refer to the reaction* $p + \text{Au}$, *squares to* $p + \text{C}$. T_{kin} *is the kinetic projectile energy.*

[1]GSI Darmstadt, [2]TU Darmstadt, [3]Univ. Marburg, [4]Univ. Frankfurt, [5]Univ. Cracow

both targets. Since this is not the case, the depth, i. e. the volume, plays a role in all these reactions. The production channels are very different for K^+ and K^- because of strangeness conservation; e. g. the threshold reaction in proton-proton collisions is given by $pp \rightarrow pK^+\Lambda$ and $pp \rightarrow ppK^+K^-$. This leads to very different threshold energies and explains the bigger difference for the quantities σ_{tot} and E_0 between K^+ and K^- than between π^+ and π^-.

As can be observed in Fig. 1c, the slope parameter E_0 is mostly larger for $\pi^\pm$ than for $K^\pm$. This is also caused by different production channels and, furthermore, by different particle masses. So, there remains more energy for the motion of pions.

Finally, the source velocities β_{em} are related to the number of reacting nucleons in the production process. Since particles near threshold can scarcely be produced in primary proton-nucleon collisions, one expects a higher number of participating nucleons for K^- and K^+ rather than for pions. This results in a lower source velocity, as can be seen in Fig. 1d. For a similar reason we see a lower β_{em} in the heavier nucleus Au compared to C.

In the following the pion data obtained at KaoS have been compared with all available data below 10 G*e*V, for which the value of the total cross section had been mentioned explicitly for inclusive pion production in proton-nucleus collisions. The cross sections in p + C are displayed as a function of the proton bombarding energy for π^+ in Fig. 2 and for π^- in Fig. 3. The only data point for π^+ at 1.6 G*e*V from [5] fits well to the KaoS data as shown in Fig. 2. We present the first data for 2.5 and 3.5 G*e*V. All data are in agreement with the BUU calculation in the range from 0.5 G*e*V up to 3.5 G*e*V. No total cross section data are available for the pion production in p + Au collisions.

Tab. 1 shows a comparision of the KaoS data and transport calculations with the BUU code [7]. For the carbon target our experimental yields are in good agreement with the theoretical ones. For Au, a heavy target, the theoretical yields overestimate the experimental yields at 2.5 G*e*V and 3.5 G*e*V for both the positive and the negative pions. The overestimate amounts to more than 50 percent for the π^- cross sections at 2.5 G*e*V and 3.5 G*e*V.

	1.6 G*e*V	2.5 G*e*V		3.5 G*e*V	
	π^+	π^+	π^-	π^-	Target
KaoS	85	109	63	82	C
BUU	89	117	66	78	
KaoS	381	558	439	566	Au
BUU	356	650	659	946	

Tab. 1 *Comparison between experiment and theory for π^+ and π^- cross sections. 'KaoS' denotes the preliminary data presented here, whose systematic errors were valued at 20 %, 'BUU' the transport calculation according to [7].*

So, varying many parameters our data allow for a comprehensive analysis of the kinematics and dynamics in proton-nucleus collisions. All the relations seen can be studied in more detail using complementary data from COSY/ANKE or ITEP/FHS. A combined investigation will be the next step of the ongoing work, supported by various transport calculations.

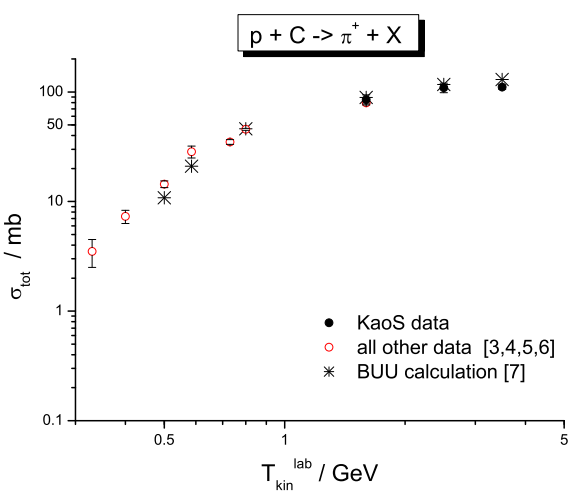

Fig. 2 *Total π^+ cross sections versus proton bombarding energy. The open circles refer to the worldwide available data [3, 4, 5, 6], the full circles to the new yields from the KaoS experiment. The asterisks refer to BUU calculations [7].*

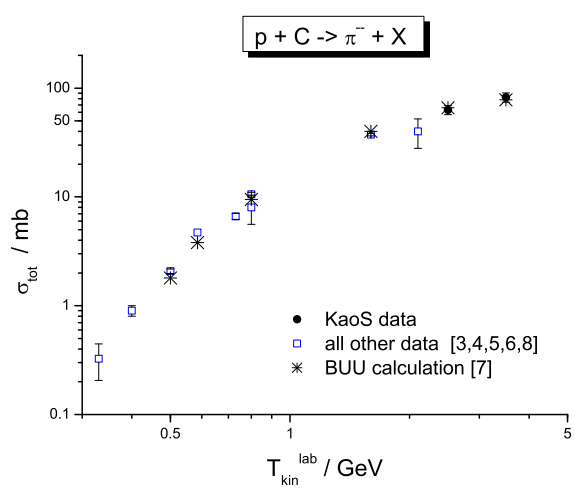

Fig. 3 *Total π^- cross sections versus proton bombarding energy. The open circles refer to the worldwide available data [3, 4, 5, 6, 8], the full squares to the new yields from the KaoS experiment. The asterisks refer to BUU calculations [7].*

[1] P. Senger et al., Nucl. Instr. Meth. A 327 (1993) 39
[2] W. Scheinast et al., Acta Physica Polonica B, Meson 2002 Workshop Proc. (2003) 493
[3] J. F. Crawford et al., Phys. Rev. C 22 (1980) 1184
[4] D. R. F. Cochran et al., Phys. Rev. D 6 (1972) 3085
[5] M. Trzaska et al., Z. Phys. A 340 (1991) 325
[6] N. J. DiGiacomo et al., Phys. Rev. C 31 (1985) 292
[7] Gy. Wolf et al., Nucl. Phys. A 552 (1993) 549
[8] S. Nagamiya et al., Phys. Rev. C 24 (1981) 971

Hyperon-Nucleon Bound States and the Electroproduction of Strangeness on $^{3,4}He$

F. Dohrmann for the Jefferson Lab E91016 Collaboration

The high intensity CW electron beams at the Jefferson Lab provide the possibility to study with high precision the electroproduction of strangeness. Experiment E91016 measured $A(e,e'K^+)YX$ for ^1H, ^2H, ^3He, ^4He, C and Al targets. Here we focus on the results for $^{3,4}He$. Angular distributions of K^+ were measured at forward angles with respect to the virtual photon, γ^*. The experiment was performed in Hall C of Jefferson Lab. For a discussion of the experimental method see [1]. The spectrometer angle for detecting the e' was kept fixed; the K^+ arm was varied. Three different angles between γ^* and K^+ were studied, $\theta^{lab}_{\gamma^* K} = 0^o$, $\simeq 6^o$, and $\simeq 12^o$.
In a previous experiment the reaction $^1H(e,e'K^+)Y$ was studied [1] using the same setup. The missing mass distribution for $^1H(e,e'K^+)Y$ exhibits two peaks corresponding to the Λ and Σ^0 hyperons. The acceptance as well as radiative processes are computed by Monte Carlo simulations. A parametrization of the $\gamma^* N$ cross section was derived by fitting the kinematic dependences of the $^1H(e,e'K^+)Y$ cross section over the acceptance [1]. This parametrization has been used for $A = 3,4$ [2], where the momentum and in-medium energy of the struck nucleon in the target are taken from spectral functions[3]. Excess yields close to the Λn and ΣN thresholds described in an effective range model[4]. For $A = 3,4$ the agreement between simulation and data is shown in Fig. 1. Near the quasifree Λ-thresholds for $A = 3,4$, Fig. 1 exhibits narrow structures, independent of the angle. These are attributed to the $^3_\Lambda H$ and $^4_\Lambda H$ bound states and are centered at the right binding energy. While barely discernible for ^3He at $\theta^{lab}_{\gamma^*,K} = 0^o$, it becomes evident for $\theta^{lab}_{\gamma^*,K} = 6^o, 12^o$. It is clearly visible for all measured angles for ^4He. Further quantitative statements are expected after completing the analysis of the data. A kinematic model derived from $^1H(e,e'K^+)Y$ is used in impulse approximation to describe the quasifree production of hyperons on $^{3,4}He$. A spectral function is used to describe the struck nucleon in the target. We observe clear evidence for the $^3_\Lambda H$, $^4_\Lambda H$ bound states produced in electroproduction.

Acknowledgement: This work has been supported in part by a Feodor Lynen-Fellowship of the Alexander v. Humboldt-Foundation.

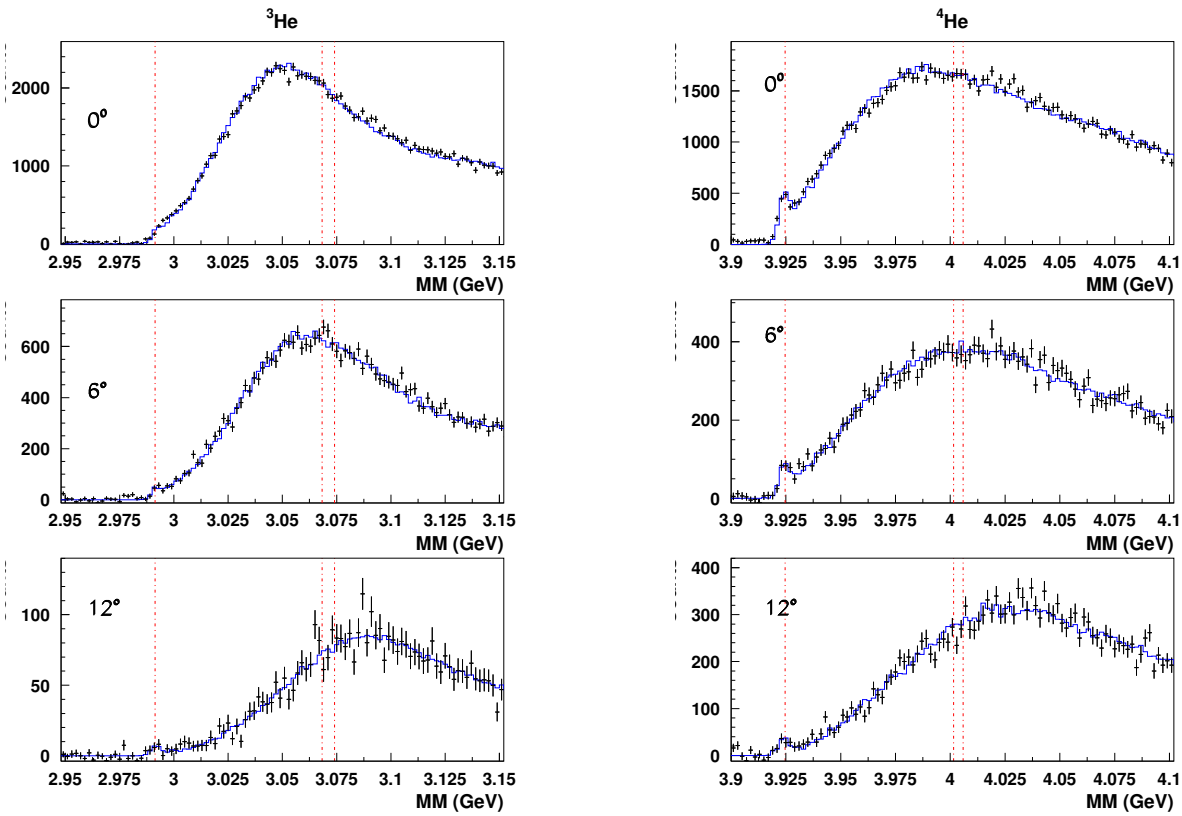

Fig. 1 *Missing mass distributions for $^{3,4}He(e,e'K^+)$ at $\theta^{lab}_{\gamma^*,K} = 0^o, 6^o, 12^o$. Simulations (solid line) of the quasifree production of Λ, Σ^0, Σ^- on $^{3,4}He$, incl. FSI corrections and $^{3,4}He(e,e'K^+)^{3,4}_\Lambda H$ are added. The thresholds for quasifree Λ, Σ^0, Σ^- production for $A = 3,4$ are shown (dot-dashed line).*

[1] B. Zeidman et al., Nucl. Phys. A 691 (2001) 37c
[2] A. Uzzle , PhD thesis, Hampton University (2002)
[3] O. Benhar et al., Nucl. Phys. A 579 (1994) 493
[4] D. Gaskell et al., Phys. Rev. Lett. 87 (2001) 202301

In-Medium Spectral Change of ω Mesons as a Probe of Four-Quark Condensate [B]

S. Zschocke, O.P. Pavlenko[1], B. Kämpfer

Our QCD sum rule evaluations [1] showed that the in-medium change of the four-quark condensate plays a crucial rule for modifications of the ω spectral function. In particular, the sign of the ω meson mass shift is changed by variation of a parameter which describes the strength of the density dependence of the four-quark condensate. In addition, the difference of the vector and axial vector correlators is proportional to the four-quark condensate. Therefore, the sign of the ω meson mass shift, to be measured via the e^+e^- channel at HADES, can serve as a tool for determining of how fast chiral symmetry restoration is approached with increasing density.

We use a correlator satisfying a twice subtracted dispersion relation to get the truncated Borel QCD sum rule

$$\frac{\int_0^{s_0} ds\; S(s,n)\; \mathrm{e}^{-s/M^2}}{\int_0^{s_0} ds\; S(s,n) s^{-1}\; \mathrm{e}^{-s/M^2}} = \tag{1}$$

$$\frac{c_0 M^2[1-\left(1+s_0/M^2\right)\mathrm{e}^{-s_0/M^2}] - c_2/M^2 - c_3/M^4}{c_0\left(1-\mathrm{e}^{-s_0/M^2}\right) + c_1/M^2 + c_2/M^4 + \frac{1}{2}c_3/M^6 - \frac{9n}{4M_N}/M^2}$$

where the imaging any part of in-medium vector meson propagator in the vicinity of the pole mass is

$$S(s,n) = -\frac{\mathrm{Im}\Sigma(s,n)}{(s-m_\omega^2(n))^2 + (\mathrm{Im}\Sigma(s,n))^2} \tag{2}$$

with $\mathrm{Im}\Sigma(s,n)$ as imaginary part of the in-medium ω meson self-energy and $m_\omega(n)$ as its physical mass. Within the linear density approximation, the ω meson self-energy is given by $\Sigma(E,n) = \Sigma^{\mathrm{vac}}(E) - n\; T^{\omega N}(E)$ with $E = \sqrt{s}$ as the ω meson energy, $\Sigma^{\mathrm{vac}}(E) = \Sigma(E, n=0)$ and $T^{\omega N}(E)$ as the off-shell forward ω-nucleon scattering amplitude in free space. c_i are the Wilson coefficients including the condensates. The coefficient c_3 contains also the four-quark condensates $\langle(\overline{q}\gamma_\mu\lambda^a q)^2\rangle_n$ and $\langle(\overline{q}\gamma_\mu\gamma^5\lambda^a q)^2\rangle_n$. The standard approach to estimate their density dependence consists in the mean-field approximation. Within such an approximation the four-quark condensates are proportional to $\langle\overline{q}q\rangle_n^2$, i.e. their density dependence is governed by the square of the chiral quark condensate. We go beyond the mean-field approximation and employ

$$\langle(\overline{q}\gamma_\mu\gamma^5\lambda^a q)^2\rangle_n = -\langle(\overline{q}\gamma_\mu\lambda^a q)^2\rangle_n = \frac{16}{9}\langle\overline{q}q\rangle_0^2\;\kappa_0\;\left[1+\frac{\kappa_N}{\kappa_0}\frac{\sigma_N}{m_q\langle\overline{q}q\rangle_0}\;n\right]\;. \tag{3}$$

In vacuum, $n=0$, the parameter κ_0 reflects a deviation from the vacuum saturation. To control the deviation of the in-medium four-quark condensate from the mean-field approximation we introduce the parameter κ_N. The limit $\kappa_N = \kappa_0$ recovers the mean-field approximation, while the case $\kappa_N > \kappa_0$ ($\kappa_N < \kappa_0$) is related to a stronger (weaker) density dependence.

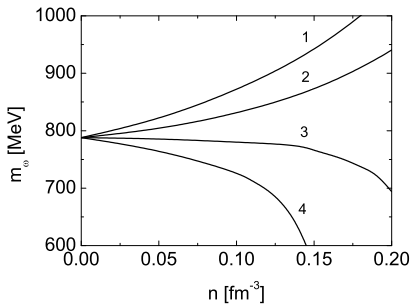

Fig. 1 *Density dependence of the ω meson mass for various values of the parameter κ_N.*

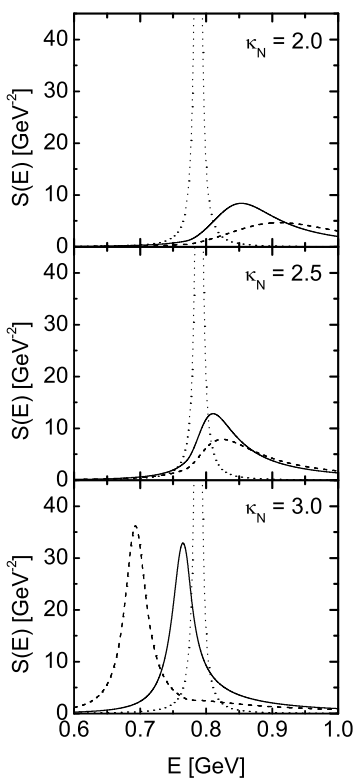

Fig. 2 *The spectral function of the ω meson for $\kappa_N = 2$, 2.5, 3. Solid curves correspond to normal nuclear density ($n = n_0 = 0.15\mathrm{fm}^{-3}$), while dotted and dashed curves are for vacuum and $n = 0.2\mathrm{fm}^{-3}$, respectively.*

We vary the parameter κ_N to estimate the contribution of the four-quark condensates with respect to the main trends of the in-medium modification of the ω meson spectral function. Numerical results of the QCD sum rule evaluation are displayed in figs. 1 and 2. For further details see [2].

[1] S. Zschocke, O.P. Pavlenko, B. Kämpfer, nucl-th/0202134, Eur. Phys. J. A15 (2002) 529
[2] S. Zschocke, O.P. Pavlenko, B. Kämpfer, hep-ph/0212201

[1] *Institute of Theoretical Physics, Kiev, Ukraine*

Modifications of the Di-Electron Spectra from ϕ Meson Decays [B]

B. Kämpfer, O.P. Pavlenko[1], S. Zschocke

The experiments with HADES provide the opportunity to measure via the di-electron channel in-medium modifications of the light vector mesons. There are at least two reasons for studying the in-medium modifications of the ϕ meson. First, within QCD sum rule approaches, the ϕ mass shift in nuclear matter is directly related to the in-medium change of the strange quark condensate $\langle\bar{s}s\rangle$ and, therefore, provides a direct access to the chiral symmetry restoration. This is in contrast to the ρ and ω mesons whose in-medium mass shifts are sensitive to the poorly known four-quark condensate. The second reason to focus on the ϕ meson in-medium effects is related to the interest in understanding the hidden strangeness content of the nucleon and nuclear matter.

Within the linear density approximation the strange quark condensate in hadronic matter can be written as

$$\langle\bar{s}s\rangle_{\rm matter} = \langle\bar{s}s\rangle_0 + \sum_h \frac{\langle h|\bar{s}s|h\rangle}{2M_h}\, n_h, \qquad (1)$$

where $\langle\bar{s}s\rangle_0$ is the vacuum condensate, $\langle h|\bar{s}s|h\rangle$ denotes the matrix element corresponding a one-hadron state, n_h stands for the hadron density, and the sum runs over all hadrons in the medium. For the nucleon matrix element the dimensionless parameter y is widely used to specify the strangeness content in the nucleon via $\frac{\langle N|\bar{s}s|N\rangle}{2M_N} = y\frac{\sigma_N}{2m_q}$, where σ_N is the nucleon sigma term and m_q the light quark mass. The strangeness content of the nucleon is a yet poorly known quantity and matter of debate so far; therefore we shall vary y. We also simplify eq. (1) by the replacement $\sum_h \to y\frac{\sigma_N}{2m_q}\, n_N$ since the presence of other hadron states can only increase y. Basing on the above parameterization of the strange quark condensate in hadron matter one can perform the QCD sum rule evaluations which give the density dependence in leading order $m_\phi = m_\phi^{\rm vac}(1-0.14y)\frac{n_N}{n_0}$.

The di-electron rate from the in-medium ϕ meson decays in ideal gas approximation at temperature T is

$$\frac{dN}{d^4x\, d^4Q} = \frac{2\,{\rm e}^{-u\cdot Q/T}}{(2\pi)^3} M\Gamma_{\phi\to e^+e^-} A(M^2, m_\phi, \Gamma^{\rm tot}), \quad (2)$$

where $\Gamma_{\phi\to e^+e^-}$ and $\Gamma^{\rm tot}$ are the di-electron and total decay widths, Q_μ denotes the four-momentum of the pair with invariant mass $M^2 = Q^2$, and u_μ is the four-velocity of the medium. We use the Breit-Wigner parameterization of the spectral function A.

To obtain the di-electron spectrum one needs to specify the space-time evolution of the matter. We employ here a variant of the blast wave model [1] with two scenarios for the ϕ multiplicity: (i) the number of ϕ mesons is assumed to be governed by chemical equilibrium, and (ii) the ϕ mesons are still in thermal equilibrium with the bulk of matter but do not maintain chemical equilibrium; to be specific, we take the number as constant. After freeze-out, the ϕ meson decays in vacuum contribute to the spectrum according to [1,2].

The numerical simulations show that, due to the expansion of nuclear matter after the maximum compression stage in the course of heavy-ion collisions, the di-electron spectrum in the ϕ meson region is governed by the superposition of peak positions within a certain interval determined by the nucleon density (see figs. 1 and 2). This causes an effective broadening of the ϕ peak when measured by e^+e^- pairs. The width of the broadening (see fig. 3) appears almost insensitive to the collision broadening in a nuclear medium but is directly related to the density dependence of the strange quark condensate $\langle\bar{s}s\rangle$. This gives a good opportunity to probe the in-medium modification of $\langle\bar{s}s\rangle$ with HADES in heavy-ion collisions.

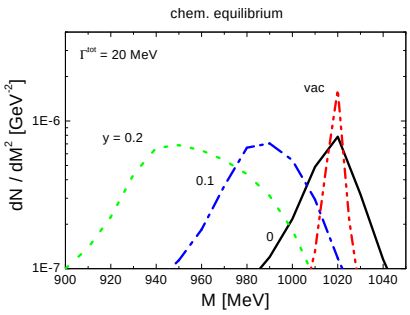

Fig. 1 *Di-electron spectra from ϕ meson decays as a function of invariant mass for case (i), i.e., assumed chemical equilibrium.*

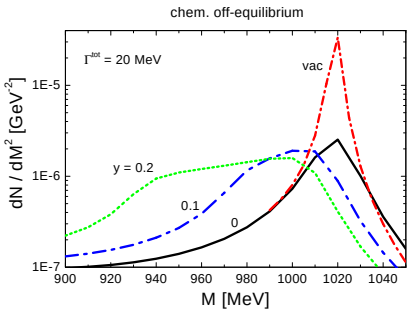

Fig. 2 *As in fig. 1 but for case (ii), i.e., chemical off-equilibrium of ϕ mesons.*

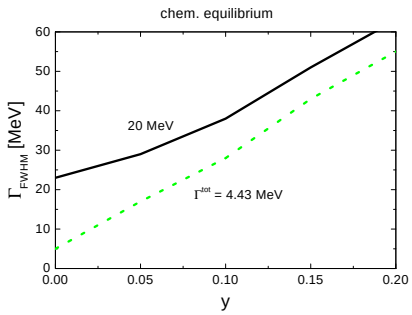

Fig. 3 *The full width half maximum of the ϕ peak as a function of the strangeness content y of nuclear matter.*

[1] B. Kämpfer, O.P. Pavlenko, Eur. Phys. J. A 10 (2001) 101
[2] B. Kämpfer, O.P. Pavlenko, S. Zschocke, nucl-th/0211067, Eur. Phys. J. A (2003) in print

[1] *Institute of Theoretical Physics, Kiev, Ukraine*

Tagging the $pn \to d\phi$ Reaction by Backward Protons in $pd \to d\phi p_{sp}$ Processes [B]

L.P. Kaptari[1], B. Kämpfer, S.S. Semikh[2]

The spectator technique [1] offers one possibility to isolate to a large extent the quasi-free meson (M) production reaction at a neutron when a proton beam impinges on a deuteron target. Since the final state interactions in the pn system differ for singlet and triplet states and can be large at threshold, it is of great advantage to consider the particular reaction $pn \to dM$, as the deuteron (d) is in one well defined state.

In this note we continue our previous study [2] and analyze the complete reaction $pd \to dMp_{sp}$ to test to which extent the spectator technique really selects a quasi-free reaction at the neutron in the deuteron target. In other words, we are going to derive a factorization theorem showing kinematical conditions for which the total cross section $\sigma(pd \to dMp_{sp})$ factorizes in a part depending on the target deuteron characteristics and a part $\sigma(pn \to dM)$. In doing so we select as a sufficiently transparent example the ϕ production. The reasons are obvious: (i) the elementary ϕ production amplitude is simple, (ii) the ϕ meson is interesting with respect to OZI rule [3] and hidden strangeness in the nucleon, and (iii) the ϕ meson is important with respect to both the inclusive K^- [4] production and the e^+e^- decay channel to be studied at HADES in near future.

With the technique described in [2,5] we calculate the process $p_p + p_d = p'_d + p_\phi + p'_p$ at kinetic energies of the incoming proton corresponding to those achievable at the Cooler Synchrotron COSY $T_p \leq 2.7$ GeV. The deuteron is here supposed to be detected in the forward direction, i.e., in direction of the incoming proton with relativistic energy, $T'_d \sim 1$ GeV, and, contrarily, the final (spectator) proton is slowly moving in the backward direction ($\theta_{sp} > 90^0$, $p'_p < 100$ MeV). The main contribution to the process comes then from the spectator mechanism, where the incoming proton interacts with the internal neutron of the deuteron and produces a meson and a deuteron in the final state. The second proton in the deuteron acts merely as a spectator. The spectator mechanism is depicted in fig. 1.

In fig. 2, the differential cross section is presented as a function of the deuteron momentum for the specific choice of variables $\theta'_d = 0^0$, and $\theta'_p = 130^o$. The kinetic energy of the initial proton is $T_p = 2.69$ GeV. Fig. 2 highlights that different models for the deuteron wave function result in vastly different cross sections. This is because the integration over the internal momentum in the final deuteron covers the region of the minimum of the S wave where different models provide essentially different wave functions.

Guided by the very proximity of the numerical results for cross section and polarization observables based on the exact formulae and on the factorized ones [5], we find that, for special kinematical conditions, selection rules are operative immediately causing the above anticipated factorization. This is equivalent to an omission of the contribution of the deuteron D wave at small values of the spectator momentum. This provides a theoretical basis for studying threshold-near processes at quasi-free neutrons.

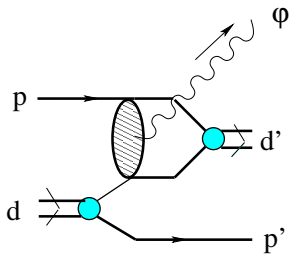

Fig. 1 *Diagram of the considered process.*

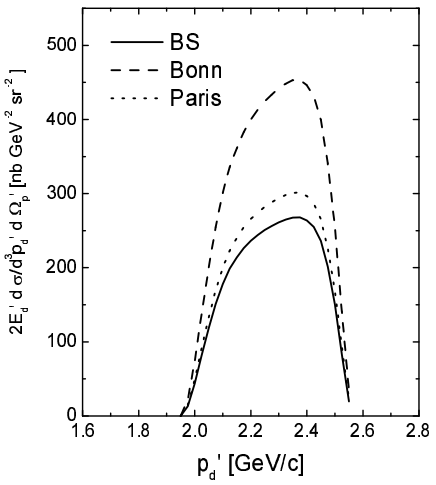

Fig. 2 *Differential cross section of the reaction $pd \to d\phi p_{sp}$ as a function of the deuteron momentum p'_d at $p_p = 3.505$ GeV/c, $\theta_{d'} = 0^o$, $\theta_{p'_{sp}} = 130^o$. The full curve is based on our solution of the Bethe-Salpeter equation, while dashed and dotted curves use Bonn and Paris deuteron wave functions.*

[1] H. Calén et al., Phys. Rev. Lett. 79 (1997) 2642, 80 (1998) 2069, Phys. Rev. C 58 (1998) 2667;
R. Bilger et al., Nucl. Phys. A 663 (2000) 1053c; Nucl. Instr. Meth. A 457 (2001) 64;
M. Büscher et al., "Study of ω and ϕ meson production in the reaction $pd \to dVp_{sp}$ at ANKE", proposal #75
[2] L.P. Kaptari, B. Kämpfer, Eur. Phys. J. A 14 (2002) 211
[3] A.I. Titov, B. Kämpfer, B.L. Reznik, Phys. Rev. C 65 (2002) 065202
[4] B. Kämpfer, R. Kotte, C. Hartnack, J. Aichelin, J. Phys. G 28 (2002) 2035c
[5] L.P. Kaptari, B. Kämpfer, S.S. Semikh, nucl-th/0212066

[1] *Department of Physics, University of Perugia, and INFN Sezione di Perugia, via A. Pascoli, I-06100, Italy*
[2] *Bogoliubov Laboratory of Theoretical Physics, JINR, Dubna 141980, Russia*

Measuring the Effect of ϕ Meson Life Time in Proton-Nucleus Collsions [B]

H.W. Barz, B. Kämpfer, M. Zétényi[1]

The study of in-medium properties of hadrons in nuclear matter is an important subject of contemporary strong interaction physics. Over the last decade a dropping in-medium mass has been considered a precursor phenomenon of chiral symmetry restoration. Using QCD sum rules and chiral dynamics the mass change of various hadrons has been predicted. Recent measurements of kaon yields generated in heavy-ion collisions seem to require a drastic reduction of the K^- mass by about 200 MeV in matter while the measured transverse flow hints to a slight increase of the K^+ mass.

The consequence of these changes of the kaon masses is that the decay width of a ϕ meson in matter should dramatically increase. The small vacuum width of 4.4 MeV is due to the small kinetic energy in the dominant K^+K^- and $K^0\bar{K}^0$ channels. If the rest mass of the kaon pair decreases as predicted then the width should increase by an order of magnitude which leads to a ϕ life time of less than 5 fm/c. This would mean that most of the ϕ mesons decay inside the nucleus mainly into kaon pairs. These kaon pairs are usually used to deduce the number of the produced ϕ mesons. However for kaon pairs created inside the reaction zone there is a great chance that at least one particle of the pair is scattered or absorbed, such that they cannot anymore signal their original invariant mass. This effect will strongly depend on the size of the nuclear system and will lead to a characteristic dependence of the ϕ meson yield on the target-mass number A.

To investigate this effect we use the BUU code with the elementary cross sections for ϕ meson production [1] and kaon rescattering and absorption. We calculate the ϕ production for collisions of protons for three target nuclei, ^{12}C, ^{64}Cu and ^{197}Au at a bombarding energy of 2.5 GeV. For the K^+, K^- and ϕ mesons we use the following scalar potentials as a function of the nuclear matter density n:

$$U_\phi = -0.025\, m_\phi \frac{n}{n_0}, \quad (1)$$

$$U_{K+} = 0.04\, m_K \frac{n}{n_0}, \quad (2)$$

$$U_{K-} = -0.39\, m_K \frac{n}{n_0}, \quad (3)$$

$$U_{K-} = -[0.11 + 0.266 \exp(-2.5p/GeV)] \times m_K \frac{n}{n_0}. \quad (4)$$

The strengths of these potentials reflect the general ideas derived from analyses of data and theoretical investigations [2-4]. The momentum dependence in Eq. (4) has been derived in [5]. The decay width of the ϕ meson is assumed to be proportional to the third power of the kaon momenta p in matter.

In the calculation we follow the evolution of the ϕ mesons and in the case of their decay also the evolution of the kaon pairs. We determine the numbers of ϕ mesons that survive together with the number of kaon pairs which do not suffer encounters with other particles. In Fig. 1 we present the cross sections (rescaled by the factor $A^{-2/3}$) calculated without and with the potentials (1-4).

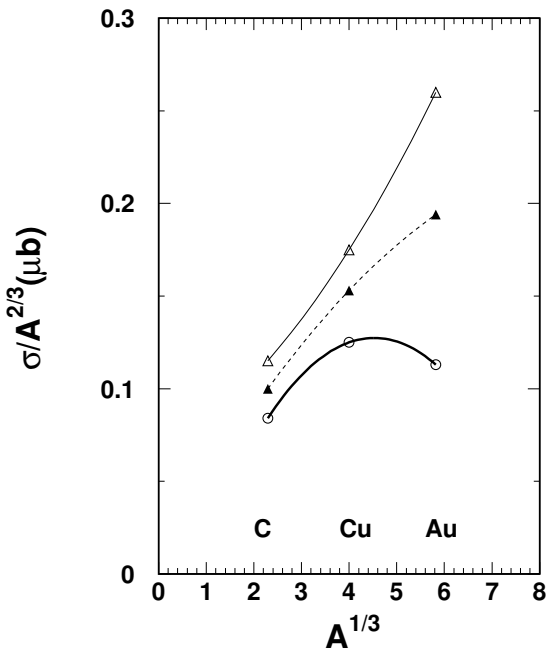

Fig. 1 *The ϕ production cross section in pA collisions as a function of the target mass calculated with momentum independent (thick curve), momentum dependent (dashed curve) and without (thin curve) in-medium modifications.*

The ϕ mesons are dominantly produced in NN and πN collisions. Without inmedium effects the cross section approximately scales with the mass number (thin curve). In very light nuclei like ^{12}C ϕ decay and rescattering does not play an essential role. However in large nuclei like gold the expected number of ϕ mesons is strongly suppressed which leads to the decrease of the yield. We conclude that such measurements are an independent tool to reveal meson properties in nuclear matter.

[1] H.W. Barz, M. Zétényi, Gy. Wolf, B. Kämpfer, Nucl. Phys. A 705 (2002) 223
[2] E.L. Bratkovskaya and W. Cassing, Phys. Rep. 308 (1999) 65
[3] F. Klingl, T. Waas, W. Weise, Phy. Lett. B 431 (1998) 254
[4] T. Hatsuda, H. Shiomi, H. Kuwabara, Prog. Theor. Phys. 95 (1996) 1009
[5] A. Sibirtsev, W. Cassing, Nucl. Phys. A 641 (1998) 476

[1] *KFKI Budapest, Hungary*

Nucleon-K$^+$ Correlations in Deuteron Induced Collisions with Nuclei at Intermediate Energies [B]

H.W. Barz, F. Dohrmann, E. Grosse, B. Kämpfer

Recently it was proposed to study neutron induced kaon production on nuclear targets. Since neutron beams are not available one may use deuteron induced reactions by measuring the correlation of the produced kaon with the high momentum proton. It is assumed that the high energetic nucleon will be a spectator nucleon from the deuteron while its partner enters the target and produces the kaon. Such an investigation is expected to reveal information about the elementary neutron cross-sections for kaon production which are poorly known from available data. Moreover, current theoretical predictions are very uncertain as the kaon production proceeds via pion or strangeness transfer. Due to this complicated mechanism relations between proton and neutron cross-section on a baryon , e.g. via isospin reflection, cannot be derived in a parameter free manner.

Several elementary reactions contribute to the kaon production within the nucleus, mainly NN and πN collisions. E.g. N-N collisions contribute to 60(70)% of the kaon yield in p+C collisions at 1.6(2.0) GeV. The variety of contributing channels will make it very challenging to relate the difference between neutron and proton induced collisions to specific channels. The comparison of results using neutron as well as proton rich targets could increase the sensitivity to the different cross sections.

Here we study deuteron induced collisions at 2 A·GeV within a Boltzmann-Ühling-Uhlenbeck (BUU) transport model which has been furnished with the elementary cross sections given in refs. [1,2] and kaon rescattering processes. The BUU model requires the knowledge of the spatial and the momentum distribution of the incoming deuteron. We have used a Hulthen wave-function $\Psi = \frac{1}{r}(\exp(-\kappa r) - \exp(-a\kappa r))$ and its Fourier transformation to derive these distributions. The parameter used are κ=0.231 fm^{-1} and $a = 6.16$.

To illustrate the effect that may be expected when using these cross sections, we calculated the multiplicity N_K of kaons when bombarding the target with neutrons or protons, respectively. For the average impact parameter we get for the ratio N_K(p+A)/N_K(n+A) the values 1.25 and 1.27 for a ^{12}C and a ^{40}Ca target, respectively.

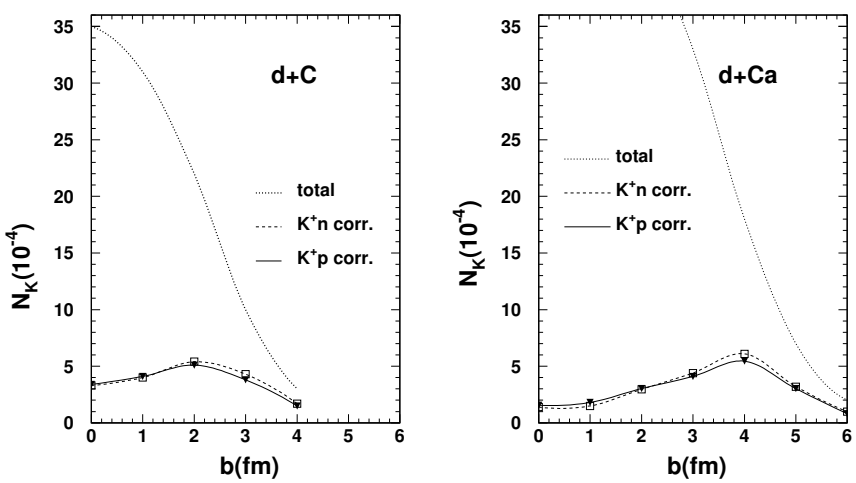

Fig. 1 *Uncorrelated kaon multiplicity (dotted line) and in correlation with a forward neutron or proton as a function of impact parameter b for the reactions d+C and d+Ca at 2 A·GeV bombarding energy.*

The multiplicity of kaons in coincidence with a nucleon (proton or neutron) going in forward direction with a maximum transverse momentum of 0.2 GeV/c and a longitudinal momentum larger than half of the incoming deuteron momentum is calculated. These multiplicities are presented in Fig. 1 together with the total kaon multiplicities (dotted lines) for collisions with carbon and calcium targets. The multiplicities clearly show a maximum for peripheral collisions with impact parameters equal to the target radius. The total kaon cross-section amounts to 0.8 mb (2.2 mb) for C(Ca). The correlated cross sections are smaller by about a factor of five. The ratio of the neutron to proton correlated kaon production is 1.1 and 1.12 for C and Ca, respectively. This means that when measuring the kaons in deuteron induced collisions in coincidence with a leading neutron (proton) the difference of the kaon rates between a proton and a neutron beam is strongly diminished. We expect a similar reduction if the actual cross section could be used. Hence the expected effect is very small. Calculations using stricter selection criteria for the forward particles (Δ p$_\perp$ = 0.05 GeV/c) did not essentially enhance this effect.

[1] Gy. Wolf, W. Cassing, U. Mosel, Nucl. Phys. A 552 (1993) 549
[2] K. Tsushima, J.W. Huang and A. Faessler, Austr. J. Phys. 50 (1997) 35
[3] K. Tsushima, A. Sibirtsev, A.W. Thomas G.Q. Li, Phys. Rev. C 55 (1999) 369

Strangeness Saturation: Dependence on System-Size, Centrality and Energy within the Thermal Model [B]

J. Cleymans[1], B. Kämpfer, P. Steinberg[2], S. Wheaton[1]

The abundances of different hadronic species in the final state of relativistic heavy-ion collisions can be well described by statistical-thermal models. Thus the observed multiplicities of a large number of hadrons can be reproduced by a small number of parameters. It is the subject of the present note to pursue this idea and to analyze the dependence of the thermal parameters, describing hadron multiplicities, on system size, centrality and energy. This will provide further information about the effects of the size of the excited strongly interacting system created at various beam energies.

The primary hadron number of species i is

$$N_i^{\rm prim} = V g_i \gamma_s^{|S_i|} \int \frac{d^3p}{(2\pi)^3}\, dm_i\, {\rm e}^{\frac{E(m_i,p)-\vec{\mu}_i\vec{Q}_i}{T}} \times BW(m_i,\Gamma_i), \quad (1)$$

where V is a fiducial volume of the system, T denotes the temperature, $\vec{\mu}_i$ and $\vec{Q}_i$ stand for the chemical potentials and corresponding conserved charges; BW is the Breit-Wigner distribution for hadron i with total width Γ_i. Eq. (1) is to be improved by the quantum statistical factors. For small values of $N_i^{\rm prim}$, the canonical expression is to be employed by the projection method. We include phenomenologically a strangeness suppression factor γ_s for hadrons with the total number S_i of strange valence quarks. The final particle numbers are $N_i = \sum_j [N_i^{\rm prim} Br(i \to j) + N_j^{\rm prim} Br(j \to i)]$ due to decays of unstable particles with branching ratios $Br(j \to i)$.

We have analyzed data of NA49 [1] (4π and mid-rapidity multiplicities of $\pi^\pm$, $K^\pm$, $N_{\rm part}$ [taken as sum over all baryons; partially also $\bar{p}$, ϕ, Λ, $\bar{\Lambda}$, $\Xi^\pm$ and K_s^0 are included] in collisions C+C, Si+Si, Pb+Pb at beam energies 40, 80 and 160 AGeV; it should be emphasized that protons are not included in our analysis as they due not belong to participants in non-central collisions) and PHENIX [2] ($\pi^\pm$, $K^\pm$, $p^\pm$ in collisions Au+Au at $\sqrt{s_{NN}} = 130$ GeV). Results of our fits are displayed in figs. 1 - 3. Fig. 1 (for fully phase space integrated yields) exhibits that strangeness saturation for peripheral lead-on-lead collisions differs from that in collisions C+C and Si+Si. The strangeness saturation increases with centrality. Fig. 2 reveals again the increase of strangeness saturation with centrality; the strangeness saturation at mid-rapidity is larger than in full phase space. Fig. 3 summarizes the energy dependence. f_2 is the fraction of multiply interacting nucleons calculated in a Glauber model. For further details see [3].

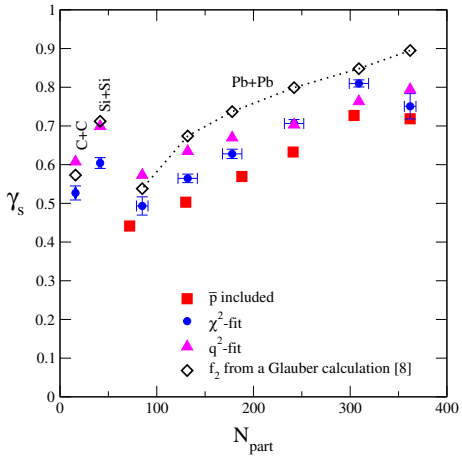

Fig. 1 *System-size and centrality dependence of γ_s as a function of the participant number $N_{\rm part}$, for the beam energy of 160 AGeV.*

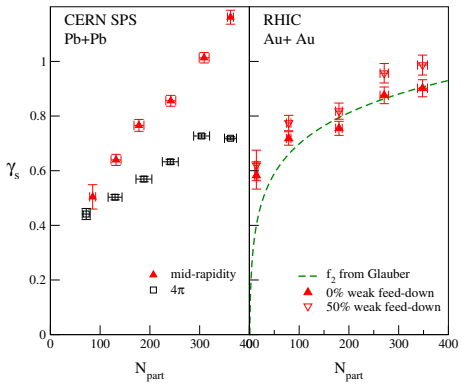

Fig. 2 *Centrality dependence of γ_s for the beam energy of 160 AGeV (left panel) and $\sqrt{s_{NN}} = 130$ GeV (right panel).*

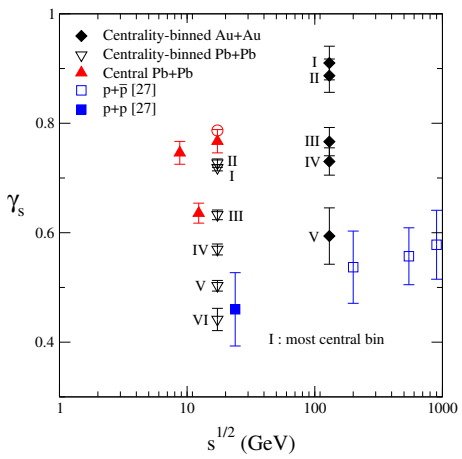

Fig. 3 *Energy dependence of γ_s. For details consult [3].*

[1] F. Sikler et al. (NA49), Nucl. Phys. A 661 (1999) 45c, C. Höhne et al. (NA49), nucl-ex/0209018
[2] K. Adcox et al. (PHENIX), Phys. Rev. Lett. C 66 (2002) 054902
[3] J. Cleymans et al., Phys. Rev. C 65 (2002) 027901, hep-ph/0203134, hep-ph/0204227, hep-ph/0208247, hep-ph/0212335

[1] *University of Cape Town, Rondebosch 7701, Cape Town, South Africa*
[2] *Brookhaven National Laboratory, Upton, NY, USA*

Energy Loss of Charm Quarks by Gluon Radiation [B]

K. Gallmeister[1], B. Kämpfer, O.P. Pavlenko[2]

Induced gluon radiation of a fast quark propagating through a deconfined medium of quarks and gluons causes an energy loss which should considerably modify various observables in relativistic heavy-ion collisions. In such a way the properties of the deconfined medium can be probed. The modified transverse momentum spectrum of final hadrons appears as a convolution of the energy loss distribution and the primary spectrum. To enable a comparison with earlier work [1], we employ here a simplified version by using a Monte Carlo averaging over tranversed path lengths and by shifting the transverse momentum of a quark before hadronizing by the mean energy loss. Remarkable in the energy loss formula is the apparent independence of the initial state, i.e. the energy loss depends on the temperature T_f at which the quark leaves the medium. As shown in [2], however, due to life time and geometrical size effects, a sensitivity on the initial conditions occurs.

Using the PYTHIA version 6.206 with parameters given in [3] one gets the charm cross section $\sigma_{c\bar{c}}^{NN} = 404\ \mu$b at $\sqrt{s_{NN}} = 130$ GeV. With the electron/positron decay channels of charmed hadrons within PYTHIA the resulting inclusive transverse momentum spectrum agrees fairly well with the PHENIX data [4] when using the appropriate thickness functions $T_{AA} = 6.2\ (22.6)$ mb^{-1} for minimum bias (central) collisions, see fig. 1.

To see which space is left for an energy loss we use the above described scheme with Bjorken symmetries and parameters decsribed in [3]. We parameterize different energy loss strengths by ζ multiplying the energy formula used in [1,2,3]. The results of our Monte Carlo sampling are exhibited in fig. 2. An optimum description of the data is accomplished by $\zeta = 0.2 \cdots 0.5$. It turns out, however, that larger energy losses are also compatible with data, as no energy loss does. Insofar, the present data do not constrain significantly the energy loss of charm quarks.

Energy loss effects can suppress the dileptons from charm decays [1]. This is a potentially important effect since these charm contributions compete with the Drell-Yan yield and hide the interesting thermal contribution. Given the above parameterization of the modifications of inclusive single electrons by energy losses of charm quarks, we proceed to estimate the possible suppression of dileptons from correlated semi-leptonic decays of open charm mesons. Our predictions are displayed in fig. 3 for various values of the strength parameter ζ. Indeed, the dilepton spectra are quite sensitive to energy losses, however, assuming a small loss, as suggested by the above analysis, the corresponding suppression is small.

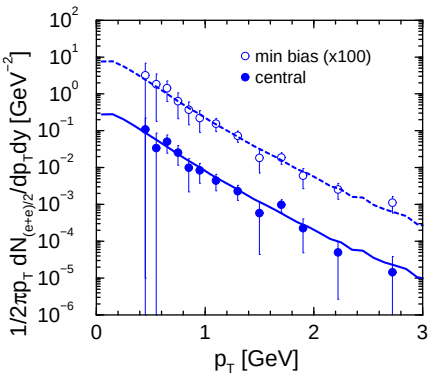

Fig. 1 *Comparison of our PYTHIA results with the PHENIX data [4] (statistical and systematical errors are quadratically added).*

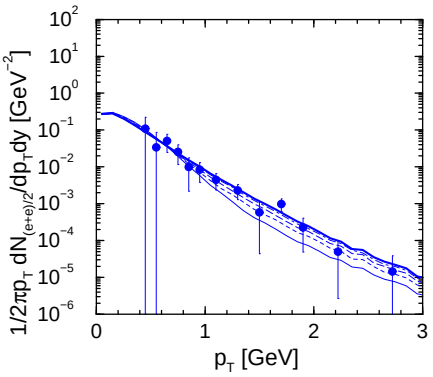

Fig. 2 *Comparison of various energy loss strengths $\zeta = 0$, 0.2, 0.5, 1.0, 2.0 (from top to bottom) with PHENIX data [4] of central collisions. For details see [3].*

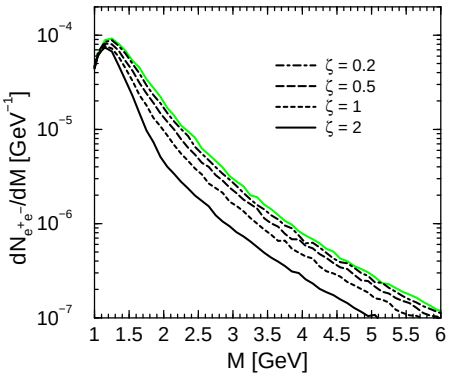

Fig. 3 *Predicted dilepton spectra from open charm mesons for various strength parameters of the energy loss within the PHENIX acceptance. $T_{AA} = 31$/mb, $\sqrt{s_{NN}} = 200$ GeV. Single-lepton $p_\perp^{\min} = 0.5$ GeV/c.*

[1] K. Gallmeister, B. Kämpfer, O.P. Pavalenko, Phys. Rev. C 57 (1998) 3276
[2] K. Gallmeister, B. Kämpfer, O.P. Pavalenko, Phys. Rev. C 66 (2002) 014908
[3] K. Gallmeister, B. Kämpfer, O.P. Pavalenko, nucl-th/0208006, Nucl. Phys. A (2003) in print
[4] K. Adcox et al. (PHENIX), Phys. Rev. Lett. 88 (2002) 192303

[1] *Institute für Theoretische Physik, Universität Giessen*
[2] *Institute for Theoretical Physics, Kiev, Ukraine*

Relativistic Effects in Deuteron Break-Up Reactions [B]

L.P. Kaptari[1], B. Kämpfer, S.S. Semikh[2], S.M. Dorkin[3]

Recently, data on proton-induced deuteron break-up at intermediate energies with forward emission of a fast proton pair has been reported [1]. One motivation for the experiment was the possibility to investigate the off-mass shell effects in NN interactions [2]. As predicted in [1],[3], at a certain initial energy of the beam protons, the cross section should exhibit a deep minimum, corresponding to the node of the non-relativistic $^1S_0$ wave function of the two outgoing protons, provided a non-relativistic picture holds and off-mass shell effects can be neglected. The data [1] exhibits, however, a completely different behavior: the cross section is smoothly decreasing; there is no sign of a pronounced minimum.

In the present note we use the Bethe-Salpeter (BS) approach to analyze the data [1] on deuteron break-up with the emission of a fast forward pp pair. The calculation is based on our solution of the BS equation for the deuteron with a realistic one-boson exchange kernel. The final state interaction of the two protons is treated also within the BS formalism, by solving the BS equation for the t matrix within the one-iteration approximation.

Let us consider the process

$$p + d = (p_1 p_2)(0^0) + n(180^0) \qquad (1)$$

at low excitation energy of the pair ($E_x \sim 0 - 3$ MeV) and intermediate initial kinetic energies $T_p \sim 0.6 - 2.0$ GeV corresponding to the conditions at the Cooler Synchrotron COSY in the ANKE experiment [1]. In the one-nucleon exchange approximation the reaction can be represented by the diagram depicted in fig. 1. With the theory described in detail in [4] we obtain for the differential cross section results as depicted in fig. 2. A non-relativistic calculation and a constraint relativistic calculation exhibit, indeed, the expected minimum. The full calculation [4] reveals, however, that the complete set of necessary relativistic effects fully masks the expected minimum. The experimental results are then correctly described, see fig. 3.

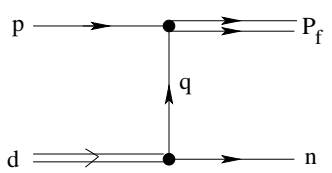

Fig. 1 *Kinematics of the process $pd \to (pp) + n$ corresponding to the experiment [1,2].*

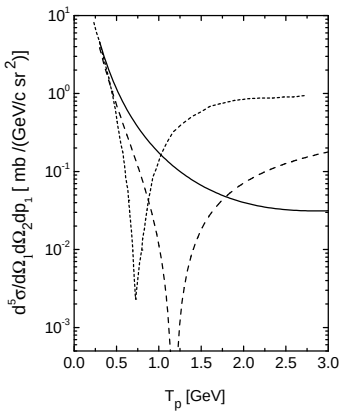

Fig. 2 *Five-fold cross section as a function of the kinetic energy T_p of the incident proton. The dotted curve corresponds to a non-relativistic calculation, i.e., to the case where only the "++" components in the $^1S_0$ state are taken into account and any Lorentz boost effects are ignored. The dashed curve depicts results of a calculation with all relativistic effects in "++" components. The solid curve is for the results of a complete calculation with taking into account all the relativistic effects including the contribution of P waves in the wave function of the pp pair. The two protons are supposed to be detected in forward direction.*

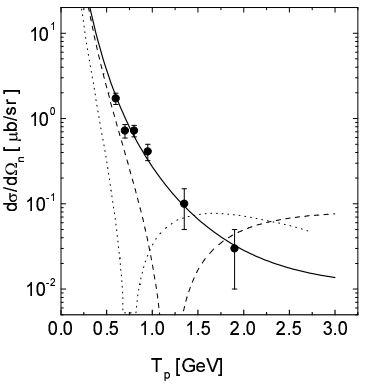

Fig. 3 *Differential cross section in the center of mass integrated over the excitation energy E_x as a function of the kinetic energy T_p of the incident proton. Notation is as in fig. 2. Experimental data are from [1].*

[1] V.I. Komarov et al., nucl-ex/0210017

[2] V.I. Komarov (spokesman) et al., COSY proposal #20 (updated 1999), "Exclusive deuteron break-up study with polarized protons and deuterons at COSY"

[3] Yu.N. Uzikov, V.I. Komarov, F. Rathmann, H. Seyfarth, nucl-th/0211001; Yu.N. Uzikov, J. Phys. G28, B13 (2002)

[4] L.P. Kaptari, B. Kämpfer, S.S. Semikh, S.M. Dorkin, nucl-th/0212062

[1] *Department of Physics, University of Perugia, and INFN Sezione di Perugia, via A. Pascoli, I-06100, Italy*
[2] *Bogoliubov Laboratory of Theoretical Physics, JINR, Dubna 141980, Russia*
[3] *Nuclear Physics Institute, Moscow State University, Moscow, Russia*

Exclusive Charge-Exchange Reaction $pD \to n(pp)$ within the Bethe-Salpeter Formalism [B]

L.P. Kaptari[1], B. Kämpfer, S.S. Semikh[2], S.M. Dorkin[3]

At the cooler synchrotron COSY in FZ Jülich, a program to study charge-exchange processes at relativistic energies has been started, and a detailed investigation of polarization observables is envisaged. Details of the deuteron wave function at short distances and the relevant reaction mechanisms can be investigated in inclusive deuteron break-up reactions.

Inspired by this, in previous work [1] we investigated the process $p\vec{D} \to n(pp)$ within the impulse approximation. The goal of the present note is to report results of our improved study [2] of the charge-exchange reaction at relativistic energies, as accessible at COSY and the upgraded Dubna accelerator by (i) taking into account the effects of final state interaction, (ii) to check whether in this case the non-relativistic predictions hold, and (iii) whether the reaction can be used as a "deuteron polarimeter". We employ a covariant generalization of the spectator mechanism (see fig. 1) based on the Bethe-Salpeter (BS) formalism and on a numerical solution of the BS equation with a realistic one-boson exchange kernel. Our amplitude of the process in an explicitly covariant form allows a determination of any polarization observable.

To test our approach, in figs. 2 and 3 we compare with experimental data from SATURN-II. The agreement is satisfactory, in particular for small excitation energies of the slow backward (pp) pair (the fast forward neutron is not detected). This gives confidence that also at COSY energies the reaction is correctly described within our formalism. The predicted cross sections [2] are large enough to use the considered reaction as "deuteron polarimeter", as proposed in [4].

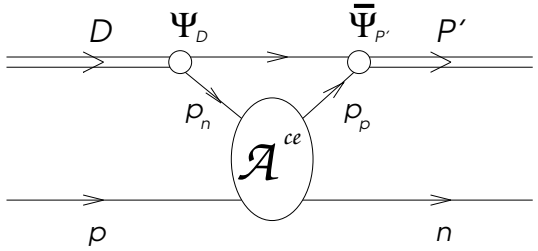

Fig. 1 *Spectator mechanism for the charge-exchange process $pD \to n(pp)$. The BS amplitude for the deuteron bound state and the pp pair in the continuum are denoted as Ψ and $\bar{\Psi}$, respectively. The elementary pn charge-exchange amplitude is symbolically represented by $\mathcal{A}^{ce}$.*

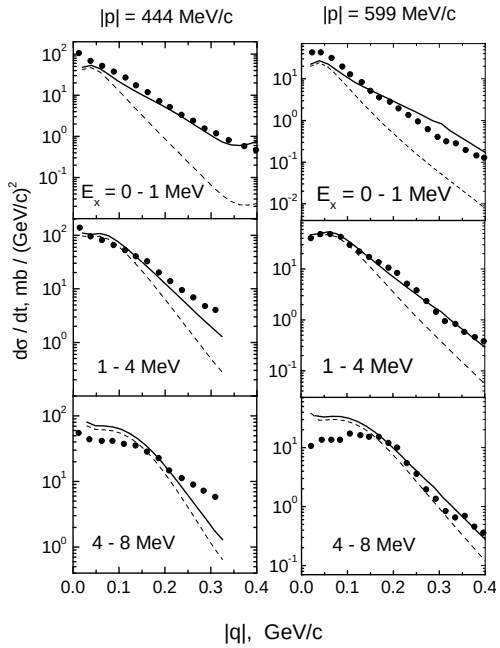

Fig. 2 *Results of calculations of the differential cross section as a function of the transferred momentum with taking into account the effects of final state interaction in the (pp) $^1S_0$ state (solid curves). Experimental data from SATURN-II [3]. The dashed curves depict the results of calculations within the impulse approximation.*

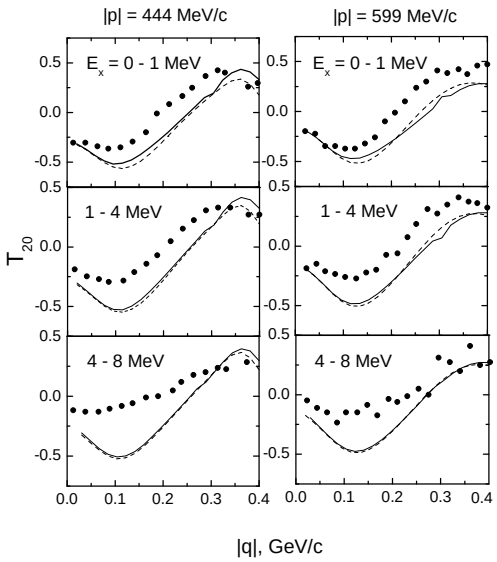

Fig. 3 *The same as in fig. 2 but for the tensor analyzing power.*

[1] S.S. Semikh, S.M. Dorkin, L.P. Kaptari, B. Kämpfer, Yad. Fiz. 65 (2002) 469
[2] L.P. Kaptari, B. Kämpfer, S.S. Semikh, S.M. Dorkin, nucl-th/0211076, Eur. Phys. J. A (2003) in print
[3] S. Kox et al., Nucl. Phys. A 556 (1993) 621
[4] D.V. Bugg, C. Wilkin, Phys. Lett. B 152 (1985) 37; Nucl. Phys. A 467 (1987) 575

[1] *Department of Physics, University of Perugia, and INFN Sezione di Perugia, via A. Pascoli, I-06100, Italy*
[2] *Bogoliubov Laboratory of Theoretical Physics, JINR, Dubna 141980, Russia*
[3] *Nuclear Physics Institute, Moscow State University, Moscow, Russia*

From QCD Lattice Calculations to the Equation of State of Quark Matter [B]

A. Peshier[1], B. Kämpfer, G. Soff[2]

One of the fundamental issues which triggered, and has influenced since, heavy ion physics is the phase structure and the thermodynamic properties of strongly interacting matter at energy densities above $1\,\mathrm{GeV/fm^3}$. Under such conditions, exceeding the energy density in nuclei but still far away from the asymptotic regime, the coupling strength is large, which makes the theoretical description of the many-body problem challenging.

In the recent past the understanding of this field has become much more particularized. The phase diagram for QCD with two massless flavors, which is the case we will consider in the following, can be briefly described as follows. At zero quark chemical potential, $\mu = 0$, the broken chiral symmetry of hadron matter is restored within the quark-gluon plasma, at a critical temperature $T_c \approx 170\,\mathrm{MeV}$. It is thought that this second order transition persists also for nonzero μ, thus defining a critical line, which changes to a first order transition line at the tricritical point. For small temperatures and $\mu \sim \mu_c$ one anticipates a color-superconducting phase of quark matter. The value of μ_c is expected to be 100...200 MeV larger than the quark chemical potential $\mu_n = 307\,\mathrm{MeV}$ in nuclear matter. Quantitative results for large couplings can be obtained from first principles by lattice calculations which were, however, restricted to finite temperature and $\mu = 0$ until very recently. Therefore, the described picture for $\mu \neq 0$ is mainly based on general arguments combined with results from various models, including first lattice QCD results [1,2].

With respect to the starting Compressed Baryon Matter project at GSI a semi-quantitative determination of the phase border line is important. We report here results of our quasi-particle model [3] to accomplish this goal.

Our model is based on dynamically excited quark and gluon modes near the light cone. The quasi-particle excitations determine the entropy density, which delivers the pressure and energy density in a thermodynamically self-consistent manner. A crucial ingredient is the effective coupling to be adjusted at lattice data. Fig. 1 exhibits an example of the pressure at $\mu = 0$.

The extrapolation to finite baryon density is based on a thermodynamic self-consistency condition and a extremum property of the potential. The emerging characteristics are shown in fig. 2. The innermost characteristic joining the chiral transition temperature T_c is considered as representative of the phase border line. It also quantifies the numerical value of the critical baryo-chemical potential.

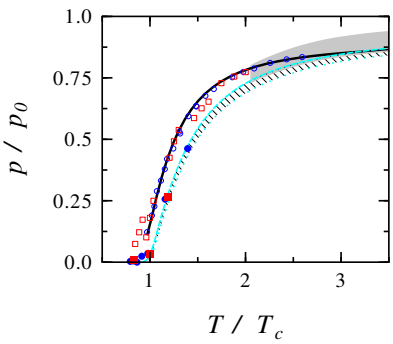

Fig. 1 *Compilation of $n_f = 2$ lattice data for the pressure in units of the free pressure p_0. Shown are the scaled data [4] for light quarks corresponding to meson mass ratios of $0.65 \leq m_{ps}/m_v \leq 0.75$ (small open circles: $N_\tau = 4$, small open squares: $N_\tau = 6$), and a continuum estimate (grey band). The full line is our quasi-particle result. The full symbols depict the data [4] for larger quark masses, with $m_{ps}/m_v = 0.95$. The hatched band represents the pure SU(3) lattice data normalized to the corresponding free pressure. For details see [5].*

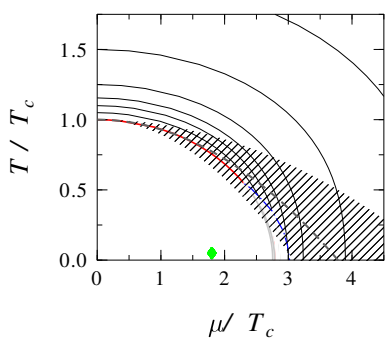

Fig. 2 *Represented by the full lines are the characteristics. The characteristic through T_c coincides for small μ with the critical line (with a hatched error band) obtained in the lattice calculation [2]. In the region under the dash-dotted line the resulting quasi-particle pressure is negative – a transition to another phase has to happen somewhere outside. Therefore, the narrow grey region under the $p = 0$ line, where the pressure is not unique, is physically irrelevant. Indicated by the symbol (assuming, for the scaling, $T_c = 170\,\mathrm{MeV}$) is the chemical potential μ_n in nuclear matter. The equation of state follows from our model in the region covered by the characteristics.*

[1] Z. Fodor, S.D. Katz, JHEP 0203 (2002) 014
[2] C. R. Allton et al., hep-lat/0204010
[3] A. Peshier, B. Kämpfer, O. P. Pavlenko, G. Soff, Phys. Rev. D 54 (1996) 2399;
A. Peshier, B. Kämpfer, G. Soff, Phys. Rev. C 61 (2000) 045203
[4] A. Ali Khan et al., Phys. Rev. D 64 (2001) 074510
[5] A. Peshier, B. Kämpfer, G. Soff, Phys. Rev. D 66 (2002) 094003

[1] *Institute für Theoretische Physik, Universität Giessen*
[2] *Institute für Theoretische Physik, TU Dresden*

Quality Assessment for Monitoring of HADES DST Production

A. Sadovski, F. Dohrmann, K. Kanaki, R. Kotte, D. Magestro[1], C.Müntz[1], L. Naumann

The purpose of HADES Quality Assessment (QA) is to provide diagnostic tools (histograms and scalers) during Data Summary Tape (DST) production in order to help assess the quality of the data for higher levels of physics analysis. Initially the program was modelled after the STAR QA/QC (quality assurance/quality control) package [1]. At the moment the program includes 92 diagnostic plots, several of these are overlays (see Fig. 1). Each physical detector of the HADES setup as well as two logical units, Kickplane and Trigger, are covered. The program is open for additional diagnostic plots.
QA works in parallel with DST production and creates its output per DST file. The output is stored in several formats, as PDF or PS format, as well as ROOT-file format [2] in order to allow for analysing of multiple outputs with dedicated scripts.

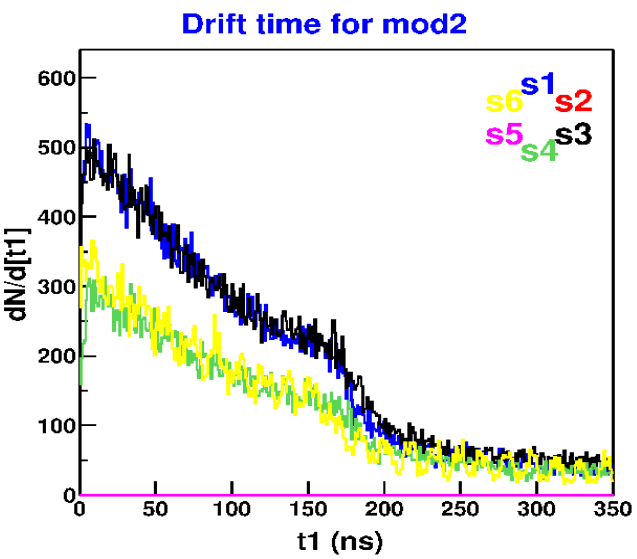

Fig. 1 *An example of overlayed picture from DST-QA PDF output from November 2002 beam time. The plot shows time distribution of the first electron of the signal for four modules MDC-III (sectors 1, 3, 4, 6). The vertical axis units are (ns^{-1}). Sectors 4 and 6 have less count rate due to only 4 out of 6 layers being operational.*

Recently two dedicated scripts were written, which allow to perform a semi-automatic analysis of diagnostic plots (see Figs. 2, 3). This is important when dealing with several hundreds of QA files. The main idea is to give the detector expert a possibility to preselect several good histograms manually and then to compare all the remaining files with this reference pattern and accept/reject any of others. This procedure is iterative. One automatic iteration takes about 40 seconds for a one-dimensional histogram over 231 files on a modern Linux cluster. At the moment it uses the mean value distribution of each one-dimensional histogram to select histograms. Experts from different detector groups are supposed either to provide the reference histograms or may evaluate files with histograms corresponding to the respective detector. Finally, the results from different detector groups are to be grouped together in a DST-QA report.
The next step of HADES DST-QA is to make preselection of histograms/files more automatic by providing a set of reference plots and to develop adequate selection criteria for respective groups of histograms.

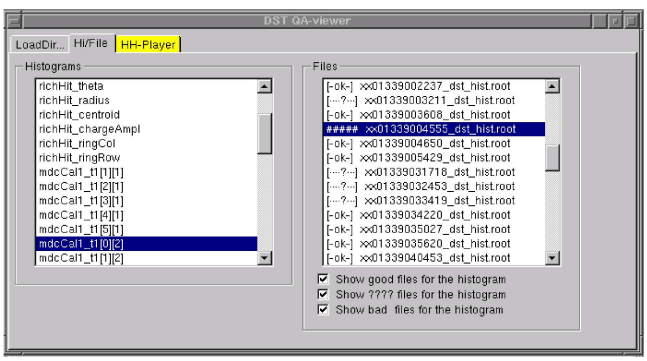

Fig. 2 *Example of the user interface for selection of good and bad histograms among QA output of DST files. A histogram is chosen from the left menu, and the results for this histogram of automatically preselected files with a quality flag (in front of the name of file) are shown in the right menu.*

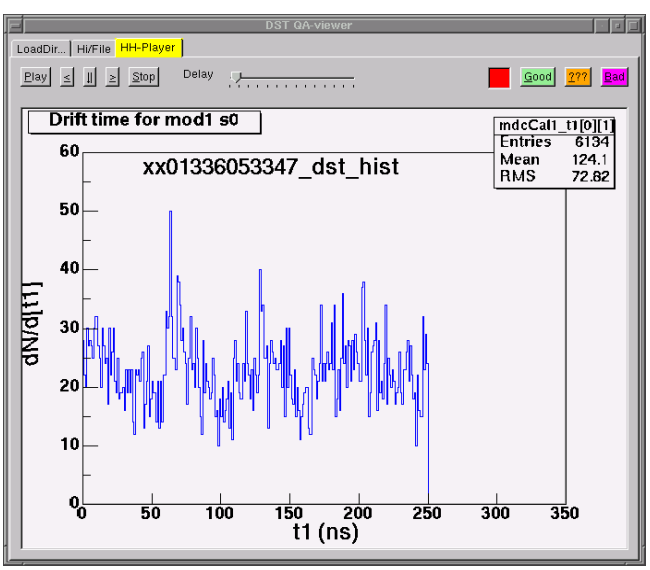

Fig. 3 *Screen shot of the quick histogram player for DST-QA. The histogram shown is MDCII sector 1 has been marked by semi-automatic quality control procedure as a "bad" one (to be compared with the corresponding reference plot). The user can always change the assigned quality flag for the histogram of the current file manually in case it was not correctly set by semi-automatic procedure. The control buttons are located at the top of the widget.*

[1] http://www.star.bnl.gov/STARAFS/comp/qa/shifts/QA_general.html
[2] http://root.cern.ch/

[1] *Gesellschaft für Schwerionenforschung mbH, Darmstadt, Germany*

A Method for Separation of Faulty Wire Connections in the HADES Drift Chambers

K. Heidel, J. Hutsch, U. Wolf, K. Kanaki, R. Kotte, L. Naumann

The tracking system of the HADES spectrometer at GSI, Darmstadt consists of four planes of Multiwire Drift Chambers (MDC). Each module contains approximately the same numbers of anode wires (∼1000) which gives us a total of about 27,000 channels.

The stable operation of an MDC module requires constant high voltage on the field and cathode layers. Yet, during the operation, it might be the case that there is a persistent local discharge around a cathode (field) wire C_i (F_i) which can lead to an instant drop of its potential. This abrupt change will lead to an attractive force between wires of sequential layers and quite often to a spark which can provide sufficient energy for the wires to weld.

The origin of this phenomenon was studied using two (dummy) layers of wires at a distance of 4 mm, on which both kinds of electrodes (field wires, Ø = 100 μm; cathode wires, Ø = 80 μm) were strung with the operational tension, i. e. 1.5 N and 1.0 N respectively. The sense wires were not included in the study. With this setup it was proven that a rise of the potential above a certain value may cause wire oscillations and sparks and moreover, even recreate a faulty connection between the layers. Here we have to point out that in the case of the dummy frames, what we have is rather a superficial attachment than welded wires, meaning that a mechanical vibration is often sufficient to cure the faulty connection. No external damage on the surface of the wire was observed.

From high-frequency engineering it is known that sparkover paths can be repaired with the help of high voltage pulsers. This method would be suitable for the repair of the faulty connection in our case. Furthermore, a short current pulse can induce a force on the wire.

When we deal with such a case in a chamber installed in the HADES setup, it is always practical and less time consuming to repair the chamber without removing and opening it. Using the above dummy frames, such a method for repairing the faulty connection of the wires was tested. The fundamental idea was to use a time controlled switcher for a pulse source (Fig. 1).

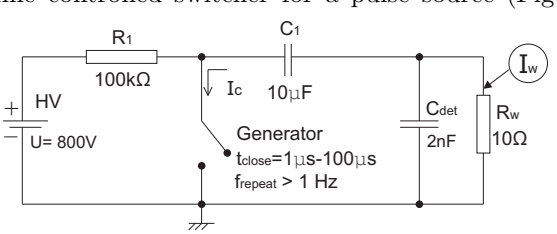

Fig. 1 *Time controlled high voltage switcher.*

Keeping the switch closed, the charged capacitor discharges on the connection of the two Al wires through the resistivity $R_w \sim 10\ \Omega$. The simulated discharge current for the time constant of $\tau = R_w C_1 \simeq 100\ \mu$s is depicted in Fig. 2. For flexibility purposes a generator is used in order to vary the duration time t_{close} and the pulse repetition rate f_{repeat}.

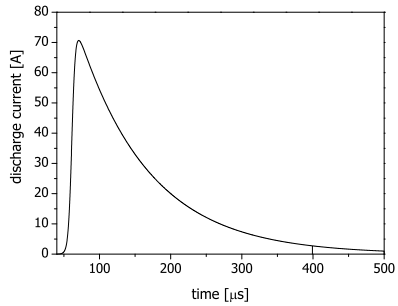

Fig. 2 *Plot of the simulated discharge current as a function of time.*

Experience showed that a duration of $t_{close} = 10\ \mu$s and frequencies f_{repeat} higher than 1 Hz are appropriate. A glow lamp (not shown in the circuit) signalizes the successful separation of the wires. The electric energy (Fig. 3) for the above circuit was simulated with PSpice [1] and was calculated from the time integral of the electric power as

$$W = \int_0^{t_{close}} U_w I_w dt. \tag{1}$$

For $t_{close} = 10\ \mu$s and $U = 800$ V the dissipated energy is $W \simeq 0.5$ J while the theoretical curve

$$E(t) = \int_0^t P(t')dt' = \frac{\tau U_{max}^2}{2R_w}\left(1 - e^{-2t/\tau}\right), \tag{2}$$

also calculated by integration, gives $E = 0.6$ J.

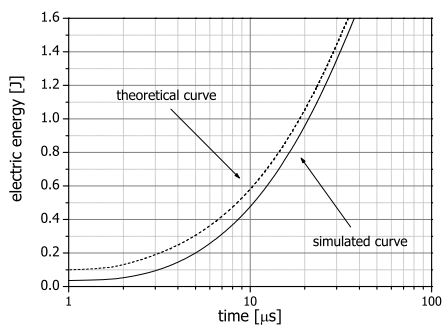

Fig. 3 *Overlay of theoretical and simulated curve of the dissipated electric energy as a function of time.*

In contrast to the direct heating method [2] which induces energies of about 25 J on the wire connection, the short energy pulses provide safety against smelting wires.

[1] http:/www.pspice.com
[2] http://www-hades.gsi.de/proceedings/collmeetXI/jboy1/jboy1.html

Examination of the Wire Deflections for the HADES Drift Chambers MDC III

K. Kanaki, J. Hutsch, F. Dohrmann, R. Kotte, L. Naumann, A. Sadovski, M. Sobiella

From the mechanical point of view, an operational drift chamber requires wires strung with tension high enough to avoid sagittas and oscillation amplitudes which are comparable to the distance between the layers of the wires. Simulations and tests were performed before the construction of the HADES modules, in order to define the right value for this force that will compensate for gravity. Apart from the gravitational forces, the wires are also subject to electrostatic forces that tend to displace them, when voltage is applied. The combined effect of these forces and of the restoring mechanical tension results in an elastic deformation of the wire. The wire deflection from the nominal position can be estimated with the program GARFIELD [1] by solving the differential equation which describes its equilibrium state.

The differential equation describing the shape $y(x)$ of a wire (x runs along its length) subjected to an external force $f(x)$ can be derived by making the following assumptions:

- the wire deflection is small compared to the length of the wire
- the wire elongation is in the elastic range of the Hooke's law.

If the wire is stretched under tension T and has a shape $y(x)$, the force per unit length F_t acting on an elementary part of the wire between x and dx is given by:

$$F_t(x)dx = T\Big(\frac{dy}{dx}\Big)_{x+dx} - T\Big(\frac{dy}{dx}\Big)_x = T\frac{d^2y}{dx^2}dx. \quad (1)$$

This is the force that tends to restore the wire back to its nominal position and balances any external applied force. The gravitational force per unit length acting on the wire is $F = g\rho\sigma$, where ρ is the density of the wire and σ its cross section, while the electrostatic force is $F = \lambda E$, where λ is the charge per unit length and E the electric field generated by the surrounding electrodes. If the field is constant, it creates a constant force per unit length, similar to the gravitational one. For a wire placed in a position of electrostatic equilibrium, a small deviation from this position generates a force acting on the wire tending to displace it. This force has the form $F = \frac{V^2}{2}\frac{dC}{dx}$, where V is the potential of the wire and dC/dx the variation of its capacitance per unit length due to displacement [2]. It can be shown that

$$F \simeq \frac{V^2}{2}\frac{4\pi\epsilon_0}{[\alpha ln(\alpha/r)]^2}x = ky \ (k = const), \quad (2)$$

where r is the radius of the wire and α the typical distance of the wire from the other electrodes. Thus, the equation describing the equilibrium position of the wire is

$$T\frac{d^2y}{dx^2} = -ky - g\rho\sigma = f(x). \quad (3)$$

For $k = 0$ we can study separately the effect of gravity. Integrating for the total wire length L, the sagitta is

$$s_g = \frac{L^2 g\rho\sigma}{8T}, \quad (4)$$

and is proportional to the inverse of the mechanical tension T. If T is increased, the effect is reduced but it cannot be arbitrarily increased, since non-elastic deformations take place. The total sagitta of the wire under the combined effect of electrostatic and gravitational forces is

$$s = \frac{8s_gT}{L^2k}\Big(\frac{1}{cos\sqrt{k/T(L/2)}} - 1\Big) = s_g\frac{2}{q^2}\Big(\frac{1}{cosq} - 1\Big). \quad (5)$$

It is clear that the electrostatic forces amplify the sagitta produced by the gravitational forces. From the above equation we can deduce the stability condition

$$q^2 = \frac{4\pi\epsilon_0}{[\alpha ln(\alpha/r)]^2}\frac{U^2}{2T}\frac{L^2}{4} \leq 1. \quad (6)$$

The above relation allows us to calculate the critical tension T_c ($q^2 = 1$) for fixed parameters U, L, α and r, below which the wires oscillate under working conditions (see Tab. 1).

wire	Ø [μm]	T_c [N]	T [N]	material
sense	20	0.31	0.5	W
cathode	80	0.65	1.0	Al
field	100	0.72	1.5	Al

Tab. 1 *Summary table of all wire tensions, actual and critical, calculated for α = 4 mm, L = 2 m and U = -2000 V.*

Following the above we attempted to calculate the sagittas for the sense wires of MDC III as a function of their tension, without varying the potential applied on the field and the cathode wires.

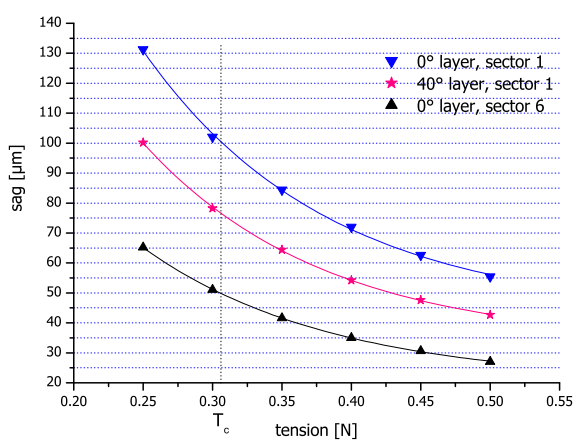

Fig. 1 *Anode wire sagittas for different layers and chamber orientations.*

The calculation was performed for a series of tension values between the strung and the critical one and for different layers and chamber orientations, i. e. for different gravitational sagittas. The results for the anode wires ($U_c = U_f$ = -2 kV) are depicted in Fig. 1.
The plot shows that the sense wires of the 0° layer of sector 1 are subject to the highest deflection from the nominal position. Due to symmetry, the wires of chambers that are installed in opposite sectors have the same deflection. The sagitta is lower for inclined layers and chambers. Nevertheless, for a loss of 20 % in tension, the sagitta does not deviate more than the designed resolution of the modules (100 μm), e. g. for 0.4 N the sagitta of 0° layer in sector 1 is below 80 μm.

The tension which the sense wires (W) are strung with remains constant in the first couple of years of operation, in contrast to the tension of the field and the cathode wires (Al) which decreases approximately 13% within three years due to the creeping process (see Fig. 2). The shape of the curves is stamped by the production process and is not influenced by aging procedures.

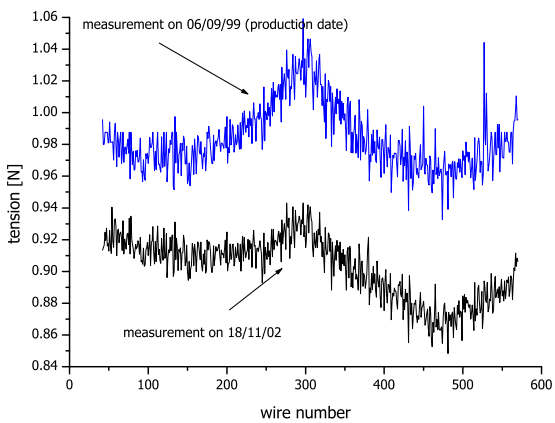

Fig. 2 *Comparison of the cathode wire tension for MDC III measured at different times.*

Apart from the creeping, the deformation of the stesalit frames can cause loss of tension as well. Such a case appears, for example, when the drift chamber is operated under gas overpressure. The mylar foils "swell" causing the stesalit frames to bend inwards. Consequently, the length of the wires changes and so does their tension. Fig. 3 depicts the frame deformation for the 0° layer as a function of gas overpressure, while Tab. 2 gives the tension values calculated for the sense wires of the same layer. The deformation was measured at the points indicated by the arrows in the figure.

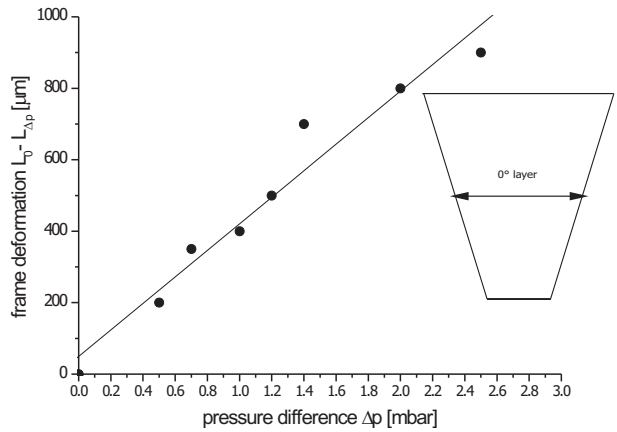

Fig. 3 *Frame deformation for 0° anode layer vs. pressure difference.*

frame deformation [μm]	corresponding tension [10^{-2}N]	change in %
0	50.00	0.00
200	46.44	6.90
350	44.00	12.00
400	43.10	13.80
500	41.40	17.20
700	37.95	24.10
800	36.20	27.60
900	34.50	31.00

Tab. 2 *The change of the anode wire tension depending on the frame deformation.*

A gas overpressure control system assures that the pressure difference will not exceed the value for which the frame deformation will lead to tensions below the critical one.

[1] Simulation of gaseous detectors, http://garfield.web.cern.ch/garfield
[2] W. Blum, L. Rolandi, Particle detection with drift chambers, Springer-Verlag, Berlin (1993)

Momentum-Reconstruction System for ANKE Side Detectors

V. I. Dimitrov, J. Seibert

Recently the ANKE spectrometer [1] at COSY-Jülich has been upgraded with a negative particle detection system [2], consisting of $2\,mm$ thick start scintillators, two MWPCs for momentum reconstruction, two groups of stop scintillators and several bent Čerenkov counters for kaon–pion discrimination for momentum values where TOF differences are too small [3]. With the help of the new detector it is possible to register negatively charged particles with momenta $120\ldots1000\,MeV/c$. This allows studying π^--, K^-- and, indirectly, $\phi-$ meson production. In addition, more complete and precise reconstruction of the reaction kinematics of particles registered in the positive particle detectors of the spectrometer becomes possible. As a part of the development of the appropriate data analysis software for the new detector system, a momentum-reconstruction software package has been designed and tested. The package fulfils the following general requirements:

- Fast operation which makes it possible to use it in online analysis;
- Low system load for seamless coexistence with other analysis tools;
- Implementation as a C++ class for an easy integration into the existing analysis framework;
- Precision consistent with that of ANKE hardware and/or software.

With regard to the above, the chosen implementation uses a GEANT [4] generated, size optimized database of pre-calculated particle tracks, and a fast interpolation engine for evaluating the vertex particle momentum from the MWPC hit coordinates. While GEANT is a well-known standard tool, the scattered data interpolator has to be developed from scratch, as the existing methods for scattered data interpolation (Nearest Neighbor Interpolation, Shepard method etc.) do not meet one or more of the above requirements.

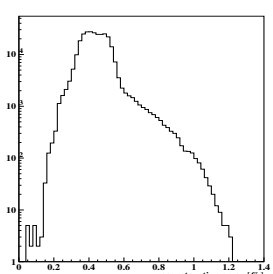

Fig. 1 *Error distribution of the reconstructed momenta. Notice the log scale.*

[1] S. Barsov et al., Nucl. Instr. Meth. A 462 (2001) 364
[2] H.R. Koch et al., FZJ Annual Report (1999) p. 28
[3] M. Büscher et al., Phys. Rev. C 65 (2002) 014603
[4] GEANT: CERN Program Library, Long Writeup W5013

The implementation chosen involves an optimized cell algorithm for locating the N-th nearest neighbour of a node, and a quasi-linear interpolation based on the functional values at the nearest neighbours. A detailed account on the method will be published elswhere.
Figures 1–3 demonstrate the performance of the momentum reconstruction system with simulated data. Checks with real ANKE data are under way.

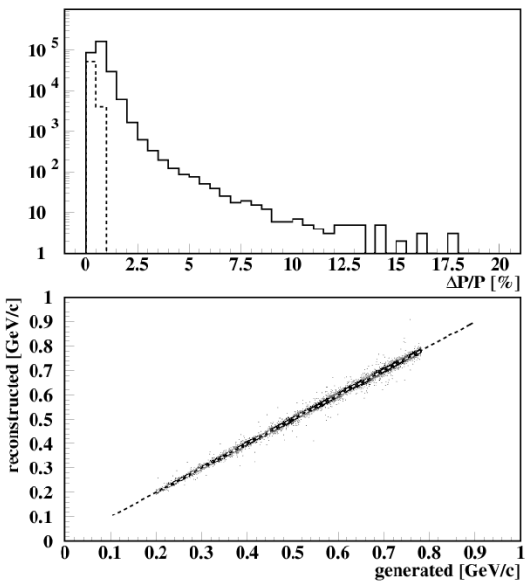

Fig. 2 *Effects of multiple scattering on the precision of the momentum reconstruction. The dashed line shows the resuls without small angle multiple scattering.*

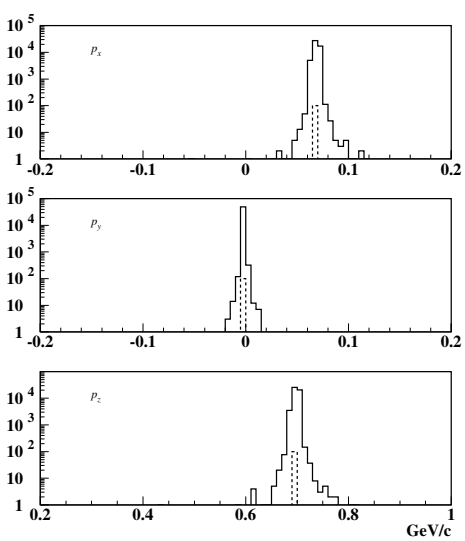

Fig. 3 *Reconstruction of the momentum components of a particle with fixed momentum with (solid lines) and without (dashed lines) small angle multiple scattering.*

ELBE-n-TOF: Comparison to other Neutron Sources and Experiments

E. Grosse, K. Möller, B. Mukherjee, L. Naumann, A. Wagner for the n-TOF collaboration

Neutron interaction cross sections are strongly varying in dependence on neutron energy and mass and charge number of the hit nucleus. Together with the low natural neutron background this makes them an ideal probe for the study of the interior of matter, which they penetrate nearly freely until they hit a high cross section nucleus. Four methods are employed for the production of neutrons in the laboratory i.e. to liberate them from their nuclear binding:

1. nuclear fission, usually accompanied with 2 - 3 neutrons.
2. specific binary nuclear reactions with a neutron in one exit channel.
3. spallation induced by fast (v≫0.25 c≈ v_n, the mean velocity of the nucleon's Fermi motion in nuclei) projectiles in a heavy target nucleus.
4. photoproduction making use of the nuclear photoeffect - the method of choice at ELBE.

In all cases the average neutron energy is much smaller than the other forms of energy coming from the neutron radiator. One may thus judge the "efficiency" of a neutron source by the amount of energy needed (or waisted) for a free neutron.

For the 4 processes listed above one estimates:

1. In a fission reactor up to 2 neutrons per fission may be taken out; the fission fragments with their 200 MeV of kinetic energy thus deposit 1 Ws per $6 \cdot 10^{10}$ neutrons. The maximum power density of a fission reactor (500 W/cm^3) results in a flux limit of $5 \cdot 10^{12} n/cm^2 \cdot s$ for the emission from a reactor volume of $1cm^3$.
2. In nuclear reactions usually considerably less than 10^9 neutrons are emitted per Ws of beam and they have narrow distributions in energy and direction, such that they are of use in special cases only.
3. One proton of 1.2 GeV hitting 35cm of Pb leads to 22 neutrons; this corresponds to 10^{11} neutrons per Ws of beam [1]. In 1 cm of Pb only $5 \cdot 10^9$ neutrons were observed per Ws of beam.
4. 30 MeV electrons deposit about half of their energy in 1 cm of Pb and the resulting bremsstrahlung leads to 10^{-2} free neutrons per electron [2]; thus $2 \cdot 10^9$ neutrons are produced per Ws of beam, and emitted from the radiators surface of 6 cm^2.

From these numbers it seems as if neutron production at an electron accelerator like ELBE is much less efficient than e.g. a spallation neutron source. But in many investigations not the neutron rate but rather the neutron flux (rate per area) is the important quantity ; as already obvious from what was noted under (3) the size of the spallation target determines the flux. If also the proton beam dimension is taken into account, the flux per power falls to $10^9 n/cm^2 \cdot Ws$ for a beam size 6x20 cm^2 as envisaged for the proposed European Spallation Source ESS. As compared to $3 \cdot 10^{12} n/cm^2 \cdot s$ to be reached at ELBE with 3.3 MHz repetition rate and thus 10 kW beam power, the ESS with its envisaged MW's of beam power may finally produce $10^{15} n/cm^2 \cdot s$; the ESS proposal [3] announces an average thermal flux of $3 \cdot 10^{14} n/cm^2 \cdot s$.

A high flux from a small radiator volume is especially important for time-of-flight studies yielding information about the energy dependence of neutron induced processes. For neutron energies above 100 keV and $\triangle E/E < 2$ % the ESS with its ejection bunch length of $\sim 1\mu$s has to use 200 m of flight path; this results in a flux of $10^7 n/cm^2 \cdot s$ at the end of the flight path.

ELBE with <200 ps pulse width and 3.6 m path length allows TOF-experiments up to 3MeV with $\triangle E/E \approx 1\%$ at several $10^6 n/cm^2 \cdot s$, and is thus fully competitive to ESS for such fast neutrons. To exploit this advantage in TOF-studies detectors with < 200 ps time resolution are required. With such detectors ELBE-n-TOF will allow energy dispersive neutron tomography and measurements of neutron scattering in materials of importance for the transmutation of nuclear waste as well as laboratory simulations for the astrophysical s-process. For neutrons of $\sim 0.1 MeV$ the parameters of ELBE allow for an improvement of up to one order of magnitude as compared to the electron linac ORELA at Oak Ridge (Tenn., USA), which is dedicated to such studies. As was shown there recently [4] energy dispersive neutron capture and transmission measurements have impact on our understanding of the "element-cooking" in stars.

One choice for neutron detectors of such good time resolution are small volume scintillators read out by photomultipliers. To compensate the small probability of signal generation (relying on proton recoil) a large total detection volume is required. Only by careful optimization of the detector geometry and the signal processing paths a cost-efficient set-up can be designed [5]; such work is in progress at the IKH.

[1] D. Hilscher for the Nessy Collaboration at FZJ-COSY, Heraeus Ferienkurs Dresden, 2002
[2] B. Naumann et al., Annual Report ELBE 2002 and ELBE/IKH 2001
[3] ESS proposal 2002
[4] P.E. Koehler et al., PRC 64(2001)065B02 and PRC62(2000)055803
[5] A. Butra et al., NIMA 455(2000) 412

Detector Setup for Nuclear-Resonance-Fluorescence Experiments at ELBE [D]

R. Schwengner, L. Käubler, M. Langer, G. Rusev, W. Schulze, A. Wagner

The bremsstrahlung facility at ELBE will be used for nuclear-structure experiments employing photon-induced reactions such as (γ, γ') (nuclear resonance fluorescence), (γ, n), (γ, p) (nuclear photoeffect) and photon-induced fission. All these experiments require an efficient setup of high-purity germanium (HPGe) detectors for the measurement of the characteristic γ radiation of the nuclides to be studied.

The setup of HPGe detectors for nuclear-resonance-fluorescence experiments is shown in Fig. 1. Four HPGe detectors are placed at 90° relative to the photon-beam direction and at 90° to each other. This orientation of the detectors was designed in particular for measuring asymmetries of γ-ray intensities in experiments with polarised photons. The detectors are mounted on frames made of sectional aluminium and can be moved on slide rails in order to vary the distance from the target. Each of these four detectors has an efficiency of 100 % relative to a 3" × 3" NaI detector. Two detectors (top and bottom) are four-fold segmented and may also be used as Compton polarimeters.

All four detectors are surrounded by escape-suppression shields consisting of eight optically separated bismuth germanate (BGO) scintillation detectors. These BGO detectors were specially designed for the present setup which is illustrated in Fig. 2. An example for the performance of the escape-suppression shield is shown in Fig. 3. This example for the energy region around 8 MeV shows that the Compton background in the HPGe detector is reduced by a factor of about two while the single-escape peak is reduced by a factor of about three in the spectrum measured in anticoincidence with the BGO detector as compared with a singles spectrum.

A fifth HPGe detector is positioned at 130° with respect to the beam direction in order to enable the measurement of angular distributions of the γ rays.

Fig. 1 *Setup of high-purity Ge detectors surrounded by escape-suppression shields. The photon beam enters the experimental area from the right.*

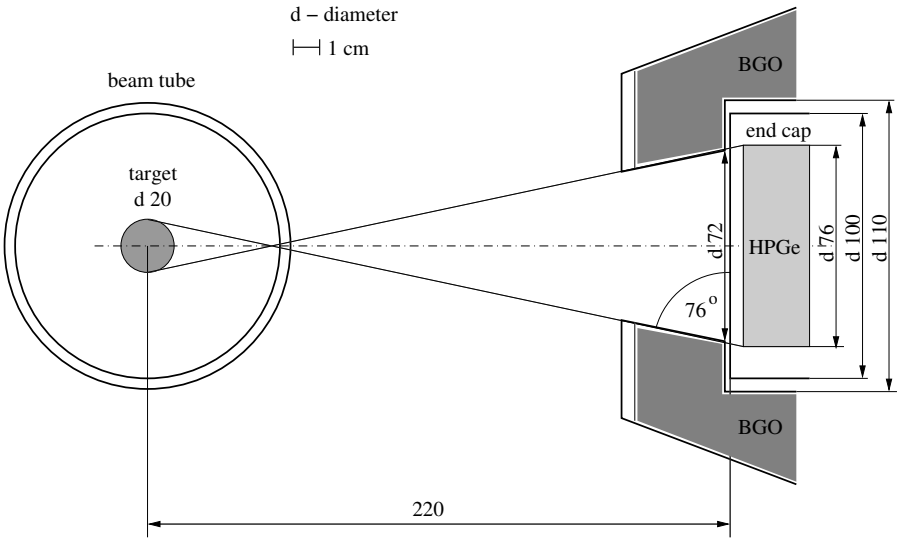

Fig. 2 *Shape of the BGO detector surrounding the end cap of the HPGe detector. The front end of the BGO detector was designed such that radiation from a target of 20 mm diameter is covered by the HPGe detector at a distance of 220 mm from the target.*

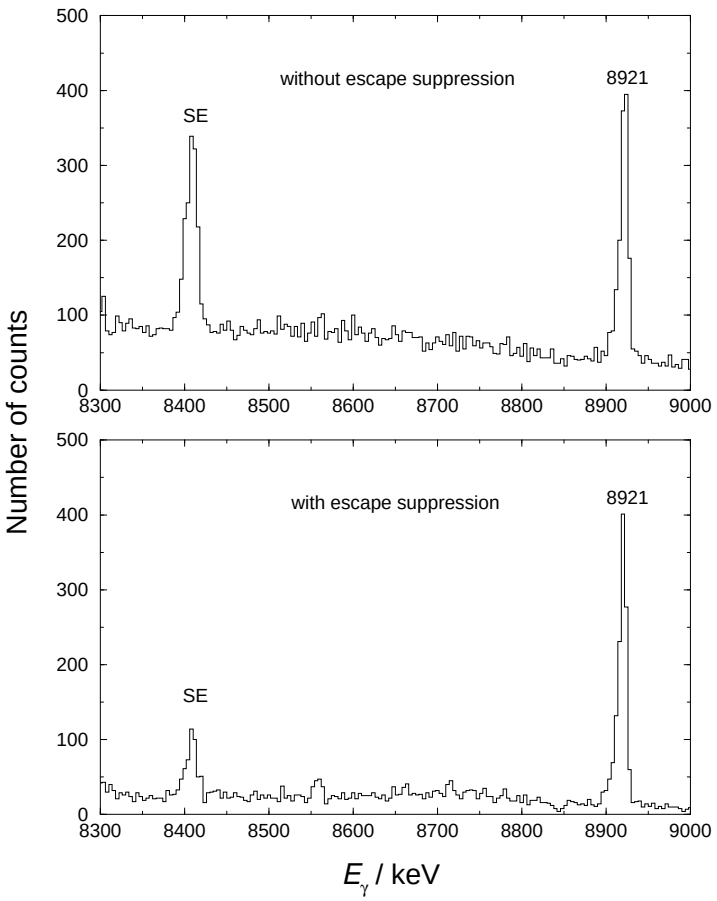

Fig. 3 *Portions of spectra of one HPGe detector containing singles events (upper panel) and events measured in anticoincidence with the surrounding BGO detector (lower panel). Peaks labelled SE are the single-escape peaks belonging to the full-energy peak at 8921 keV.*

Collimators for the BGO Escape-Suppression Shields [D]

G. Rusev[1], R. Schwengner, A. Wagner, L. Käubler, F. Dönau, E. Grosse

In nuclear spectroscopy high-purity germanium (HPGe) detectors are used for γ-ray detection with high energy resolution. However, these detectors have a rather small detection efficiency at high γ-ray energies. In order to suppress the signals of not fully absorbed photons in the HPGe crystal we use an escape-suppression shield of bismuth germanate (BGO) scintillation detectors [1]. The BGO surrounds the HPGe detector and works as a veto to photons scattered out of the HPGe crystal.

The escape-suppression shield has to be protected from direct radiation from the nuclear-resonance-fluorescence (NRF) target. We designed a lead collimator by performing Monte-Carlo simulations with the GEANT3 [2] program package, where the real detector-setup geometry was implemented. Monoenergetic photons with energies of 7, 10, 13 and 16 MeV were generated from the place of the NRF target. These energies represent the range where we expect to observe resonance lines. The entrance and exit diameters of the collimator were varied from 24 to 32 mm and from 26 to 72 mm, respectively, in steps of 1 mm. For each collimator geometry a spectrum of the deposited energy in the HPGe crystal in anticoincidence with the BGO escape-suppression shield was collected. From the spectrum the area of the photo-peaks and the common background due to Compton scattering and pair creation was extracted.

We used two competing criteria to obtain the optimal geometry of the collimator. The first criterion is to maximise the ratio of photo-peak to background. Fig. 1 shows this ratio versus the entrance and exit diameters of the collimator cone. It shows a flat distribution with a maximum at smaller diameters. The second criterion is to get a big photo-peak area. Fig. 2 shows the photo-peak area versus the two collimator diameters. This quantity increases with increasing opening angle of the collimator.

One good compromise is a point in the flat part of ratio peak-to-background for which the photo-peak area is as big as possible. We chose values for the entrance and exit diameters of 30 and 50 mm, respectively. The point is marked with a cross in Figs. 1 and 2.

Lead was chosen as a material for the collimator because it has a big density and well known NRF lines. The collimator thickness is 70 mm. This is equivalent to about five half-thicknesses for the absorption of 3 MeV photons. The collimator length was divided into one part of 3 cm and four parts of 1 cm in order to adjust experimentally the collimator thickness. The technical outline is shown in Fig. 3.

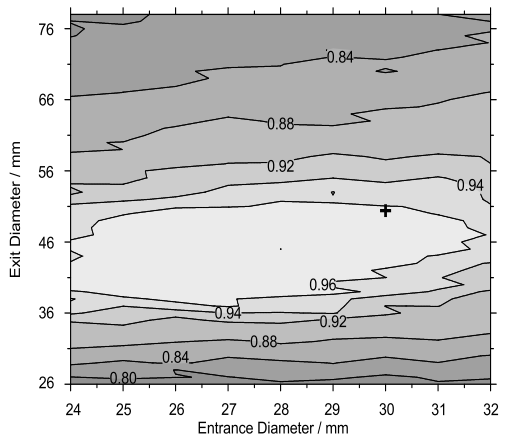

Fig. 1 *Normalised ratio of photo-peak to background versus the entrance (abscissa) and the exit diameter (ordinate). The cross marks the chosen diameters.*

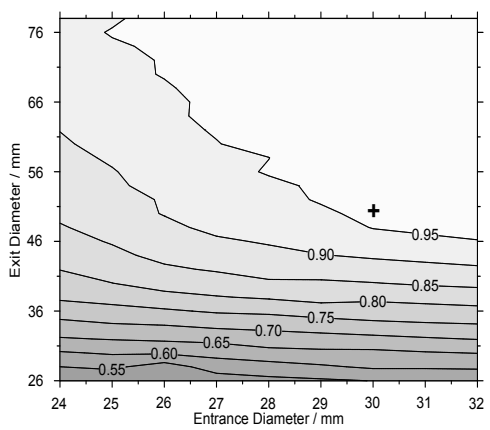

Fig. 2 *Normalised area of photo-peak versus the two diameters. The cross shows the chosen diameters.*

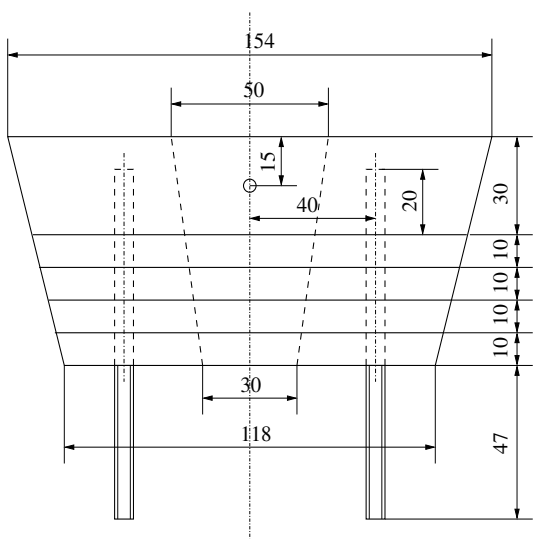

Fig. 3 *Technical outline of the collimator.*

[1] R. Schwengner et al., This Report, p. 27
[2] CERN Program Library Long Writeup Q121, CERN, Geneva (CH), 1994

[1] *FZR and INRNE, Sofia, Bulgaria*

Radiator for the Production of Bremsstrahlung at ELBE

K.D. Schilling, F. Dönau, E. Grosse, L. Käubler, R. Schwengner, A. Wagner, B. Wustmann[1], U. Lehnert[2], A. Nowak[1], B. Rimarzig, R. Schlenk[1]

The radiator occupies a key position in the nuclear physics beam line at ELBE, in particular, for the nuclear resonance fluorescence (NRF) experiments [1]. It converts the kinetic energy of the electrons into electromagnetic radiation, more precisely, into bremsstrahlung. The radiator itself consists of a thin metallic foil (e.g. Nb or Al) or of a thin slice of other material (e.g. CVD diamond) and is embedded in a water-cooled holder construction as shown in Fig. 1.

The radiator foil (slice) is hit by the electron beam and absorbs typically only about one part per thousand of the incident electron energy. The radiator thickness has to be optimized for each material by making a compromise: to maximize the production yield of bremsstrahlung, on the one hand, and to minimize the small-angle scattering of the electrons during their passage through the radiator material, on the other hand. The latter effect has two important consequences: (i) a definite polarization degree of the bremsstrahlung beam can be achieved, which is important for parity determinations of high-energy excited states to be measured, and (ii) the radiation background resulting from the interaction of the scattered electrons in the beam envelope with beam-line components downstream of the radiator can be reduced. Thus, the use of thin radiators has been decided in the present case. The typical thickness ranges from $3\text{x}10^{-4}$ to 10^{-3} times the radiation length X_0, that means , for instance, 4 to 12 μm Nb, 25 to 75 μm Al and 70 to 180 μm diamond radiators.

Some preparatory considerations and simulations regarding the choice of optimum radiator materials have been performed earlier [2]. They result in the preference of the above mentioned Nb and Al radiators for reasons given here and in [2]. Diamond is another candidate with superior heat conductivity, heat resistivity as well as neutron separation energy (cf. also [3]). The diameter of the radiator foils (slices) was chosen primarily with regard to the best possible heat dissipation; but possible instabilities of the beam alignment were also taken into account.

The beam position on the radiator is continuously observed by a video camera in the following way: a mirror positioned about 600 mm in front of the radiator inside the beam tube but outside of the electron beam reflects the optical transition radiation (OTR) of the beam spot emitted backwards into the video camera, thus imaging the radiator and the beam spot completely.

Furthermore, the temperature of the radiator at the beam spot (Ø ≈ 2 mm) is controlled by radiation thermometry. For this purpose, a pyrometer (RAYTEK Corporation, Santa Cruz, CA) with a laser viewfinder and a high optical resolution (300:1) is monitoring the infrared radiation (of 1.6 μm wavelength) emitted from the hottest spot of the radiator in a distance of 300 mm at the backward angle of 135°. Thus, we are able to determine the maximum temperature in the centre of the radiator with about 1 mm spatial resolution. This is an important information to prevent melting of materials like aluminium. The range of the expected critical temperatures has been calculated in advance with the finite-element code ANSYS [4] for various materials. This was of decisive importance for the design and construction of the radiator holder (Fig. 1).

After having passed the radiator, the geometrically widened (spread) electron beam is deflected by a dipole magnet [5] and led through a vacuum separation window made from beryllium (1 mm thick, Ø = 90 mm) into the electron beam dump, where far the most of the beam power is deposited (cf. Fig. 1 in [6]).

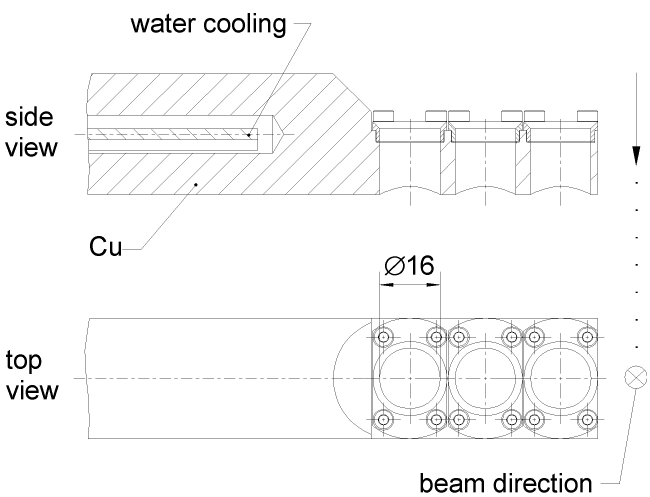

Fig. 1 *Schematic view of the radiator holder consisting of a massive, water-cooled Cu rod with three fixings for the radiator foils at the top (on the right). The net diameter of the radiators is 16 mm. The beam direction is indicated.*

[1] K.D. Schilling et al., Wiss.-Tech. Ber. FZR-271 (1999) 32; K.D. Schilling, http://www.fz-rossendorf.de /ELBE/en/np; R. Schwengner, http://www.fz-rossendorf.de /FWK/MITARB/rs/krf-elbe.html
[2] A. Wagner et al., Wiss.-Tech. Ber. FZR-271 (1999) 33
[3] A. Wagner et al., Wiss.-Tech. Ber. FZR-319 (2001) 40
[4] M. Werner, FZ Rossendorf, FWS, priv. comm.
[5] K.D. Schilling et al., This Report, p. 33
[6] K.D. Schilling et al., This Report, p. 31

[1] *FZ Rossendorf, FWF*
[2] *FZ Rossendorf, FWL*

Steering Magnets for the Production of Polarized Bremsstrahlung at ELBE

K.D. Schilling, U. Lehnert[1], F. Herbrand[2], R. Schwengner, A. Wagner, B. Caspar[2], M. Langer, T. Riedel[2], A. Wagner II

The electron beam is transported by a non-dispersive system of two dipole and three quadrupole magnets into the nuclear physics beamline and focused onto the radiator [1] as schematically displayed in Fig. 1. The collimated beam of bremsstrahlung photons excites the target nuclei to be investigated in the nuclear resonance fluorescence (NRF) experiments. The de-excitation of the excited states occurs via the emission of characteristic γ-rays, which are the subject of investigation [2].

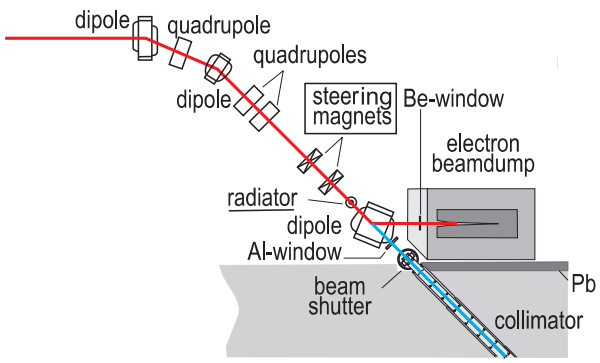

Fig. 1 *Nuclear physics beam line for the production of polarized bremsstrahlung at ELBE (red = electron beam, blue = bremsstrahlung beam).*

In order to deduce the parity of the excited states, it is necessary to measure the linear polarization of the $\gamma-$transitions. The knowledge of the polarization enables a discrimination between electric and magnetic multipole radiation, especially between electric dipole (E1) and magnetic dipole (M1) transitions. For this purpose, the target will be irradiated with polarized bremsstrahlung. The method for polarized bremsstrahlung production is shown in Fig. 2. It makes use of the fact [3] that the electric field vector $\vec{E}$ of the radiation is aligned tangentially around a cross section of the spatial distribution of the photons. With two steering magnets described below, the electron beam will be deflected from the normal direction and back such that it hits the radiator in the centre under a particular angle Θ_o. As a consequence, an off-axis portion of the spatial distribution of the photons is cut out by the collimator. This off-axis portion of the bremsstrahlung cone is dominated by a definite direction of the electric field vector $\vec{E}$, which means that the photon beam passing through the collimator is partially polarized. The degree of polarization depends on the angle Θ_o and has a maximum at $\Theta_o = m_0 \cdot c^2 \ / \ E$, wh ere $m_0 \cdot c^2 = 511$ keV is the rest energy of the electron and E is the total energy of the incident electrons. The polarized incident photons cause an azimuthal asymmetry of the intensity of the γ-transitions emitted from the excited states of the target nuclei. The asymmetry of E1 radiation is opposite to the one of M1 radiation. Therefore, one can discriminate between electric and magnetic radiation by measuring the asymmetry with detectors at different azimuthal angles (see Fig. 2).

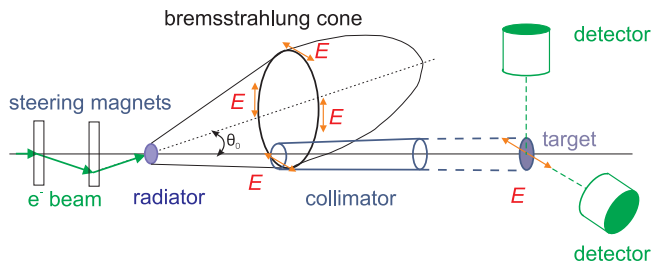

Fig. 2 *Principle of generation of linearly-polarized off-axis bremsstrahlung.*

The two steering magnets of identical construction are positioned 340 mm and 680 mm in front of the radiator, respectively (cf. Fig. 1). They were built up symmetrically (see Fig. 3) to deflect the electron beam periodically into the four directions in space: left(l) and right(r), up(u) and down(d). Thus - in spite of possible fluctuations of the electron current - the effective photon flux for each deflection angle will be the same. In this way, possible systematic asymmetries in the steerer positions and in the beam alignment will be averaged resp. minimized. The monitoring of the photon flux and the determination of its energy distribution is performed with the setup described in [4]. A sketch of one of the two steering magnets is presented in Fig. 3. The four identical coils are symmetrically arranged at the steel (ST37) yoke around the beam tube of 70 mm outer diameter (66 mm inside diameter). The shape of the four pole shoes has been optimized for the best field homogeneity [5]. The magnetic field strength in the middle plane of the steerer on the symmetry axis reaches about 30 mT - whereas 25 mT (83 %) are achieved on a trajectory displaced by 22 mm perpendicularly to the field lines, which corresponds to the maximum required displacement (deflection) of the electron beam.
In order to achieve the highest degree of polarization, the typical deflection angles range from about 3.5° to 1.5° for electron energies from 8 to 20 MeV. The deflection angles of the electron beam are visually optimized before and controlled after each measurement by two view screens at definite positions using the diagnostic mode of the accelerator, i.e. at low beam currents. The first view screen is positioned downstream of the second

[1] *FZ Rossendorf, FWL*
[2] *FZ Rossendorf, FWF*

steering magnet 210 mm in front of the radiator, where the beam is relatively far displaced from the beam axis; the second view screen is at radiator position, where the beam crosses the centre of the radiator.
Continuous monitoring of the polarization degree of the bremsstrahlung beam is required during the experiment. This is realized by the polarization monitor presented in [6]. The switching signal for the steerer coils is also delivered from the polarization monitor such that the electron beam is deflected after a definite number of events into the next of the four directions in space in the order: l - u - r - d. Self-made 15V/5A linear regulation moduls are used to supply the steering coils. The polarization degree and the coil currents are controlled by a progammable logic controller (PLC) SIMATIC S7 for each coil separately. This PLC is embedded in the ELBE machine control system. The sets of current for each deflection angle can be stored and reloaded by the human-machine interface (HMI) WinCC of the ELBE machine control system.

The effective length L_{eff} of the magnetic field in beam direction - as a characteristic property of the steering magnet - has been deduced by a Hall-probe measurement to be 186 mm. The product of the latter quantity with the required magnetic field strength in the middle plane determines the deflection angles.
A third steering magnet is placed between the radiator and the dipole (deflecting) magnet (cf. Fig. 1) in order to correct the vertical component of the tilted beam direction. The horizontal beam component can be corrected by an additional contribution to the magnetic field value of the deflecting dipole magnet. This steering magnet has the shape of a C-magnet with horizontal field direction produced by four coils that are arranged in the following way: each one of them at the two vertical legs and two at the horizontal leg of the yoke. Thus, magnetic fields of more than 20 mT can easily be achieved. The effective field length of the third steering magnet has been measured to be $L_{eff} = 133$ mm.

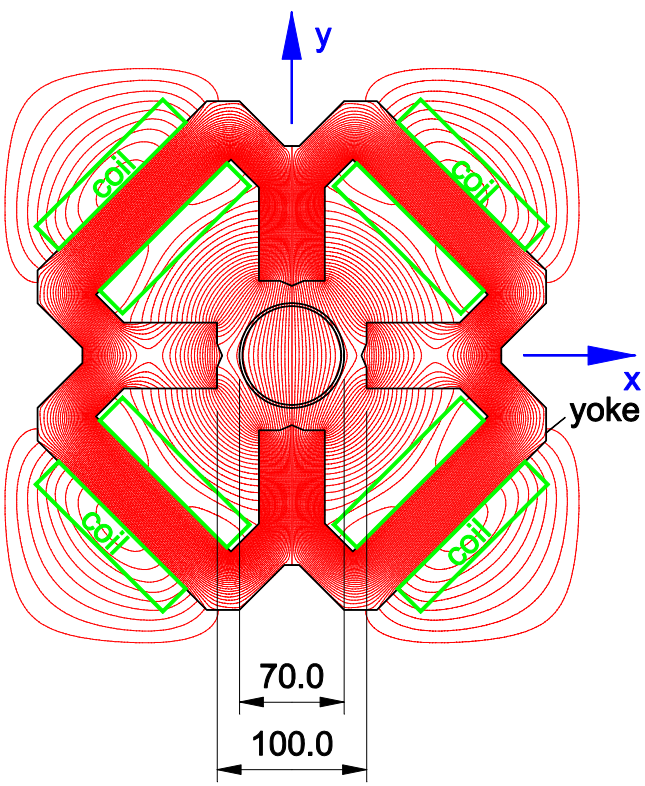

Fig. 3 *Sectional drawing of a steering magnet with the magnetic field pattern calculated with the code POISSON [5]. The cross-section of the beam tube is indicated in the centre. Sizes are in mm.*

[1] K.D. Schilling et al., This Report, p. 30
[2] R. Schwengner, http://www.fz-rossendorf.de/FWK/MITARB/rs/krf-elbe.html
[3] M. May and G.C. Wick, Phys. Rev. 81 (1951) 628
[4] A. Wagner et al., FZ Rossendorf, Wiss.-Tech. Ber. FZR-341 (2002) 38
[5] J.H. Billen and L.M. Young, Poisson Superfish, version 6, LAACG, LANL, NM (2000)
[6] R. Schwengner et al., FZ Rossendorf, Wiss.-Tech. Ber. FZR-341 (2002) 39

Beam Separation Magnet of the Bremsstrahlung Facility at ELBE

K.D. Schilling, M. Langer, U. Lehnert[1], W. Schulze

The electron beam impinging upon the radiator [1] of the nuclear physics beam line generates bremsstrahlung for NRF and photofission experiments [2]. Shortly after having passed the radiator, the electrons are deflected by a large dipole magnet to be described here into the electron beam dump, whereas the bremsstrahlung photon beam goes straight ahead through the collimator [3] to the nuclear physics cave. The dipole magnet, thus, separates the electron beam from the photon beam (cf. also Fig. 1 in [4]). The magnet was delivered originally as a standard dipole magnet (DANFYSIK A/S) with a 40 mm gap.

This gap has been enlarged to 117 mm in order to meet the requirements discussed in [1], i.e. to enable the beam, which is widened by small-angle scattering after having passed through the radiator foil, the passage through the vacuum chamber of the magnet with minimum interaction with the chamber walls. After this change of the construction, a series of detailed magnetic field measurements with a Hall probe have been performed and compared with model calculations with the POISSON code [5].

Two important results have been obtained: (i) the magnetic field distribution has been measured including the maximum field value of $B_{max} = 363$ mT (at $I_{max} = 160$ A) in the centre of the pole shoes and (ii) the effective field length L_{eff} has been derived to be 309 mm. The calculated value [5] of B_{max} is 373 mT in good agreement with the experimental result. The calculated L_{eff} value [5] is with 281 mm somewhat smaller ($\approx$ 10 %) than the result derived from the measured field distribution. This slight difference is within the usual model uncertainties for a dipole magnet with such a large ratio of gap/pole-shoe length.

On the basis of the measured L_{eff} value, the functional dependence of the magnetic field strength - and, in this way, of the electron beam energy - on the coil current has been deduced, which serves now as a basis for the determination of the electron beam energy at the nuclear physics beam line. The analytical expression is:

$$E_{kin}(MeV) = 0.267 \cdot I(A) - 0.402.$$

The graphic representation of this dependence is shown in Fig. 1. It can also be seen here that there are reserves in the applicability of the magnet for even higher beam energies - if desired in future.

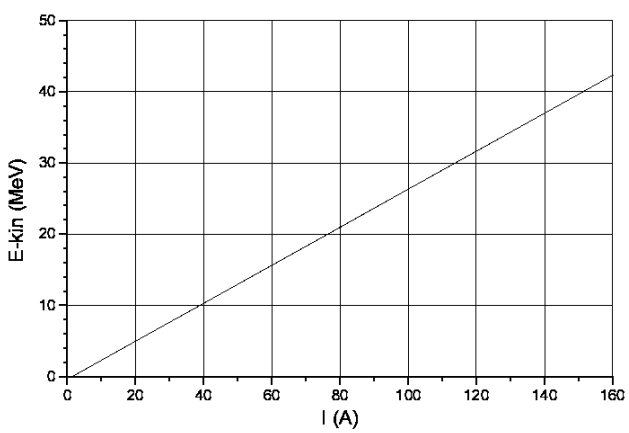

Fig. 1 *Electron beam energy vs. coil current for the 45° deflecting dipole magnet of the bremsstrahlung facility.*

[1] K.D. Schilling et al., This Report, p. 30
[2] R. Schwengner, http://www.fz-rossendorf.de/FWK/MITARB/rs/krf-elbe.html
[3] K.D. Schilling et al., FZ Rossendorf, Wiss.-Tech. Ber. FZR-341 (2002) 37
[4] K.D. Schilling et al., This Report, p. 30
[5] J.H. Billen and L.M. Young, Poisson Superfish, version 6, LAACG, LANL, NM

[1] *FZ Rossendorf, FWL*

Dipole Excitations in ^{98}Mo [B]

G. Rusev[1], R. Schwengner, F. Dönau, L. Käubler, S. Mallion, K. D. Schilling, A. Wagner, L. K. Kostov[1], H. von Garrel[2], U. Kneissl[2], C. Kohstall[2], M. Kreutz[2], H. H. Pitz[2], M. Scheck[2], F. Stedile[2], P. von Brentano[3], J. Jolie[3], A. Linnemann[3], N. Pietralla[3], V. Werner[3]

The chain of stable Mo isotopes is an interesting object for the investigation of the interaction between protons and neutrons. In ^{94}Mo, 1^+, 2^+ and 3^+ mixed-symmetry states were found which deexcite via $M1$ transitions with strengths of up to 0.3 μ_N^2 [1,2]. Possible candidates for such states were also found in ^{96}Mo [3]. In the next heavier isotope ^{98}Mo, the influence of the $N = 56$ subshell closure on the properties of dipole states may be studied. Nuclear resonance fluorescence (NRF) experiments were carried out at the Stuttgart Dynamitron accelerator at electron energies of 3.3 and 3.8 MeV. The target consisted of a sample of ^{98}Mo with a mass of 1998 mg and an enrichment of 98.55%, combined with 756.7 mg ^{27}Al and 102 mg ^{13}C for photon flux calibration.

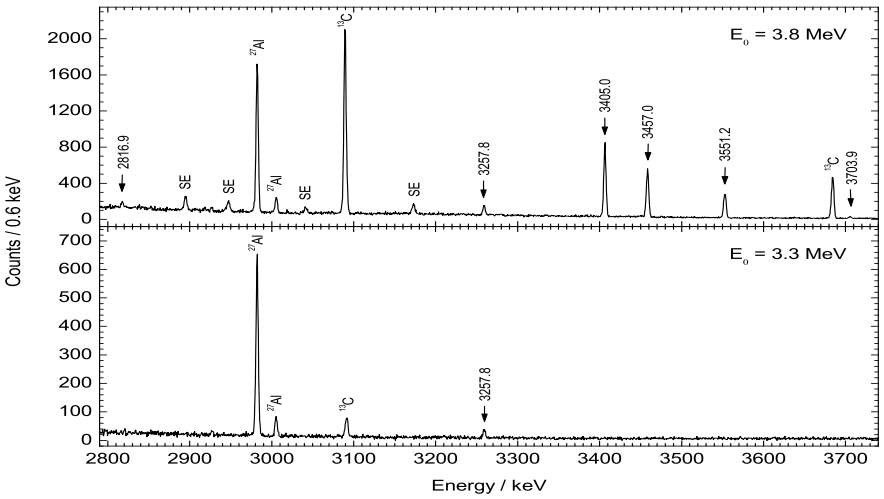

Fig. 1 *Parts of spectra of photons scattered from ^{98}Mo, measured at 127° relative to the beam and at electron energies of 3.8 MeV (top) and 3.3 MeV (bottom). SE marks the single-escape peaks.*

We observed six transitions in ^{98}Mo for the first time [4]. Spectra including these transitions are shown in Fig. 1. The angular distributions indicate dipole character for the newly observed transitions.

The comparison of the spectra measured at different energies reveals that the transition at 2817.1 keV is not a ground-state transition, but deexcites a state at an energy greater than 3.3 MeV. Indeed, it fits well the energy spacing between the dipole state at 3552.2 keV and the second 0^+ state.

A level scheme including the dipole states found in the present experiments and known low-lying states is shown in Fig. 2. The deexcitation of a $J = 1$ state to the excited 0^+ state is a specific feature of this nuclide and one of the first observations of such transitions from dipole states to intruder states.

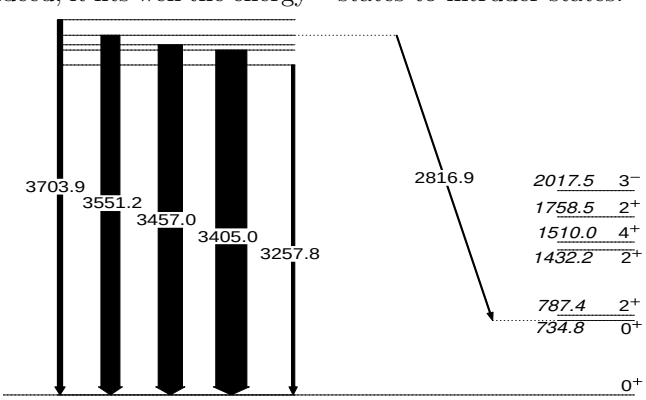

Fig. 2 *Level scheme of ^{98}Mo including the dipole states found in the present work (left) and known low-lying states (right).*

[1] N. Pietralla et al., Phys. Rev. Lett. 83 (1999) 1303
[2] N. Pietralla et al., Phys. Rev. Lett. 84 (2000) 3775
[3] V. Werner et al., IfS Annual Report 1999, p. 18
[4] G. Rusev et al., Fz Rossendorf, Wiss.-Tech. Ber. FZR-341 (2002) 77

[1] *FZR and INRNE, Sofia, Bulgaria*
[2] *IfS, Universität Stuttgart*
[3] *Institut für Kernphysik, Universität zu Köln*

Nuclear Resonance Fluorescence Experiments on ^{100}Mo [D]

G. Rusev[1], R. Schwengner, F. Dönau, L. Käubler, S. Mallion, K. D. Schilling, A. Wagner, L. K. Kostov[1], H. von Garrel[2], U. Kneissl[2], C. Kohstall[2], M. Kreutz[2], H. H. Pitz[2], M. Scheck[2], F. Stedile[2], P. von Brentano[3], J. Jolie[3], A. Linnemann[3], N. Pietralla[3], V. Werner[3]

In order to extend our study of dipole excitations in Mo isotopes to greater neutron numbers we investigated the nuclide ^{100}Mo. This isotope has 58 neutrons and may allow us to study the onset of collectivity and its influence on the properties of dipole excitations.

We performed nuclear resonance fluorescence experiments at the Stuttgart Dynamitron accelerator at electron energies of 3.2, 3.4 and 3.8 MeV. A sample of 1620 mg ^{100}Mo, enriched to 99.0 %, was used as a target in the NRF measurements. The target was combined with 758.4 mg ^{27}Al and 102 mg ^{13}C for photon flux calibration. In the present experiments, we observed 19 γ rays for the first time. These γ rays are marked with their energies in the spectra shown in Fig. 1. Based on the analysis of the angular distributions we consider them as dipole transitions.

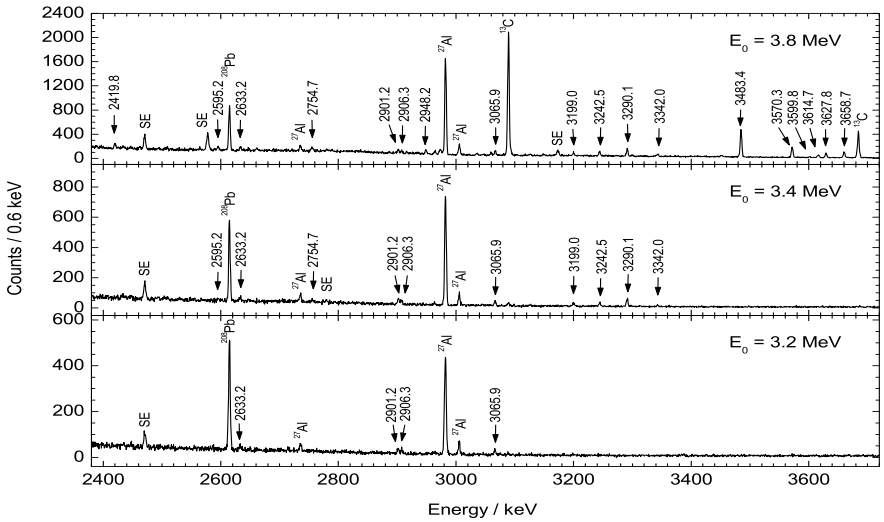

Fig. 1 *Comparison of partial spectra of photons scattered from ^{100}Mo at 127° relative to the beam axis for different electron energies. SE marks the single-escape peaks.*

The comparison of the spectra measured at the different energies allows us to distinguish between ground-state transitions and transitions that populate low-lying levels. Based on this comparison and on the respective level spacings we established the level scheme shown in Fig. 2. In addition to ground-state transitions, we observed transitions populating the lowest 2^+ state as well as excited 0^+ and 2^+ states. The observation of a transition to the excited 0^+ state is analogous to the neighbouring isotope ^{98}Mo [1]. The transititon at 2595.0 keV fits the energy spacing between the 3659.6 keV state and the 2_2^+ state as well as the spacing between the state at 3290.7 keV and the 0_2^+ state. The measurement at 3.4 MeV proves that both 2595.0 keV transitions exist and have nearly the same intensity.

In addition to the deexcitation of dipole states to the 0^+ intruder state, which was also found in ^{98}Mo, we observed transitions to low-lying 2^+ states in ^{100}Mo.

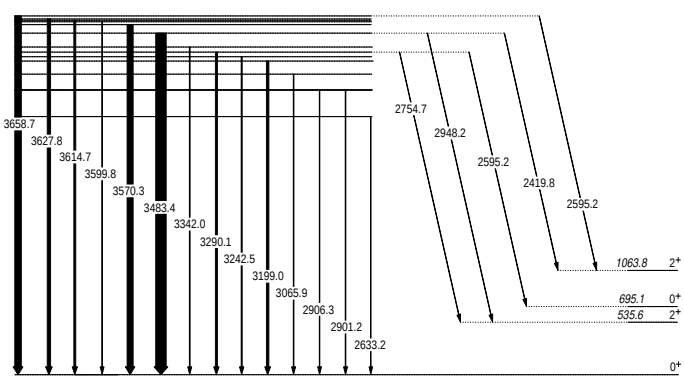

Fig. 2 *Level scheme of ^{100}Mo. The widths of the arrows are proportional to the intensities of the transitions.*

[1] G. Rusev et al., This Report p. 34

[1] *FZR and INRNE, Sofia, Bulgaria*
[2] *IfS, Universität Stuttgart*
[3] *Institut für Kernphysik, Universität zu Köln*

Simulations for a Double Time-of-Flight Spectrometer for Fission Fragments[G]

H. Sharma, A. Wagner, E. Grosse

The study of exotic nuclei is one of the most active and interesting areas of research in nuclear physics. Indeed, some of such studies have already opened a new area of research in nuclear physics. The nuclei with extreme neutron to proton ratio are very important in nuclear astrophysics because of their relevance to the r-process in nucleosynthesis. Informations on their structure and their properties would help us to better understand the r-process and also other violent stellar events. Experiments are planned to study these exotic nuclei at ELBE.

Theoretical calculations by Fan et al. [1] have shown the possibility of producing neutron-rich exotic nuclei at ELBE via bremsstrahlung-induced fission of ^{238}U. The next challenging task is to detect these low-energy fission fragments (FFs) with the highest attainable mass and charge resolution. The time-of-flight (TOF) measurements can be carried out with a high precision of the start signal due to the very good time structure ($<$ 10ps) of the electron beam at ELBE [2]. Using this precise timing of the electron beam for the identification of the fission fragments, the velocity change of the moving fragments can be measured by a double TOF method as shown in Fig. 1. The double TOF, i.e., first TOF (t1) of the fragments before passing the foil and the second TOF (t2) after passing them through the foil may provide a separation of mass and charge of the fission fragments. The technical information about the foils, MCPs, anodes, mirrors as illustrated in Fig. 1, will be given in a separate report.

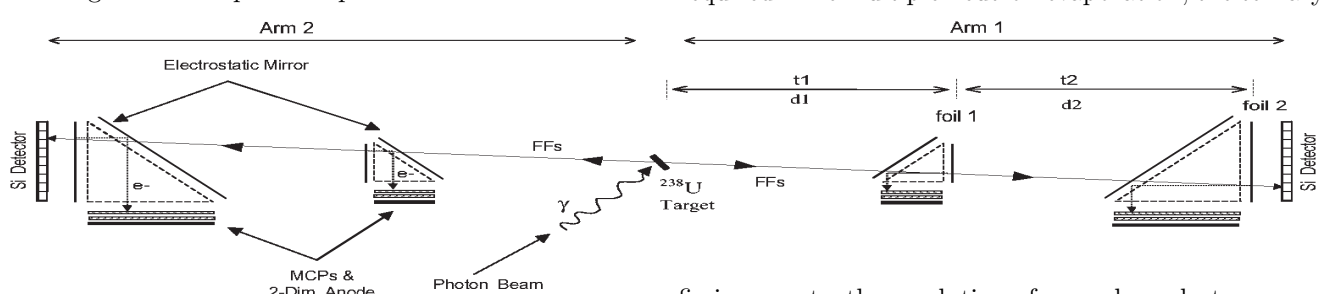

Fig. 1 *A schematic lay-out of the double TOF spectrometer.*

In the first elaborate attempt to understand the response of the double TOF spectrometer a simulation program based on a Monte Carlo method has been developed for an event-by-event analysis of the FFs. The calculated yield distribution is normalised to the experimental fragment yield distribution for a given fissioning nucleus. The fragment's kinetic energy is calculated using standard liquid drop parameters for the fissioning nucleus and the procedure reported in the literature [3]. The prompt neutron emission probability for the excited FFs is also calculated following the description given by Fraser [4]. At maximum two neutrons are evaporated from the excited fragment and the resulting velocity change of the fragment is taken into account. The fragment's kinetic energy-loss in the foil (foil1) is calculated and the energy straggling is estimated empirically as a function of fragment's Z and A and its energy. The input of the simulation program requires: (i) Fragment yield distribution; (ii) Liquid drop parameters; (iii) Neutron emission parameters for the fissioning nucleus; (iv) Composition of the foil and areal density; (v) Length of various flight paths.

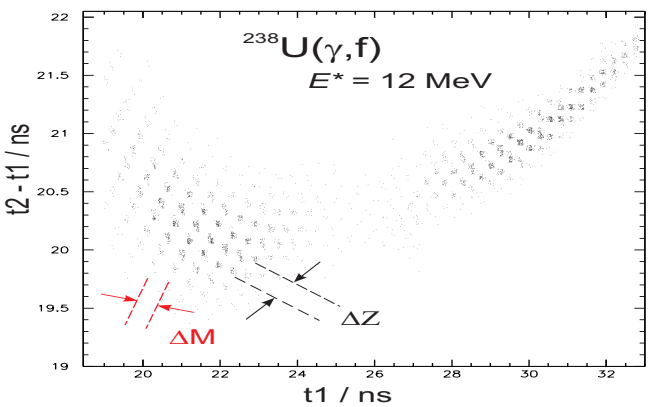

Fig. 2 *Calculated correlation between t1 and t2 for the double TOF spectrometer.*

Fig. 2 shows TOF spectra calculated for the ^{238}U(γ, f) reaction with an electron end-point energy of 12 MeV, distances $d1 = d2 =$ 300mm and a carbon foil of $500\mu g/cm^2$. The results indicate that for the fragment's M and Z separation time resolutions better than $\Delta t1 =$ 100 psec and $\Delta t2 =$ 300 psec, respectively, are required. The multiple neutron evaporation, the ternary fission events, the resolution of secondary electron measurements, energy-loss of the FFs the target material, inhomogeneity in foil thickness and the energy-straggling in the foil will deteriorate the quality of the time spectrum and hence ΔM and ΔZ resolutions. These sources of deterioration in the precise M and Z determination of the FFs are subject of further investigations.

Present calculation has demonstrated that the simultaneous determination of mass and charge of the FFs can be possible by a double time-of-flight measurement at ELBE if the TOF measurement can be realised with a time resolution better than 100 ps.

[1] S. Fan, A. Wagner, E. Grosse, Wiss.-Tech. Ber. FZR-319 (2001) 39
[2] P. Evtushenko et al., Wiss.-Tech. Ber. FZR-341 (2002) 19
[3] The Nuclear Fission Process, Ed. C. Wagemans, CRC Press, 1991
[4] J. S. Fraser, Phys. Rev. 88 (1952) 536

A Time Coincidence Test Setup for an MCP Detector[G]

H. Sharma, K. Kosev, A. Wagner, K. D. Schilling, A. Wagner II, W. Schulze, K. Heidel

A double time-of-flight (TOF) spectrometer for the identification of fission fragments is under construction [1]. The TOF spectrometer will be tested offline with a spontaneous fission source ^{252}Cf. Secondary electrons emitted simultaneously with fragments from the ^{252}Cf source can be detected in order to get a trigger signal which is necessary as start signal for the TOF measurements with the source.

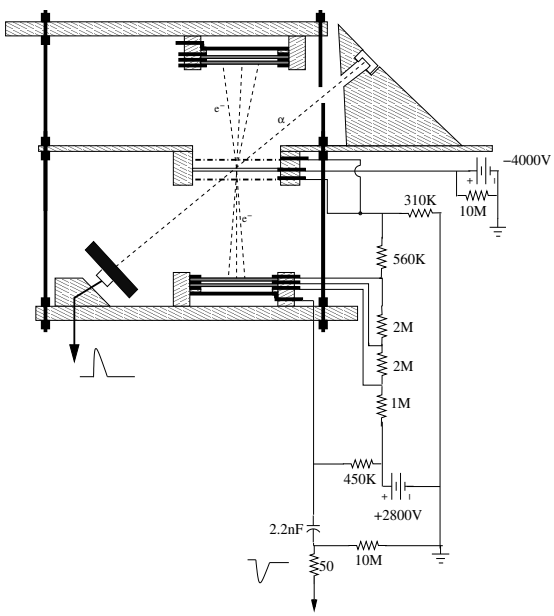

Fig. 1 *The provisional experimental setup.*

For this purpose a zero-time detector has been designed using two microchannel plates (MCPs) for amplification of the secondary electron signal. In order to test the performance of the MCPs, a coincidence measurement between the MCP and a silicon (Si) detector has been carried out by using a provisional experimental setup as shown in Fig. 1. We have also measured the coincidence between two MCP detectors by measuring backward and forward secondary electrons from the foil, as shown in Fig. 1

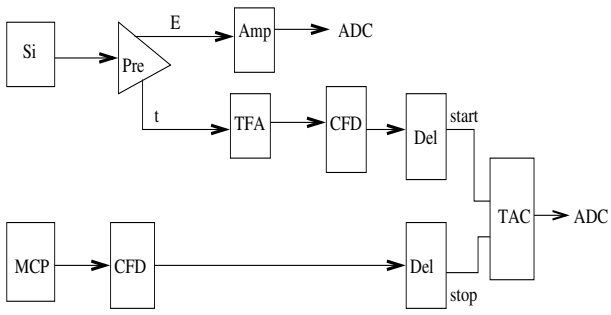

Fig. 2 *Block diagram of the slow-fast electronics setup used in the coincidence measurements.*

The measurements were performed with a collimated mixed radioactive alpha source (^{239}Pu, ^{241}Am and ^{244}Cm) in a vacuum chamber at a pressure of about 4x10^{-6} mbar.The alpha particles impinge on a thin aluminum foil (2.0μm thick) at an incidence angle of 45°. The secondary electrons emitted from the foil were accelerated by -3.8 kV potential and collected onto the MCP. The foil and the Si and MCP detectors were mounted in very close geometry to the alpha source. The distance between alpha source and the Si-detector was about 80mm and the distance between foil and the MCPs was about 45mm. The accelerating grid was mounted below the foil at a separation of 3mm.

The anode, the MCPs and the accelerating grids were biased with a single positive bias supply by using a resistor chain. The foil was biased with a separate negative bias supply according to Fig. 1. The fast signals from the MCP were directly fed to constant-fraction-discriminator (CFD) whereas the signals from the Si-detector were processed through a charge-sensitive preamplifier. A standard fast-slow coincidence setup was used as shown in Fig. 2. In order to avoid any pickup in the Si detector from the high voltage discharges at the foil or from a discharge of the MCPs, both MCP and foil frames had metallized grounded surfaces.

The data were acquired using a multi-channel analyser. Fig. 3 shows the collected time-to-amplitude-convertor (TAC) spectra. In case of MCP versus Si detector a typical time resolution of 15 nsec was observed (Fig. 3) which mainly contributed by the the Si-detector. In case of coincidence between MCP versus MCP the time resolution of about 550 ps (FWHM) was obtained as shown in Fig. 3. Improvements to improve the time resolution are under way.

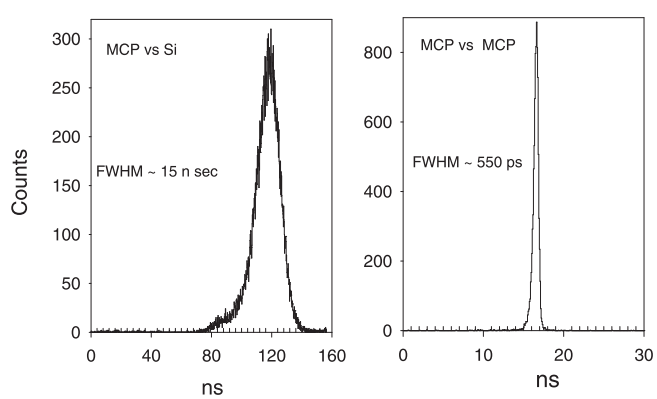

Fig. 3 *The TAC spectrum shows the observed time resolutions of 15 ns for MCP versus Si (left) and of about 550 ps for MCP versus MCP (right).*

[1] H. Sharma et al., This Report p. 36
[2] G. Pausch et al., Nucl. Instr. Meth. A 443 (2000) 304

Secondary Electron Trajectories for an Electrostatic Mirror[G]

H. Sharma, K. Kosev, A. Wagner, K. D. Schilling, M. Sobiella, K. Kanaki

Experimental studies of exotic neutron-rich nuclei are planned at ELBE. These nuclei will be produced via bremsstrahlung induced photo-fission. The fission fragments will be detected by a proposed double time-of-flight (TOF) method [1].

For this purpose a two-dimensional position-sensitive TOF spectrometer is under construction. The mounting system of the spectrometer is designed with coupling flanges of standard dimensions in order to use it at the heavy-ion syncrotron at GSI and at the electron accelerator ELBE. The spectrometer is composed of four TOF detectors [1]. Each of the TOF detectors consists of a thin foil producing secondary electrons, accelerating grids, an electrostatic mirror, a stack of micro-channel plates (MCPs) as a signal amplifier and a two-dimensional position-sensitive delay-line anode as shown in Fig. 1. The MCPs and delay-line anodes of active diameter of Ø = 40mm (DLD40) and Ø = 80mm (DLD80) have been procured from RoentDek[2].

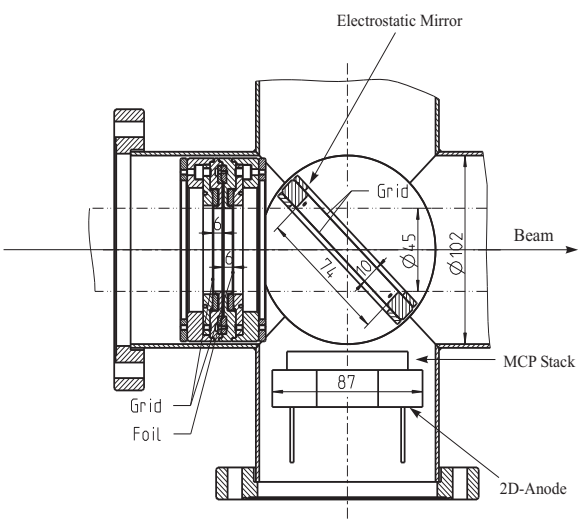

Fig. 1 *Setup for the position sensitive TOF detector with an active area of about 1250 mm^2.*

The electrostatic mirror, a decisive part of the TOF detector, has been designed and tested. The main function of the mirror is to deflect the secondary electrons (SEs) towards the MCP's surface isochronously. The mirror consists of two stainless-steel frames and two grids made of tungsten wires of Ø = 31μm with a separation of 0.5 mm. A ceramic [3] ring has been designed in order to keep the 10 mm separation between the two grids. The grids mounted with sufficient tension provide approximately 78 % transmission for the beam particles and can be biased up to 7500 V in high vacuum conditions.

Due to the large emittance and broad energy distribution of the SEs a proper acceleration and transport of these electrons is mandatory to obtain a good position and time resolution. Therefore, SEs trajectories have been calculated using OPERA-3D [4] in order to simulate the detector response and to optimize the setup accordingly.

A three-dimensional model space equivalent to the geometry of the TOF detector was defined as shown in Fig. 2. The distribution of the SEs emitted from the foils was considered isotropic [5]. The Maxwellian energy distribution of the SEs is also known from the literature [6]. Considering these two distributions the SEs trajectories were calculated.

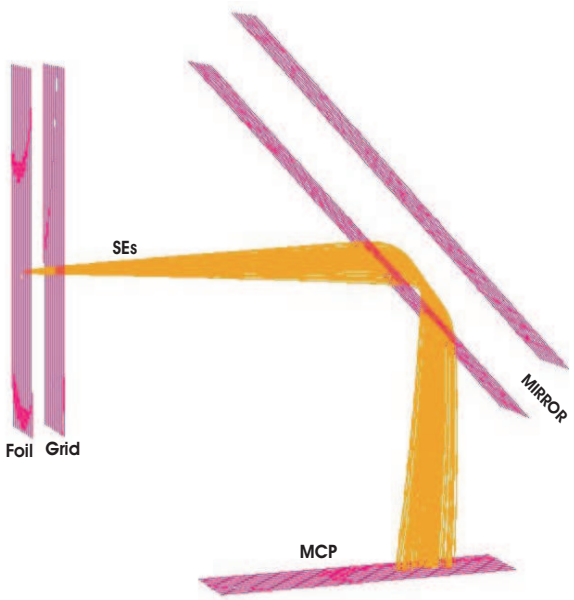

Fig. 2 *Model space equivalent to the TOF detector and corresponding secondary electrons trajectories.*

From these simulations the response of the mirror is found to be satisfactory and the necessary electrical potentials for the mirror and the foil have been optimised as : -4500V at the foil, and -5000V at the mirror and -500V at the grids. According to the present geometry of the TOF detector, the flight path for the SEs is about 120 mm. For this flight path the corresponding transversal spread in the SE-beam is determined as about 8 mm from these calculations. However, this is an upper limit of the lateral diffusion for the SEs.

[1] H. Sharma et al., This Report p. 36
[2] RoentDek GmbH: http://www.roentdek.com
[3] Vitronit©, http://www.vitron.de
[4] Vector Fields Ltd. Oxford OX51JE, England
[5] K. Kruglov, Nucl. Instr. Meth. A 441 (2000) 595
[6] B. L. Henke et al., J. Appl. Phys. 52 (1981) 1509

Measuring Foil Thicknesses for a Time-of-Flight Spectrometer[G]

K. Kosev, H. Sharma, A. Wagner

At ELBE, the high-intensity photon-beam from Bremsstrahlung-production will be used to produce exotic nuclei by photon-induced fission. For the detection of the fission fragments a double time-of-flight spectrometer is under construction. In this spectrometer several thin foils will be used. For secondary electron production a 4 micron thick polypropylene foil with an area of 46x70 mm^2 was metallised with 100 Å aluminium layer in order to reduce the electrical resistivity. The precise thickness profile of the foils is an important requirement for the TOF spectrometer [1].

In order to extract a precise thickness profile of the foil, energy-loss measurements have been carried out using a collimated mixed (^{239}Pu/^{241}Am/^{244}Cm) alpha source. To measure the thickness profile of the foil it was mounted on a frame in between the alpha source and a silicon detector inside a vacuum chamber set at about 6.7x10^{-6} mbar. The foil frame was moved along two dimensions with the help of two stepper motors remotely controlled. The position resolution for this setup was in the order of few a microns. For each run 24 measurements were taken with a step size of 2mm while keeping the other direction fixed.

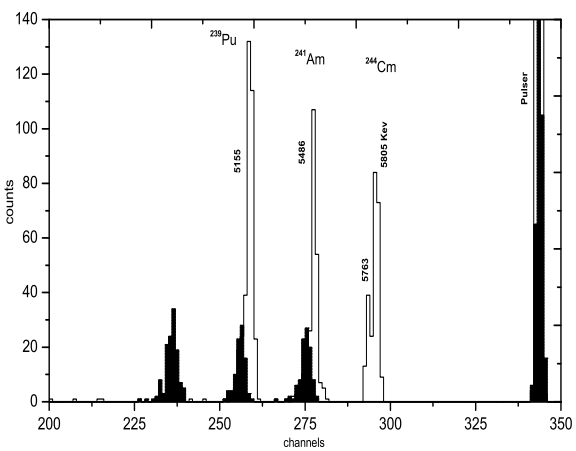

Fig. 1 *Comparison between a calibration spectrum (hollow peaks) and a spectrum with foil (full peaks).*

A spectroscopic electronics setup was used to determine the rest energy of the alpha particles after passing the foil. The silicon detector (type EURISYS LEC 200-4000) having sensitive areas of 200 mm (diameter 16 mm) and useful thickness of 4.25 to 4.88 mm was connected to a ZfK-VV5 preamplifier and an ORTEC 570 main amplifier set at a shaping time 0.5 μsec. The observed FWHM at 5486 keV for this detector was around 30 keV. For monitoring any gain shift in the electronics an ORTEC 440 research pulser was used. The data was acquired using Interwinner MCA. More than 1200 spectra were collected while scanning the whole area of the foil. Fig. 1 shows a comparison of spectra taken with and without the foil.

A dedicated program was developed for an automated analysis which locates the peaks and fits them with Gaussian distributions. From the peak's centroid the energy-loss of the alpha particles in the foils is determined and the thickness derived (see Fig 2).

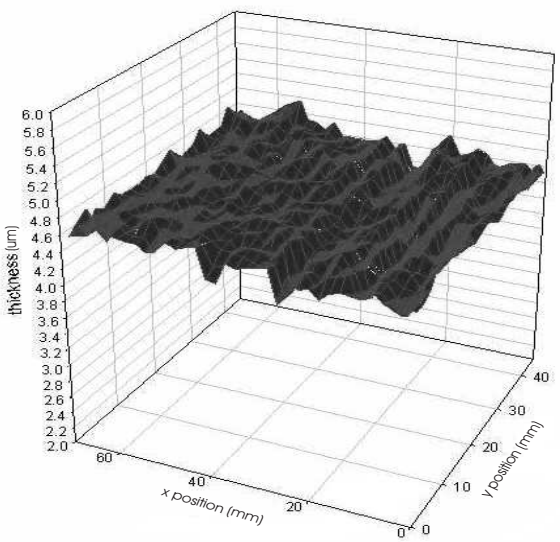

Fig. 2 *Two-dimensional distribution of the foil thickness profile using energy loss of alpha particles.*

The measurements show a satisfactory uniform thickness distribution of the foil as shown in Fig. 3.

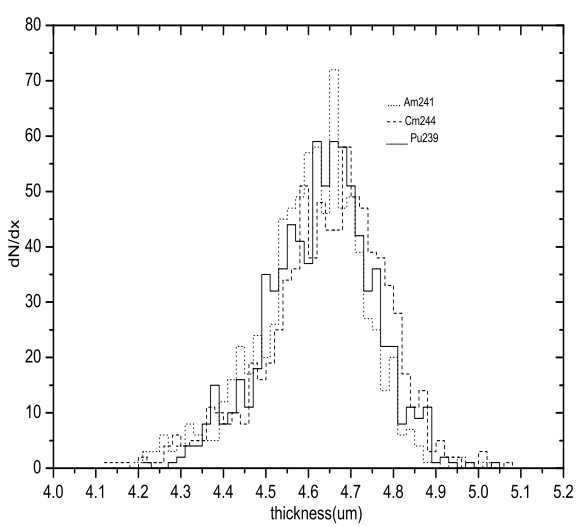

Fig. 3 *Thickness distribution of the foil.*

[1] H.Sharma et al., This Report, p. 36

Probing the Gateway to Superheavy Nuclei in Cranked Relativistic Hartree-Bogoliubov Theory

A. V. Afanasjev, S. Frauendorf, T. L. Khoo[1], I. Ahmad[2], G. A. Lalazissis[2]

The cranked relativistic Hartree-Bogoliubov (CRHB) theory [1], including approximate particle number projection through the Lipkin-Nogami method and the Gogny force in the particle-particle pairing channel, has been applied for a systematic study of the nuclei around ^{254}No [2]. These are the heaviest elements with a large body of spectroscopic data for testing the reliability of mean-field theory predictions for superheavy nuclei. The deformation, rotational response, pair correlations, quasiparticle spectra, nucleon separation energies and shell structure of these nuclei have been extensively studied with different RMF forces.

While the deformation properties are well reproduced, the calculations reveal that an accurate description of other observables requires better effective forces both in the particle-hole and particle-particle channels. The calculated moments of inertia show only small sensitivity to the RMF force and thus to the details of the single-particle structure. In contrast to previous studies, where the moments of inertia in lighter systems are well reproduced (see Ref. [2] for details), good agreement in the heaviest nuclei can be obtained only with a decrease ($\approx 12\%$) of the strength of the D1S Gogny force in the pairing channel.

The CRHB theory has been extended for a detailed description of quasi-particle states in odd and odd-odd nuclei. For the first time, the blocking procedure in such nuclei has been performed fully self-consistently, with effects of the breaking of time-reversal symmetry (nuclear magnetism) taken into account. Analysis of quasiparticle spectra in odd ^{249,251}Cf and ^{249}Bk nuclei with the NL1 and NL3 forces (see Fig. 1) suggests that the energies of most of the spherical orbitals, from which active deformed states of these nuclei emerge, are described with an accuracy better than 0.5 MeV. However, for a few subshells the discrepancies reach 1.0 MeV. Considering that the RMF forces were fitted only to bulk properties of spherical nuclei without considering single-particle energies, this level of agreement is impressive. However, in very heavy systems, where the level density is high, the accuracy is not sufficient for reliable predictions of the location of deformed shell gaps, which are small (≈ 1 MeV).

The results of the present investigation have a number of implications for the study of superheavy nuclei. The NL-SH and NL-RA1 forces do not provide satisfactory descriptions of the single-particle energies: the deviation between experiment and theory in the $A \sim 250$ mass region reach 2 MeV for some spherical subshells. Thus their application to superheavy nuclei is not recommended. The extrapolation of the results for quasiparticle states obtained in the $A \sim 250$ mass region suggest that the NL1, NL3 and NL-Z forces provide reasonable descriptions of most of the states in the vicinity of the $Z = 120$ and $N = 172$ spherical shell gaps. These are magic gaps in most parametrizations of the RMF theory. However, it is not possible to estimate the accuracy of the description of some low-j states, such as $\nu 3d_{3/2}$, $\nu 4s_{1/2}$ and $\pi 3p_{3/2}$, $\pi 3p_{1/2}$, which are located near these gaps by studying lighter deformed nuclei. Thus the particle numbers corresponding to magic gaps in superheavy nuclei still remain an open question. In addition, the study of number of effects in superheavy nuclei, such as pairing and the importance of self-consistency, is in progress.

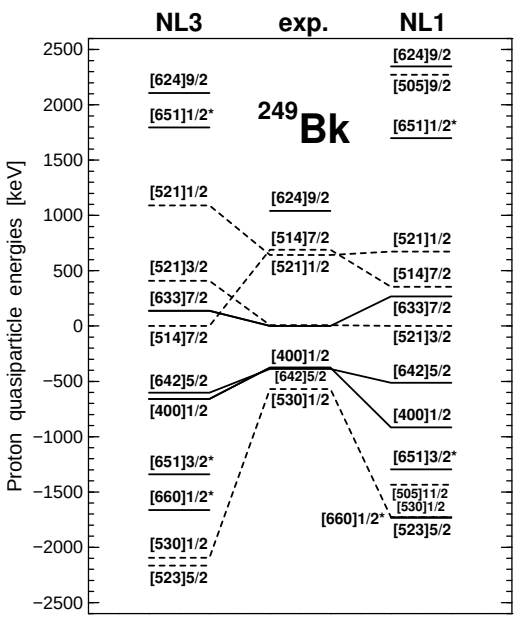

Fig. 1 *Experimental and theoretical quasiparticle energies of neutron states in ^{249}Bk. Positive and negative energies are used for particle and hole states, respectively. Solid and dashed lines are used for positive and negative parity states, respectively. The symbols 'NL3' and 'NL1' indicate the RMF force used in calculations.*

[1] A. V. Afanasjev, P. Ring and J. Konig, Nucl. Phys. A 676 (2000) 196

[2] A. V. Afanasjev, T. L. Khoo, S. Frauendorf et al., Phys. Rev. C 67 (2003) 024309; Proc. Conf. on "Frontiers of Nuclear Structure", Berkeley, USA, AIP Conf. Proc. 656 (2003) 379

[1] *Argonne National Laboratory, USA*
[2] *Aristotle University, Thessaloniki, Greece*

Proton-Neutron Pairing in Rotating $N \approx Z$ Nuclei

A. V. Afanasjev[1], S. Frauendorf

The rotational features of the $N \approx Z$, $A \sim 60 - 80$ nuclei were studied in a systematic way within the cranked relativistic mean field (CRMF) theory, cranked relativistic Hartree-Bogoliubov theory with only like-particle T=1 pairing, and cranked Nilsson-Strutinsky (CNS) approach. These nuclei are expected to provide important information on the nature (i.e. isoscalar T=0 or/and isovector T=1) and strength of proton-neutron (pn) pairing correlations [1]. The structure of ^{70}Br [2], ^{72,73}Kr [3, 4, 5] and ^{74}Rb [6] nuclei has been investigated in detail.

The Coriolis antipairing (CAP) effect breaks the $T = 1$ pairs, but there is no CAP effect for the $T = 0$ pairs [8] in which the n and p occupy identical space-spin orbitals. Thus isoscalar np pairing is expected to survive up to very high rotational frequencies and may influence the moments of inertia at these frequencies. However, the good agreement between calculations with and without pairing and experiment at high rotational frequencies (see Fig. 1 and discussion in a forthcoming article [9]) clearly shows that both types of pairing (like-particle and unlike-particle) are weak at these frequencies and have little impact on rotational properties of the $N \approx Z$ nuclei. This strongly suggests that high spin rotational structures do not provide evidence for possible existence of isoscalar np pairing.

It was also suggested that the presence of the isoscalar pn pairing leads to the delayed band crossing in the $N = Z$ nuclei as compared with its $N \neq Z$ neighbors. The bands in ^{72}Kr and ^{60}Zn were in focus of such discussions. Early data [7] shown by open circles in Fig. 1b indicated considerable delay of band crossing in ^{72}Kr. However, recent experiment [4, 5] revealed a previously unobserved side band shown by solid circles in Fig. 1b. This band, which is yrast above $I = 16\hbar$, represents missing doubly aligned S-band. The properties of this band above band crossing are excellently described both in the CRMF and CRHB+LN calculations. The CRHB+LN theory reproduces the band crossing frequencies in ^{74}Kr (see Fig. 1c) and suggest the lowering of crossing frequency in ^{72}Kr by $\approx$ 100 keV as compared with ^{74}Kr. Unfortunately, due to some uncertainties in the lowest few transitions of new band the frequency of paired band crossing in ^{72}Kr is not firmly established. However, the new data remove the largest part of discrepancies seen before between theory and experiment. These results for ^{72}Kr combined with the ones for ^{60}Zn (see Fig. 1a and Ref. []) considerably weaken the arguments in favor of delayed band crossing as a fingerprint of isoscalar pn pairing. On the contrary, the spectra of ^{74}Rb compared with the CRHB+LN calculations corrected for the $t = 1$ np-pair field by restoring isospin symmetry [1] give strong evidence for the existence of the isovector np pairing [6].

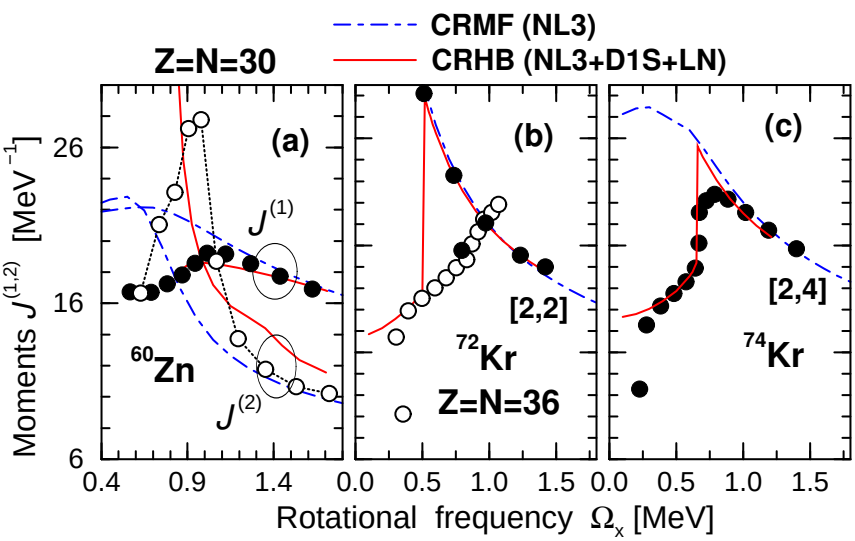

Fig. 1 *Panels (b-c) Experimental (circles) and calculated (lines) kinematic moments of inertia in ^{72,74}Kr nuclei. The results of the paired CRHB+LN and unpaired CRMF calculations are shown. The unpaired configurations are labeled by [p,n] where p(n) is a number of occupied $g_{9/2}$ proton (neutron) orbitals. Panel (a) shows the experimental and calculated kinematic and dynamic moments of inertia of magic SD band in ^{60}Zn.*

[1] S. G. Frauendorf and J. A. Sheikh, Nucl. Phys. A645 (1999) 509
[2] D. G. Jenkins et al., Phys. Rev. C 65 (2002) 064307
[3] N. S. Kelsall et al., Phys. Rev. C 65 (2002) 044331
[4] N. S. Kelsall et al., Proc. Conf. on ´´Frontiers of Nuclear Structure´´, Berkeley, USA, AIP Conf. Proc. 656 (2003) 261
[5] N. S. Kelsall et al., EuroPhysical Journal A, in press
[6] C. D. O'Leary et al., Phys. Rev. C 67 (2003) 021301(R)
[7] S. M. Fischer et al, Phys. Rev. Lett. 87 (2001) 132501
[8] A. L. Goodman, Phys. Rev. C 63 (2001) 044325
[9] A. V. Afanasjev and S. Frauendorf, in preparation

[1] *University of Notre-Dame*

Beta-Decay Studies of Neutron-Deficient Tin Isotopes [G]

M. Karny[1], Z. Janas[1], L. Batist[2], J. Döring[3], I. Mukha[3], C. Plettner[3], A. Banu[3], A. Blazhev[3], F. Becker[3], W. Brüchle[3], T. Faestermann[4], M. Górska[3], H. Grawe[3], A. Jungclaus[5], M. Kavatsyuk[3], O. Kavatsyuk[3], R. Kirchner[3], M. La Commara[6], S. Mandal[3], C. Mazzocchi[3], A. Płochocki[1], E. Roeckl[3], M. Romoli[7], M. Schädel[3], R. Schwengner, J.Żylicz[1]

Studies of nuclei in the ^{100}Sn region offer the possibility to test nuclear models describing structure and decay properties of nuclei in which protons and neutrons occupy identical orbitals near a double shell closure. An insight into the structure of nuclei close to ^{100}Sn can be gained by studying their β decay which is dominated by $\pi g_{9/2} \rightarrow \nu g_{7/2}$ Gamow-Teller (GT) transitions. An attractive feature of such nuclei is that most of the GT strength lies within the $Q_{\rm EC}$-value window. Such a concentration of strength has recently been observed in a series of light indium and silver isotopes (see [1] and references therein). ^{100}Sn has been predicted to decay by one GT transition to a single 1^+ 1p-1h state in ^{100}In at an excitation energy of about 1.8 MeV, while the closest even-even neighbours of ^{100}Sn, ^{98}Cd and ^{102}Sn, show a spreading of the GT strength over a number of 1^+ states in the daughter nucleus.

In the recent experiments at the GSI-ISOL facility we used the FEBIAD-B3C ion sources with the addition of CS_2 [2] for the mass separation of SnS^+ ions. In this way routinely about 60% of the intensity of the Sn^+ beam was shifted to the SnS^+ molecular side-band, where the strong suppression of contaminants [2] cleaned the beams from In, Cd, and Pd isobars. Only the strongly produced activities of Ag were traced in on-line experiments, the suppression of which was 4-5 times lower than the anticipated value of 10^4 found in off-line studies. The latter effect may be due to an operation of the ion source at lower temperature compared to the off-line measurement, which was made to enhance the SnS^+ intensity. We measured β-γ-γ decay properties of $^{101-105}$Sn with two complementary set-ups, namely (i) the Total Absorption Spectrometer (TAS) for the measurement of GT strength distributions and (ii) an array of germanium detectors (including the FZR-Cluster and two GSI-Clover detectors) operated in coincidence with silicon β-detectors. Beta-delayed protons of ^{101}Sn were measured by using $\Delta E - E$ silicon telescopes. The intensities of the mass-separated $^{101-105}$Sn beams were obtained from the experimental decay properties. By using a 40 particle-nA ^{58}Ni beam, a 3 mg/cm^2 ^{50}Cr target, and a catcher of ZrO_2 fibers inside the FEBIAD source, we reached secondary beam intensities given in Table 1. These values are about one to two orders of magnitude higher than those obtained by a previous FRS experiment [3].

The data on the ^{102}Sn decay collected with the high-resolution setup (ii) as well as spectra obtained by the small germanium detector in the TAS confirm the main features of the ^{102}Sn decay scheme proposed by Stolz [3] on the basis of an FRS experiment. The main difference is that we do not confirm the 53 keV transition (see Fig. 1), which was previously [3] placed at the very bottom of the ^{102}In level scheme. Removing this transition from the decay scheme may affect the spin assignment of the ground state of ^{102}In. Figure 2 presents the β-gated TAS spectrum of ^{102}Sn after subtraction of contributions from daughter activities which were determined in separate measurements. The maximum occurring at a recorded TAS energy of about 2.5 MeV is interpreted as being due to the $\pi g_{9/2} \rightarrow \nu g_{7/2}$ GT resonance at a ^{102}In excitation energy of about 1.5 MeV.

In summary, the development of SnS^+ beams at the GSI ISOL allowed us to study in detail the β-decay properties of $^{101-105}$Sn. These data, in particular those on γ-γ coincidences, are under evaluation. An extrapolation of the experimental beam intensities, yields 8 at/h for ^{100}Sn indicating that the measurement of β-delayed γ rays of this nucleus will indeed be a very challenging task.

Table 1 *Measured ISOL rates of the $^{101-105}$Sn isotopes.*

Isotope	^{101}Sn	^{102}Sn	^{103}Sn	^{104}Sn	^{105}Sn
at/min	2.4	31	$1.4 \cdot 10^3$	$3.0 \cdot 10^4$	$2.0 \cdot 10^5$

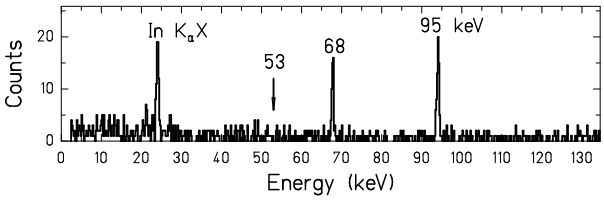

Fig. 1 *Low-energy γ-ray spectrum obtained for mass 102. An arrow shows the expected position of the 53 keV line which remained unobserved in this experiment.*

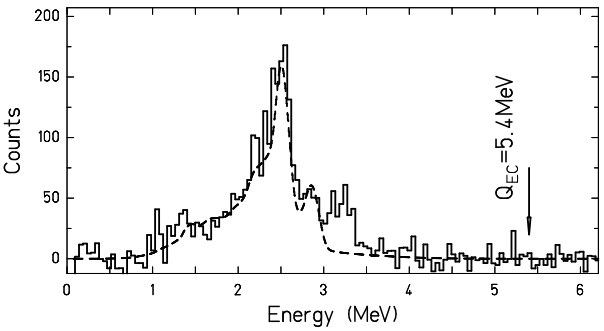

Fig. 2 *Beta-gated TAS spectrum of ^{102}Sn from the experiment (solid line) and from a GEANT simulation based on the modified level scheme of [3] (dashed line).*

[1] C. Plettner et al., Phys. Rev. C 66 (2002) 044319
[2] R. Kirchner, Nucl. Instr. Meth. B, in print, and www.gsi.de/annrep2001 (page 211)
[3] A. Stolz, Ph.D. Thesis, TU München (2001)

[1] *University of Warsaw, PL00681 Warsaw;* [2] *St. Petersburg Nuclear Physics Institute, RU-188350 Gatchina;* [3] *GSI, 64291 Darmstadt;* [4] *Technische Universität München, 85747 Garching;* [5] *Instituto de Estructura de la Materia, IEM CSIC, 28006 Madrid, Spain;* [6] *Universitá di Napoli, 80126 Napoli, Italy;* [7] *INFN Napoli, Italy*

Beta Decay of ^{103}Sn [G]

O. Kavatsyuk[1,2], M. Kavatsyuk[1,2], J. Döring[1], L. Batist[3], A. Banu[1], F. Becker[1], A. Blazhev[1,4], W. Brüchle[1], T. Faestermann[5], M. Górska[1], H. Grawe[1], Z. Janas[6], A. Jungclaus[7], M. Karny[6], R. Kirchner[1], M. La Commara[8], S. Mandal[1], C. Mazzocchi[1], I. Mukha[1], C. Plettner[1], A. Płochocki[4], E. Roeckl[1], M. Romoli[8], M. Schädel[1], R. Schwengner, J.Żylicz[6]

Doubly closed-shell nuclei and neighbouring isotopes/isotones provide a sensitive test ground for the nuclear shell model. ^{100}Sn is the heaviest doubly magic $N = Z$ nucleus, located at the proton drip line, where protons and neutrons occupy identical shell-model orbitals. The overlap of their wave functions is large, which further causes a strong proton-neutron interaction to be expected. Beta decay in this region is dominated by an allowed Gamow-Teller (GT) transformation $\pi g_{9/2} \rightarrow \nu g_{7/2}$, which populates the $I^\pi = 1^+$ GT resonance in the decay of an even-even nucleus. For an odd-neutron parent nucleus the coupling of this resonance to the unpaired nucleon can be studied. This provides a test of the residual interaction via the β-delayed γ-ray spectroscopy.

Measurements of β-delayed γ rays and protons were performed at the GSI-ISOL facility for ^{101,103,105}Sn. It was essential for this experiment to suppress efficiently the isobaric indium, cadmium, silver and palladium contaminants by using the novel sulphurisation technique [1]. The β-delayed γ-ray spectra were measured with an array of high-resolution germanium detectors (17 crystals) in grow-in mode as well as with the Total-Absorption Spectrometer (TAS) in decay mode. Moreover, a $\Delta E - E$ telescope was used to record β-delayed protons [2, 3] Further experimental details are given in refs. [1-3].

We report on the new data for the β decay of ^{103}Sn. In Fig. 1 the β-gated γ-ray spectrum for ^{103}Sn, taken at mass $A = 103 + 32$ (SnS, cf. [1, 2]) with the germanium array, is shown. The 720, 726 and 740 keV lines are known to belong to the decay of the ^{103}In daughter activity [4]. The 1077 keV line has been identified by in-beam spectroscopy [5] to represent the $11/2^+ \rightarrow 9/2^+$ transition in ^{103}In. The data shown in Fig. 1 yield the first evidence for β-delayed γ rays at 643, 821, 1077, 1356, 1397 and 1428 keV, which are preliminarily assigned to the decay of ^{103}Sn. The TAS spectrum gated by protons is shown in Fig. 2. The 776 and 776 + 1022 keV lines correspond to the 2^+ state in ^{102}Cd fed by β-delayed protons after a EC and β^+-decay of ^{103}Sn, respectively. Based on these data, a β^+/EC ratio of 0.06 for the proton emission to the 2^+ state in ^{102}Cd was estimated. A corresponding ratio of 0.6 for the proton emission to the ground state in ^{102}Cd was obtained using a proton-γ anti-coincidence condition. The $Q_{\rm EC}$ value of ^{103}Sn was preliminarily determined from these β^+/EC ratios and the average energy of β-delayed protons [6] to be (7.5 ± 0.5) MeV.

The half-life of ^{103}Sn, obtained from the β-delayed proton time distribution, is shown in the inset of Fig. 2. The result of the fit being $T_{1/2} = (7.0 \pm 0.6)$ s is in agreement with the previously measured values of (7 ± 3) s [5], (7.5 ± 1.5) s [6] and in disagreement with (8.7 ± 0.6) s [7] by two standard deviations.

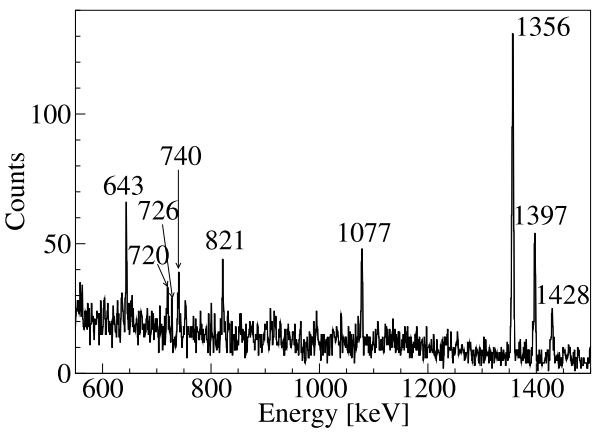

Fig. 1 *Gamma-ray spectrum obtained for mass A = 103 + 32 in coincidence with positrons. The strongest lines are marked with their energies in keV.*

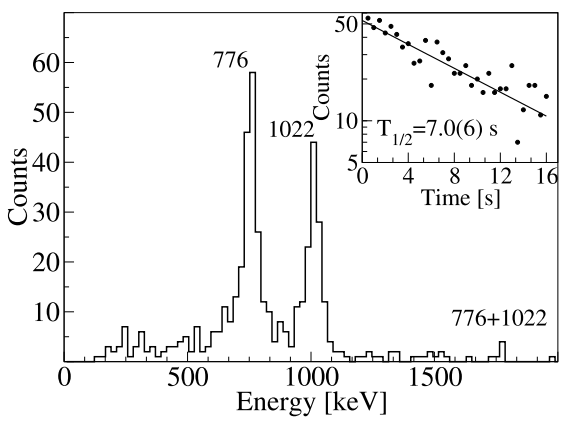

Fig. 2 *TAS spectrum taken in coincidence with β-delayed protons from the ^{103}Sn decay. The inset shows the time characteristic of β-delayed protons.*

[1] R. Kirchner, Proc. Conf. to EMIS-14, Nucl. Instr. Meth. A, in print
[2] M. Karny et al., This Report, p. 42
[3] I. Mukha et al., GSI Sci. Rep. 2002
[4] J. Szerypo et al., Z. Phys. A 359 (1997) 117
[5] J. Kownacki et al., Nucl. Phys. A 627 (1997) 239
[6] P. Tidemand-Petersson et al., Z. Phys. A 302 (1981) 343
[7] K. Rykaczewski, Report GSI-95-09, 1995
[8] A. Stolz, Ph.D. Thesis, TU München (2001)

[1] *GSI, 64291 Darmstadt;* [2] *Kiev National University, Ukraine;* [3] *St. Petersburg Nuclear Physics Institute, Russia;* [4] *University of Sofia, Bulgaria;* [5] *Technische Universität München;* [6] *University of Warsaw, Poland;* [7] *Instituto Estructura de la Materia, CSIC, and Departamento de Fisica Teórica, UAM Madrid, Spain;* [8] *Universitá di Napoli, Italy*

Gamma-Ray Spectroscopy of Fission Fragments with Super Clover Ge Detectors [G]

H. Sharma, A. Wagner, P. Adrich[1], P. Jesinger[2], J. Kopatch[3], J.v. Kalben[2], I. Kojouharov[4], A. Krasznahorkay[5], E. Lubkiewicz[1], Z. Mezentseva[3], M. Mutterer[6], W. Trzaska[7], H.-J. Wollersheim[4]

Gamma-ray spectroscopy of ternary and binary fission fragments have been carried out with a spontaneous fission source at GSI. A very thin and open ^{252}Cf fission source with activity of about 25kBq (fission/s) was mounted in the centre of a double ionization chamber. Both sides of the source were evaporated with 10μg/cm^2 gold in order to prevent the loss of ^{252}Cf by sputtering. The prompt gamma-rays were measured with the GSI super-clover segmented Ge detectors and the fission fragments were detected by a double ionization chamber. The light charged particles from ternary fission were also measured with an array of 24 $\Delta E - E$ telescopes mounted in the double ionization chamber. These telescopes consist of small segmented ionization chambers (for ΔE measurement) and silicon PIN diodes (for E measurement). All these detectors inside the ionization chamber were operated in CH_4 environment at pressure of about 570 torr. The gamma-rays, the light charged particles, and the fission fragments were measured in coincidence. A fragmented cathode was used in the ionization chamber for the determination of polar and azimuthal emission angles of the fragments. The sketch of the experimental setup is shown in Fig. 1. More details of the experiment are availabe at the GSI web site [1].

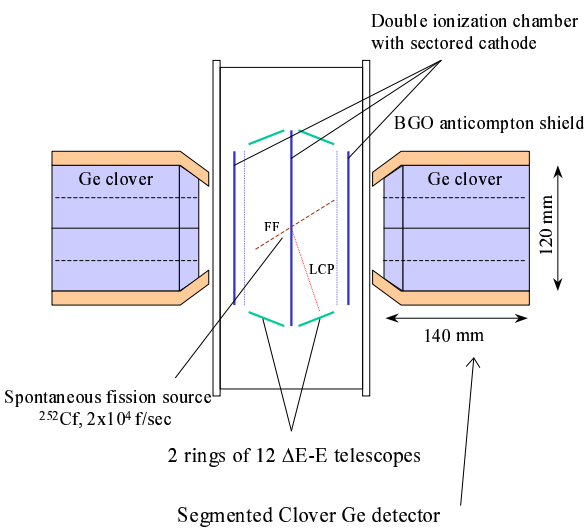

Fig. 1 *The sketch of the experimental setup at GSI.*

The list-mode coincidence data of more than 800 GB were taken during several weeks of experiment. The analysis of the data is in progress in order to extract the information of angular anisotropy of gamma-rays, fragments and light charged particle correlation, gamma-ray emission from light charged particles in ternary fission. The preliminary results of the analysis are shown in Figs. 2 and 3. Fig. 2 shows the energy versus mass distribution (upper) and the typical fission fragments mass distribution (lower). Fig. 3 represents the gamma-ray spectra with and without mass gating and also the spectra with improved quality after the Doppler correction.

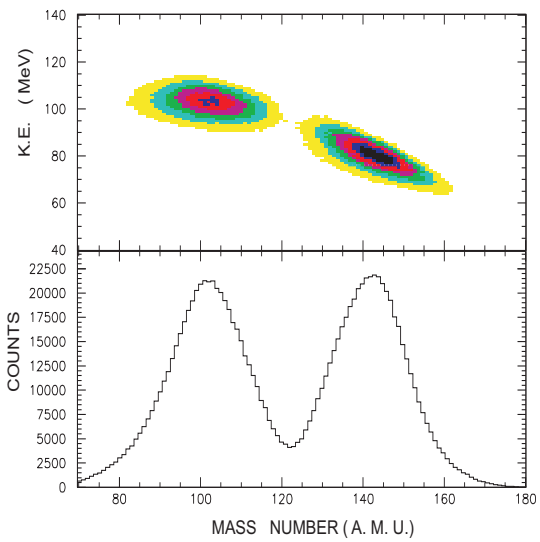

Fig. 2 *Energy versus mass number (top), fragment mass distributions (bottom).*

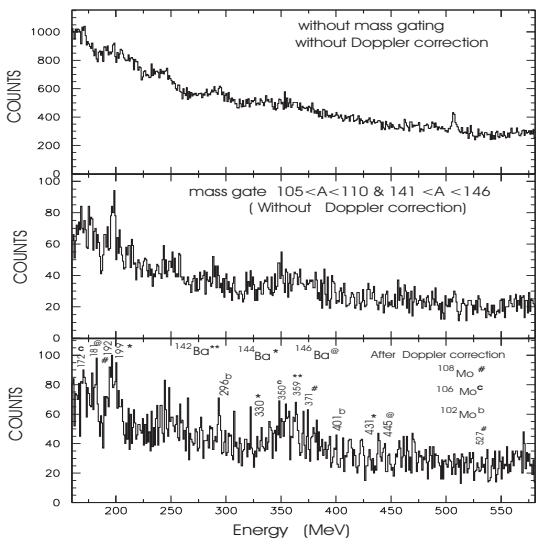

Fig. 3 *The gamma-ray spectra without any mass gating (top) with mass gating (middle) and with mass gating and with Doppler correction (lower).*

[1] http://www-aix.gsi.de/∼wolle/FISSION/fission.html

[1] *Jagellonian Univ., Cracow (Poland),* [2] *Tech. Univ., Darmstadt (Germany),* [3] *Joint Institute for Nuclear Research, Dubna (Russia),* [4] *Gesellschaft für Schwerionenforschung Darmstadt (Germany),* [5] *ATOMKI, Debrecen (Hungary),* [6] *Tech. Univ. Darmstadt (Germany),* [7] *Univ. of Jväskylä (Finland)*

Study of the Neutron-Rich Isotopes ^{91}Sr and ^{92}Sr in a Fusion-Fission Experiment

E.A. Stefanova[1], M. Danchev[2], R. Schwengner, D.L. Balabanski[2,3], M.P. Carpenter[4], M. Djongolov[3], S.M. Fischer[4], D.J. Hartley[3], R.V.F. Janssens[4], W.F. Mueller[5], D. Nisius[4], W. Reviol[6], L.L. Riedinger[3], O. Zeidan[3]

The Sr isotopes lying between the magic nuclide ^{88}Sr (N = 50) and the nuclide ^{94}Sr ($N = 56$) at the $1d_{5/2}$ neutron subshell closure represent one of the regions of very low collectivity in the nuclear chart. Almost constant $B(E2, 2_1^+ \rightarrow 0_1^+)$ values of ≈ 8 W.u. and 13 W.u. were found for $^{90-94}$Sr ($N = 52 - 56$) and ^{96}Sr ($N = 58$), respectively [1]. On the other hand, an onset of collective motion may be expected for nuclei with a few nucleons outside the shell closures. In order to study the interplay between single-particle excitations and collective motion as, e.g., vibrational-like excitations, we studied the nuclides ^{91}Sr and ^{92}Sr having three and four $1d_{5/2}$ neutrons, respectively, outside the shell closure at $N = 50$.

The nuclei ^{91}Sr and ^{92}Sr were produced as fission fragments via the fusion reaction ^{36}S + ^{159}Tb at a beam energy of 165 MeV. The ^{36}S beam was delivered by the 88-inch cyclotron of the Lawrence Berkeley National Laboratory. The target consisted of a ^{159}Tb layer of 0.78 mg cm^{-2} thickness evaporated on to a 13 mg cm^{-2} Au backing. Gamma rays were detected with the Gammasphere array [2] consisting of 93 Compton suppressed Ge detectors arranged in 17 angular rings. A minimum of four coincident γ rays was required, and a total of about 5 $\times 10^9$ events was collected.

The level scheme of ^{92}Sr resulting from the present experiment is shown in Fig. 1. On the basis of the present DCO analysis spin assignments were made for the first time.

Excited states in ^{91}Sr and ^{92}Sr were interpreted in the framework of the spherical shell model. The calculations were performed in a model space including the proton orbitals $(0f_{5/2}, 1p_{3/2}, 1p_{1/2}, g_{9/2})$ and the neutron orbitals $(1p_{1/2}, 0g_{9/2}, 1d_{5/2})$. Experimental and calculated level energies in ^{92}Sr are compared in Fig. 2. The calculations give a good overall description of the observed states. The 3^-, 5^-, and 7^- states in ^{92}Sr are described by coupling the proton excitations creating the octupole 3^- state of the core nucleus ^{88}Sr to the $1d^4_{5/2}$ neutrons. The observed equidistant $\Delta J = 2$ level sequence on top of the 8^+ state, which resembles a vibrational-like sequence, could be well described by the configuration $\pi[(0f^{-2}_{5/2})(0g^2_{9/2})]\nu(1d^4_{5/2})$ that favours even spins (cf. Fig. 2). The results of this study have been published in Ref. [3].

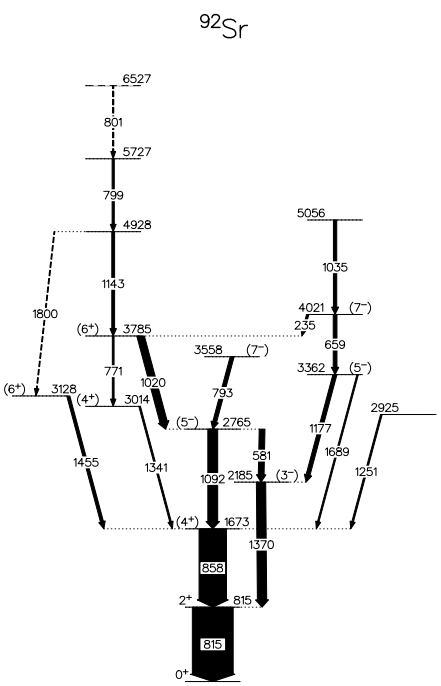

Fig. 1 *Level scheme of ^{92}Sr deduced from the present study.*

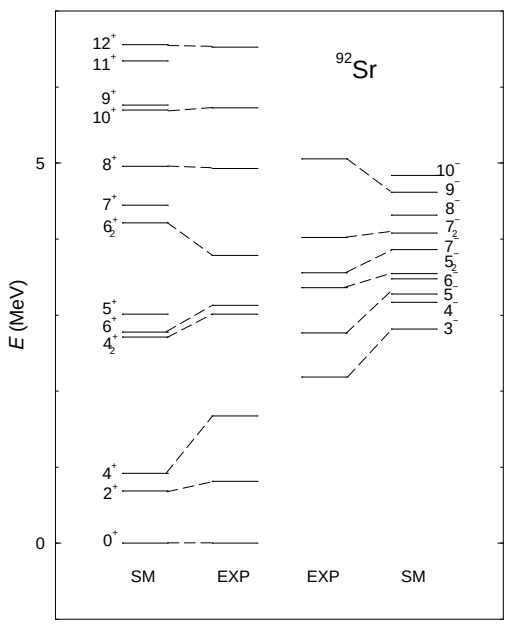

Fig. 2 *Experimental and calculated level energies in ^{92}Sr.*

[1] H. Mach et al., Nucl. Phys. A 523 (1991) 197
[2] I.Y. Lee, Nucl. Phys. A 520 (1990) 641c
[3] E.A. Stefanova et al., Phys. Rev. C 65 (2002) 034323

[1] *FZR and INRNE Sofia, 1784 Sofia, Bulgaria*
[2] *Faculty of Physics, University of Sofia, 1164 Sofia, Bulgaria*
[3] *Department of Physics and Astronomy, University of Tennessee, Knoxville, Tennessee 37996*
[4] *Physics Divison, Argonne National Laboratory, Argonne, Illinois 60439*
[5] *NSCL, Michigan State University, East Lansing, Michigan 48824*
[6] *Chemistry Department, Washington University, St. Louis, Missouri 63130*

Life Sciences:
Biostructures and Radiation

The competence of the Institute of Nuclear and Hadron Physics in producing, handling and detecting electromagnetic radiation in a wide photon energy range is the basis of biological research and medical applications. About one half of the ressources of the institute are devoted to this field of research. The work is concentrated onto three main topics:
(i) Studies on structural dynamics of biomolecules by means of infrared radiation;
(ii) Cell radiobiology with soft, quasi-monochromatic X-rays;
(iii) Positron emission tomography (PET) for quality assurance of charged hadron therapy.
Structural dynamics of biomolecules: The analysis of molecular processes that underly biological functions is of prime interest for basic research in the field of life science as well as for the development of new diagnostic and ultimately therapeutical applications in medicine. In the past, biochemical investigations have revealed the chemical pathways that determine the turn over of all essential metabolites. Likewise, the machinery of protein interactions at cell membranes and in the cytosol involved in the perception of extracellular signals which form the basis for cellular communication and regulated gene expression have been characterised in detail. Many proteins that are essential for these processes have been crystallised and their structure analysed by X-ray crystallography from which models on structure function relations have been obtained. The sketched success in the elucidation of biomolecular function was made possible by modern methods in isolation, purification, and detection of cellular components and by the use of modern methods in molecular biology. However, the dissection of the complex biomolecular interactions into tractable entities requires the disruption of the cell. Today, information on the kinetics of individual biomolecular transitions, of entire reaction chains, and on the spatial distribution of macromolecular complexes or metabolites in a single cell or a living higher organism is required. It has become clear that the function of many biomolecules is determined by noncovalent changes, therefore, it cannot be approached by biochemical isolation of reaction intermediates. Here, physical, rather than biochemical approaches are required. The IKH has developed new projects in which its competence in the generation and detection of different types of electromagnetic radiation and their exploitation for spectroscopy and imaging is central for these modern aspects of life sciences. IR-radiation generated by a free-electron-laser (FEL) promises new insight into the structural dynamics of biomolecules. Absorption of IR-radiation is an inherent property of the vibrational modes within proteins, lipids and DNA, thereby, allowing label-free detection of biomolecules. Vibrational frequencies are directly related to molecular structure and their analysis is extremely informative on structural changes during biomolecular function. By this technique we study for example conformational changes in the visual photoreceptor which triggers cellular responses to visible light. Homology with hormone receptors renders this system an interesting model system for molecular pharmacology. To allow a broad application of static and time-resolved IR-absorption measurements exploiting the unique features of IR-FEL radiation, the design of dedicated equipment for the investigation of biomolecules under native conditions is a major activity at the IKH.
Cell radiobiology: This activity is aimed at the determination of the relative biological effectiveness (RBE) of X-rays with photon energy values between 10 and 100 keV for different biological endpoints. Since such photon radiation is widely used in diagnostic and therapeutic radiology, a precise knowledge of RBE values is highly desirable. The investigations will be performed with quasi-monochromatic X-rays delivered by the channeling radiator at the ELBE superconducting electron accelerator. In parallel to the installation of the beam line, the radiobiological methods and the dosimetric techniques established in preparation of the experiments at the ELBE beam, have already been applied to cell irradiation studies at conventional low-energy X-ray sources. For four cell lines the biological endpoints cell death and micronucleus formation (as the indication

of a radiation induced genetic cell defect) have been studied. The results of these experiments revealed that the RBE of X-rays applied for mammographic diagnostics is slightly larger than one; however, the RBE enhancement is not as pronounced as it has been expected from investigations reported in the literature. In a common project with the Institute of Bioinorganic and Radiopharmaceutical Chemistry (IBR) of the FZR the ELBE channeling radiation will be applied to the investigation of a conjectured photon energy dependent RBE due to the accumulation of metallo-organic molecules bearing atoms of high atomic number within radiosensitive structures of cells. These studies are prepared on the one hand by synthesising appropriate compounds in the IBR and on the other hand by Monte Carlo descriptions of local dose enhancement by Auger electrons following the photo electric effect at heavy atoms in the IKH.
Heavy ion therapy: In the framework of the German Heavy Ion Therapy Project the treatment of patients primarily suffering from tumours of the head and neck region has been routinely continued. During three therapeutic beam times of four weeks each at the carbon ion therapy facility of the Gesellschaft für Schwerionenforschung Darmstadt (GSI) 42 patients have been treated in the year 2002. All the therapeutic irradiations have been monitored by means of in-beam PET for quality assurance. The PET data evaluation has been especially focused on locating dose deviations from the treatment plan caused by minor patient mispositioning or by local changes of the tissue density distribution. There are now strong indications that the efforts to install the heavy ion therapy facility at GSI in a highly innovative scientific and technological way (which includes the dose applications by means of intensity controlled raster scanning, the biologically optimised treatment planning and the in-situ PET therapy monitoring) result in successful treatments: For the local control of radioresistant chordomas of the skull base carbon ions are superior to photon irradiations. On this basis the installation of a clinical charged hadron therapy facility at Heidelberg has been decided. Therefore, the physical and technical investigations are directed to a second generation of in-beam PET scanners for this facility. This comprises the development of suitable photon detectors, the construction of a PET-gantry which can be combined with a rotating beam delivery, new PET data acquisition methods for rapidly fluctuating photon fluxes, refined tomographic reconstruction methods and the extension of the PET method from carbon to other ion species.

Structural dynamics of biomolecules

- *Rockefeller University, New York*
- *Universität Orenburg*
- *MPI für Physik Komplexer Systeme, Dresden*
- *MPI für Festkörperphysik, Stuttgart*
- *ENEA, Frascati (Italien)*
- *CLIO, Paris (Frankreich)*

Cell radiobiology

- *Klinik für Strahlentherapie und Radioonkologie, TU Dresden*
- *Institut für Strahlenschutzphysik, TU Dresden*
- *Institut für Bioanorganische und Radiopharmazeuthische Chemie(FZ Rossendorf)*

Heavy ion tumour therapy

- *GSI Darmstadt*
- *Radiologische Klinik der Universität Heidelberg*
- *Deutsches Krebsforschungszentrum Heidelberg*
- *Institut für Bioanorganische und Radiopharmazeuthische Chemie(FZ Rossendorf)*
- *Soltan Institute for Nuclear Studies, Otwock-Swierk, Poland*
- *National Institute of Radiological Sciences, Chiba, Japan*

Installation of Biochemical and Biophysical Working Facilities at the IKH

K. Fahmy

The start of novel experimental activities in the area of life sciences has made necessary the installation of new working facilities for biochemical and biophysical manipulations and preparation of biological samples. For this purpose, a laboratory has been established in close proximity to the ELBE building and has been equipped with a dark working place for preparation of light-sensitive samples such as the visual photoreceptor rhodopsin, or inorganic metal-containing solutions used for metal cluster formation. In addition a routine FTIR spectrophotometer has been set up allowing extensive vibrational characterisation of biosamples that are to be used in FEL applications. Time-resolved spectra in the ms time range from flash lamp-induced reactions can be obtained in house. Equipment for the preparation of monomolecular biofilms and their investigation by Brewster angle microscopy has also been brought to operation. Finally a biochemical bench including the supply with standard laboratory gases has been installed. This allows in place biochemical operations and immediate use of thus prepared samples for spectroscopic, microscopic, and FEL applications. Thus, experiments using advanced spectroscopic equipment for the study of biomolecular structure function relations in life science can now be performed in house. The following sections describe the focus of our works on structural dynamics of biomolecules, where these new facilities have been used extensively.

Fig. 1a

Fig. 1b

Fig. 1c

Fig. 1 *Facilities for biochemical and biophysical manipulations.*
a. *Biochemical work bench for sample preparation.*
b. *Routine FTIR spectrophotometer in dark working place allowing static and time-resolved characterisation of the IR-absorption of samples to be used in IR-FEL applications.*
c. *Film balance and Brewster angle microscope for the analysis of lipidic monolayers.*

Whole Cell Characterisation by Second-Derivative FTIR Spectroscopy for the Detection of Radiation Damage

A. Panteleeva, O. Savchuk, K. Fahmy

Radiation-induced damage of cultured cells serves as a model system for the characterisation and prediction of radiation effects in higher organisms. Several chemical changes in the cell's constituents linked to radiation-induced processes such as radical formation, direct and indirect DNA modification, lipid oxidation and others alter the chemical structure of certain biomolecules. Therefore, label-free detection of these alteration in whole cells is a promising way to reveal radiation effects. This approach requires monitoring of an intrinsic physical property that is related to chemical composition and biomolecular structure. The frequency of molecular vibrations in the mid infrared range (5-10 μm, corresponding to 2000-1000 cm^{-1}) are determined by the atomic masses and force constants of chemical bonds connecting the vibrating nuclei. This gives rise to absorption frequencies which are characteristic of the local chemical constituents in macromolecules(group frequencies). Additional factors such as intermolecular forces further affect the exact frequency, thereby providing a sensitive measure of chemical alterations in multicomponent systems. We have applied IR-spectroscopy to identify mid infrared absorption bands of whole cells that correlate with radiation-induced damage. Lethal and sublethal doses of UV-radiation have been applied to cells cultured in the ELBE cell culture lab. The IR measurement requires detection of very small absorption differences on a large absorption background. Therefore, Fourier transform IR spectroscopy was used to record high signal to noise spectra of whole cells. A cell preparation protocol has been established that allows reproducible mid infrared absorption measurements of irradiated and subsequently dried cells as well as of control cells. To resolve small absorption bands in the total absorption and to exclude artifacts from baseline drifts, second derivative spectra were evaluated. Figure 1 shows 2nd spectra of cells that were measured different times after sample preparation, thus exhibiting increasing contribution from non-specific oxidative reaction products. In contrast to the normal absorption spectrum (Fig. 2) the structure underlying the amide I band is clearly resolved. We have compared the alterations by non-specific oxidative processes with UV-induced spectral changes. Thereby, absorption peaks have been identified that correlate with exposure of the cells to UV-radiation. Absorption differences in the 1700 to 1800 cm^{-1} range indicate formation of oxidised reaction products after increasing UV irradiation.Changes in the amide I range at 1658 cm^{-1} suggest altered protein secondary structure in non-specifically oxidised cells. In irradiated versus normal cells, protein structure is not altered. This indicates that radiation-induced oxidative affect primarily lipids and DNA, whereas non-specific oxidation additional affects proteins. The data evidence that FTIR 2nd derivative spectroscopy provides a sensitive and reproducible measure of radiation-induced chemical modifications in whole cells.

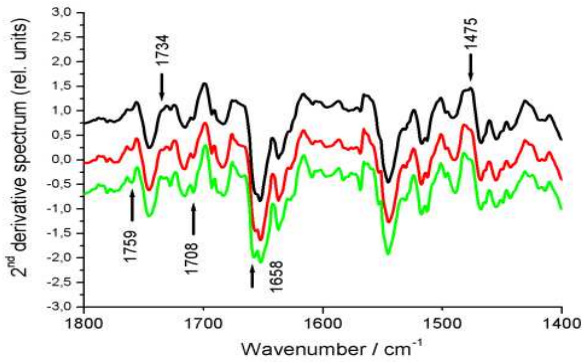

Fig. 1 *2nd derivative FTIR spectra of NIH / 3T3 mouse fibroblast cells. Cells where cultured in DMEM 10 % FCS. UVC irradiation was at 254 nm (2x15W) in petri dishes through 400 μm polypropylene film. For FTIR analysis cells where centrifuged in 0.9 % NaCl solution and the pellet resuspended in the same solution at 10000 cells/μl. Spectra from top to bottom: non-irradiated cells measured 0,2, and 48h after sample preparation At the indicated frequencies, non-specific oxidative processes cause absorption changes over time. Effects of UVC at these positions have been observed for NIH/3T3 cells as well as for mammary epithelial cells (MCF12).*

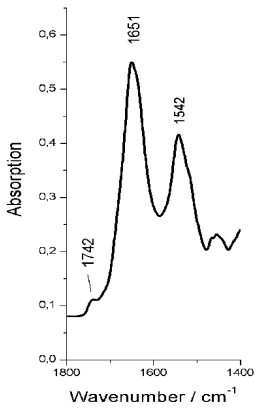

Fig. 2 *Absorption spectrum of whole cells dried on ZnSe. Band structures resolved in the 2nd derivative spectrum are barely visible in the raw data. Likewise, small differences between different passages of the same cell line not visible in the absolute spectrum become resolved in the 2nd derivative spectrum. Corresponding changes can be of the same size as those induced by UV-radiation. Therefore, non-irradiated controls have to be taken from identical passages treated in the same manner as the irradiated samples.*

Analysis of Structural Flexibility in S-Layer Proteins from *Bacillus Sphaericus*

O. Savchuk, J. Raff[1], S. Selenska-Pobell[1], K. Fahmy

Crystalline bacterial surface layers (S-layers) are formed by self-assembling of S-layer proteins. These proteins retain their ability to crystallise in two dimensions after isolation from bacterial cells. Such arrays may serve as attractive templates for the formation of nanostructured surfaces with a repeating pattern of defined physicochemical properties. This approach is based on the ability of S-layer proteins to bind metal cations which may serve as initiation sites for the formation of metal nanoclusters. Metal binding by S-layers is also the basis for approaches to bioremediation using S-layer proteins to adsorb uranium complexes from contaminated solutions. In these biotechnological applications it is necessary to characterise the structural and functional features of S-layer proteins on a molecular and, where possible, on an atomic level in order to optimise desired features through genetic engineering. We have designed and constructed equipment to allow the real time- monitoring of exchange processes occurring between suspensions of S-layer proteins and aqueous solutions of defined compositions. The pH-sensitivity of the secondary structure of isolated S-layers from two strains of *Bacillus sphaericus* has thus been investigated in collaboration with the Radiochemistry Department of the FZR. Using attenuated total reflection FTIR-spectroscopy, mid infrared spectra were recorded in aqueous suspension. This is possible, because the penetration depth of the IR beam is restricted to the μm range without the need of mechanical realisation of μm-sized optical path lengths (see formula 1). As the IR-measuring beam does not transmit the sample, this geometry allows to perform dialysis experiments during spectral recordings. The S-layer proteins from both strands exhibit mainly β-sheet secondary structure as indicated by the amide I (C=O stretching) absorption peak at 1632 cm^{-1}. Decrease in pH induces a frequency upshift of the amide I absorption arguing for the formation of helical or unordered structures. These results demonstrate that S-layer proteins can exhibit structural flexibility. This has to be taken into account for the further development of S-layer-based technical applications and may itself be exploited. Additionally, the data reveal different structural stability against acid denaturation in the two strains. JGA-12 exhibits faster denaturation than the reference strain NCTC-9602.

The secondary structure of the S-Layer of both strains was further analysed by spectral decomposition of the amide I modes. Using band fitting routines, a minimal number of four spectral components in the amide I range was determined (Fig. 2). Their pH dependence strongly supports the acidification-dependent relative decrease in β-structure. The integrated intensity of the fitted component at 1632 cm^{-1} (corresponding to β-sheet) relative to that of the 1640-1660 cm^{-1} absorption is 1.5 and 1.2 at pH 5.7 and 2.0, respectively.

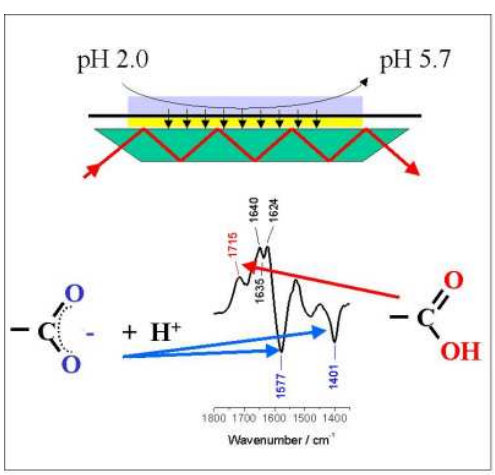

Fig.1 *Attenuated total reflection FTIR-spectroscopy of the pH-induced conformational changes in S-Layer proteins from Bacillus sphaericus. Top: Experimental setup of ATR-cell, allowing dialysis of protons into the sample volume. Absorption changes are detected by attenuation of the IR-beam which is reflected in the ATR crystal(ZnSe). The penetration depth of the electric field amplitude in the rarer medium decays exponentially with the distance z from the crystal surface according to*

$$E = E_0 e^{-z/d}, \text{with } d = \lambda_{n1}/2\pi(sin^2\gamma - (n_2/n_1)^2)^{1/2}$$

where λ is the wavelength of the IR radiation, n_1 and n_2 are the refractive indices of the IRE and the sample, respectively, and γ is the angle between the surface normal and the IR beam.

Bottom: *Acidification not only causes protonation of carboxylic acids (increase of C=O stretching absorption, decrease of COO- absorption) but also changes of the mainly β-sheet structure of the S-layer as evidenced by the absorption changes around 1620-1640 cm^{-1}.*

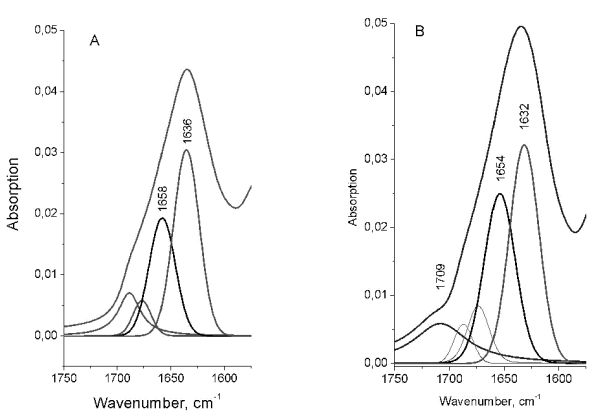

Fig.2 *Amide I band analysis of B sphaericus strain JGA-12. A) Absorption spectrum at pH 5.7 Major contributions to the amide I absorption are found at 1658 and 1636 cm^{-1} indicative of helial and β-sheet structure, respectively.*
B) Absorption spectrum at pH 5.7. The increased relative intensity of the 1654 cm^{-1} band indicates proton-induced formation of random or helical structures. The broad absorption at 1709 cm^{-1} corresponds to the carbonyl stretching mode of prtonated carboxylic acids (Glu and Asp side chains). Bands between 1675 and 1700cm^{-1} are indicative of β-turns.

[1] *FZR, Institute of Radiochemistry*

Investigation of Structure and Function of the Visual Photoreceptor Rhodopsin [D]

N. Lehmann, T.P. Sakmar[1], K. Fahmy

G-protein-coupled receptors (GPCRs) play a central role in diverse cellular signalling cascades mediating the action of hormones, neurotransmitters, and odours. They are heptahelical transmembrane proteins that bind extracellular ligands and respond with conformational changes that alter their intracellular surface. This change in surface structure is recognised by cellular guanosine nucleotide-binding proteins (G-proteins) which release bound guanosinediphosphate (GDP) and take up the corresponding triphosphate GTP. We study structure function relationships in bovine rhodopsin, a vertebrate photoreceptor. Although activated through light absorption by covalently bound 11-cis retinal, this systems shares many similarities with other GPCRs. We have used FTIR difference spectroscopy to monitor structural changes during photoactivation. This technique compares the IR-absorption after photoactivation with that in the dark. The difference spectrum contains information only on those chemical groups that have undergone specific light-induced structural or physical changes. Absorption by the large majority of amino acids and peptide backbone vibrations that are not involved in conformational changes vanish in the difference spectrum. It is of special importance to elucidate structural changes in the cytoplasmic surface of the membrane protein. Our previous ATR-FTIR studies have revealed protonation changes during rhodopsin transducin interactions (Fig. 1). We have now started to investigate interaction domains using biochemical modifications of the rhodopsin surface and synthetic peptides from exposed protein regions (Fig. 2).

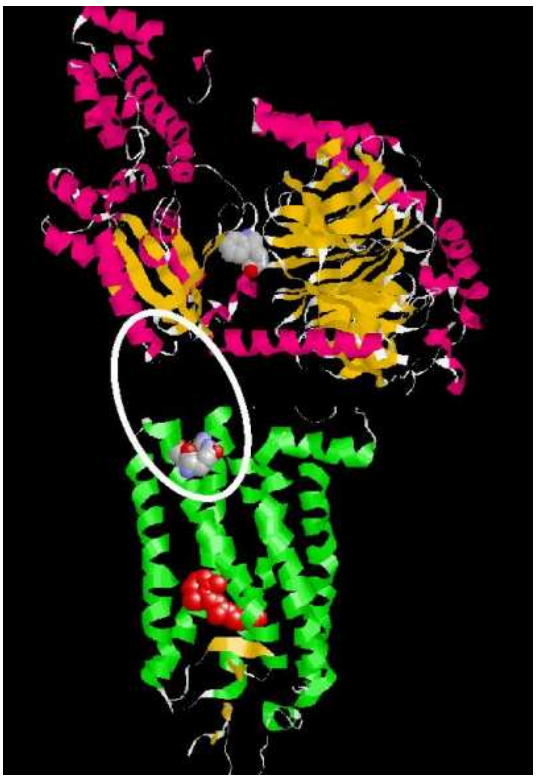

Fig. 1 *Proposed mutual orientation of rhodopsin (green) and transducin. After photoisomerisation of 11-cis retinal (red space-filling representation) the cytosolic conformation (upper part of the molecule) changes and interacts with transducin, the G-protein in photoreceptor rod cells. The Interaction site at Glu^{134} has been suggested by earlier FTIR investigations [1,2].*

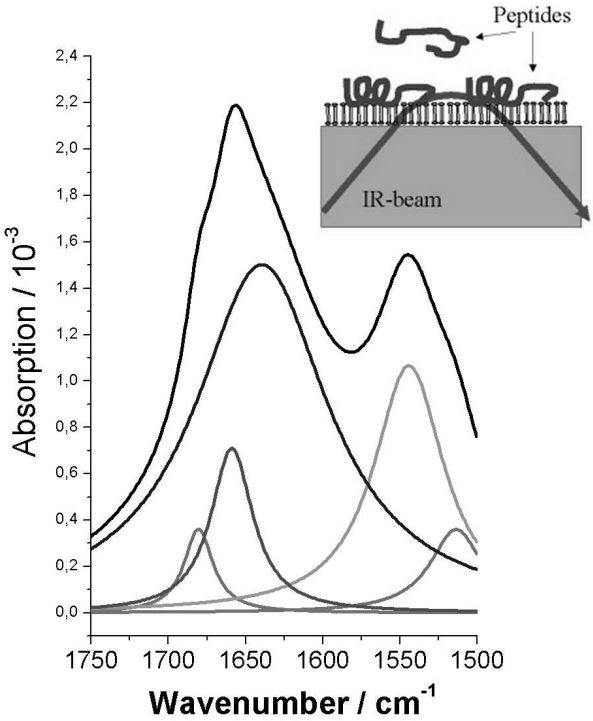

Fig. 2 *The folding capacity of peptides corresponding to residues 310 to 321 in helix 8 of rhodopsin, i.e. the small carboxyl-terminal stretch running vertical the transmembrane helices, has been investigated. The native sequence partially adopts a helical structure on the surface of liposomes. This is deduced from the amide I absorption maximum at 1656 cm^{-1}. The component bands have been determined by fitting the measured curved (top). A scrambled sequence of identical length and amino acid composition does not show the helical component. The native helix 8, which is involved in transducin recognition, may thus constitute an independently folding receptor domain. The inset shows how the spectra were obtained by ATR-FTIR difference spectroscopy. In this geometry, the absorption by the lipid-binding fraction of peptides is specifically enhanced over the non-binding fraction.*

[1] K. Fahmy; Binding of transducin and transducin-derived peptides to rhodopsin studied by attenuated total reflection-Fourier transform infrared difference spectroscopy;q Biophys. J. 75 (1998) 1306-1318

[2] K. Fahmy, T.P. Sakmar, and F. Siebert; Transducin-dependent protonation of glutamic acid 134 in rhodopsin; Biochemistry 39 (2000) 10607-10612

[1] *Rockefeller, University New York, New York, USA*

Analysis of Dye DNA Interactions

O. Savchuk, K. Fahmy

With the deciphering of the human genome, direct targeting of DNA has become a major challenge in drug research. Expression of specific genes related to disease may be inhibited if drugs can specifically recognise and possibly destroy undesired genomic information. This may be done by direct chemical attack or indirectly by site-specific generation of reactive singlet oxygen species. The latter is achieved in photodynamic therapy, which in combination with DNA-binding ligands, may increase directed DNA damage. Likewise, directed destruction of DNA is required in therapeutic approaches against cancer. Radiotherapy may particularly profit from a gain in DNA damage, when the site of radical formation is in close proximity of the target DNA. In this case DNA-binding ligands that carry covalently bound metals as efficient X-ray absorbers are promising substances to be optimised for therapy. Different dyes such as Rhodamine 6G, acridine and methylene blue can be used as the energy-transferring groups for the creation of specific changes (modification, cleavage) of the DNA backbone. IR has proven useful as a non-destructive, highly sensitive method to detect conformational changes in biomolecules. We have designed and carried out preliminary experiments that use FTIR spectroscopy to detect ligand binding events in DNA. Several intercalating and non-intercalating dyes are used as test substances for the detection of vibrational modes that can be used as monitors for drug DNA interactions. Thereby, the kinetics of reassociation of thermally dissociated ligand DNA complexes can be followed in real time by reappearance of vibrational modes typical of the complex. Binding of rhodamine has thus been shown to be accompanied by changes in the asymmetric PO_2- stretching modes around 1220 cm^{-1} of the phosphate sugar backbone. This agrees with the expected interaction of the positive charges of amino groups of rhodamine with the negatively charged DNA backbone. The experiments establish the basis for a comprehensive study of DNA structural dynamics by FEL IR-pump probe experiments. Observing the formation and disruption of the electrostatic interactions will provide fundamental as well as application-oriented knowledge on DNA ligand binding.

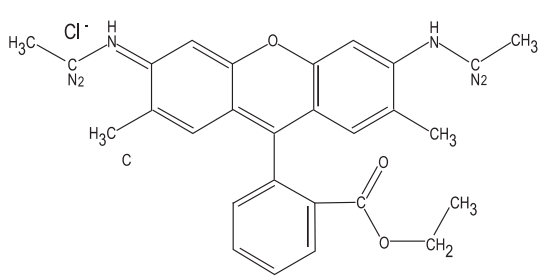

Fig. 1 *Structure of rhodamine 6G used as a DNA-binding ligand in the IR-based label-free investigation of DNA-ligand interactions.*

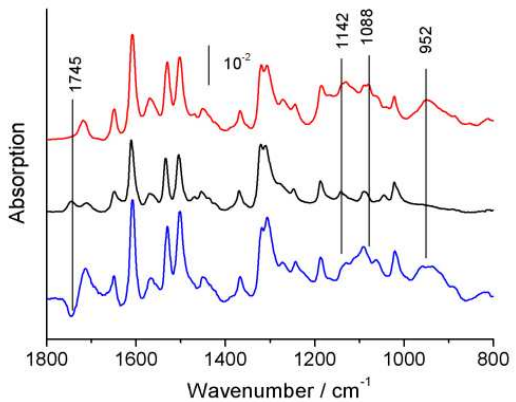

Fig. 2 *IR absorption spectra of rhodamine. In the pure compound (middle), the C=O stretching mode of the acetyl ester between 1700 and 1800 cm_{-1} is split in two frequencies, indicating populations with strong and low H-bonding. In the presence of DNA (molar ratio 1:10, top; 1:1, bottom) a single C=O stretch is observed at an intermediate frequency, indicative of the formation of a single DNA-binding population of rhodamine molecules. Additional differences are seen in the 1100-1200 cm^{-1} range of the symmetric PO_2- stretching modes of DNA, evidencing the interaction of rhodamine with the DNA backbone.*

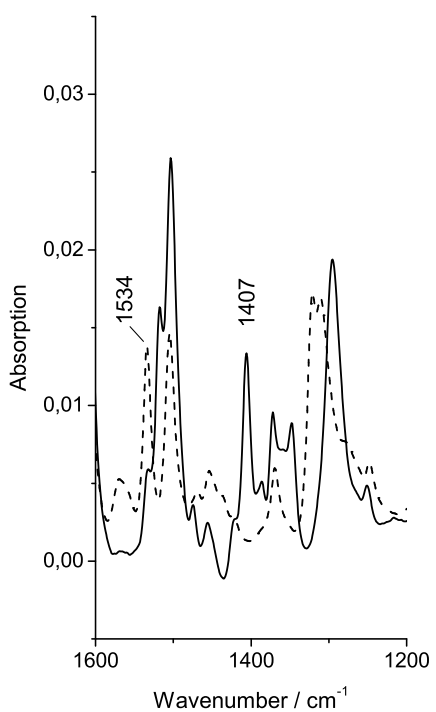

Fig. 3 *Comparison of the IR absorption of rhodamine 6G in H_2O and D_2O. The predominant effect of H/D exchange is the shift of the intense absorption at 1534 cm^{-1} to 1407 cm^{-1}. Therefore, we assign this band to the N-H and N-D bending vibrations of rhodamine, respectively.*

Experimental Set-Up for IR Measurements of Dynamics of Water-Lipid Interaction

G.I. Furlinski, K. Fahmy

Biomembranes are crucial to the life of the cell. Despite their differing functions, all biological membranes have a common general structure: each is a very thin film of lipid and protein molecules, held together mainly by noncovalent interactions. Cell membranes are dynamic, fluid structures, and most of their molecules are able to move about in plane of the membrane. The lipid molecules are arranged as a continuous double layer about 5nm thick.

Lipids constitute about 50% of the mass of most animal cell membranes, nearly all of the remainder being proteins. There are approximately $5x10^6$ lipid molecules in a 1μm x 1μm area of lipid bilayer [1]. All of the lipid molecules are amphipathic - that is, they have a hydrophilic or polar end (head) and a hydrophobic or nonpolar end (tail).

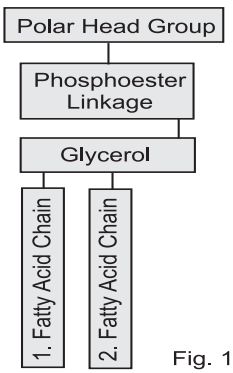

Fig. 1

The most abundant membrane lipids are the phospholipids (Fig. 1). These have a polar head group and two hydrophobic hydrocarbon tails. The tails are usually fatty acids, and they can differ in length (they normally contain between 14 and 24 carbon atoms).

One of the most important properties of the lipid bilayer is its fluidity, which is crucial to many membrane functions. Fluidity allows lipid molecules are able to diffuse freely within lipid bilayers. Our goal is to excite vibration levels of the hydrogen bonds between phosphate groups and water molecules and find their relaxation time by pump-probe experiments. In other words, we want to monitore the dynamics of water-lipid interaction. The experiments will be implemented with two types of lipid molecules - phosphatidylcholine and phosphatidylserine. For this purpose an experimental set-up shown in Fig. 2 has been designed. The system is compact and movable. The last feature is important, because experiments with two different laser sources are planned. The two tuneable sources are a femtosecond laser system equipped with a wavelength converter system "TOPAS" and a Free electron laser (FEL).

The femtosecond system after the wavelength converter, covers 2.8μm - 18μm spectral region with 1kHz repetition rate and energy from 0.2μJ to 2.5μJ. With a pulse duration of about 60fs, it allows to measure in the femtosecond and subpicosecond time scale.

The FEL, which will be tunable in the mid- and far-IR regions with pulses from 0.5ps up to several picoseconds, will allow to measure in the picosecond and nanosecond time scale. Our experimental set-up is based on InfraRed Reflection-Absorption Spectroscopy (IRRAS). This technique allows to measure the chemical composition and conformation of the lipid monolayer and its conformational changes. A comprehensive description of this method is found in the review paper by Gericke et al [2].

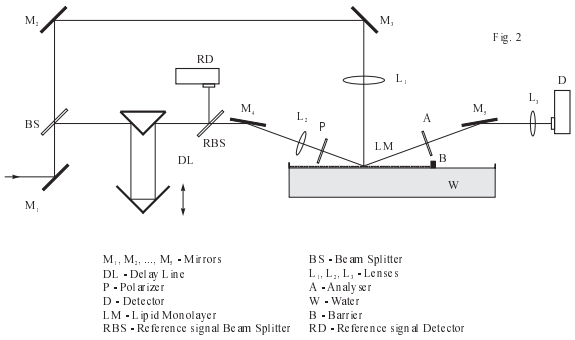

It describes the theoretical models and results for reflection coefficients in three-layer systems consisting of a transparent, isotropic, semi-infinite, incidence medium; an absorbing, anisotropic uniaxial homogeneous film; and an absorbing, isotropic uniaxial homogeneous film; and an absorbing, isotropic, semi-infinite substrate. Below we present some requirements for the experimental setup, generalising experimental experience with IRRAS.

Because the state of the monolayer is strongly affected by impurities, the setup should be completely enclosed. For experiments to determine transition dipole moment directions, an optical setup with flat mirrors (or at least curved mirrors with a long focal length) to direct the IR beam onto the water surface is necessary.

To determine transition dipole moment directions with reasonable accuracy close to the Brewster angle, high efficiency of the polarizer (at least 99%) is essential. Due to the low intensity of the light reflected from water, MCT detectors are necessary.

Compensation of the water vapour rotation-vibration bands is necessary. Three different experimental approaches have been developed to overcome the problem of water vapour.

- the bands may be effectively compensated by accurately regulating the humidity in the sample compartment with help of an adjustable very low flow of dry nitrogen in the chamber.
- the Langmuir trough must be designed with miniaturised surface film sample well and reference well.
- a combination of these two methods along with substitution D_2O for H_2O in the subphase may provide additional advantages.

[1] B. Alberts, A. Johnson, J. Lewis, M. Raff, K. Roberts, P. Walter, The Cell, Garland Science, (2002)
[2] R. Mendelson, J. W. Brauner, and A. Gericke, Ann. Rev. Phys. Chem., 46 (1995) 305-334

Infrared Characterization of Environmental Samples by Pulsed Photo-Thermal Spectroscopy

H. Foerstendorf[1], W. Seidel, K.H. Heise[1], R. Nicolai[1], A. Schamlott[2], J.M. Ortega[3], F. Glotin[3], R. Prazeres[3]

The low metal concentration in environmental samples often limits the interpretation of results of studies investigating the interaction processes between metal ions and environmental compartments by vibrational spectroscopy. The aim of this investigation is to reduce the limits for IR-spectroscopic analyses and to develop in situ methods for environmental samples. For this purpose the photo-thermal infrared spectroscopy of different concentrations of solid neodymium nitrate ($Nd(NO_3)_3 6H_2O$) dissolved in a potassium bromide (KBr) matrix serving as a model system was used.

The photo-thermal detection method is based on a thermo-elastic deformation bump generated by intermittent laser heating and thermal expansion [1]. A solid sample is irradiated by a modulated beam of monochromatic light produced by a tuneable free electron laser (FEL) and a probe beam (e.g. HeNe laser) which is reflected from the sample. Depending on the modulated intensity of the pump beam the photoinduced displacement of the probe beam changes periodically and thus a different reflection angle is observed (Fig. 1). At first order the thermal beam deflection (TBD) is proportional to the absorption coefficient of the material under investigation, thus providing direct access to acquisition of absorption spectra. The detection limit is expected to be extremely low since absorptions as low as 10^{-6} to 10^{-8} have been measured in the visible region by this method [2].

The spectra were recorded within a small spectral range where narrow bands show up. The observed spectral features can be assigned to vibrational modes of the nitrate anion. A comparison of the spectra recorded with FTIR and TBD spectroscopy show a good agreement for the high and middle salt concentration (Fig. 2B,C). whereas spectral deviations are observed at low concentration (Fig. 2A).

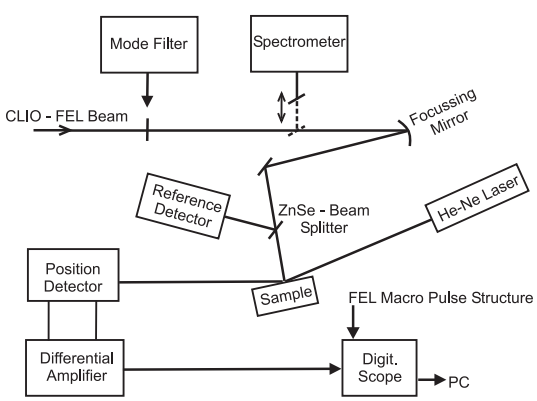

Fig. 1 *Schematic diagram of the thermal deflection experiment setup, at CLIO FEL in Orsay/France.*

From these spectra it appears that the deflection method is more efficient to detect low amounts of substance than conventional FTIR spectroscopy, since weak bands around 815 and 743 cm^{-1} are clearly observed in the FEL spectra which are hardly present in the respective FTIR spectra due to the low concentration. Furthermore, in contrast to transmission FTIR spectroscopy only a small fraction of the sample is detected in the TBD experiment. Therefore, the high quality of the photo-thermal spectra presented here emphasises the high detection efficiency of this acquisition technique [3].

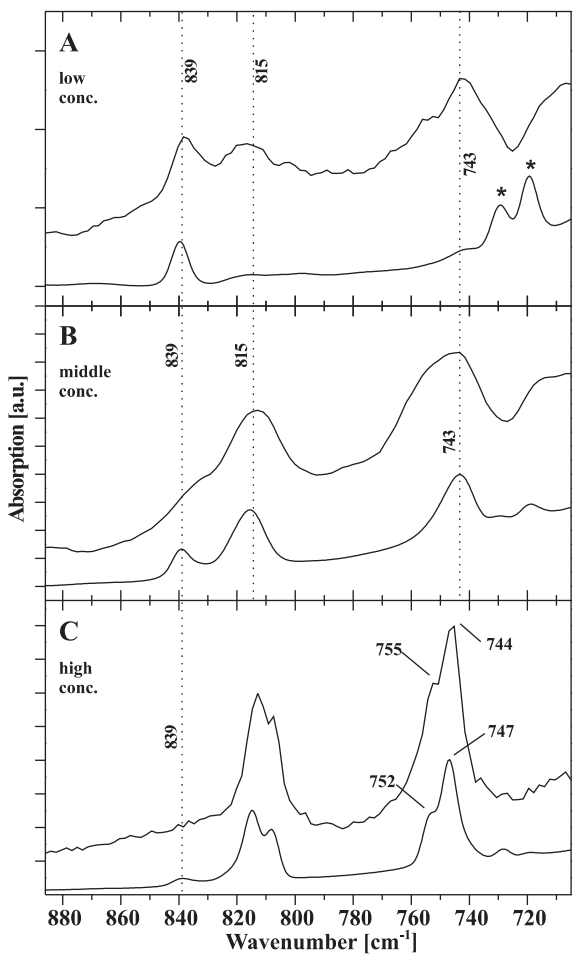

Fig. 2 *Photo-thermal (upper traces) and FT-IR (lower traces) spectra of $Nd(NO_3)_3 \cdot 6H_2O$ in KBr matrix (300 mg) at different concentrations. Low conc.: 0.08 mg; 0.6 mM (A). Medium conc.: 0.3 mg; ∼2 mM (B). High conc.: 0.7 mg; ∼5 mM (C). Bands representing impurities of the KBr matrix are indicated by ⋆(A).*

[1] M.A. Olmstead et al., Appl. Phys. A32 (1983) 144
[2] A. Mandelis, Physics Today, (Aug. 2000) 29
[3] W. Seidel et al., (submitted to Eur. Phys. J. - Applied Physics)

[1] *FZR, Institute of Radiochemistry*
[2] *FZR, Radiation Source ELBE*
[3] *LURE, Université de Paris-Sud, Orsay, France*

Using Pulsed Photo-Thermal Spectroscopy for Microspectroscopy in the Infrared Region. A First Approach

W. Seidel, H. Foerstendorf[1], K.H. Heise[1], J.M. Ortega[2], F. Glotin[2], R. Prazeres[2]

Photo-thermal spectroscopy using a pulsed pump source potentially provides spatial information of a sample surface. This may result in a microspectrometric technique for determining the distribution of metal species on mineral surfaces. The border range between an implanted and an untreated region of the surface of a germanium substrate was investigated by photo-thermal spectroscopy. The substrate was implanted by oxygen ions (O^+) which were restricted to a distinct region of the substrate by partially covering the surface with a metal plate during the implantation process. This substrate serves as a model system for future investigations of mineral surfaces.

We have used this method in order to take advantage of the pulsed character of the infrared laser. The incident energy is deposited in a short time. The heat generation will exhibit a corresponding time dependence, its time constant being of the order of the lifetime of the excited level (ps to ns). A temperature profile then develops in the sample via heat diffusion which can be described by a thermal diffusion length which was found in the μm range for solid states [1,2]. Let us assume that the optical absorption is due to a small defect: Therefore, if one measures the induced deflection with a sufficiently small laser probe, the signal will be found only in the vicinity of this defect within one thermal diffusion length. With a probe beam having a small spot diameter one can hope for spatial resolution of a few micrometers, possibly even smaller than the infrared FEL wavelength. This will allow to perform mappings of the absorption profile at the surface of the sample, i. e. microspectrometry. It seems even possible to reach a sub-wavelength resolution.

The experiment was carried out at the CLIO FEL in Orsay/France. The border range between the O^+-implanted and pure germanium region was investigated by recording time curves of the deflection signal at distinct positions of the substrate surface.

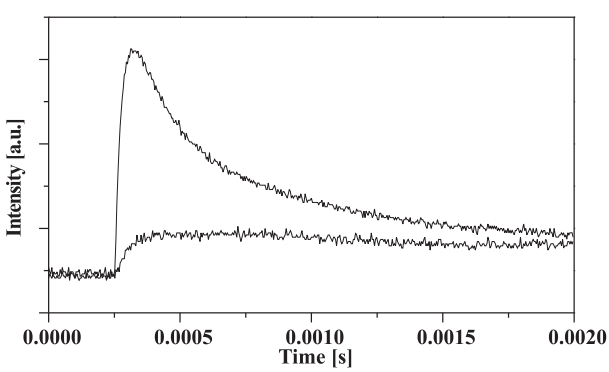

Fig. 1 *Beam deflection signal, measured for different regions of the Ge-substrate at a FEL wavelength of 11.6 μm. Upper trace: O^+-implanted region. Lower trace: untreated region of the substrate.*

For these measurements a constant FEL wavelength of 11.6 μm, which corresponds to the maximum of an absorption line in the generated Ge-oxids was used. Due to absorption the produced germaniumoxide shows an enhanced deflection signal whereas pure germanium is nearly transparent and only a weak deflection signal is observed (Fig.1).

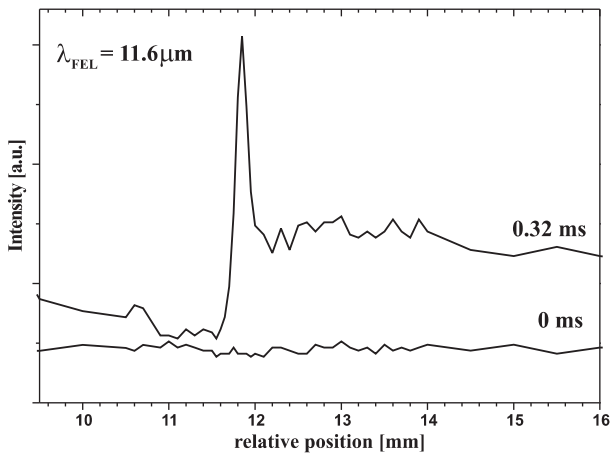

Fig. 2 *Intensity of the deflection signal at distinct positions of the Ge-substrate at 0.32 ms and 0 ms after the FEL pulse, respectively.*

From these time curves profiles representing the absorption at each position of the sample can be obtained reflecting the distribution of the implanted oxygen in the substrate. Figure 2 shows the profiles obtained 0.32 ms after the FEL pulse where maximum deflection was observed. For comparison, the profile at 0 ms where no deflection occurs is also shown. In the border range the step width between two acquisition points was 50 μm and was increased to 100 and 500 μm, respectively, in the outer regions of the substrate. This results in a slightly increased noise of the profiles between 11 and 14 mm relative position. The two different regions of the substrate can be clearly distinguished by different levels of absorption around 10 and 17 mm relative sample position, respectively. Surprisingly, in the border range around 11.8 mm relative position the concentration of the produced oxide seems to be considerably increased. If this is due to the implantation process, to surface effects or to artifacts of the spectroscopic technique applied has still to be verified. In further studies our aim is to increase the spatial resolution to a few microns which will be achieved by a better focusing of the probe beam and a more sophisticated sample translation.

[1] O. Benchikh et. al., J. Phys. 727 (1985) 727

[2] W. Seidel et al., FZ Rossendorf, Wiss. Tech.-Ber. FZR-319 (2001) 36

[1] *FZR, Institute of Radiochemistry,* [2] *LURE, Université de Paris-Sud, Orsay, France*

Temperature Stabilization of the Out-Coupling Mirror Wheel

W. Seidel, M. Sobiella, D. Wohlfarth, U. Wolf, B. Rimarzig

For the U27 Free-Electron Laser (FEL) the so-called hole coupling method, using broad-band metal mirrors with an on-axis hole in one of the mirrors was selected. To optimize the extraction ratio in the whole wavelength range we use 5 mirrors with different holes [1].

The Au coated Cu-mirrors are mounted on a revolvable holder (wheel). To bring one of the mirrors in the right position for lasing, we use a high-precision rotating stage. Despite the small absorption of about 1 % in the mirror, the entire construction will be heated up to a higher temperature during the normal laser operation. This will lead to a change in the resonator adjustment (length and angle) by thermal expansion and to an unacceptable heat load of the precession mechanics.

We estimate a permanent heating power of about 10 W at the mirror for an intracavity power of up to about 1 kW. Heating the mirror in vacuum with this power, we measured a saturation temperature of the wheel of around 100° C after 20 hours. In this case the heat exchange was realized mainly by thermal radiation in vacuum. This temperature is to high for the mechanical layout of the high-precision rotation stage of the construction. At a movable precession construction in ultra-high vacuum a temperature-stabilized system based on water cooling is difficult to be realized. Therefore, we introduced a special heat isolation between the high-precision rotation stage and the wheel. The wheel is also made from Cu to reduce mechanical tension between the mirrors and the surrounding material. Furthermore, the heat exchange is improved by a more flexible heat dissipation to the outside of the vacuum chamber (peltier element or air cooling) rather than by thermal radiation only. To stabilize the mirror wheel temperature we installed a heater in the center of the wheel. In this way, all the components are at the same equilibrium temperature independently of whether the laser is working or not.

Fig. 1 shows the measured temperature in dependence on time applying a permanent heating power of 15 Watt (instead of 10 W for safety reasons). The temperature sensor for the wheel was located at the opposite side of the heated mirror. After 22 hours the saturation temperature of about 50° C was achieved using the peltier cooler outside. We observed a temperature difference between mirror and wheel of about 4° C, which originates from the temperature gradient inside the wheel. Using air cooling we get a temperature of about 54° C at the mirror. The stabilization of the mirror temperature around 57° C, i.e. slightly above laser saturation temperature of 54° C, is demonstrated in fig. 2. By switching the laser (external heating at one mirror with 15 W) on (△) and off (▽), we simulated a working regime of the FEL. The • indicates that moment when the heating system for the wheel is switched on. The maximum temperature difference of 3.5^o C over 20 minutes in the mirror leads to a change in the cavity length of about 1 μm. This effect has a small influence on the FEL operation.

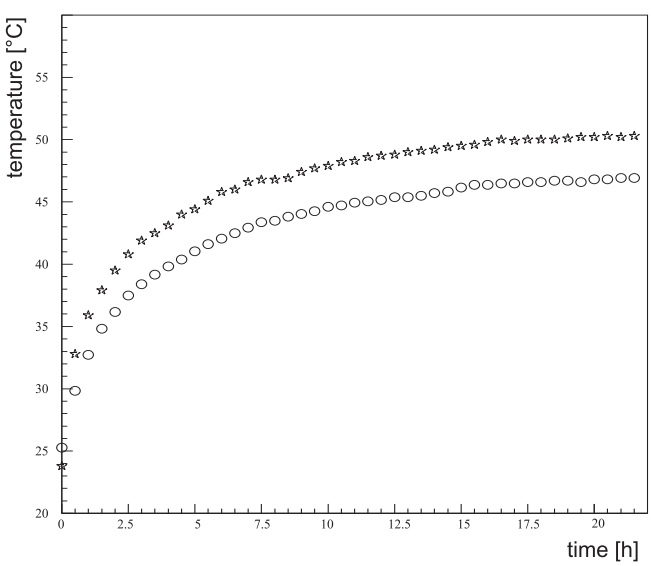

Fig. 1 *Temperature dependence of the working mirror (⋆) and the wheel (∘) with permanent heating (15 Watt) and cooling using a peltier element (see text).*

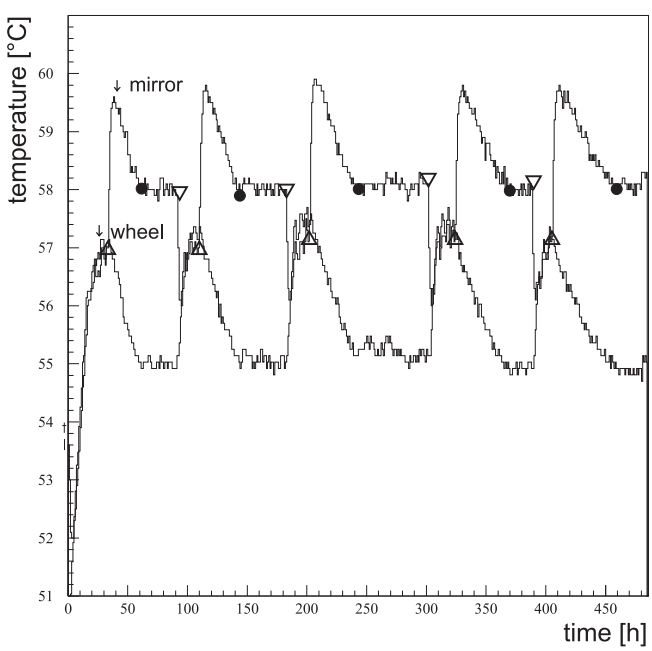

Fig. 2 *Temperature behaviour of the mirror and the wheel during a simulation of a working regime of a FEL (see text; △ laser switched on, ▽ laser switched off, • heating of the mirror wheel switched on).*

[1] W. Seidel, E. Grosse, D. Oepts, B. Rimarzig, U. Wolf, FZ Rossendorf, Wiss.-Tech. Ber. FZR-341 (2002) 26

A Four Pole Magnetic Chicane for Phase Matching

P. Gippner

The undulator U27 consists of two separate sub-systems with a drift space d (free of field) between them. By variation of the gap width g the optical wave length is changed and consequently the phasing between the undulator sections has to be changed as well. This is usually done by properly choosing the electron flight path between the sections by varying the drift space d or by a chicane increasing the electron beam path length with respect to a copropagating light ray. Such a chicane may consist of three [1-3] or four dipoles [4] deflecting the electrons only to one side or to both, the left and the right hand side, respectively. The design of a suitable chicane consisting of 4 dipols is shown in fig. 1. The corresponding calculations have been done using the code RADIA[5].

The fig. 2(a) indicates three typical field distributions within a chicane adjusted along the z-axis. The outer and the inner magnets exhibit the same absolute field values $|B_0|$ since the coils of the dipols (D1, D4) and (D2, D3) operate in series and will be supplied by the currents I_1 and I_2, respectively. The trajectories of electrons with a kinetic energy of E = 20 MeV for three different field strenghts are shown in fig. 2(c). For dedicated current values the electrons cross the z-axis at the same intersection point, what can be used for Compton scattering of infrared light quanta stored within the resonator. Fig. 2(b) indicates the angle of the electron velocity vector with respect to the z-axis. The value of this angle can easily be changed by the currents. The table contains the calculated parameters of the electron path within the chicane at E = 20 MeV.

It is the main purpose of future investigations to confirm experimentally the calculated current ratios I_1/I_2 for which the chicane should deliver a correct phasing.

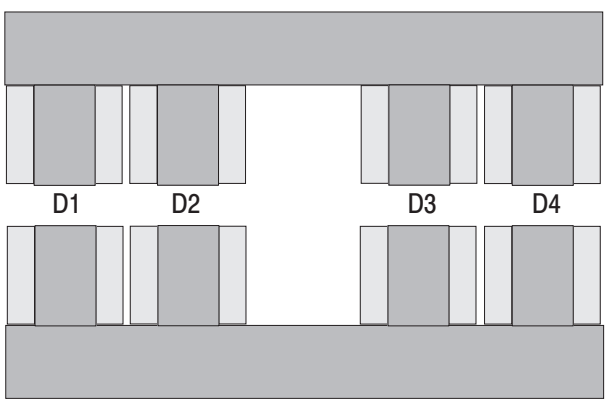

Fig. 1 *Cross section of the projected four pole chicane. The dipoles D1 ... D4 have the same dimensions. The wide interval between the dipoles D2 and D3 forms a space for a flange of the vacuum chamber.*

I_1xn	I_2xn	$\frac{\alpha}{rad}$	$\frac{x_s}{mm}$	$\frac{L}{mm}$	$\frac{\tau}{10^{-9}s}$
-600	+963	0.035	0.0056	320.057	1.0679
-800	+1338	0.049	0.0003	320.108	1.0681
-1000	+1720	0.062	0.0029	320.177	1.0683

Table 1 *Parameters of the electron path (E=20 MeV) within the chicane; α, x_s: angle and displacement at the intertsection point z=0 mm; L, τ: path length and time of flight within the z-interval [-160, +160].*

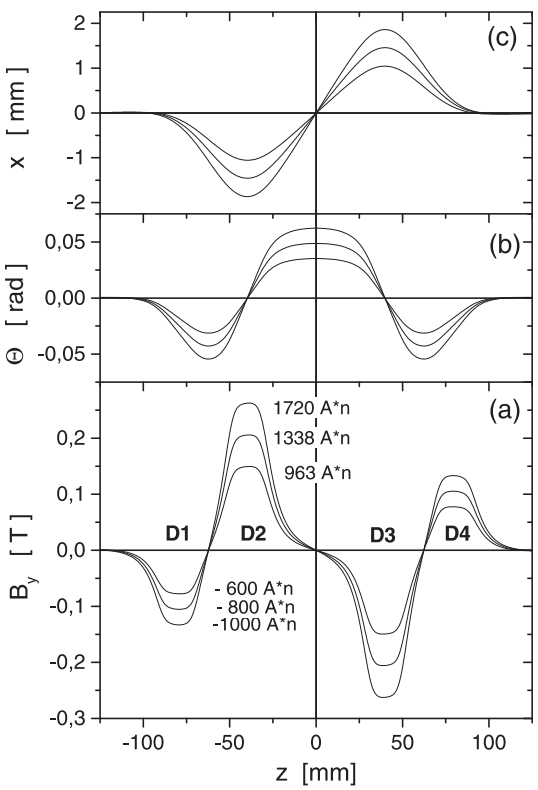

Fig. 2 *Field distributions within the four pole chicane (a) for three dedicated values Ampere* turns and the corresponding trajectories for an electron with the kinetic energy of E = 20 MeV(c). The symbol θ indicates the angle of the electron velocity vector relative to the z-axis (b).*

[1] J. Pflüger, M. Tischer, TESLA FEL 2000-08, December 2000
[2] R. Wünsch et al., Contributions to the 23rd International free Electron Laser Conference, II-61, Darmstadt, Germany, August 20-24, 2001
[3] P. Gippner, FZ Rossendorf, Wiss.-Tech. Ber. FZR-341 (2002) 28
[4] S. Benson, G. Biallas, T. Hiatt, J. Karn, Jefferson Nat. Acc. Facility
[5] P. Elleaume, O. Chubar, J. Chavanne, Journ. Syn. Rad. 5 (1998) 481

New Elements of the GPT Code to Simulate a Resonator Free-Electron Laser

R. Wünsch, C. A. J. van der Geer[1], S. B. van der Geer[1], M. J. de Loos[1]

New elements of the computer code GPT [1] are being developed to simulate the energy transfer in a free-electron laser. In contrast to the single-frequency simulations applied so far the new elements allow us to study the spectral evolution of short laser pulses in a sufficiently large frequency range around the resonance frequency. For that reason we expand the electromagnetic field in a series of resonator eigenmodes with the frequency spacing $\Delta\nu = c/2L_R$ with the resonator length L_R. For the 11.53 m long ELBE resonator the spacing is $\Delta\nu = 13$ MHz. To study the evolution of a laser pulse one has to consider an interval in the order of 1 THz, i. e. roughly 80 000 eigenmodes.

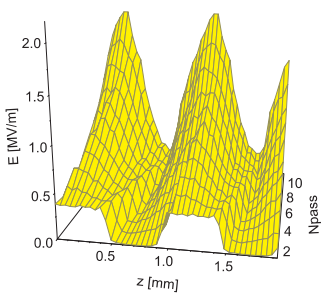

Fig. 1 *Amplification of a wavetrain during 20 passes in a* FEL. *The radiation is modeled with 20 ($N = 21922$) modes. The corresponding pulse repetition frequency is obviously too high. The radiation pulses overlap.*

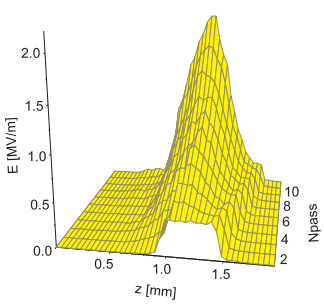

Fig. 2 *The same as in Fig. 1 but modeled with 200 ($N = 2296$) modes, a ten times lower* PRF. *The pulses do not overlap.*

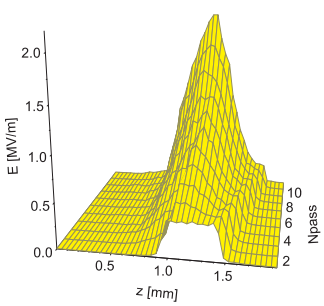

Fig. 3 *As Fig. 1 but with 2000 ($N = 230$) modes. The result is the same*

To reduce the number of modes to a manageable level we increase the frequency spacing by a factor N with the consequence that a single optical pulse in the resonator is replaced by a series of N pulses separated by a distance $D = 2L_R/N$ from each other. If D is much larger than the length of the pulses they do not overlap and we can consider any member of that pulse train as a representative of the actual pulse. Considering their interaction one has to take into account that a short electron pulse interacts with only one member of the optical pulse train.

The pulses produced by an IR FEL, driven by a RF accelerator, are not longer than a few millimeters. In this case, N can be chosen as large as 10000 with the reduction in CPU time by the same factor without overlapping of the various pulses. Figs. 1-3 show the evolution of a pulse, roughly 1 ps long, within different bases of frequency spacing.

The introduction of macro-particles, which are necessary to manage the large number of electrons in the pulse, distorts the ratio between induced and spontaneous emission in favor of the latter. To get a realistic picture of the induced emission one has to reduce artificially the contribution of the spontaneous process. One way to do that is the introduction of copropagating positively charged macro-particles annihilating the spontaneous emission [2], or by copropagating identical bunches at the opposite side of the ponderomotive wave [3]. We have combined both methods to suppress the exaggerated spontaneous emission almost completely. To describe the start-up from noise where the spontaneous process is essential we introduce a seed electron without copropagating positive charge.

Fig. 4 shows the calculated gain of optical power for a very low initial field strength for our electron bunch modeled with 100 macro-particles accompanied by the corresponding positive charge and copropagating bunches. The data reproduce the expected behavior of induced emission without any visible contribution from spontaneous emission.

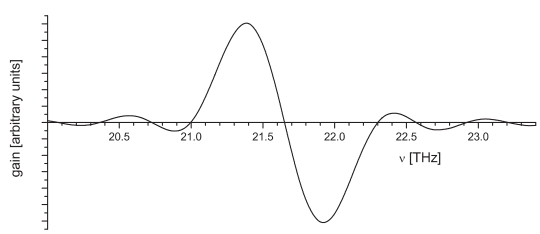

Fig. 4 *Single-pass gain versus frequency ν calculated for 0.1 V/m initial field strength and 100 macro-particles representing a monoenergetic electron bunch with a charge of $Q = 50$ pC and 20 MeV kinetic energy.*

The power of the optical pulse in the equilibrium after a few hundreds of passes through the resonator is an important quantity to be predicted. To accelerate the power build-up we use a seed particle as described above. In this way the calculation time is remarkably reduced.

[1] M. J. de Loos, C. A. J. van der Geer, S. B. van der Geer, 3D Multi-Frequency FEL Simulations with the General Particle Tracer Code, EPAC 2002, Paris, France, pp. 849; S. B. van der Geer, M. J. de Loos, The General Particle Tracer Code, Thesis TU Eindhoven 2002, ISBN 90-386-1739-9; Pulsar Physics, General Particle Tracer, http://*www.pulsar.nl*

[2] V. Litvinenko, O. Shevchenko, Proc. of the 24th Int. Free Electron Laser Conference 2002, Argonne, USA

[3] M.J. de Loos, C.A.J. van der Geer, S.B. van der Geer, A.F.G. van der Meer, D. Oepts, R. Wünsch, Proc. of the 24th Int. Free Electron Laser Conference 2002, Argonne, USA

[1] *Pulsar Physics, The Netherlands*

Start-Up Simulations of the Spectral and Spatial Evolution of the ELBE FEL

R. Wünsch, C. A. J. van der Geer[1], S. B. van der Geer[1], M. J. de Loos[1]

We have used the new elements [1] of the GPT code [2] to simulate the temporal evolution of the optical beam in the ELBE FELs. The parameters of undulator and electron beam used in the calculation are displayed in table 1.

Undulator	
Number of periods	34
Period length	27.3 mm
Undulator parameter K_{rms}	1
Electron beam	
Energy	20 MeV
Energy spread	72 keV
Pulse charge	50 pC*
Pulse length	0.7 ps (210 μm)
Optical beam	
Resonance frequency	21.56 THz
Frequency range	19.8 .. 22.9 THz
Number of long. modes	200
Round trip loss	5%
Resonator length	11.53 m
Rayleigh range	1 m

Table 1 *Parameters of undulator, electron and optical beam as used in the calculations.*
**The 77 pC pulse charge of ELBE has been reduced to 50 pC. This is to simulate the gain degradation caused by the roughness of the undulator field.*

Fig. 1 shows the evolution of the total laser power without resonator detuning, i. e. the round-trip time of the light corresponds exactly to the repetition rate of the electron bunches. The effect of a finite resonator detuning will be investigated in a separate paper [3]. The calculations have been performed with 200 longitudinal modes equidistantly distributed between 19.8 and 22.9 THz. The build-up time has artificially been reduced by means of a seed particle with the charge $Q = -1$ pC.

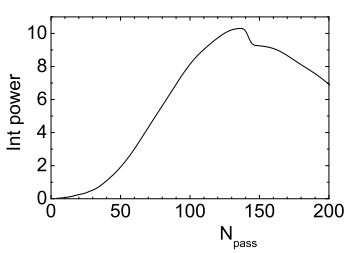

Fig. 1 *Evolution of the total intracavity radiation power (in arbitrary units) as a function of the number of passes N_{pass}.*

Figs. 2 and 3 display the spectral and spatial evolution of the first 200 passes.

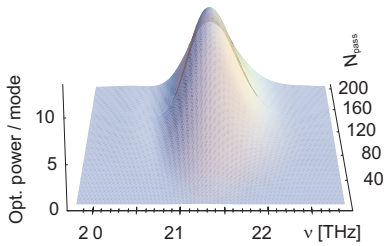

Fig. 2 *Internal laser power per mode as a function of frequency ν and number of passes N_{pass}*

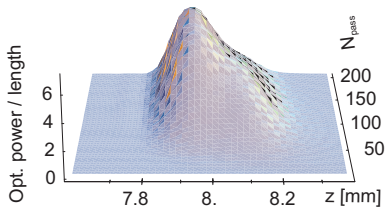

Fig. 3 *Internal laser power as a function of the longitudinal coordinate z and the number of passes N_{pass}*

The optical pulses evolve in quite a smooth manner, both in frequency and real space. When the power increases, the spatial distribution narrows and the peak shifts towards the rear end of the pulse. This part of the optical pulse has been amplified at the rear part of the undulator where the gain is larger than in the front part due to the onset of microbunching. Consequently, the centroid of the light pulse is traveling slower than light in vacuum (c). The light pulse drifts away from the electron pulse, the gain reduces and falls below the loss in the resonator and the optical power begins to decay.

The effect described above is denoted as laser lethargy. It occurs when the electron pulses are shorter than the slippage length $\Delta = N_{\mathrm{u}}\lambda$. We have used $\mu_{\mathrm{c}} = \Delta/\sigma_z \approx 2.3 > 1$ in the calculation.

Laser lethargy can be compensated by reducing the resonator length L_{R} from the value synchronized with the repetition rate of the electron bunches, so that the smaller group velocity of the light pulse is compensated.

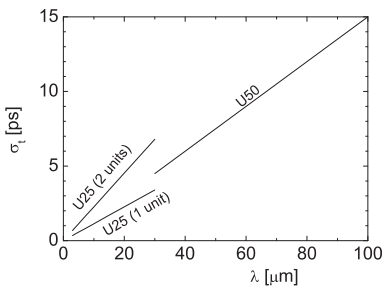

Fig. 4 *Electron pulse lengths σ_t corresponding to the condition $\mu_{\mathrm{c}} = 1$ as a function of the laser wavelength calculated for the undulators of ELBE.*

Fig. 4 displays the rms electron pulse lengths satisfying the condition $\mu_{\mathrm{c}} = 1$ (pulse length equals slippage length). Pulses around this value or shorter are expected to be affected by the lethargy problem.

[1] R. Wünsch,C. A. J. van der Geer, S. B. van der Geer, M. J. de Loos, This Report, p. 57
[2] M. J. de Loos, C. A. J. van der Geer, S. B. van der Geer,
3D Multi-Frequency FEL Simulations with the General Particle Tracer Code, EPAC 2002, Paris, France, pp. 849;
S. B. van der Geer, M. J. de Loos, The General Particle Tracer Code, Thesis TU Eindhoven 2002, ISBN 90-386-1739-9;
Pulsar Physics, General Particle Tracer, http://*www.pulsar.nl*
[3] R. Wünsch,C. A. J. van der Geer, S. B. van der Geer, M. J. de Loos, This Report, p. 61

[1] *Pulsar Physics, The Netherlands*

Simulation of Limit Cycle Oscillations in the U27 FEL

R. Wünsch, C. A. J. van der Geer[1], S. B. van der Geer[1], M. J. de Loos[1]

Limit cycle oscillations in a short-pulse FEL, as a result of a periodic, self-replicating micropulse structure on successive cavity transits, were first predicted by Colson [1]. First experimental evidence was given in ref. [2]. To understand this phenomenon one has to remember the following features of the interaction in a FEL. Electrons slip back relative to an optical micropulse on their mutual travel through the undulator, due to the difference in forward velocity. As a consequence, the optical micropulse is stronger amplified at its trailing edge. In other words, its group velocity is somewhat smaller than the vacuum value. A micropulse stored in a perfectly synchronized resonator grows, narrows and retards on successive passes through the undulator, with the consequence that the laser gain is reduced (laser lethargy). In order to restore the gain, it is necessary to slightly desynchronize the resonator, which usually is done by reducing the cavity length. When the laser intensity approaches saturation the gain at the highest intensity is reduced first. As a result the center of power is shifted forward and the group velocity becomes larger than the value of optimum overlap between optical and electron pulse. The gain starts to decrease and the power falls below the saturation level. From now on another oscillation starts whereby the center of optical power performs an oscillation in the well of the ponderomotive potential. Limit cycle oscillations do only occur when the electron pulse is shorter than the slippage length $N_u\lambda$ (N_u: number of undulator periods, λ: radiation wavelength). Otherwise the oscillations are washed out.

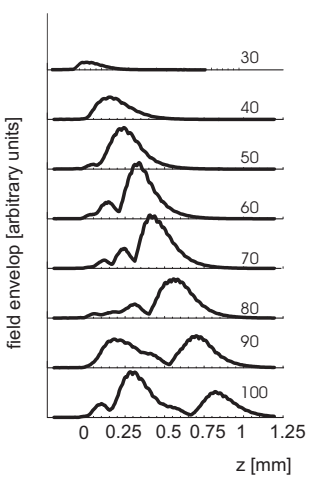

Fig. 1 *Envelope of the radiation field at the undulator exit after 30, 40, ..., 100 passes calculated for one unit of the U27 undulator of ELBE (parameters see table 1 of ref. [4]). The resonator detuning is -0.5λ and 5% round-trip loss has been assumed.*

We have simulated such kind of oscillations for the ELBE FEL by means of the code GPT [3]. Fig. 1 shows the evolution of the envelope of the optical pulse. First, the optical pulse grows with the peak near to the trailing edge. Since the resonator is shorter than the value corresponding to the electron repetition rate the optical pulse moves forward from pass to pass. After 50 passes a second peak starts to grow at the trailing edge where the overlap with the electron pulse is large. This peak grows fast since the electron pulse has been prebunched by the strong field in the first part of the undulator. The leading edge of the pulse looses the overlap with the electron pulse and decays in dependence on the resonator loss. As a result, the center of the optical peak moves forth and back in the ponderomotive well. This oscillation produces side lobes in the spectrum which emerge and vanish periodically (see Fig. 2).

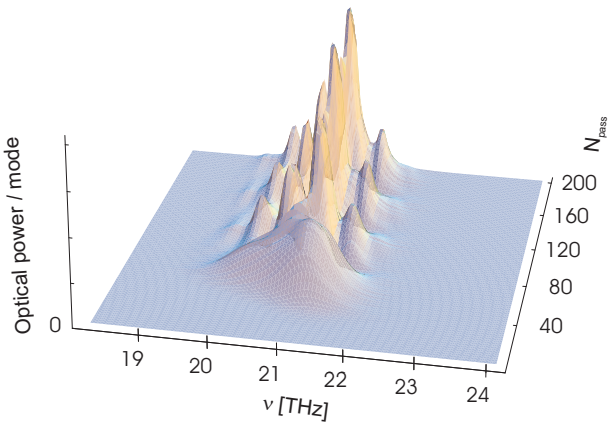

Fig. 2 *Evolution of the total radiation power as a function of frequency ν and number of passes N_{pass} calculated for the same parameters as in Fig. 1.*

Frequency and amplitude of the observed limit cycle oscillations depend on resonator detuning and round-trip loss. In Fig. 3, we vary the detuning from a value much smaller to a value much larger than the value giving optimum gain. At lower detuning the laser starts slowly but saturates at a higher power level which is characterized by remarkable oscillations. Detuning the resonator stronger than the value of optimum gain leads to both a small gain and a lower power level at saturation.

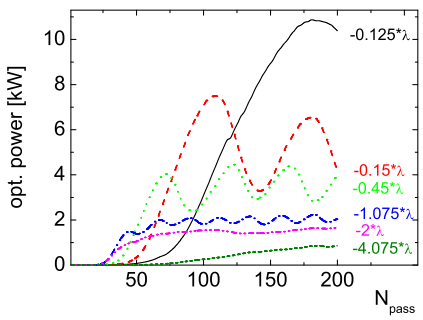

Fig. 3 *Evolution of the total laser power as a function of the number of passes N_{pass} calculated for the same parameters as in Fig. 1 and the indicated values of the resonator detuning.*

[1] W. B. Colson, Phys. Quantum Electron. 8 (1982) 457
[2] D. A. Jaroszinski, R. J. Bakker, A. F. G. van der Meer, D. Oepts, P. W. Amersfoort, Phys. Rev. Lett. 70 (1993) 3412-3415
[3] R. Wünsch,C. A. J. van der Geer, S. B. van der Geer, M. J. de Loos, This Report, p. 59
[4] R. Wünsch,C. A. J. van der Geer, S. B. van der Geer, M. J. de Loos, This Report, p. 60

[1] *Pulsar Physics, The Netherlands*

Dynamics of Matrix–Isolated Molecules [E]

J.A. Piest

Gaining insight in intra- and intermolecular processes is an important issue in order to understand physical, chemical, and biological reactions in micro- and macroscopic systems. Such reactions determine the way molecules interact with their environment. For example, formation of amino-acids takes place in interstellar ice analogues [4, 5], which can be studied in more detail by time-resolved IR experiments [3].

Detection of time-resolved optical parameters of molecules reveals the time scales of energy redistribution, which governs such processes. Therefore, it can be used as a powerful method to study the dynamics of molecular systems.

The advantage of doing experiments in the region slightly above zero Kelvin is clear: in this condition molecules have much lower internal energies than at room temperature. Generally, in the spectra of such cold molecules there are 1) less transitions present, and 2) the band width per transition is smaller. Thus, spectra of these molecules are less complicated than those recorded for warm species and can be interpreted with less ambiguity.

In particular, time-resolved spectral data of cold molecules may lead to knowledge of the time scales on which intra- and intermolecular energy redistribution takes place, and inform us about the time response of physical or chemical inter(re)actions in molecular systems. Due to lack of bright IR short-pulse light sources, time-resolved spectral data in the sub-nanosecond domain for matrix-isolated species are scarce, where spectra in the available μs region do not yield relevant information [1, 2, 3].

In a user lab of the ELBE building a high vacuum setup is under construction in order to do such experiments with cold molecules. In this setup, isolated molecules are embedded in a molecular or inert gas ice. By mixing of gases more exotic ices, such as interstellar ice analogues, can be generated easily.

The setup consists of two chambers pumped by two Varian V301 Navigator turbo-molecular pumps. Two Varian SH100 membrane pumps provide a sufficiently low roughing pressure.

A liquid helium-cooled Janis ST - 400 UHV cold head, operating between temperatures of 1.5 K and 300 K, and with a cooling power of 3 W at 5 K, is to be mounted on one of the chambers. *In situ* sample generation takes place on a transparant surface mounted on the tip of this cold head. Purified gases are mixed with sample species to well defined concentrations, before being deposited on the cryogenically cooled window. Also externally prepared samples can be mounted on the tip of the cold head before evacuating the vacuum chambers and cooling the sample.

Experiments to be done with this setup in order to yield time-resolved spectral information vary from simple one-color pump-probe experiments in direct absorption, to more sophisticated background-free detection methods such as: detection of the photon echo, scattering of IR or UV light on a transient grating, or laser induced fluorescence (LIF). The two latter experiments desire a resonant IR-UV excitation scheme.

In all of these proposed experiments, the absorption of IR light is governed mainly by two laws:

$$\frac{n(\tau,\delta z)}{n(0,\delta z)} = \exp\left(-\frac{\overline{\sigma}}{h\nu}\int_0^{\tau} I(t,\delta z)dt\right), \qquad (1)$$

and:

$$\frac{I(t,\delta z)}{I(t,0)} = \exp\left(-\overline{\sigma}\int_0^{\delta z} n(t,z)dz\right), \qquad (2)$$

the first of which describes the change in the local absorber density $n(t,z)$ in a two level approximation as a function of the time-averaged pulse intensity $I(t,z)$. The second expression is known as the Beer-Lambert law, describing the decay of averaged pulse intensity along a path $(0,\delta x)$ through the sample as a function of the averaged absorber density. The central wavenumber of the IR spectral profile is represented by ν, while the line-integrated absorption cross section is symbolized with $\overline{\sigma}$. Linear absorption is assumed in both expressions, though, similar laws can be derived for non-linear absorption processes.

For the experiments in direct absorption the variation of IR absorption of the probe pulse as a function of time-delay is the relevant parameter to be determined. Depending on the line-integrated cross section of the sample molecule, this variation is usually not larger than a few percent of the total absorption strength. Considering the spectral width of the transition smaller than the IR spectral profile the change in the signal detected may be only a fraction of a percent. Therefore, it is highly desirable to resolve the IR pulse spectrally, for instance by coupling it into a fourier transform infrared spectrometer (FTIR) after passing the sample. The IR pulse, with elongated duration either due to the absorption lines present under the IR spectral profile, or due to an artificial modulation, can then be analyzed. Because natural pulse elongation due to presence of small absorption features may not lead to the desired intensities of the signal to be deteced, simulations to modulate the IR pulse artificially, in order to reveal (partial) information about small structures of the spectral distribution are currently carried out.

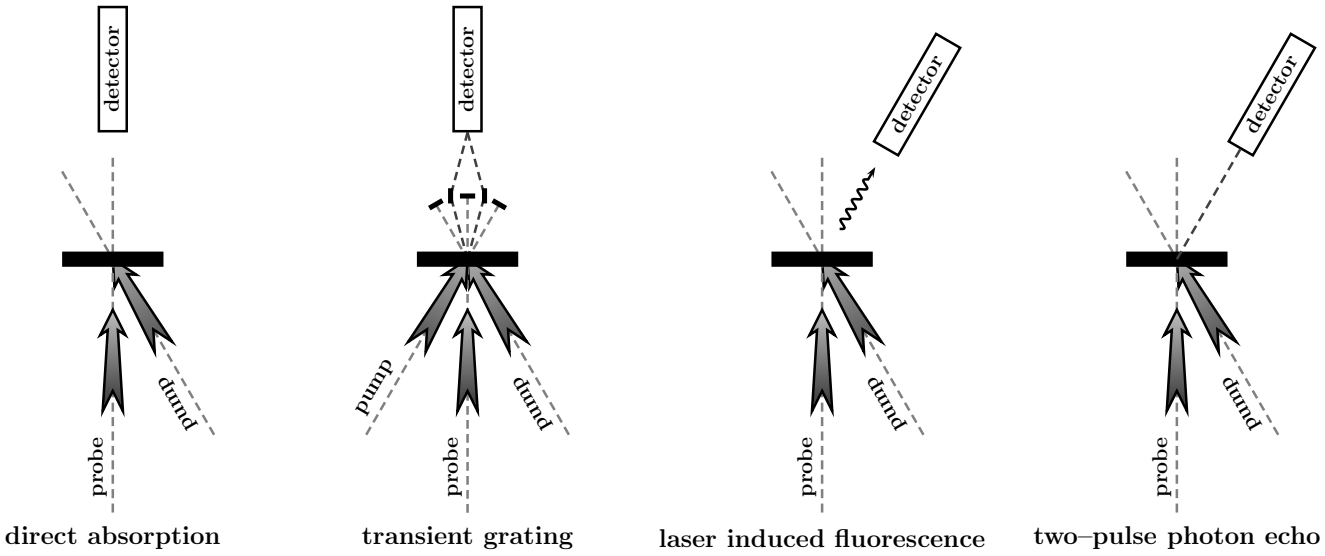

Fig. 1 Experimental setup schemes for time-resolved spectroscopy of matrix-isolated molecules. The sample is represented with a thick black line. Pump and time-delayed probe laser pulses irradiate the sample. (ll) In direct absorption the change in intensity of the probe pulse is recorded as function of the time-delay. (l) Photon yield scattered from a transient grating, generated with two mutually interfering pump pulses, as function of the time-delay yields information about the population of excited molecules in the grating. (r) In an IR-UV double-resonance scheme fluorescence from an excited electronic state is recorded as a function of time-delay between IR pump and UV probe pulse. (rr) Coherent fluorescence is detected as a function of the time-delay between pump and probe pulse.

In case of transient grating scattering and LIF a tunable laser in the UV is desirable. When a resonant IR-UV excitation scheme is applied, the fluorescence or the scattering of UV light on a IR-IR induced grating can be detected against zero background, in fluorescent or non-fluorescent species, respectively. The transient grating scattering method may also yield detectable signal without application of a UV laser, by scattering of IR light on an IR induced grating. Simulations are currently carried out, in order to estimate the yield of scattered photons.

The IR light has to be provided by either the FEL or the Topas, whith a strong preference for the FEL, because of its higher averaged output power as a result of a much higher repetition rate. Scattering of IR light on an IR induced grating may possibly only work with the FEL, due to the feeble signals expected, *i.e.,* some mW of scattered signal with some Watt of resonant input photons.

Applying the two pulse photon echo method the coherent fluorescence (the "photon echo"), yielding information particularly about homogeneous relaxation processes, is detected. The setup for this experiment is apparently similar to the direct absorption pump-probe setup, though, the experiment is more subtle because special care has to be taken for the pump and probe pulse intensities, and for the position of the detector. The direction of the detected signal is determined by momentum conservation: $\mathbf{k}_{photon-echo} = 2\mathbf{k}_{probe} - \mathbf{k}_{pump}$, implying an intensity ratio between the pump and probe beam of 1:2.

The schemes for each of these experiments are depicted in Fig. 1.

In future, besides the matrix-isolation experiments, the setup can be extended easily to do experiments on molecules or ions applying either effasive or supersonic, pulsed or continuous, jets, while exploiting high sensitive ion detection methods.

[1] Allamandola and Nibler, Chemical Physics Letters 28 (1974) 335-340
[2] Allamandola et al., Journal of Chemical Physics 67 (1977) 99-109
[3] L.J. Allamandola, NASA/Ames Research Center, private communications, 2002
[4] Bernstein et al., Nature 416 (2002) 401
[5] Muñoz Caro et al., Nature 416 (2002) 403

Clonogenic Survival of Mammary Epithelial Cells MCF-12A after Irradiation with 200 kV X-Rays

A. Panteleeva, W. Dörr[1], E. Lessmann, J. Pawelke

Precise determination of the relative biological effectiveness (RBE) of low-energy X-rays ($E_{ph} \leq 50$ keV) is important because of their widespread use in diagnostic radiology and radiotherapy. However, literature data on this topic is still not conclusive. Recently, RBE of 25 kV X-rays was determined for the survival and chromosomal damage by micronucleus test for 4 human and rodent cell lines [2]. Since X-rays of this energy range are used especially in mammography, the study was extended to human mammary epithelial cells. Most human cancers are of epithelial origin, therefore, they represent an appropriate model system for testing the cell kill and induction of genetic damage. The established cell line MCF-12A was cultured in the cell laboratory at ELBE (Fig. 1) and cell culture parameters were optimized. The cell line, purchased from ATCC (USA), is a non-tumorigenic epithelial cell line established from tissue taken at reduction mammoplasty. The line was produced by long term culture in serum free medium with low calcium concentration. MCF-12A was derived from adherent cells in the population, by a transformation resulting from a 72 h exposure to 45^0C [2]. The cells were incubated at 37^0C in humidified athmosphere containing 5% CO_2, in a one to one mixture of DMEM and Ham's F12 supplemented with 5 % horse serum, 500 ng/ml hydrocortisone, 0.01 mg/ml insulin, 100 ng/ml cholera toxin and 20 ng/ml epidermal growth factor.

The cell line was proved to be suitable for long-term culture, necessary for the future experiments on RBE determination by cell survival and micronucleus test. The plating efficiency was determined to be 51.8 ± 0.9 %, independent on the passage number (Fig. 2). The cells were irradiated at the Radiotherapy Department of the Medical Faculty of the TU Dresden. The X-ray tube (tungsten anode, 0.5 mm Cu filtration) was operated at 200 kV and 20 mA. The cells were seeded in 25 cm^2 polystyrene flasks and irradiated as monolayers in the exponential growth phase, before reaching 70 % confluence. The dose rate was 1.2 Gy/min, and doses of 1 to 10 Gy were applied. Immediately after irradiation, cells were trypsinized and seeded at low density in Petri dishes at 10 replications per dose point. After 11 days incubation, the colonies were fixed and stained. Colonies with more than 50 cells were scored as survivors. The data were fitted to the linear-quadratic model $S = exp(-\alpha D - \beta D^2)$. The survival data as well as the fitting parameters α and β are presented in Fig. 3. The surviving fraction at 2 Gy (SF2) was calculated to be 0.43 ± 0.03. Data were also fitted to the single hit - multitarget model $S = 1 - (1 - exp(-D/D_0))^n$, revealing the parameters $D_0 = 1.43 \pm 0.06$ and $n = 2.2 \pm 0.1$, showing very good agreement with survival data of normal primary mammary cells [3]. As a next step, the determination of survival and chromosomal damage by 25 kV X-ray tube irradiation will be performed.

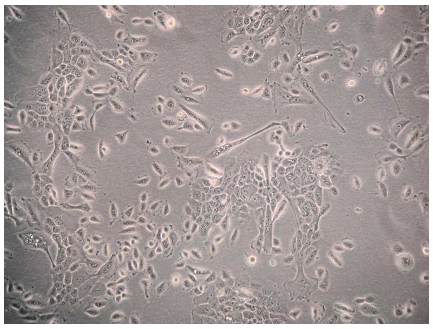

Fig. 1 *Culture of MCF-12A with characteristical epithelial-shaped cells.*

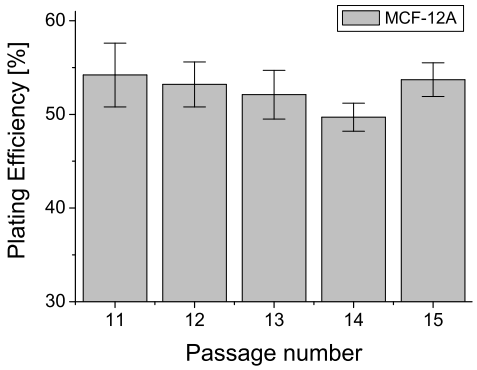

Fig. 2 *Dependence of the plating efficiency on the passage number. The mean values from several experiments are shown together with the standard error of the mean.*

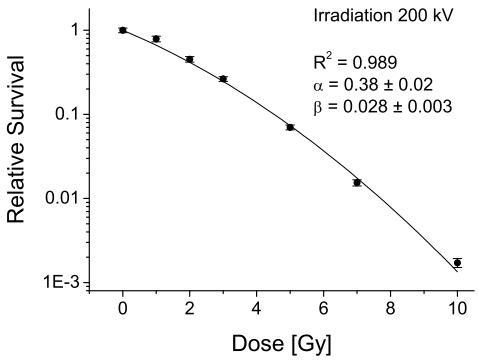

Fig. 3 *Survival of MCF-12A after irradiation with 200 kV X-rays. The values are representing the mean from 8 experiments and the standard error of the mean.*

[1] A. Panteleeva et. al., FZ Rossendorf, Wiss.-Tech. Ber. FZR-341 (2002) 90
[2] T.M. Paine et. al., Int. J. Cancer 50 (1992) 463
[3] L.E. Cathers and M.N. Gould, Int. J. Radiat. Biol. Relat. Stud. Phys. Chem. Med. 44 (1983) 1

[1] *Dept. of Radiotherapy, Medical Faculty, Technical University of Dresden*

Influence of the Handling Procedure During Irradiation on Cell Survival and Micronucleus Test Results

A. Panteleeva, E. Lessmann

The first radiobiological experiment planned to be performed at the ELBE X-ray beam is the determination of RBE of soft X-rays. Obtaining of dose-response curves for at least 5 dose points is required for the exact determination of the curve parameters. Cell survival and chromosomal damage by micronucleus test as biological endpoints will be studied. The required irradiation times at the expected dose rate of ~ 1 Gy/min and required dose range of 1 - 10 Gy are estimated to be in the order of 0.5 - 1 hour. Taking into account the time-consuming closing and opening the radiation protection doors of the radiation physics cave, a total time of several hours has to be expected for the complete handling procedure of cell irradiation. Since the cells have to be outside the optimal environment (37^0C, humidified atmosphere containing 5% CO_2) during this time, additional stress reactions, resulting in increased cell kill or chromosomal damage, have to be expected. On the other hand, determination of damage by micronucleus test requires blocking of the cell cycle. Since the time scale of repair of potential lethal damage is for mammalian cells in the order of up to ~ 3 hours, it could interfere with the primary damage and result in a reduction of the irradiation effect.

To prove this possibility, experiments on determination of the effect of cell handling in non-optimal conditions were performed. For the cell survival assay, the cells were seeded in the cell culture dishes, filled with medium and sealed. The cell culture dishes PetriPerm with a 25 μm membrane base (Sartorius, Göttingen) have been chosen for cell irradiation at the ELBE X-ray beam [2]. Since the X-ray beam at ELBE is horizontal, the cell dishes were kept in a vertical position during this simulation procedure for 0, 2, 4, 6 or 8 hours. A cell culture flask was used for additional control. Afterwards, the cells were trypsinized and the standard clonogenic assay was performed. The results shown in Fig. 1 for the cell line MCF-12A and in Fig. 2 for NIH/3T3 show no significant change in plating efficiency due to the handling in non-optimal conditions.

The influence of the handling procedure on the micronuclei outcome was also studied for these cell lines. The cells were irradiated with UVC light (253.7 nm) and then left for 0, 0.5, 2, 4 or 6 hours at 20^0C or at 0^0C (ice). Afterwards, the standard micronucleus test was performed. The results in Table 1 show that the time interval of up to ~ 2 h is not influencing the test result (keeping the cells on ice or at room temperature), however, the spread of the fraction of binucleated cells after 6 h handling shows the influence of the inoptimal conditions. Therefore, for this test it is desirable to keep the handling times less than 2 hours.

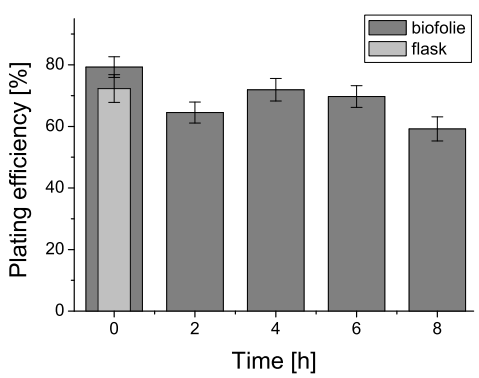

Fig. 1 *Dependence of the plating efficiency for MCF-12A on the handling time. The mean value of 1 experiment (10 replications) together with the standard error of the mean is shown.*

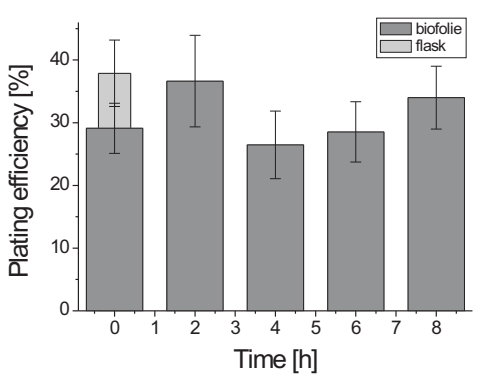

Fig. 2 *Dependence of the plating efficiency for NIH/3T3 on the handling time. The mean value of 1 experiment (10 replications) together with the standard error of the mean is shown.*

Tab. 2 *Fraction of binucleated cells with micronuclei after 0, 0.5, 1, 2, 4, 6 h handling procedure for NIH/3T3 (1 experiment) and MCF-12A (3 experiments).*

Cell line	T [^{0}C]	0 h, no irradiation	0 h	0.5 h	1 h	2 h	4 h	6 h
3T3	20^0C	0.8±0.2	3.4±0.4	4.3±0.3	5.3±1.1	4.8±0.6	-	4.2±0.6
	0^0C			4.2±0.2	4.3±0.2	3.8±0.2	-	2.8±0.2
MCF-12A	20^0C	4.7±0.7	13±2	13±2	16±2	14±2	9.3±1.0	16±2
	0^0C			14±2	16±1	13±2	14±2	19±2

[1] A. Panteleeva et. al., FZ Rossendorf, Wiss.-Tech. Ber. FZR-341 (2002) 89

Measurements of Spectral Dose Distributions of a Soft X-Ray Tube

J. Pawelke, A. Panteleeva, C. Hoinkis[1]

RBE values of X-rays from a conventional 25 kV soft X-ray tube have been determined for cell survival and chromosomal damage (formation of micronuclei) by irradiation of several cell lines [1]. Significantly higher induction of micronuclei was observed after irradiation with 25 kV X-rays in comparison to the reference radiation from a 200 kV X-ray tube. RBE values for the different cell lines were found to be between 1.1 and 1.3. In contrast, the RBE at 10 % survival was found to be not significantly different from 1 for all cell lines. Further experiments at lower X-ray energy are desirable in order to study the X-ray energy dependence of the RBE.

The tungsten anode soft X-ray tube (Darpaq 150-MC) is used for therapy. When operated at 25 kV and 20 mA with 0.3 mm Al filter, the dose rate at the target position was measured by an air filled ionisation chamber (23342, PTW Freiburg) to be 1.67 Gy/min. Since photon energy dependent dose cannot be measured by ionisation chambers (IC), it was calculated after determination of spectral photon flux density by considering the energy dependent energy absorption coefficient for water. The photon flux was measured with a high resolution 13 mm^2 Si-PIN diode (XR100-CR, Amptek, Bedford, USA). The necessary flux reduction was achieved by operating the tube at 0.2 mA current and by mounting a 25 μm iron slit collimator (5 mm thick) in front of the detector. By moving the detector perpendicular to the slit orientation with a step motor unit the maximum photon intensity was determined for dose calculation. Energy distribution was acquired at a count rate of about 1000 photons/s in order to minimise detector pile-up effect. For this purpose, the detector was placed within the X-ray cone at farthest possible distance from the focal spot and moved up to $\approx$3 mm out of center. The detector was calibrated by measuring the spectra of several sources (^{55}Fe, ^{241}Am, ^{210}Pb) as well as of X-ray fluorescence produced in a thin lead foil. The detector energy resolution was measured to be 304 eV FWHM at 5.9 keV.

Removal of the 0.3 mm Al filter results in a more than threefold increase of photon flux density and a decrease of mean X-ray energy (Fig. 1). Reducing the tube high voltage further decreases the mean photon energy and simultaneously the intensity. This intensity loss is compensated by the increase of the mass energy absorption coefficient with decreasing photon energy (see Table 1). Consideration of detector and collimator geometry as well as detector dead time and efficiency correction results in a reasonable agreement between dose rate directly measured by IC with those calculated on the base of photon flux measurement (Table 1). The dose rate calculated in this way is less accurate than the one measured by IC, however, useful in determining the spectral dose distribution (Table 2). Measurements were repeated with a 9 mm^2 cadmium zinc telluride detector (XR-100T-CZT, AmpTek, USA) which confirms all results mentioned above. The next cell irradiations will be performed for tube operation at 10 kV.

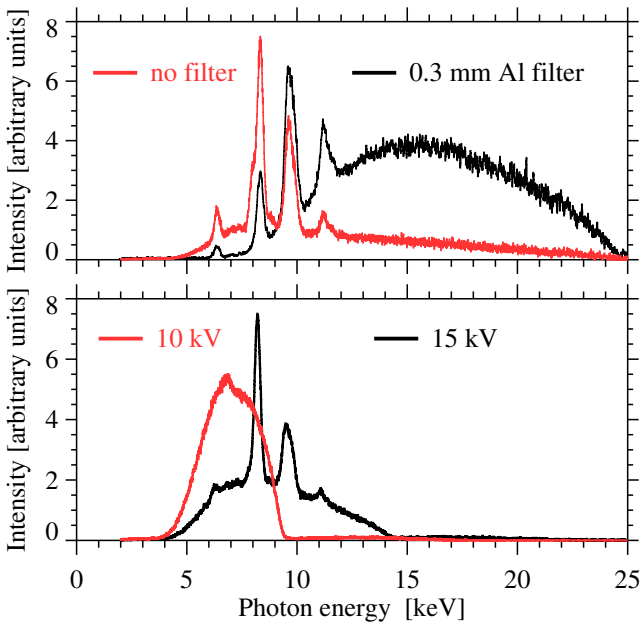

Fig. 1 *Energy distribution of the soft X-ray tube intensity, measured with a low-energy X-ray detector (XR100-CR), corrected for the detection efficiency. The upper part shows the effect of X-ray filtration for tube operation at 25 kV, whereas the influence of the tube high voltage is shown in the lower part (no filtration). The small peak at 6.4 keV arises from the K_α line of iron fluorescence of the collimator.*

Tab. 1 *Photon intensity I_γ and dose rate $\dot{D}$ at the target position for tube operation at 0.2 mA current.*

Tube parameter	I_γ ph/s	$\dot{D}$ $[mGy/min]$ IC	Detector
25 kV, Al filter	12285	2.1±0.2	2.6±0.9
10 kV, no filter	7080	2.6±0.2	3.3±1.0

Tab. 2 *Spectral dose contribution from soft X-ray tube in dependence on tube operation parameters.*

Photon energy [keV]	Dose contribution [%] 10 kV no filter	15 kV no filter	25 kV no filter	25 kV 0.3 mm Al
4... 7	47.6	19.3	12.0	1.4
7...10	50.9	60.7	60.1	23.5
10...13	0.9	17.1	15.8	28.0
13...19	0.6	2.7	10.1	37.2
19...25	0.0	0.2	2.0	9.9

[1] A. Panteleeva et al., FZ Rossendorf, Wiss.-Tech. Ber. FZR-341 (2002) 90

[1] *Dept. of Radiotherapy, Medical Faculty, Technical University of Dresden*

Changing the Dose Range of TSEE Dosimeters

A. Panteleeva, E. Lessmann, J. Pawelke

The TSEE detectors have been studied as a possible solution for dosimetry in a living cell. The small thickness of the sensitive layer ($\sim$ 10 nm) allows to sample the depth-dose distribution even on the scale of cell dimensions (thickness $\sim$ 5 μm), an important feature in the case of soft X-rays. The study of these detectors proved their good reproducibility under laboratory conditions [1]. Another important characteristics is the possibility of simulation of irradiations in real cell environment conditions such as liquid medium. This was proved possible, with stable detector response also in liquid (propanol) [2]. However, the saturation of dose response due to the limited pulse resolution of the gas-flow counter resulted in an upper detection limit of $\sim$ 0.1 Gy, far from the range required for cell survival studies ($\leq$ 10 Gy). This limitation can be overcome by manipulation of the read-out system (counter geometry, gas flow), which however results in little increase of upper response limit. Another possibility is to change the irradiated detector area, but it results in difficult detector handling. Therefore, detectors produced by two new methods were tested. The first method is the sedimentation of BeO water suspension on a graphite substrate (detector type II). This method is very simple, results in one TSEE peak (Fig. 1) and allows to vary the amount of the BeO and therefore the detector sensitivity. However, a fading effect was observed, expressed in several orders of magnitude drop of the response to irradiation on the first days after production (Fig. 2). The properties of the detectors, studied after stabilisation of the response, are presented in Table 1. Detectors type III were produced by impregnation of a 1 mm graphite plates with Be and subsequent oxidation at 1400^{0}C by Dr. Holzapfel Messgerätelabor, Teltow. Three detectors produced in this way with low, medium and high sensitivity were studied and compared to detector type I, which shows up to now the best reproducibility [1]. A fading effect for detector type III was not observed (Fig. 2). The irradiation in liquid (propanol) for both detector types II and III resulted in good reproducibility of response, however, the mean response for detector type II was reduced, although the expected attenuation in this layer thickness is negligible (Table 2). Therefore, detectors type II can be used in cases where the simplicity of detector structure is more important than the reproducibility of response and are inappropriate for simulation of the real cell geometry. The method of production of detector type III can be used to vary the dose response, but the reproducibility of response of these detectors has to be still optimised.

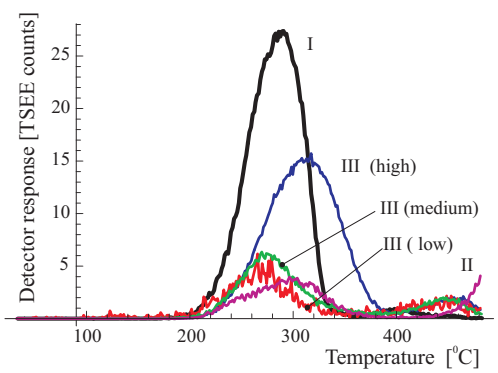

Fig. 1 *Glow curves of the new detector types II and III. For better illustration, the glow curve of detector type III (low) is multiplied by a factor of 100. The response of detector type I is shown for comparison.*

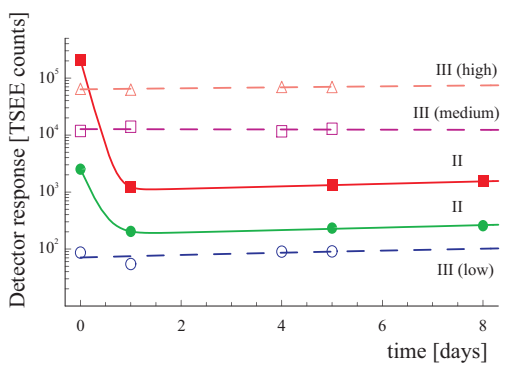

Fig. 2 *Fading effect: the detecor response is evaluated immediately after the irradiation with a ^{90}Sr source in air. This procedure is performed on several consecutive days after the detector production.*

Tab. 1 *Main properties of TSEE detectors.*

Detector type	Sensitivity [counts/mGy]	Reproducibility [a] in air (^{90}Sr) [%]
II	5690	9.2
III (low)	49	8.6
III (medium)	6406	13.2
III (high)	30637	4.7
I	7790	0.82

[a]) Average deviation from the mean of 10 measurements

Tab. 2 *Response of detectors type II and III to irradiation in liquid.*

Detector type	Reproducibility [a] in propanol (^{22}Na) [%]	Spacing [b] [mm]	Response [a] ratio air to propanol (^{22}Na)
II	13.8	2.8±0.2	1.6±0.2
III	15.3	2.0±0.2	1.4±0.3

[a]) Average deviation from the mean of 8 - 10 measurements
[b]) Detector to source distance, filled up with air or liquid

[1] J. Pawelke and A. Panteleeva, FZ Rossendorf, Wiss.-Tech. Ber. FZR-319 (2001) 102
[2] A. Panteleeva et. al., FZ Rossendorf, Wiss.-Tech. Ber. FZR-341 (2002) 92

An X-Ray Monochromator for the Channeling Source at ELBE

J. Pawelke, A. Heitsch[1], A. Panteleeva, M. Sobiella

An X-ray source is being developed at ELBE, where quasi-monochromatic X-rays will be produced by electron channeling in diamond crystals [1]. In order to separate the channeling radiation (CR) from the polychromatic bremsstrahlung background a first X-ray monochromator has been designed for CR of 18.4 keV mean energy. Optimal monochromator properties will be achieved by coating the curved surface of a stepped mould with highly oriented pyrolytic graphite (HOPG) crystals [2]. The mould geometry is shown in Fig. 1 where steps of same curvature are merged and the outer part is extended to result in a rectangular shape for practical reasons (cf. Fig. 2 in [2]).

For the mould a material with the following properties is required: *(i)* radiation resistant, *(ii)* low Z in order to minimise photon scattering, *(iii)* machinability with high precision of the final curvature, *(iv)* adherence of the HOPG crystals to mould surface without glue and *(v)* reasonable costs. One technological solution is shaping of Zerodur glass ceramic (Schott Glas, Mainz) which is used for manufacturing precision spherical optics. Since adhesion of HOPG crystals to Zerodur in dependence on surface processing was never tested, it was investigated by coating small blocks with crystals produced by Bourevestnik Inc., Sankt-Petersburg. These crystals are especially suited for covering bended moulds. After polishing (surface defects of 5/3x0.25, DIN 3140) the crystals adhere to the surface, but not after fine sanding (micro roughness $R_Z < 3\,\mu$m). However, the time consuming curving and polishing procedure of Zerodur results in costs of more than 50.000 € for one mould (Berliner Glas KG, Berlin). Therefore, adherence of HOPG crystals to three different plastics was investigated: polymethylmethacrylate (PMMA, $C_5H_8O_2$), a more common mould material for HOPG monochromators, and two high performance plastics which are resistant to photon radiation (SINTIMID and TECAPEEK, Ensinger GmbH, Nufringen). Adhesion to PMMA was proved to be excellent after polishing (diamond suspension, $R_Z = 0.4\,\mu$m) and still reasonable after milling with a diamond face cutter ($R_Z = 1.1\,\mu$m), whereas from the other two materials, only SINTIMID shows reasonable adhesion after high quality polishing ($R_Z = 0.8\,\mu$m). Therefore, a PMMA mould was decided to be produced.

At first, the steps were made as individual rectangular blocks with high accuracy. Furthermore, a mortise was shaped in step 1 to receive the tenons, i.e. step 2 to 6 (cf. Fig. 1). Then the curvature of step 1 was shaped by CNC-moving a hob along X and Z, whereas bending along Y was achieved by the shape of the hob. In the same way, the other steps were shaped by joining them subsequently with step 1, the most sticking out last. The resulting surface roughness was measured to be $R_Z = 0.2\,\mu$m (along X) and $R_Z = 1.8\,\mu$m (along Y), respectively. Curvature measurement of a test sample of step 1 showed deviations in the radius of curvature as well as influence of sample torsion (Fig. 2, above). Improvements in support, fixation, alignment procedure and CNC software resulted in better agreement for the final mould (Fig. 2, below). Finally, the mould was coated with HOPG crystals of several microlayers up to 0.2 mm total thickness (Fig. 3). The overall offset of 0.2 mm can be adjusted by positioning at the beam line, whereas the offset of steps 2 and 3 (cf. Figs. 1 and 2) was compensated by 0.07 mm increase of HOPG thickness. Since the small steps (2 - 6, Fig. 1) didn't show stable adherence, a minimum amount of glue had to be used.

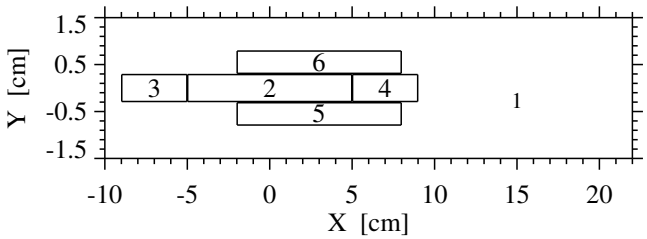

Fig. 1 *Geometry of the stepped monochromator design.*

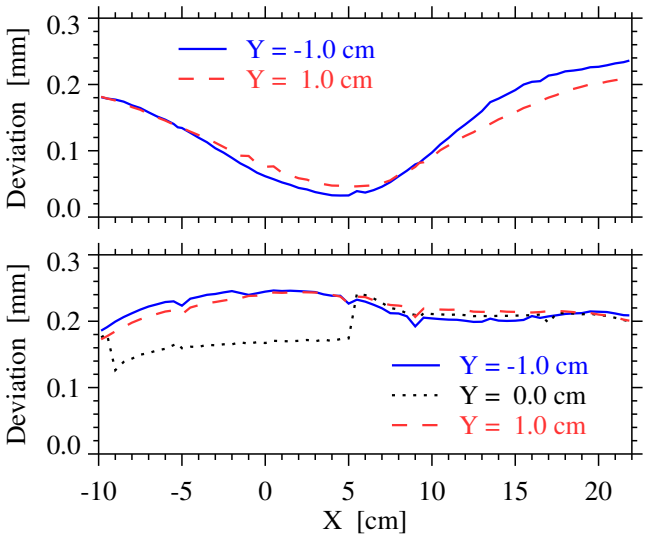

Fig. 2 *Difference between measured and nominal height value of curvature for the test sample of step 1 (above) and final mould (below), respectively.*

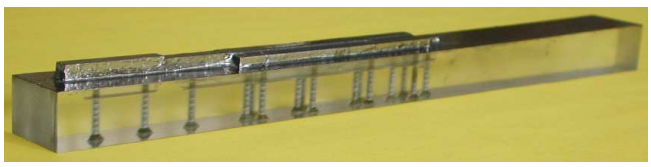

Fig. 3 *Photo of the final monochromator.*

[1] W. Neubert et al., FZ Rossendorf, Wiss.-Tech. Ber. FZR-319 (2001) 41
[2] J. Pawelke et al., FZ Rossendorf, Wiss.-Tech. Ber. FZR-341 (2002) 91

[1] *Kunststofftechnik GmbH, Dresden*

The Influence of Electron Scattering in the Target on the Beam Transmission

H. Müller, W. Neubert, U. Lehnert[1]

The interaction of the electron beam with targets increases the divergence and leads to collisions with the beamline materials producing bremsstrahlung and, to a lower extend, neutrons. According to the demands of radiation protection in the radiation physics cave such beam loss must be less than 5 μA at ELBE. The intended irradiation of cell cultures with quasi-monochromatic channeling radiation requires also a very low background level. These requirements can be fulfilled only by an optimized beam transport to the beam dump. Since beam transport codes usually do not take into account interactions with target materials specific simulations with other transport codes like GEANT become necessary. In our calculations we defined the transmission as the ratio of the number of electrons at the exit of the bending magnet or at the entry of the beam dump, respectively, to the number of electrons started in front of the target. Earlier simulations carried out with GEANT 3.21 [1] have shown that the original beamline design [2] had to be upgrated with an increased beam tube 66 mm in diameter connecting goniometer chamber and bending magnet. Further, an increase of the gap of the original 45° bending magnet to 90 mm was necesssary. Simulations carried out with targets of carbon (35 and 100 μm thick, with the density of diamond) showed that the above requirements can be fulfilled for this new design for beam energies above 15 MeV only. But the limited power of the dipole magnet allows at 90 mm gap and higher electron energies only deflections less than 45°. Therefore, the new vacuum chamber was designed for the bending angle of 35°.

The complete upgrated beamline with the 35° bending magnet and the beam tubes to the beam dump [4] with additional quadrupol lenses has been implemented into a geometry file for GEANT 4. Instead of the constant magnetic field in the GEANT 3.21 simulations the complete magnetic field chards [2] have been used in the GEANT 4 version. Fig. 1 shows the results of these simulations with incident energies from 5 MeV to 40 MeV. In Table 1 we summarize and compare the results obtained by GEANT 3.21 and GEANT 4.4.1 behind the beam bending magnet. Both code versions show a reasonable agreement at the reference energy of 20 MeV. Slight differences in Table 1 are due to different bending angles and the treatment of the magnetic field. There are considerable differences at lower energies between GEANT 3 and 4 results but both simulations show that beam losses will limit the available beam current, especially at electron energies below 20 MeV.

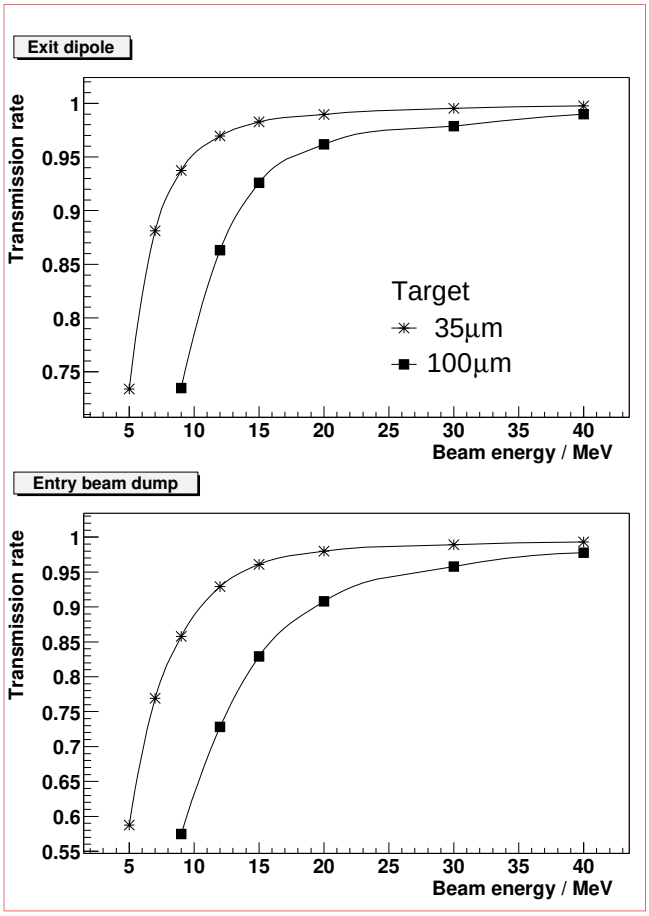

Fig. 1 *Transmission rate for the exit of the dipole (upper panel) and the entry of the beam dump (lower panel) as function of the electron energy obtained from GEANT 4.4.1 simulations.*

Table 1 *Transmission rates for the exit of the dipole magnet calculated by GEANT 4.4 (g4) and GEANT 3.21 (g3). 35 deg bending in g 4 ; 45 deg. bending in g 3.*

GEANT version	g4	g3	g4	g3
d_{target}/μ	35	35	100	100
E_e=7 MeV	0.88	0.76	0.60	0.55
E_e=9 MeV	0.94	0.86	0.73	0.70
E_e=12 MeV	0.97	0.94	0.87	0.86
E_e=15 MeV	0.98	0.97	0.93	0.92
E_e=20 MeV	0.99	0.99	0.96	0.97
E_e=40 MeV	1.00	-	0.99	-

[1] W. Neubert, W. Enghardt, U. Lehnert, E. Müller, B. Naumann, A. Panteleeva, J. Pawelke, Proceedings Monte Carlo 2000 Conference, Lisbon, 23–26 Oct. 2000, p. 123

[2] U. Lehnert, FZ Rossendorf, Wiss.-Tech. Ber. FZR-319 (2001) 18-19

[3] B. Naumann, Berechnung des Strahlungsuntergrundes in der Umgebung der Strahlfänger an der Strahlungsquelle ELBE, Wiss.-Tech. Ber. FZR-345 (2001)

[1] *FZR, Radiation Source ELBE*

Background at the Radiation Physics Beam Line

H. Müller, W. Enghardt

One area of research at the new ELBE facility at the FZR will be devoted to radiobiological experiments with quasimonochromatic X-rays, which are produced by channeling the electrons from the accelerator in crystalline targets. The interaction of the electrons with the target increases the divergence of the electron beam. This enlarges the number of collisions with the beam line materials producing bremsstrahlung and, at sufficiently high energies, also neutrons.

For carrying out experiments with photons the electron beam has to be separated from the X-rays produced in forward direction. This is performed by means of a dipole magnet. Its field map has been calculated [1] using the code Poisson [2]. In order to minimize the background arising from electrons hitting the beam line two quadrupoles are arranged behind the dipole to focus the electron beam on the beam dump. For the correct understanding of the main background sources a Monte-Carlo simulation of the whole beam line starting from the channeling target up to the beam dump is carried out on the basis of the code GEANT4 [2]. The beam profile after the dipole for a point-like electron beam of 50 MeV impinging on a 100 μm thick diamond target is shown in the left panel of Fig. 1. In the right panel the focusing effect of the two quadrupoles is demonstrated. At the entry of the beam dump the beam is much narrower than at the exit of the dipole.

Fig. 2 shows the radial dependence of the flux of particles backscattered by the beam dump in the upper panel, while the lower panel shows the energy spectra. Compared to earlier calculations [4] where a beam diameter of 8 cm was assumed the present calculations yield a reduced background. This can be understood by the smaller beam diameter. The majority of electrons hits the dump material in a larger distance from the entry due to the cone-like opening of the beam dump (see [4]).

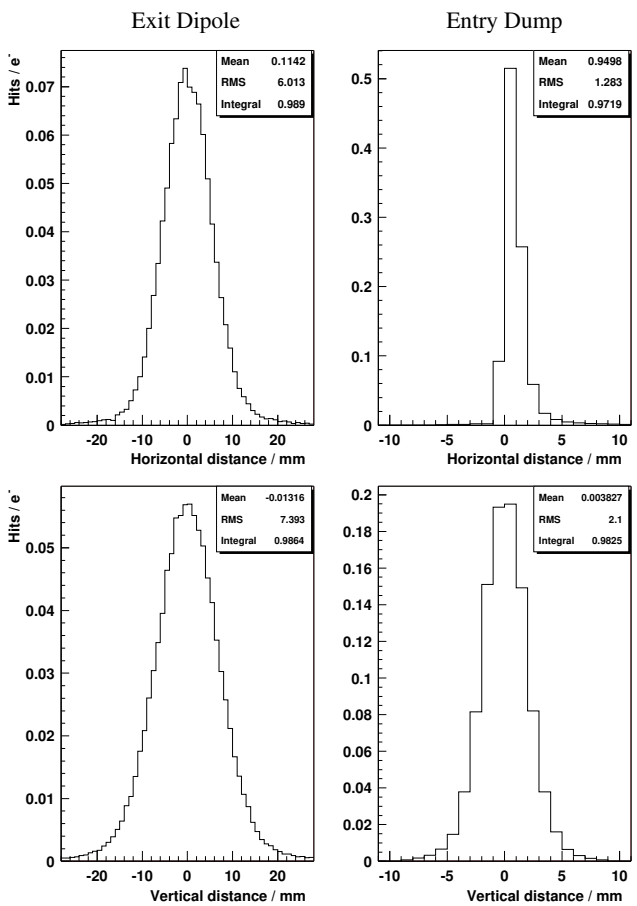

Fig. 1 *Profile of a 50 MeV electron beam in horizontal (upper panel) and vertical (lower panel) direction at the exit of the dipole (left panel) and the entry of the beam dump (right panel).*

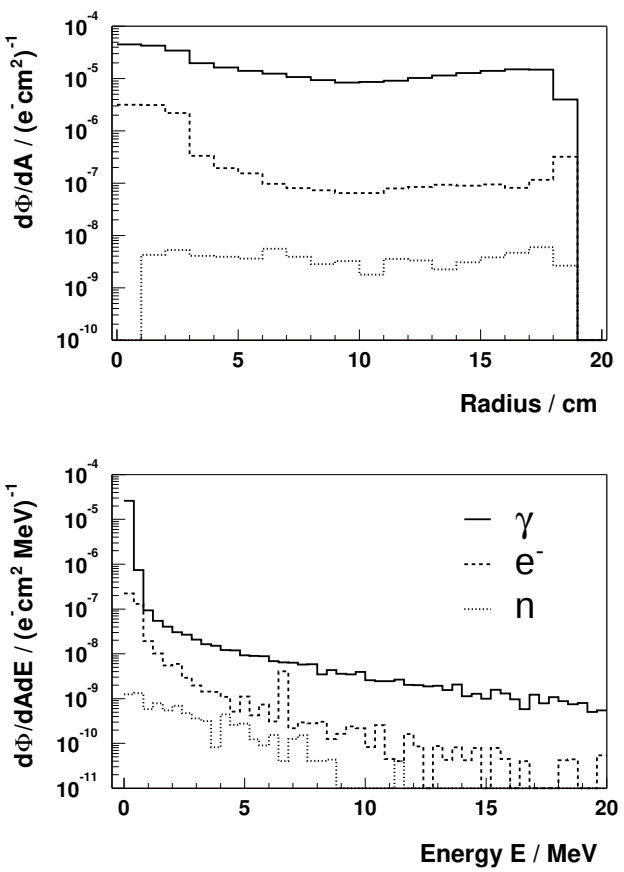

Fig. 2 *Radial flux of background particles escaping the beam dump in backward direction as function of the radius (upper panel) and the corresponding energy dependence averaged over the whole area (lower panel).*

[1] U. Lehnert, private communication
[2] J.H. Billen, LA-UR-06-1834, Los Alamos (1998)
[3] http://wwwinfo.cern.ch/asd/geant4/geant4.html
[4] B. Naumann, Berechnung des Strahlungsuntergrundes in der Umgebung der Strahlfänger an der Strahlungsquelle ELBE, Wiss.-Tech. Ber. FZR-345 (2001)

Shielding Calculations for an X-Ray Laboratory

U. Reichelt, J. Henniger[1], W. Neubert, J. Pawelke

In preparation of projected experiments with X-rays at the ELBE facility of the FZR, it is intended to build up an appropriate laboratory. For dimensioning the radiation shielding a transport simulation had to be done.
The X-ray tube ISOVOLT 320/13 made by Agfa NDT Pantak Seifert will be used as source. The maximal tube voltage is 320 kV and the maximum anode current is 13 mA [1]. The exit window collimates the photons to a cone with 20 degrees opening angle. The laboratory will be installed in the ELBE experimental hall. The outline is shown in Fig. 1. Two of its walls consist of heavy concrete. They are at least two meters thick. The other walls are made of 2.8 or 10 cm thick lead panels. The positioning of the horizontal emitting source assures that the hole radiation cone impinges at the left concrete wall. Thus no unscattered photons will leave the cave through the top.

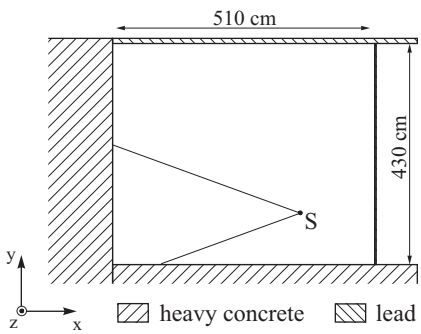

Fig. 1 *Topview of the cave, position of x-ray tube 'S' and its radiation cone*

The calculations can be devided into two parts. First the X-ray spectrum was determined by bombarding a tungsten target with 320 keV electrons. The spectrum of bremstrahlung photons emitted inside the radiation cone was calculated by means of Geant3. Its results were the source term of the second simulation part, where photon transport was performed with the Monte Carlo code AMOS [2], developed at the TU Dresden. This program is implemented on a straight probabilistic base. All cross section functions are represented by cumulated probability density functions (cpdf). Therefore 10^8 particle histories could be simulated and results of low statistical error were achieved with a normal effort of computing power. The conversion factors from ICRP 51 [3] were used to transform the spectral photon flux density to effective equivalent dose rate. For this purpose frontal irradiation was conservatively assumed.
A first simulation was done without shielding the ceiling of the laboratory. The dose distribution at a height of 2.80 meters shows a maximum of 103 mSv/h (Fig. 2), what exceeds the allowed limit by several orders of magnitude. Therefore a ceiling of 1cm lead was added in a second simulation. Because of large incident angles and low energy values of backscattered photons, no transmission was determined behind all lead shieldings with the exception of areas, where the lead shieldings are mounted to the concrete walls. The larger mean free path in concrete results in backscattered photons, which bypass the lead shielding. This fact explains the detected dose rates along all edges of lead to concrete what is shown in Fig. 3.
The physical problem, wich difficulty is in its large dimension, could be solved with the used Monte Carlo code. The results evince that one centimeter lead for the ceiling will be enough to allow the access also during experiments. Additional small shieldings along the edges should be installed.

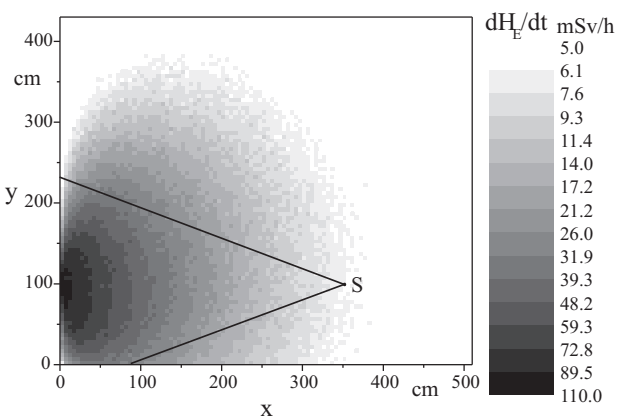

Fig. 2 *Dose rate distribution at the unshielded ceiling (height 2.80 m; at: 320 kV, 13 mA)*

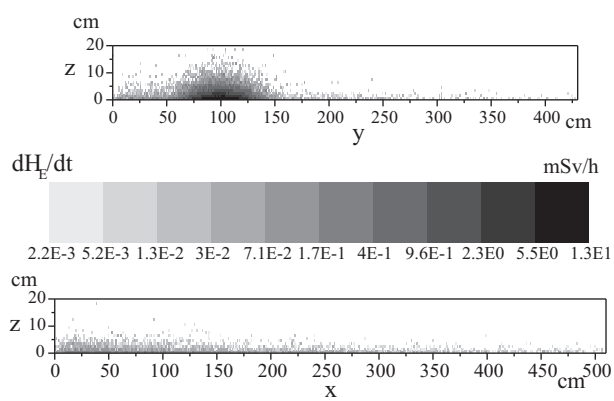

Fig. 3 *Dose rate distribution at the sides of the 1 cm lead shielded ceiling along the left (upper graph) and lower (lower graph) concrete wall of Fig. 1*

[1] Bedienungsanleitung ISOVOLT 160/225/320/450HS, Agfa NDT Pantak Seifert, 2002
[2] J. Henniger, AMOS - ein multivalent nutzbares Programmsystem zur Berechnung von Strahlungstransportproblemen, Strahlenschutz: Physik und Messtechnik, Band 1, Verlag TÜV Rheinland, S.145-150, 1994
[3] ICRP 51, Data for Use in Protection Against External Radiation, Annals of the ICRP, Vol.17, No.2/3, 1987

[1] *Institute for Radiation Protection Physics, TU Dresden*

Comparison of Bremsstrahlung Distributions with Results from Monte-Carlo Codes

W. Neubert, H. Müller

Bremsstrahlung is frequently an undesired background in many applications at electron accelerators. One way to identify the sources of bremsstrahlung and to minimize this disturbance are proper simulations with electro-magnetic transport codes which take into account the setup geometry.

Here we analyze the reliability of two Monte-Carlo codes by comparison of simulation results with experimental data. In ref. [1] double differential bremsstrahlung distributions at $\Theta = 0^o$ and 0.62^o with respect to the electron beam with kinetic energies of 2.72, 4.54 and 9.66 MeV were obtained from thin targets of Be, Al and Au. We chose the data set for 9.66 MeV because this energy is close to the energy now available at the accelerator ELBE. The simulations were performed for the solid angle acceptance determined by the experimental setup in ref. [1].

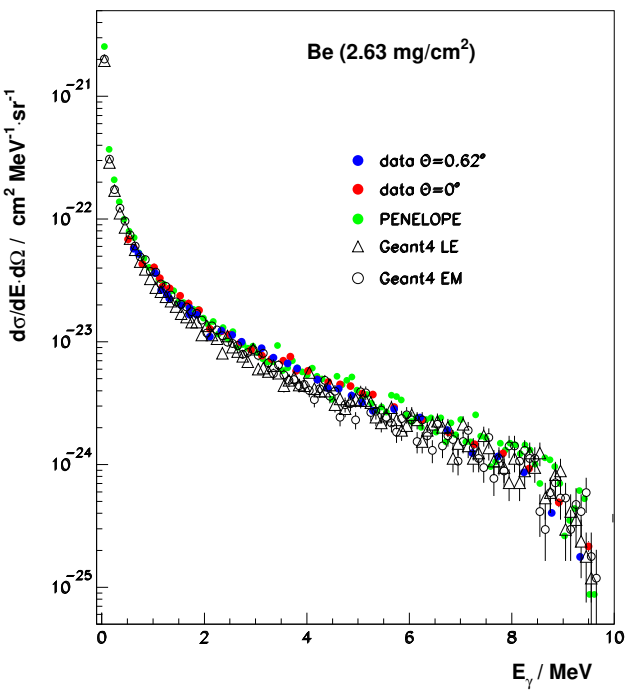

Fig. 1 *Experimental and simulated bremsstrahlungs distribution induced by 9.66 MeV electron on Berylliums.*

Overall, the agreement between the experimental data and the simulation results obtained with PENELOPE (version 2001) is excellent within the error bars. Simulations with GEANT 4 (version 5.0) [2] were performed for both the low-energy (LE) and for the standard electromagnetic versions (EM). Both results are also in good agreement both with that from PENELOPE and with the experimental data. We mention that the former discrepancies between the experimental data of aluminium and the corresponding simulations with the low-energy version of GEANT 4.4.1 [4] are not observed with the latest release 5.0 of GEANT 4.

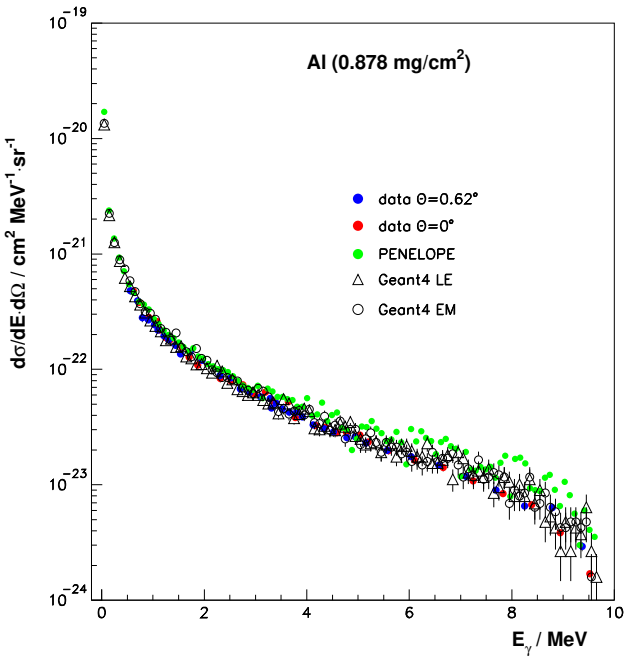

Fig. 2 *The same for Aluminium.*

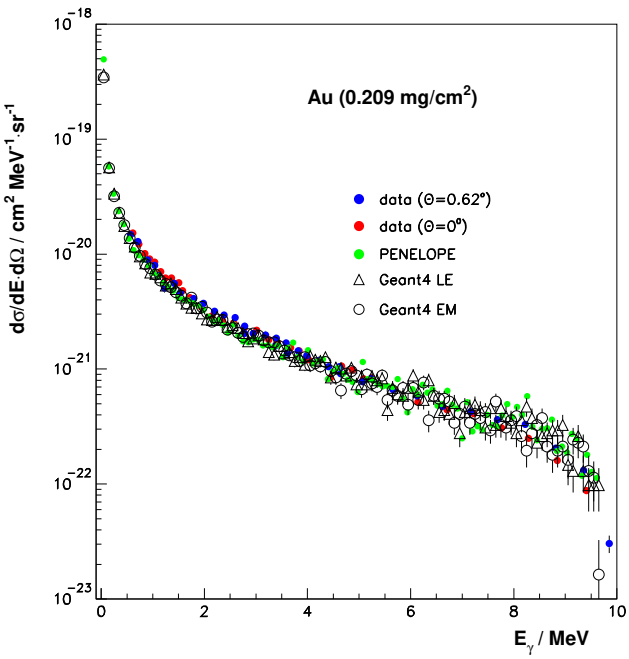

Fig. 3 *The same for Gold.*

[1] N. Starfelt and H.W. Koch, Phys. Rev. 102 (1956) 1598
[2] http://wwwinfo.cern.ch/asd/geant4/geant4.html
[3] F. Salvat et al., PENELOPE, A code System for Monte Carlo Simulations of Electron and Photon Transport, Workshop Proceedings Issy-Ies-Moulineaux, France, 5-7 Nov. 2001, Data Bank OECD, Nuclear Energy Agency
[4] W. Neubert, talk at the MCNEG user meeting, Stoke-on-Trent, England, April 22-23, 2002

Calculation of Photon-Induced Auger Transitions in Tc and Re

W. Neubert, W. Enghardt

The code package PENELOPE [1] allows to simulate the atomic relaxation process of singly ionized atoms with an initial vacancy in the K or L subshells for atoms from Z = 6 to Z = 92. The necessary transition probabilities for the simulation of radiative and non-radiative transitions are taken from the EADL data base [4] with the adoption of experimetal X-ray energies from ref. [3].

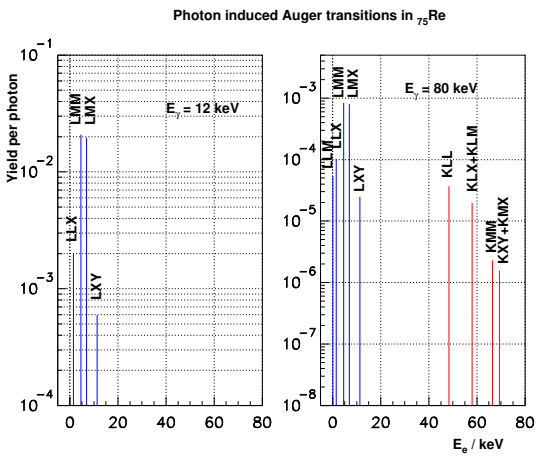

Fig. 1 *Auger electron spectra calculated for photon energies below (left panel) and above (rigth panel) the K-absorption edge of Rhenium.*

The photoelectric absorption in a given medium is simulated by means of the corresponding cross sections which determine the shell that has been ionized. The program was modified such that only the interaction events with non-radiative transitions were registered. This allows to survey the Auger electron spectra within the complex electron emission like photoelectrons and electrons from the Compton scattering. Special flags were set to proceed certain Auger cascades after photoabsorption using a special label code, see [1]. Here we show the emission spectra of Tc and Re. Both elements are of special interest as constituents of metallo-organic compounds which can be attached closely to the DNA. Table 1 shows a comparison of transition energies in Tc. The results obtained with PENELOPE are in good agreement with that from refs. [4, 2]. There are only small differences for transitions like LMX, LXY and LLX where the X and Y contributions are not well defined. The deterministic [4] and the MC calculations [2] assume vacancy production accompanied by the radioactive decay of ^{99m}Tc whereas PENELOPE assumes randomly distributed single vacancies in the K and L subshells. Auger electron spectra of Rhenium induced by two fixed photon energies are shown in fig. 2. The excitation function of transitions related to initial vacancies in the L subshells show that their yield follow closely the energy dependence of the photo-absorption coefficients.

Table 1 *Energies of Auger transitions in Technetium. The first column gives the Auger process, where the first letter denotes the shell with the vacancy before the Auger transition, the second and third letters indicate where the new vacancies are created, where X or Y denote shells above the specified ones.*

Transition type	Energy PENELOPE	Energy Stepanek [4]	Energy Howell [2]
KLL	15.4 keV	15.4 keV	15.3 keV
KLX	17.8 keV	17.8 keV	17.8 keV
KXY	20.3 keV	20.2 keV	
LMM	2.06 keV	2.06 keV	2.05 keV
LMX	2.41 keV	2.33 keV	2.32 keV
LXY	2.76 keV	2.64 keV	2.66 keV
LLX	146.0 eV	106.0 eV	

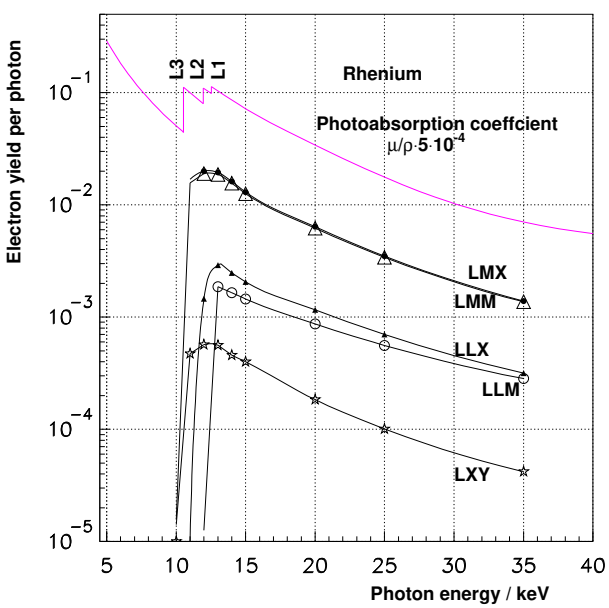

Fig. 2 *Excitation function of transitions related to L subshell vacancies. The photon energies are larger than the L_3 absorption edge.*

[1] F. Salvat et al., PENELOPE, A code System for Monte Carlo Simulations of Electron and Photon Transport, Workshop Proceedings Issy-Ies-Moulineaux, France, 5 - 7 Nov. 2001, Data Bank OECD, Nuclear Energy Agency

[2] S.T. Perkins et al., Tables and graphs of atomic subshell and relaxation data from LLNL evaluated atomic data library, Vol. 30, UCRL-50400 (Livermore, CA, 1991)

[3] J.A. Bearden and A.F. Burr, Rev. Mod. Phys. 39 (1967) 125

[4] J. Stepanek, Med. Phys. 27 (2000) 1544

[5] R.W. Howell, Med. Phys. 19 (1992) 1371

Auger Electron Emission in Tc: Photon Induced versus Radioactive Decay

W. Neubert, W. Enghardt

The method described in [1] allows Auger electron spectra for monoenergetic photons to be calculated. Here we consider the more realistic case of a complex X-ray spectrum delivered by the commercial X-ray tube ISOVOLT/320-2. The emission spectrum was simulated by GEANT 3.21 for 320 keV electron impact on a tungsten anode and for an emission angle of 40°. The obtained spectrum in Fig. 1 shows the prominent K_α and K_β lines of tungsten located on the continous bremsstrahlung background. The reliability of this calculation was verified by the good agreement of the measured X-ray spectrum with the corresponding simulation for 100 keV.

The intense characteristic X-rays of tungsten are far above the K-absorption edges of Tc so that vacancies in both the K and L subshells can be created. Auger cascades induced by this X-ray spectrum were calculated for fixed energies in steps of 7 keV, weigthed by the corresponding X-ray yields from Fig. 1 and then they were summed up. This spectrum of Auger transitions obtained without consideration of the electron propagation in the thin slab of Tc (0.1 μm) is shown in Fig. 2. In this figure the intensities are compared with the results for the radioactice decay of ^{99m}Tc taken from ref. [3]. These deterministic calculations utilize the same data base EADL [4] which is implemented in the Monte-Carlo code PENELOPE. The relative intensities of Auger transitions related to initial vacancies in the K and L subshells are similar. But the absolute intensities for the external irradiation of any isotope of Tc by X-rays are about two orders of magnitude less compared with those from the radioactive decay although the relevant photon energies are comparable, i. e. 142.7 keV of the isomeric M4 transition in ^{99m}Tc. If any isotope of Tc is attached to biological structures of interest and K- and L-shell Auger cascades are induced by external photon irradiation then the yield of these Auger electrons per photon is essential lower compared with the case that it is replaced by the radioactive ^{99m}Tc.

The expected enhancement of the RBE of photons by suitable atoms becomes ineffective due to the reduction via the photoabsorption cross sections. The higher the photon energy the lower the Auger electron yields. Since the yield of Auger cascades is strongly coupled to the photoabsorption coefficients, the most promising scenario for the increase of the RBE of photons are photon energies around the L absorption edges which can produce vacancies both in the M- and in the higher subshells followed by Auger cascades of very low energy.

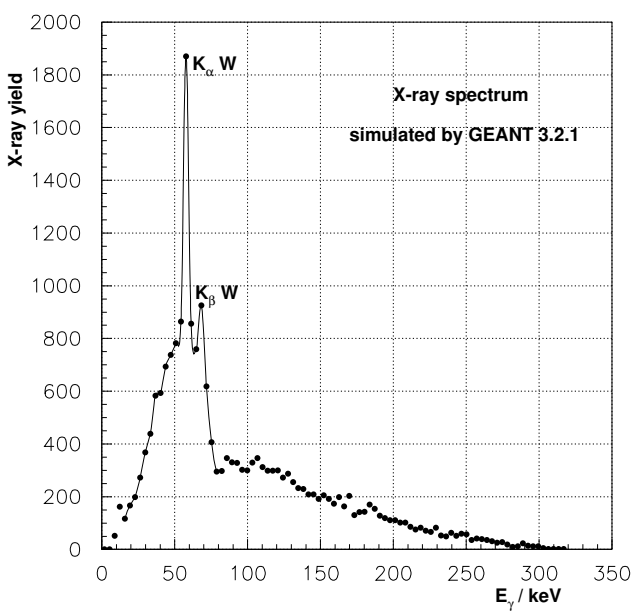

Fig. 1 *Simulated emission spectrum of a X-ray tube.*

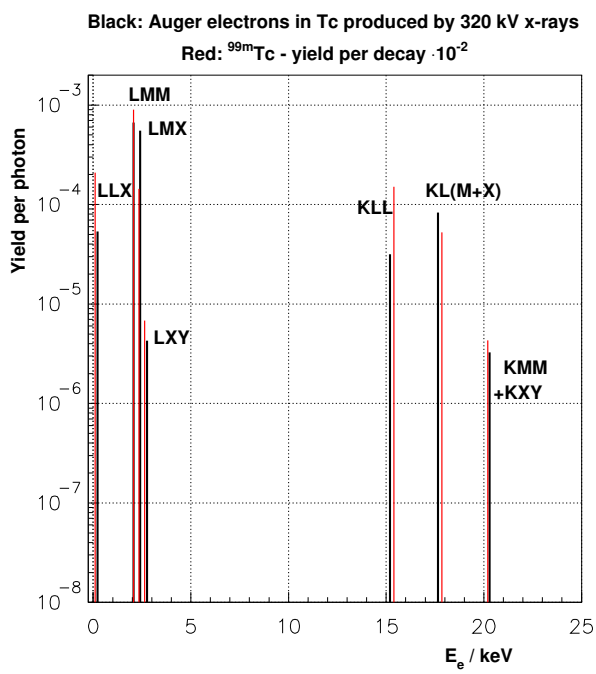

Fig. 2 *Comparison of the photon-induced Auger transitions in Tc with those from the radioactive decay of ^{99m}Tc.*

[1] W. Neubert et al., This Report, p. 73

[2] F. Salvat et al., PENELOPE, A code System for Monte Carlo Simulations of Electron and Photon Transport, Workshop Proceedings Issy-Ies-Moulineaux, France, 5-7 Nov.2001, Data Bank OECD, Nuclear Energy Agency

[3] J. Stepanek et al., Acta Oncologica 35 (1996) 863

[4] S.T. Perkins et al., Tables and graphs of atomic subshell and relaxation data from LLNL evaluated atomic data library, Vol. 30, UCRL-50400 (Livermore, CA, 1991)

Dose Distributions of Photon-Induced Secondary Electrons in Tc

W. Neubert, W. Enghardt

The code package PENELOPE [1] is to our knowledge the only tool which allows to propagate electrons with energies down to 100 eV in arbitrary media. MCNP4 and EGS4nrc are restricted to about 1 keV. This low tracking threshold allows to investigate the complex atomic relaxation process following single vacancies in the K and L subshells. We chose Technetium which is characterized by a balanced competition between radiative and non-radiative transitions. Moreover, Tc is of biochemical interest because it can be inserted into special organic compounds.

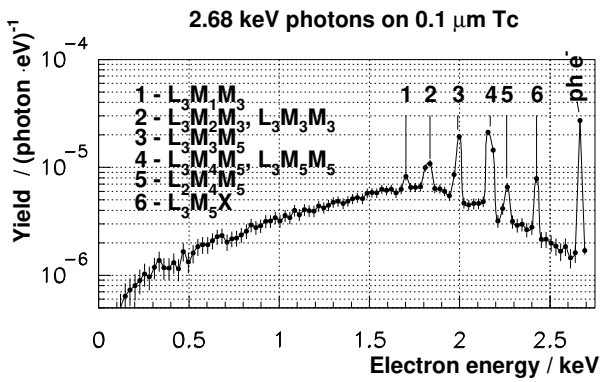

Fig. 1 *Simulated Auger electron spectrum induced by photons equal to the L_3 absorption energy.*

Fig. 1 shows the simulated spectrum of secondary electrons produced in a thin layer of Tc irradiated by photons. This figure demonstrates the increasing complexity of the spectrum. Photons with an energy equal to the L_3 absorption edge produce a proper Auger electron spectrum with a single contribution of photoelectrons. A slight increase of the photon energy above the L_1 absorption energy leads to further disturbing contributions of L-shell photoelectrons and of such ones produced by a secondary process, i.e. by the $L_{\alpha,\beta}$ radiative transitions, both placed on a complex distribution of backscattered electrons.

In order to calculate the corresponding dose distributions we chose a cylindrical water phantom (10 μm thick). First of all we assumed a direct impact of 2.05 keV electrons which corresponds to the average energy of the LMM Auger transition type in Tc [2]. Such electrons provide a high local energy deposition of about 10^8 eV/cm $\cdot$ e$^-$ within a slab thickness ≤ 0.5 μm. Then the phantom was covered by 0.1 μm Tc in order to simulate the energy deposition by primary photons and induced Auger transitions. The assigment of low-energy LMM/LMX Auger transitions was performed by means of the label code [1] which allows also to score the corresponding dose distributions. As shown in fig. 2 the tail of this distribution corresponds to the known range of these electrons in water [2]. But the maximum dose released by photon induced Auger electrons is about two orders of magnitude less compared with those from the direct impact of equivalent electrons. A similar behaviour was found for the KLL Auger transition of an average energy of 15.3 keV. An insignificant enhancement of the dose with respect to that from the primary photons was found only within some sub-μm on the front side of the phantom.

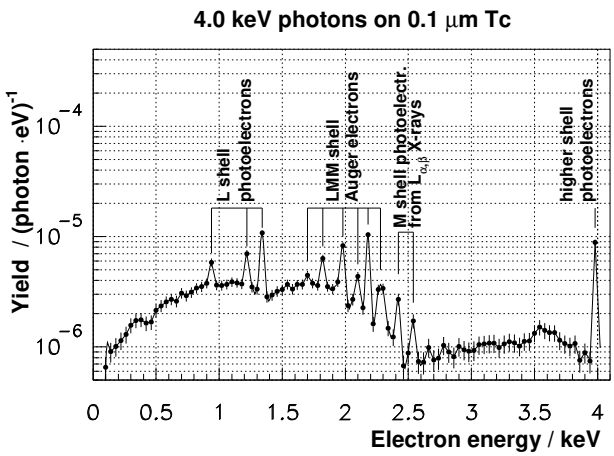

Fig. 2 *The same as fig. 1 but for 4 keV incident photons.*

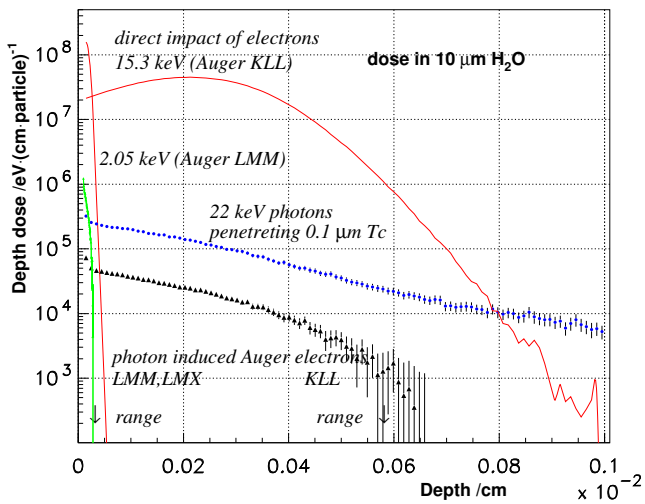

Fig. 3 *Comparison of depth dose distributions of selected Auger transitions (direct impact and photon induced).*

[1] F. Salvat et al., PENELOPE, A code System for Monte Carlo Simulations of Electron and Photon Transport, Workshop Proceedings Issy-Ies-Moulineaux, France, 5-7 Nov.2001, Data Bank OECD, Nuclear Energy Agency

[2] R.W. Howell, Med. Phys. 19 (1992) 1371

Scatter Correction for In-Beam PET Monitoring of Heavy Ion Therapy [G]

F. Pönisch, W. Enghardt

The process of scattering of the annihilation gamma quanta reduces the quality of PET images. About 30 % of the true coincidences registered during *in situ* PET monitoring of head and neck carbon ion tumour irradiations are influenced by Compton or Rayleigh scattering. These physical processes may deteriorate the correspondence between the source and the reconstructed radioactivity distribution especially in highly inhomogeneous regions of the human body like the head and neck. Therefore, an attenuation and scatter correction algorithm is necessary for quantitative PET imaging [1]. This algorithm has been successfully applied for the reconstruction of PET data sets generated by means of Monte Carlo methods and obtained from measurements during phantom experiments [1]. In 2002 the feasibility of the iterative scatter correction algorithm has been demonstrated for the reconstruction of measured as well as model-based calculated patient listmode data.

The scatter correction algorithm requires the knowledge of the density information within and nearby the positron camera field of view. This is derived from the X-ray computed tomograms (CT) of the patient (taken for treatment planning purpose) and the head rest CT [2]. This attenuation map is the basis of the calculation of the attenuation correction factors along each line of response (LOR). The number of events measured for each LOR are corrected for the individual detector efficiency and the length of the emission line within the image space. Additionally, random events are subtracted from prompt events. The classical Maximum Likelihood Expectation Maximization algorithm of Shepp and Vardi [3] estimates the expectation step by computing the ray sums in each projection. We modified this procedure by applying the attenuation correction factors to the forward projection and adding furthermore, the scattered components. The latter is calculated according to the approximation of Watson [4], the Single Scatter Simulation (SSS). The SSS algorithm neglects multiple scatter, calculates the scatter contribution to a certain LOR for a finite number of discrete points of the scatter volume only and does not take into account the efficiencies of the individual crystals. Therefore, the total number of scattered events obtained from the calculation has to be normalised to the number of acquired coincidences. For this purpose, we calculate the global scatter fraction (SF) by means of an additional Monte Carlo (MC) simulation. The simulation uses the activity distribution of the previous iteration step and the information of the attenuation map. The MC code has been optimised for accuracy and execution time. The number of histories has been chosen that the statistical error in the calculated SF is less than 0.3 %. The scatter correction reconstruction algorithm is rather complex and demands high computational effort, but it has the advantage that no assumption of the shape of the activity and scatter distribution is made.

The reliability of the proposed algorithm for the particular application in limited angle PET has been shown for patient data. Figure 1 shows evident improvements in the reconstructed PET image. Scatter correction drastically reduces the spurious activity occurring laterally to the beam path as it is revealed by comparing the images of figure 1. Furthermore, the shape of the contour lines in the central part of the image is nearly identical. That means, that the scatter correction algorithm eliminates the Compton scattering in the image and preserves the true β^+-activity distribution.

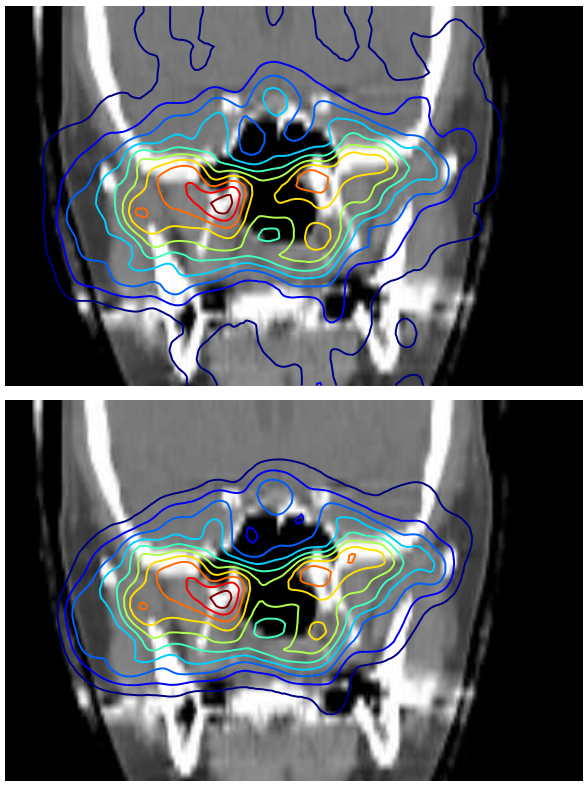

Fig. 1 *Frontal slice of the head CT of a patient (grey scaled in the background). Comparison of the measured PET activity distributions for a beam portal that is typical for treating skull base tumours. The beam enters the patient from the right side (left on the figures). The β^+-activity are reconstructed with attenuation correction (top), with attenuation and scatter correction (bottom).*

[1] F. Pönisch and W. Enghardt, FZ Rossendorf, Wiss.-Tech. Ber. FZR-341 (2002) 99
[2] F. Pönisch et al., FZ Rossendorf, Wiss.-Tech. Ber. FZR-319 (2001) 95
[3] L.A. Shepp, Y. Vardi, IEEE Trans. Med. Imag. MI-1 (1982) 113
[4] C.C. Watson et al., in Three-Dimensional Image Reconstruction in Radiation and Nuclear Medicine (1996) 255-268

The Time Dependence of the γ-Ray Intensity Seen by an In-Beam PET Monitor [E,G]

K. Parodi, P. Crespo, W. Enghardt, T. Haberer[1], J. Pawelke, D. Schardt[1]

The design study of the new generation in-beam PET scanner to be developed and installed at the dedicated ion beam tumour therapy facility of Heidelberg, Germany [1], demands a deep understanding of physical processes affecting in-beam PET acquisition. The current experience in the monitoring of carbon ion therapy at GSI Darmstadt shows that techniques well established in radiotracer imaging may fail in the non-conventional case of in-beam PET therapy monitoring. In fact the data acquired by the in-beam positron camera during particle extraction (spill) from the GSI synchrotron are corrupted by a high noise level. They are therefore discarded for tomographic reconstruction. Previous investigations have suggested the reason of high noise to be random concidences not properly corrected for during beam extraction. The standard random correction technique implemented by the manufacturer of our PET data acquisition system (CTI PET Systems, Knoxville, TN, USA) is based on subtraction of delayed (by 128 ns) from prompt coincidences. The failure of the correction during particle extraction is thought to be due to a non-stationary (in the sub-μs scale) γ-background originating from nuclear reactions induced by the beam and hence following the time microstructure of the carbon ions [2]. The time dependence may result in a reduction of delayed coincidences affecting the proper correction for the random coincidences detected in the prompt window. This conjecture has been supported by previous in-spill measurements of time correlation between the γ-rays produced in ^{12}C irradiation of organic matter and the synchrotron radiofrequency (RF) using a GSO scintillating crystal (2 cm radius and 2.5 cm thickness) coupled to a fast PMT [3]. In the presented experiment an improved electronics was set-up in order to add photon energy discrimination to the time information. A further record of the spill number was introduced in order to perform dynamic acquisition and establish the relationship between the single photons detected by the GSO crystal and the coincidences simultaneously recorded by the positron camera during particle extraction. The same experimental configuration of [3] was chosen. Monoenergetic carbon ion beams (energy: $88.83 - 426.11\,A$MeV, intensity: $1{\cdot}10^8 - 4{\cdot}10^6$ ions per 2 s spill) were completely stopped in blocks of PMMA ($C_5H_8O_2$) placed at the isocentre of the treatment unit in the middle of the positron camera field of view. The GSO detector was set perpendicular to the beam at the same distance (41 cm) as the positron camera heads from the isocentre. The experiment confirmed a time correlation of the γ-background seen by the in-beam PET scanner with the RF signal (Fig. 1) and hence with the previously measured ion beam microstructure [2]. The physical interpretation of the time distribution has been already discussed in [3]. The data analysis has addressed the comparison between (*i*) the calculated prompt and delayed coincidence rate induced by single γ-rays modulated in time according to the GSO data and (*ii*) the "beam-induced" (i.e. not related to β^+-activity) prompt and delayed rate extrapolated from the measured PET data. The rather good agreement (Fig. 1, right) supports the explanation of random correction failure due to a γ-background correlated in time with the beam microstructure. A more detailed analysis will be reported soon in a forthcoming paper. This work will be the basis for a new data acquisition concept for in-beam PET.

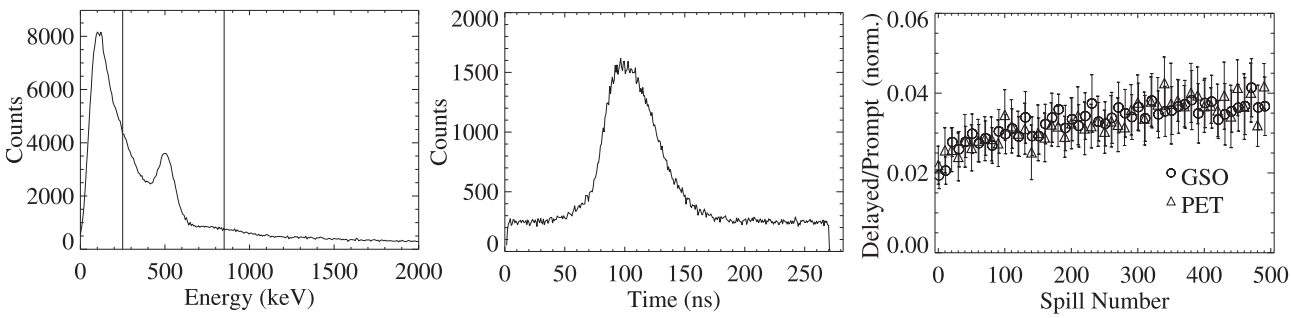

Fig. 1 *Energy (left) and γ-RF time (middle) spectrum detected by the GSO crystal during 500 spills of ^{12}C irradiation at 280.48 AMeV energy (RF period of 282.4 ns) and $8.5{\cdot}10^6$ ions/spill intensity. Only the time distribution of photons with energy in the marked $250-850$ keV window accepted by the positron camera is shown. Right: Ratio of the "beam-induced" delayed and prompt coincidence rate deduced from the GSO and PET data in dependence of the extracted spill. The delayed to prompt ratio from the GSO data was normalised to the average delayed to prompt ratio extracted from the PET data.*

[1] K. D. Gross and M. Pavlovic (eds), Proposal for a dedicated ion beam facility for cancer therapy, GSI Darmstadt, 1998
[2] K. Parodi et al., FZ Rossendorf, Wiss.-Tech. Ber. FZR-319 (2001) 97
[3] K. Parodi et al., FZ Rossendorf, Wiss.-Tech. Ber. FZR-341 (2002) 103

[1] *Gesellschaft für Schwerionenforschung Darmstadt*

The Quantification of the Mechanical Deformation of the Rotating Double Head PET Scanner at the ^{12}C Ion Therapy Facility at GSI Darmstadt [B,G]

F. Fiedler, M. Sobiella, W. Enghardt, F. Mönsters[1]

For treating patients in a sitting position at the horizontal beam of the ion therapy facility at GSI Darmstadt a dedicated patient chair has been installed [1]. In order to monitor these irradiations by means of positron emission tomography (PET) the PET gantry has been completely rebuilt [2], which allows now the detector heads to be rotated around the beam axis. The two detector heads with a total mass of 120 kg are mounted on a turnable support. This leads to a deformation of the PET gantry dependent on the rotation angle. The deformation results in a displacement of the crystal positions in comparison to those, which are expected when assuming a rigid body rotation. Furthermore, it has to be supposed that the axis of rotation slightly deviates from the isocentre. Moreover, minor deviations in the parallelism between the axis of rotation and the appropriate axis of the treatment room coordinate system cannot be excluded. In order to obtain a spatially correct superposition of the in-situ PET measurement onto the planning X-ray computed tomograms, which is mandatory for a correct PET data evaluation, we present here a procedure for determining the crystal positions in dependence on the PET gantry angle.

The crystal positions are known in the room coordinate system at 0 deg. It is assumed that the detectors itself behave like rigid bodies during the rotation. Thus the tracking of at least three non-collinear points fixed on the heads during the rotation will give the necessary information to calculate the crystal positions for each angle. These measurements have been performed using a laser tracker.

For this on each head four reference points were defined by means of fastening sphere mounts, which magnetically fix the retroreflectors for laser tracking (fig. 1). The relative accuracy for tracking one point is ± 10 ppm. The measurement was proceeded in steps of 10 deg. Each position was measured twice, moving the gantry clockwise and anticlockwise. The accuracy of setting the angles was ± 0.01 deg, leading to absolute positioning accuracy of ± 0.07 mm according to the distance of the retroreflectors from the axis of about 400 mm.

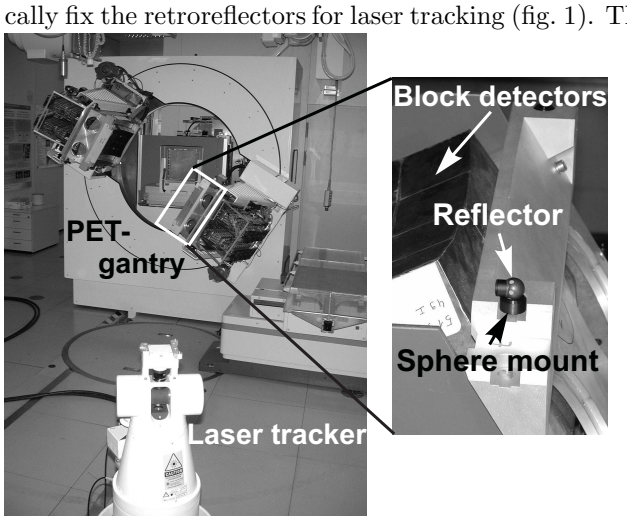

Fig. 1 *The measurement setup for quantifing the mechanical deformation of the PET gantry.*

The results depicted in fig. 2 clearly indicate that a considerable angle dependent deviation between the positions of the detector heads measured and those calculated under the assumption of an ideal rotation is observed. This requires an appropriate correction of the crystal coordinates within the tomographic reconstruction algorithm.

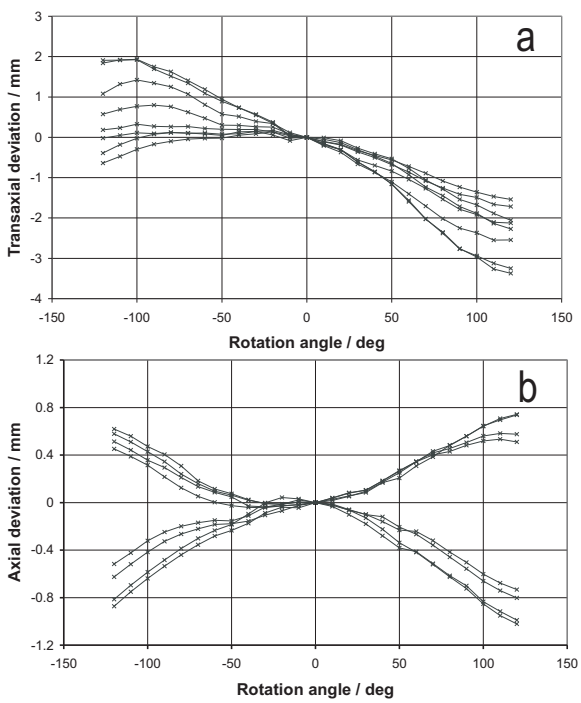

Fig. 2 *The measured deviations of the reference points mounted on the detector heads from the positions deduced from a rigid body rotation.*

a) Deviations within transaxial planes, i.e. perpendicular to the beam.

b) Deviations in axial direction, i.e. parallel to the beam direction.

By means of tracking the positon of four points for each detector head the intrinsic head deformation could be assessed. Maximum deformations along the edges and the diagonales of the detector heads of 0.08 mm and 0.27 mm, respectively, indicate that the influence of the intrinsic head deformation on the crystal positions can be neglected.

[1] P. Heeg et al., GSI, Scientific Report (2000-1) 167
[2] W. Enghardt et al., FZ Rossendorf, Wiss.-Tech. Ber. FZR-319 (2001) 93

[1] *sigma3D GmbH, Gladbeck*

Nuclear Reaction Cross Sections for the Assessment of Positron Emitter Generation by Therapeutic Irradiations with ^{4}He Beams [B, E, G]

F. Fiedler, K. Parodi, W. Enghardt

At the clincal ion therapy facility that will be installed at Heidelberg a variety of ion beams with atomic numbers $1 \leq Z \leq 8$ will be available. Irradiation quality assurance by means of positron emission tomography (PET) is based on the comparison of the β^+-activity distribution predicted from the treatment plan with that measured during the irradiation. Since the β^+-activity distributions strongly depend on the projectile the algorithms developed for carbon therapy [1] has to be extended to other ion beams. To predict the probability of positron emitter generation via nuclear fragmentation reactions, the cross sections for a variety of reaction channels have to be known. Unfortunately, with the exception of proton beams, there is a considerable lack of experimental data in the therapy relevant energy range. Therefore, experimental data have to be completed by model predictions. Here we report on ^{4}He beam induced nuclear reactions since a ^{4}He beam may be of considerable therapeutic interest. A ^{4}He beam has nearly the same radiobiological characteristics as a proton beam but it is superior to protons in respect of lateral scattering. To predict the partial cross sections for reactions with β^+-emitters in the exit channel the code of Silberberg and Tsao (Cross Section Code, [2]) has been applied. It is based on the model of Silberberg and Tsao [3]. This is a semiempirical cross section formula for proton-nucleus reactions. Furthermore the model considers special cases like α- and peripheral reactions. The used formula is:

$$\sigma = \sigma_0 f(A) f(E) e^{-P\Delta A} e^{(-R|Z-SA+TA^2|^\nu)} \Omega \eta \xi$$

where σ_0 is the normalisation factor for the cross section, $f(A), f(E)$ are correction factors for products from heavy targets with atomic number $Z_T > 30$, $exp(-P\Delta A)$ takes into account the difference of target and product mass, the factor $exp(-R|Z - SA + TA^2|^\nu)$ gives the statistical distribution of cross sections for the production of various isotopes of an element of atomic number Z in dependence on mass number A, Ω is a factor related to the nuclear structure, η is the nuclear pairing factor and ξ is a factor for light evaporation products. For nucleus-nucleus reactions a scaling was done according to [4] and [1]. The model reproduces the experimental values for light target nuclei as ^{12}C (fig. 1) and ^{16}O, as the main components in tissue in a satisfactory way (tab. 1). However, even heavier target nuclei, e.g. phosphorus and calcium as constituents of bone has to be taken into account.

In these cases, experimental data are not available and the model predictions have to be relied on (fig. 2).

Energy / AMeV	Target	Fragment	Experiment σ / mb	Absolute error / mb	Calculation σ / mb	Ref.
600	^{12}C	^{11}C	46.2	0.7	43.9	[5]
600	^{12}C	^{10}C	2.1	0.2	1.9	[5]
600	^{14}N	^{13}N	10.5	0.3	17.1	[5]
600	^{14}N	^{12}N	0.9	0.1	2.0	[5]
600	^{14}N	^{11}C	19.8	0.3	19.8	[5]
600	^{14}N	^{10}C	1.6	0.2	0.9	[5]
600	^{16}O	^{15}O	50.3	0.8	49.2	[5]
600	^{16}O	^{14}O	3.1	0.3	2.7	[5]
600	^{16}O	^{13}N	6.8	0.3	5.7	[5]
600	^{16}O	^{11}C	15.8	0.5	16.7	[5]
600	^{16}O	^{10}C	1.8	0.2	0.8	[5]
230	^{16}O	^{15}O	46.4	3.0	45.1	[6]
230	^{16}O	^{13}N	6.8	0.5	5.9	[6]
230	^{16}O	^{11}C	18.5	0.9	17.0	[6]
230	^{27}Al	^{18}F	12.5	0.5	9.7	[6]
95	^{12}C	^{11}C	58.1	2.1	43.9	[7]
230	^{12}C	^{11}C	49.4	1.8	43.9	[7]

Tab. 1 *Comparison between experimental data taken from the literature and calculated values for partial cross sections of alpha particle induced fragmentation reactions.*

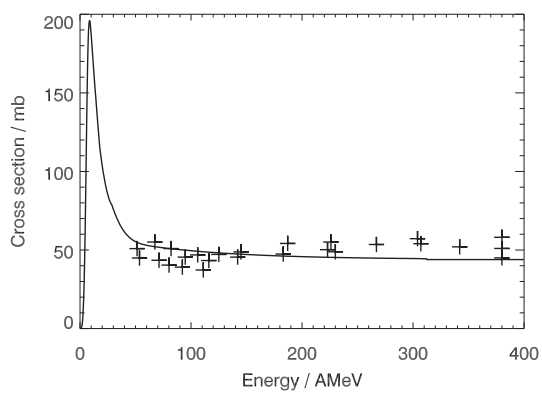

Fig. 1 *Comparison between experimental data for partial cross sections for the reaction $^{12}C(\alpha, \alpha{+}n)^{11}C$ (crosses) [6] [8] with calculated values.*

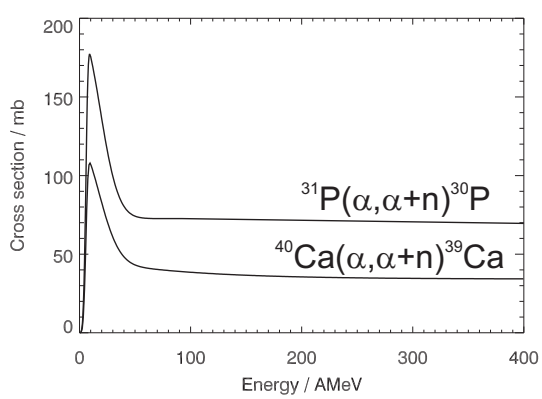

Fig. 2 *Calculated partial cross sections for the reactions $^{40}Ca(\alpha, \alpha{+}n)^{39}Ca$ and $^{31}P(\alpha, \alpha{+}n)^{30}P$*

[1] B. G. Hasch, PhD Thesis, TU Dresden (1996)
[2] C. H. Tsao, private communication (2002)
[3] R. Silberberg and C. H. Tsao, Astrophys. J. Suppl. 25 (1973) 315
[4] L. Sihver et al., Phys. Rev. C 47 (1993) 1225
[5] W. R. Webber et al., Phys. Rev. C 41 (1990) 5471
[6] J. R. Radin et al., Phys. Rev. C 9 (1974) 1718
[7] J. R. Radin, Phys. Rev. C (1970) 793
[8] M. Lindner and R. N. Osborne, Phys. Rev. 91 (1953) 1501

Hamamatsu S8550 APD Arrays for High-Resolution Scintillator Matrices Readout

B, S

M. Kapusta[1], P. Crespo, M. Moszyński[1], W. Enghardt, D. Wolski[1]

The performance of Hamamatsu S8550 avalanche photodiode (APD) arrays for scintillator matrices readout has been evaluated in order to prepare a pair of detectors to simulate a positron emission tomography (PET) system at the medical beam line of GSI Darmstadt. The S8550 device is a monolithic 8×4 pixels structure with an active area of 2.56 mm^2 for each pixel. The device allows stable operation in pulse mode at gains up to 74, with a detection efficiency of about 60 % for photons of 420 nm wavelength.

Fig. 1 presents energy spectra obtained for one pixel of S8550 using 5.9 keV X-rays as well as a 420 nm light pulser and test pulser peaks. Note that the gain of 5.9 keV X-rays is reduced because of a lower APD gain for X-rays than for light. This effect is evidently associated with the internal structure of the APD [1, 2, 3]. The measured test pulser resolution of 232 eV corresponds to an equivalent noise charge of 27 electrons.

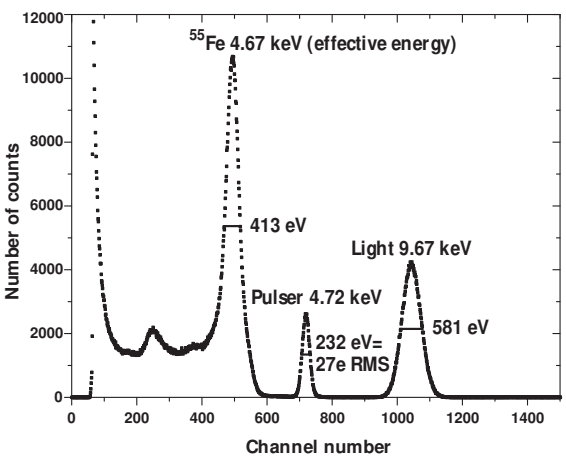

Fig. 1 *Pulse height spectra from 5.9 keV X-rays, a light pulser and a test pulser, measured for one pixel of the S8550 Hamamatsu APD array at a gain of 60. The position of the 5.9 keV X-ray peak is shifted to lower energy values, since the APD gain is lower for X-rays than for light.*

The pixel-to-pixel gain non-uniformity measured by comparing the positions of the 5.9 keV photopeak in the spectra of individual pixels was found to be less than 3.6 % at a gain of 60. Crosstalk measurements were performed in pulse mode operation by illuminating the centre of a pixel with a light spot and recording the amplitude spectra from the neighbouring pixels protected against light. The highest crosstalk between adjacent pixels was found to be 4 % at a device gain of 60. The energy resolution of 14.6 %, for the 511 keV peak from a ^{22}Na source has been recorded with a $2 \times 2 \times 10$ mm^3 LSO crystal coupled to one pixel. The number of electron-hole pairs (e-h) produced by the 511 keV photopeak absorbed in LSO is equal to 4830 ± 240 e-h/MeV.

Fig. 2 shows the coincidence time spectrum measured with precise selection of the energy windows around the full energy peak. The measured time resolution of 3.0 ± 0.2 ns FWHM obtained against BaF_2 coupled to an XP2020Q photomultiplier tube corresponds to 4.2 ± 0.3 ns FWHM for two APD-LSO detectors operating in coincidence.

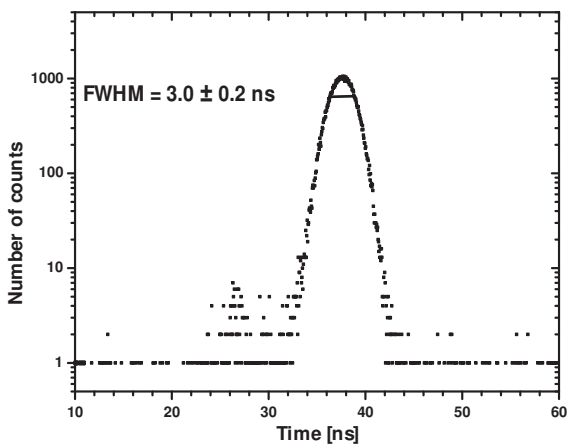

Fig. 2 *The time spectrum measured with the annihilation quanta from a ^{22}Na source.*

The Hamamatsu APD array shows good performance, but the investigations done in this work by means of the same experimental conditions and the same methods as in our previous work [3] clearly reveal that a diode layout based on the beveled structure results in superior parameters. The main disadvantage of the S8550 is its low internal gain and, consequently, its low signal-to-noise ratio. Additionally, surface effects reduce its quantum efficiency for LSO light. These drawbacks are similar to those existing with single devices produced by Hamamatsu [1], whereas the great advantage of the Hamamatsu layout is its high reliability, which has been proven in several PET applications for high resolution imaging [2].

[1] M. Moszynski, et. al., IEEE Trans. Nucl. Sci. 48 (2001) 1205
[2] B.J. Pichler, et al., IEEE Trans. Nucl. Sci. 48 (2001) 1391
[3] M. Kapusta, et al., IEEE Trans. Nucl. Sci. 49 (2002)

[1] *Soltan Institut for Nuclear Studies, 05-400 Świerk-Otwock, Poland*

Position Sensitive Photon Detectors of Lutetium Oxyorthosilicate Crystals Coupled to Avalanche Photodiode Arrays [B,S]

P. Crespo, M. Kapusta[1], K. Heidel, L. Heinrich, J. Hutsch,
J. Pawelke, M. Sobiella, D. Wolski[1], W. Enghardt, M. Moszyński[1]

In order to evaluate their performance when operated as photon detectors for in-beam ion therapy monitoring by means of positron emission tomography (PET), we have assembled and tested two position sensitive photon detectors, each consisting of 32 LSO crystals (cerium-doped Lutetium Oxyorthosilicate: Lu_2SiO_5:Ce^{3+}) coupled to a 4 x 8 pixels avalanche photodiode array (APDA). The crystals were cut from a single block delivered by CTI Inc. and their dimensions after polishing were 2 x 2 x 15 mm^3. Each crystal had all faces but one wrapped in teflon tape, with the non-covered face fixed with silicon glue to each pixel of the APDA. Fig. 1 (top) shows the assembling process, with the top of the crystals still uncovered. The whole assembly was later isolated from light with an aluminium cover. The properties of the Hamamatsu 4 x 8 APDA are described in [1]. Silicon glue was used to fix the LSO crystals to the APDA after a seven days test that compared the glue with high viscosity silicon oils (up to a viscosity factor of 2 million). During the first day the oil creeps along the teflon tape and makes it transparent to light, resulting in a decrease in light collection of 2.5 % measured after 12 hours, together with a decrease in energy resolution of 1.9 %. This effect is reduced if silicon glue is used since it solidifies in a few hours. Furthermore, by using glue crystal displacements are avoided. Before assembling the LSO crystals in the APDA their light yield homogeneity was checked with a PMT. In the horizontal position, the measured Gaussian mean was 26200 photons/MeV with 9.4 % FWHM, against 10400 photons/MeV with 22 % FWHM in the vertical position.

Once the two detector prototypes were ready we have placed them on dedicated motherboards with each pixel connected to a special purpose charge sensitive preamplifier (PA) built at the Soltan Institute for Nuclear Studies, in Warsaw, Poland. Each PA has a charge integrating output for the energy measurements and a fast output optimized for time measurements with the 40 ns decay time of LSO. Each motherboard, with its LSO/APDA detector and 32 PAs, was closed in a ventilated aluminium case offering electromagnetic protection. The timing signals of each detector were ORed with conventional electronic modules in order to operate the two detectors in coincidence.

All energy and time spectra were recorded with the hardware/software solution described in [2]. A ^{22}Na point source placed between the detectors allowed the energy spectra to be collected for all pixels (Fig. 1, middle, shows one pixel) as well as the coincidence time spectrum (Fig. 1, bottom). A non-linear least squares fit approached a Gaussian distribution with a 2nd order polynomial background

to the 511 keV photopeak in the energy spectrum, as shown by the vertical dashed lines in Fig. 1 (middle). The 14.6 % FWHM energy resolution obtained is in good agreement with the mean energy resolution of 14 % FWHM obtained with the crystals vertically coupled to a XP2020Q PMT. The final gain variation between all pixels was 13 % FWHM at an APD internal gain of 70.

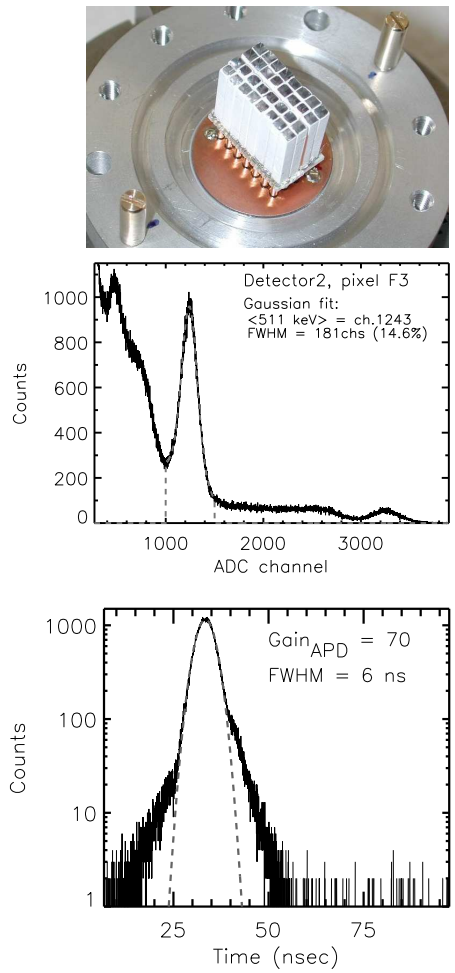

Fig. 1 *Top: Assembling of the first detector. Middle: Energy spectrum measured with a ^{22}Na source. Bottom: Coincindence time spectrum of 511 keV photons.*

[1] M. Kapusta et al., Hamamatsu S8550 APD arrays for high-resolution scintillator matrices readout, This Report, p. 80
[2] P. Crespo et al., A CAMAC data acquisition system for multi parameter measurements, This Report, p. 82

[1] *Soltan Institute for Nuclear Studies, 05-400 Otwock-Świerk, Poland.*

A CAMAC Data Acquisition System for Multi Parameter Measurements [B]

P. Crespo, J. Pawelke, W. Enghardt

We have developed a data acquisition system performing multi parameter readout of electronic modules operating under the CAMAC standard. The goal of this development was to provide a solution for the readout of two position sensitive photon detectors under study and operated in coincidence at the GSI medical beam line [1]. Each detector provides 32 energy outputs resulting in a minimum of 65 channels to be read if one considers the additional coincidence time spectrum only. Four CAMAC peak sensing ADCs are used (Phillips Scientific, model 7164), with 16 channels each. A CAMAC/GPIB crate controller (Kinetic Systems 3988) reads the ADCs and sends the data through the GPIB protocol to a GPIB/Ethernet converter (National Intruments GPIB-ENET/100). The GPIB/Ethernet converter can be accessed by any linux-running machine logged to the local network. For that, we have developed a C/C++ based application (CAGE, Camac Acquisition through GPIB and Ethernet [2]) that allows the user to control the CAMAC acquisition and to see, on-line, the spectra being collected. The GPIB/ENET driver software for linux is publicly available [3] and the control routines for the display are based on the Qt open-source package [4].

CAGE is prepared to automatically perform and display single spectrum acquisitions (rates above 40 K counts/sec achieved), two simultaneous spectra (Fig. 1), 16 spectra (Fig. 2), 64 and 66 spectra (Table 1).

When acquiring 16 spectra or less, the 65 Kword buffer (24 bit words) of the crate controller is used to maximize speed throughput by reading one ADC in the so called Q-repeat mode. In this mode, a CAMAC read function can be repeatedly executed at CAMAC bus speed ($\sim$ 1 MHz, 24 bit, parallel) and the result is stored in the buffer only when the ADC delivers a CAMAC Q-signal (valid read cycle). CAGE starts the connection protocol only when the buffer is full and, once the hand-shake between the host computer and the crate controller is performed, the full buffer is transferred in direct memory access (DMA) mode at the maximum speed of the intervening buses (8 Mbit, parallel, for the GPIB bus and 10 to 100 Mbit, serial, for the TCPIP).

If the number of spectra exceeds 16, than more than one ADC is needed as one repeated read function does not suffice. In this case, an auxilliary crate controller from Kinetic Systems (3982) is used which has two internal buffers: one for function storage and one for data, with 8 Kword each. CAGE first stores in the 3982 function buffer the CAMAC operations to be performed every time an event arrives. An Ortec ADC (811), with the slowest conversion time, sets its look-at-me (LAM) when it has finished conversion and with this starts the 3982 acquisition cycle. The 3982 runs on standalone mode, handling the arriving events and storing them in the data buffer. CAGE checks the data buffer and only reads it, in DMA mode, after it is more than half full, again optimizing the buses transfer capabilities.

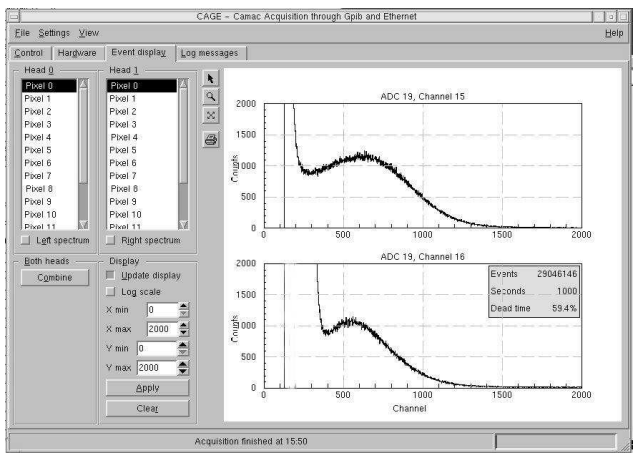

Fig. 1 *Single photoelectron spectra simultaneously acquired with two Phillips PMTs (top: XP2020Q at -2650 V, and bottom: XP3312B at -1300 V).*

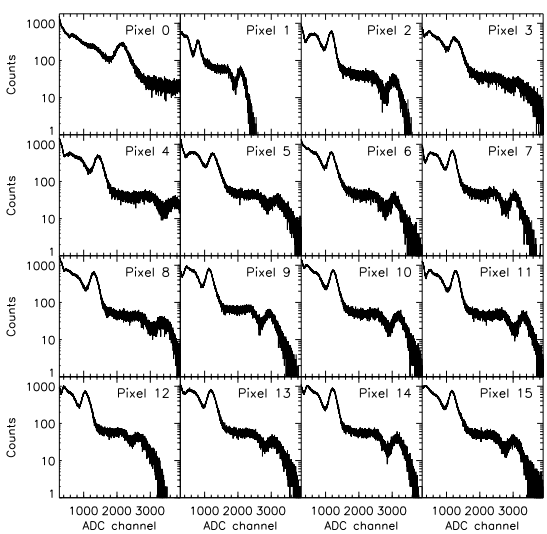

Fig. 2 *Energy spectra from a ^{22}Na source, simultaneously collected (one hour) in one of the detectors described in [1].*

Table 1 *Values obtained with a white spectrum generator.*

Output / Input	1 ch		2 chs		16 chs		32 chs		64 chs		66 chs	
	CR (cps)	DT (%)	CR (cps)	DT (%)	CR (cps)	DT (%)	CR (cps)	DT (%)	CR (cps)	DT (%)	CR (cps)	DT (%)
100 cps	98.7	1.3	98.4	1.6	96	4	92	8	87	13	86	14
1 Kcps	977	2.3	974	2.6	900	10	624	37	446	55	398	60
10 Kcps	9k	9.8	9.1k	9.5	4.4k	56	1.4k	86	745	93	611	94
100 Kcps	43k	57	29k	71	6k	94	1.6k	98.4	794	99.2	650	99.4

CR = Count Rate (counts per second), **DT** = Dead Time (%)

[1] P. Crespo et al., Position sensitive photon detectors of Lutetium Oxyorthosilicate crystals coupled to avalanche photodiode arrays, This Report, p. 81
[2] http://www.fz-rossendorf.de/FWK/MITARB/crespo/cage.html
[3] http://www.ni.com/linux/ni488dl.htm
[4] http://www.trolltech.com

A Technical Feasibility Study for a PET Therapy Monitor Combined with a Rotating Ion Beam Delivery [G]

W. Enghardt, P. Crespo, W. Bourgeois[1], A. Winter[2]

The charged hadron therapy unit that will be built on the campus of the University of Heidelberg clinics [1] will be equipped with a rotating beam delivery (gantry). An analysis of geometrical treatment configurations for skull base tumours [2] revealed that the flexibility in choosing beam portals at a gantry will provide additional benefit to the patients compared to a fixed beam delivery. It is expected that for delicate therapeutic irradiations the gantry beam delivery will be preferred rather than using a fixed beam, and, therefore, the gantry beam delivery should be equipped with an in-beam positron emission tomography (PET) system for performing in-situ monitoring of therapeutic irradiations. More than 5000 PET scans for in-situ monitoring the fractionated therapeutic irradiations of over 150 patients at the ^{12}C ion therapy facility of the Gesellschaft für Schwerionenforschung Darmstadt revealed that in-beam PET is a valuable tool for quality assurance in precision therapy with ion beams [3]. From this clinical experience the main design criteria for a novel in-beam PET scanner have been derived:

(1) Since the count rate is limited by the dose per fraction, a detector system of large solid angle and high intrisic sensitivity, i. e. detector material of superiour γ-ray registration efficiency, is required

(2) A PET-scanner to be combined with a beam delivery has to be of limited angle geometry (double head or split ring) in order to provide space for the primary beam and for the light fragments escaping the patient downbeam. As it has been shown in [4] the width of these gaps has to be minimized to reduce image degradation due to limited angle artefacts.

(3) Since the range of the primary particles as well as the position of the irradiated volume are derived from global parameters of the reconstructed β^+-activity distributions, the range and the position resolution is much better than the intrinsic spatial resolution of the PET detectors [3]. Furthermore, severe deviations from the treatment plan will cause structures with typical dimensions of several millimetres in the β^+-activity distributions [5, 6]. Thus, a PET system with a moderate spatial resolution of about 5 mm (FWHM) is sufficient for the purpose of in-beam PET therapy monitoring.

As the result of investigating the technical feasibility of several combinations of a PET-scanner with a rotating beam delivery, a configuration as depicted in Fig. 1 seems to be an optimal solution in the sense of the requirements (1) - (3) above. The integration of this tomograph into the tunnel-like treatment room is depicted in Fig. 2.

The technical features of the PET-scanner should be shortly summarized: Position sensitive block detectors of Bismuth Germanate (ECAT EXACT detectors, CPS Knoxville, TN, USA) have been proven to be reliably operable in-beam at the GSI therapy facility. Therefore, in a first conservative approach the present feasibility study is based on this detector type. Two detector heads each comprising 96 block detectors (16 in azimutal, 6 in axial direction) form a split ring with two gaps of 32 cm width covering about 50 deg of azimutal angle, which is necessary for irradiating portals with a cross section up to 20 cm $\times$ 20 cm (Fig. 3). From the investigations of [4] it is expected that the limited angle artefacts due to

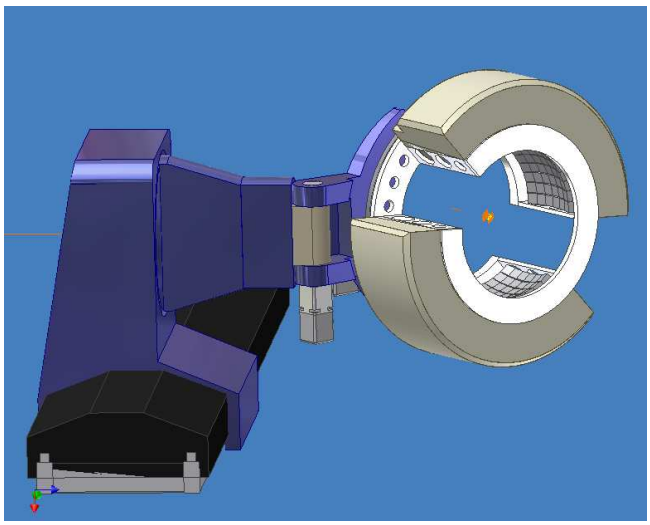

Fig. 1 *The technical concept of a positron emission tomograph for combining with a ion beam gantry*

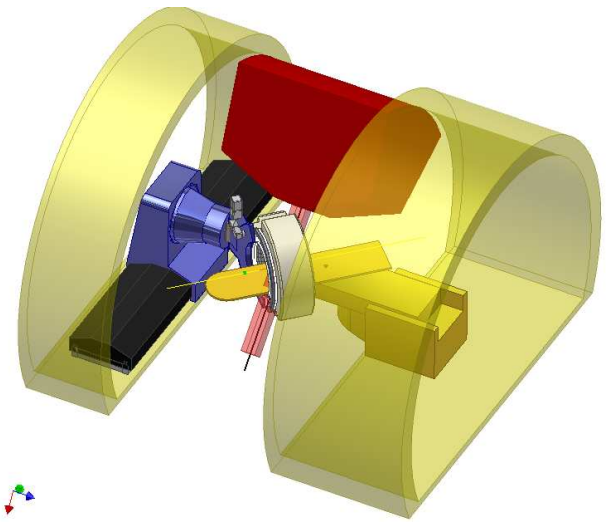

Fig. 2 *Integration of the positron emission tomograph into the treatment room. The ion beam nozzle is rotatable by 360 deg between the basements for the patient couch (right) and the PET-scanner (left). The margins of the raster scanned beam at maximal deflection (20 $\times$ 20 cm) are schematically displayed.*

[1] *Gesellschaft für Schwerionenforschung, Darmstadt*
[2] *Institut für Energetik und Umwelt GmbH, Dresden*

gaps of that size should be negligible in imaging situations which are typical for ion therapy. The length of the axial field-of-view (FOV) of the positron camera is 31 cm. The patient port has a diameter of 74 cm and the outer diameter of the camera is 144 cm.

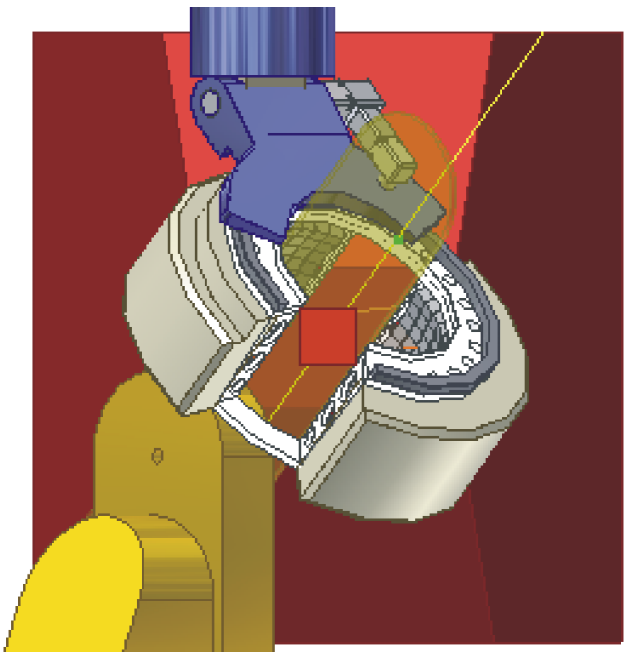

Fig. 3 *This view opposite to the beam direction proves the gaps of the split ring positron camera to be sufficiently large for irradiating portals of a maximum cross section of 20 cm × 20 cm (the square in the centre of the figure). The positions of the nozzle, the patient table and the positron camera are the same as in Fig. 2*

During imaging, i. e. during therapeutic irradiations of the patient in supine position, the positron camera covers the patient like a conventional tomograph. Since the PET-scanner has to be moved into this position after patient positioning, it is independently mounted opposite to the treatment table (Fig. 2). This arrangement allows the positron camera to be completely removed from the treatment table providing the necessary free space for patient positioning. (Fig. 4). To cover all treatment situations, the PET-gantry has to provide five degrees of freedom: *(i)* rotation of the split detector ring, *(ii)* swivelling the detector ring around a vertical excentric axis to align the scanner and the table axes, *(iii)* horizontal translation between parking and measurement positions parallel to and *(iv)* perpendicular to the longitudinal axis of the treatment tunnel, *(v)* swivelling the detector ring in the park position between the the left and right side of the pivot bearing (see Fig. 4).

A collision analysis involving the movements of the nozzle, the patient table and the positron camera for irradiation of head and neck tumours revealed a flexibility of positioning being superiour of that of a conventional therapeutic electron linear accelerator (Fig. 5).

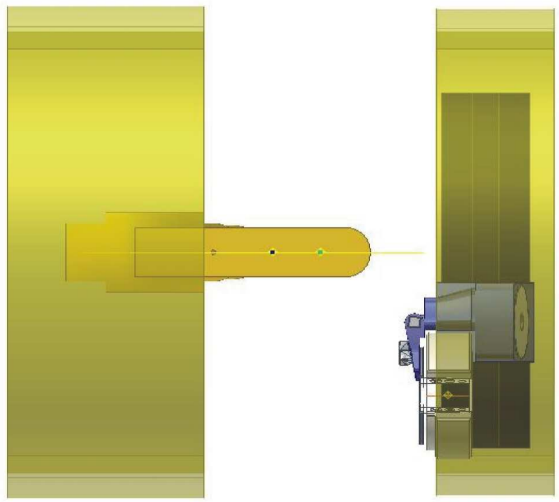

Fig. 4 *The PET scanner in the parking position (top view) provides the necessary free space for patient positioning*

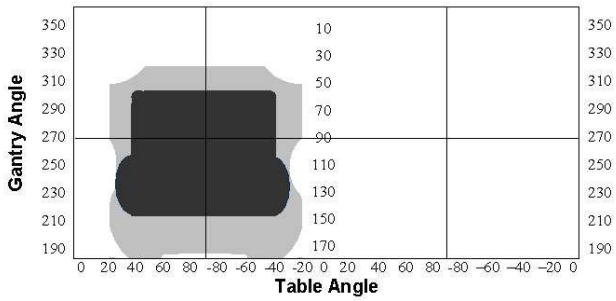

Fig. 5 *Result of the collision analysis for the combination of a gantry beam delivery and a split ring PET scanner as shown in Fig. 2. The diagram displays the gantry (nozzle) angle versus the table angle. It is separated into an inner and two outer parts; the inner part covers gantry angles between 0 and 180 deg and the outer ones between 180 and 360 deg. The light and dark grey areas in the left part of the diagram are not accessible or are unsuitable for head treatments with conventional electron linear accelerators [2] and the heavy ion beam delivery investigated here, respectively.*

[1] Heavy Ion Therapy Unit at the University of Heidelberg Clinics, Universitätsbauamt Heidelberg, 2002

[2] O. Jäkel, J. Debus, Phys. Med. Biol. 45 (2000) 1229

[3] K. Parodi, W. Enghardt, T. Haberer, Phys. Med. Biol. 47 (2002) 21

[4] P. Crespo, K. Lauckner, W. Enghardt, FZ Rossendorf, Wiss.-Tech. Ber. FZR-341 (2002) 104

[5] K. Parodi, W. Enghardt, Wiss.-Tech. Ber. FZR-341 (2002) 98

[6] W. Enghardt et al. Wiss.-Tech. Ber. FZR-271 (2000) 89

Author Index

Adrich, P. 44
Afanasjev, A.V. 40,41
Ahmad, I. 40
Balabanski, D.L. 45
Banu, A. 42,43
Barz, H.W. 8,14,15
Batist, L. 42,43
Becker, F. 42,43
Blazhev, A. 42,43
Böttcher, I. 8
Bourgeois, W. 83
von Brentano, P. 34,35
Brüchle, W. 42,43
Carpenter, M.P. 45
Caspar, B. 31
Cleymans, J. 16
Crespo, P. 77,80,81,82,83
Danchev, M. 45
Dębowski, M. 8
Dimitrov, V.I. 25
Djongolov, M. 45
Dönau, F. 29,30,34,35
Döring, J. 42,43
Dörr, W. 64
Dohrmann, F. 5,8,10,15,21,23
Dorkin, S.M. 18,19
Enghardt, W. 5,70,73,74,75,76,77,78,79,80,81,82,83
Faestermann, T. 42,43
Fahmy, K. 49,50,51,52,53,54
Fiedler, F. 78,79
Fischer, S.M. 45
Foerstendorf, H. 55,56
Förster, A. 8
Frauendorf, S. 40,41
Furlinski, G.I. 54
Gallmeister, K. 17
von Garrel, H. 34,35
van der Geer, C.A.J. 59,60,61
van der Geer, S.B. 59,60,61
Gippner, P. 58
Glotin, F. 55,56
Górska, M. 42,43
Grawe, H. 42,43
Grosse, E. 5,8,15,26,29,30,36
Haberer, T. 77
Hartley, D.J. 45
Heidel, K. 5,22,37,81
Heinrich, L. 81
Heise, K.H. 55,56
Heitsch, A. 68
Henniger, J. 71
Herbrand, F. 31
Hoinkis, C. 66
Hutsch, J. 5,22,23,81
Janas, Z. 42,43
Janssens, R.V.F. 45
Jesinger, P. 44
Jolie, J. 34,35
Jungclaus, A. 42,43
Kalben, J.v. 44
Kämpfer, B. 5,11,12,13,14,15,16,17,18,19,20
Käubler, L. 27,29,30,34,35
Kamys, B. 8
Kanaki, K. 5,21,22,23,38
Kaptari, L.P. 13,18,19
Kapusta, M. 80,81
Karny, M. 42,43
Kavatsyuk, M. 42,43
Kavatsyuk, O. 42,43
Khoo, T.L. 40
Kirchner, R. 42,43
Kneissl, U. 34,35
Koczoń, P. 8
Kohlmeyer, B. 8
Kohstall, C. 34,35
Kojouharov, I. 44
Kopatch, J. 44
Kosev, K. 37,38,39
Kostov, L.K. 34,35
Kotte, R. 5,7,21,22,23
Krasznahorkay, A. 44
Kreutz, M. 34,35
La Commara, M. 42,43
Lalazissis, G.A. 40
Langer, M. 27,31,33
Laue, F. 8
Lehmann, N. 52
Lehnert, U. 30,31,33,69
Lessmann, E. 64,65,67
Linnemann, A. 34,35
de Loos, M.J. 59,60,61
Lubkiewicz, E. 44
Magestro, D. 21
Mallion, S. 34,35
Mandal, S. 42,43
Mazzocchi, C. 42,43
Menzel, M. 8
Mezentseva, Z. 44
Möller, K. 26
Mönsters, F. 78
Moszyński, M. 80,81
Müller, H. 69,70,72

Mueller, W.F. 45
Müntz, C. 21
Mukha, I. 42,43
Mukherjee, B. 26
Mutterer, M. 44
Naumann, L. 5,8,21,22,23,26
Neubert, W. 69,71,72,73,74,75
Nicolai, R. 55
Nisius, D. 45
Nowak, A. 30
Oeschler, H. 8
Ortega, J.M. 55,56
Panteleeva, A. 50,64,65,66,67,68
Parodi, K. 77,79
Pavlenko, O.P. 11,12,17
Pawelke, J. 64,66,67,68, 71,77,81,82
Peshier, A. 20
Piest, J.A. 62
Pietralla, N. 34,35
Pitz, H.H. 34,35
Plettner, C. 42,43
Płochocki, A. 42,43
Pönisch, F. 76
Prazeres, R. 55,56
Pühlhofer, F. 8
Raff, J. 51
Reichelt, U. 71
Reviol, W. 45
Riedel, T. 31
Riedinger, L.L. 45
Rimarzig, B. 30,57
Roeckl, E. 42,43
Romoli, M. 42,43
Rusev, G. 27,29,34,35
Sadovski, A. 5,21,23
Sakmar, T.P. 52
Savchuk, O. 50,51,53
Schädel, M. 42,43
Schamlott, A. 55
Schardt, D. 77
Scheck, M. 34,35
Scheinast, W. 8
Schilling, K.D. 30,31,33,34,35, 37,38
Schlenk, R. 30
Schneider, Ch. 8
Schulze, W. 27,33,37
Schwab, E. 8
Schwengner, R. 27,29,30,31,34, 35,42,43,45
Seibert, J. 5,25
Seidel, W. 55,56,57
Selenska-Pobell, S. 51
Semikh, S.S. 13,18,19
Senger, P. 8
Sharma, H. 36,37,38,39,44
Shin, Y. 8
Sobiella, M. 5,23,38,57,68,78,81
Soff, G. 20
Stedile, F. 34,35
Stefanova, E.A. 45
Steinberg, P. 16
Ströbele, H. 8
Sturm, Ch. 8
Surówka, G. 8
Trzaska, W. 44
Uhlig, F. 8
Wagner, A. 8,26,27,29,30,31,34,35, 36,37,38,39,44
Wagner II, A. 31,37
Waluś, W. 8
Werner, V. 34,35
Wheaton, S. 16
Winter, A. 83
Wohlfarth, D. 57
Wolf, U. 22,57
Wollersheim, H.-J. 44
Wolski, D. 80,81
Wünsch, R. 59,60,61
Wustmann, B. 30
Zétényi, M. 14
Zeidan, O. 45
Zschocke, S. 11,12
Zylicz, J, 42,43

Publications and Talks

Publications [1]

Subthreshold ϕ Meson Production in Heavy-Ion Collisions
(Nucl. Phys. A 705 (2002) 223)

Barz, H.W., M. Zétényi, Gy. Wolf, **B. Kämpfer**

Abstract: Within a transport code of BUU type the production of ϕ-mesons in the reactions Ni + Ni at 1.93 A·GeV and Ru + Ru at 1.69 A·GeV is studied. New elementary reaction channels ρN(Δ) $\rightarrow$ ϕN and πN(1520) $\rightarrow$ ϕN are included. In spite of a substantial increase of the ϕ multiplicities by these channels the results stay below the tentative numbers extracted from experimental data.

The Longitudinal Polarimeter at HERA
(Nucl. Instr. Meth. A 479 (2002) 334)

Beckmann, M., A. Borissov, S. Brauksiepe, F. Burkart, H. Fischer, J. Franz, F.H. Heinsius, K. Königsmann, W. Lorenzon, F.M. Menden, A. Most, S. Rudnitsky, C. Schill, **J. Seibert**, A. Simon

Abstract: The design, construction and operation of a Compton back-scattering laser polarimeter at the HERA storage ring at DESY are described. The device measures the longitudinal polarization of the electron beam between the spin rotators at the HERMES experiment with a fractional systematic uncertainty of 1.6 %. A measurement of the beam polarization to an absolute statistical precision of 0.01 requires typically one minute when the device is operated in the multi-photon mode. The polarimeter also measures the polarization of each individual electron bunch to an absolute statistical precision of 0.06 in approximately five minutes. It was found that colliding and non-colliding bunches can have substantially different polarizations. This information is important for the collider experiments H1 and ZEUS for their future longitudinally polarized electron program because those experiments use the colliding bunches only.

Development of Low-Mass Drift Chambers for the HADES Spectrometer
(Nucl. Instr. Meth. A 477 (2002) 397)

H. Bokemeyer, J.L. Boyard, V. Chepurnov, S. Chernenko, H. Daues, **F. Dohrmann,**
W. Enghardt, O. Fateev, C. Garabatos, L. Glonti, **E. Grosse**, J. Hehner, T. Hennino, J. Kempter, W. Koenig, C. Müntz, **L. Naumann**, A. Petrov, J. Pouthas, P. Rosier, L. Smykov, H. Stelzer, **M. Sobiella**, J. Stroth, J. Wüstenfeld, Yu. Zanevsky, P. Zumbruch

Abstract: The High Acceptance Di-Electron Spectrometer (HADES) is a detector arrangement combined with a superconducting toroid for lepton pair spectroscopy presently built up at GSI (Darmstadt). HADES is designed to cope with the high-multiplicity environment of heavy ion collisions at 1 AGeV and intensities of up to 10^8 beam particles per second and central event rates of 10^5 s^{-1}. The detector has a geometrical acceptance of almost 50 % for e^+e^- pairs and a mass resolution of 0.8 % for ρ and ω mesons. Four low-mass drift chamber systems, two before and two behind the magnet, serve for charged particle track reconstruction. Design aspects of the drift chambers and first results from beam tests are presented.

In-band and inter-band B(E2) values within the Triaxial Projected Shell Model
(Eur. Phys. J. A 15 (2002) 455)

Boutachkov, P., A. Aprahamian, Y. Sun, J.A. Sheikh, **S. Frauendorf**

Abstract: The Triaxial Projected Shell Model (TPSM) has been successful in providing a microscopic description of the energies of multi-phonon vibrational bands in deformed nuclei. We report here on an extension of the TPSM to allow, for the first time, calculations of B(E2) values connecting γ- and $\gamma\gamma$-vibrational bands and the ground-state band. The method is applied to 166,168Er. It is shown that most of the existing B(E2) data can be reproduced rather well, thus strongly supporting the classification of these states as γ-vibrational states. However, significant differences between the data and the calculation are seen in those B(E2) values which involve odd-spin states of the γ-band. Understanding these discrepancies requires accurate experimental measurements and perhaps further improvements of the TPSM.

[1] From the authors printed in **bold** further information can be obtained

Indentification of K^+-Mesoms from Subthreshold pA Collisions with ANKE at COSY-Jülich
(Nucl. Instrum. Meth. A 481 (2002) 378)

Büscher, M., H. Junghans, V. Koptev, M. Nekipelov, K. Sistemich, H. Ströher, S. Barsov, G. Borchert, W. Borgs, **M. Debowski**, W. Erven, R. Esser, P. Fedorets, D. Gotta, M. Hartmann, V. Hejny, A. Kacharava, H.R. Koch, V. Komarov, P. Kulessa, A. Kulikov, G. Macharashvili, S. Merzlyakov, S. Mikirtychyants, **H. Müller**, A. Mussgiller, R. Nellen, M. Nioradze, H. Ohm, A. Petrus, F. Rathmann, Z. Rudy, R. Schleichert, **C. Schneider**, O.W.B. Schult, H.J. Stein, I. Zychor

Abstract: The spectrometer ANKE has been put into operation at the accelerator COSY of the Forschungszentrum Jülich in spring 1998. An initial scientific goal is to study K^+-production in pA collisions at subthreshold energies far below the free NN-threshold at $T_p = 1.58$GeV. This requires the identification of K^+-mesons in a background of pions and protons, about 10^6 times more intense. In this paper the sophisticated detection system and the software procedures for kaon identification are described. With the help of TOF, energy-loss and range measurements as well as the track information from wire chambers, it is possible to measure $d^2\sigma/d\Omega dp$ for deep subthreshold K^+ production at beam energies down to $T_p = 1.0$GeV.

Centrality Dependence of Thermal Parameters in Heavy-Ion Collisions at Relativistic Energies
(Phys. Rev. C 65 (2002) 027901)

Cleymans, J., **B. Kämpfer**, S. Wheaton

Abstract: The centrality dependence of thermal parameters, characterizing the hadron multiplicities, is determined phenomenologically for lead-on-lead collisions at CERN-SPS for a beam energy of 158 A GeV. The strangeness equilibration factor shows a clear, approximately linear, increase with increasing centrality, while the freeze-out temperature and chemical potential remain constant.

FTIR- and Fluorescence-Spectroscopic Analyses of Receptor G-Protein Coupling in Photoreception
(Curr. Org. Chem. 6 (2002) 1259)

Fahmy, K.

Abstract: G protein-coupled receptors (GPCRs) are heptahelical transmembrane proteins. They transduce a large variety of extracellular signals, allowing perception of taste, odor, hormones, and light. Binding of an extracellular ligand induces structural changes in the cytosolic domain of a GPCR which, thereby, catalyzes nucleotide exchange in a G-protein. Rhodopsins, the visual pigments, are prototypical GPCRs that are activated by photoisomerization of covalently bound 11-cis retinal. Unlike other GPCRs, bovine rhodopsin and transducin, its cognate G-protein, can be prepared from cow eyes in large quantities for spectroscopic and biochemical investigations. Rhodopsin is the best studied GPCR and the only one for which an X-ray structure has been solved. Structural information together with the wealth of biophysical data on native and recombinant rhodopsins allows to determine structure function relationships that are relevant to GPCR-dependent signaling in general. Here, results from Fourier-transform-infrared (FTIR) spectrocopic studies of rhodopsin and measurements of nucleotide-dependent transducin fluorescence are reviewed. Intra- and intermolecular processes during signaling by the photoreceptor have thus been identified and analyzed kinetically. Recent applications of these techniques concern rhodopsin transducin coupling in synthetic lipidic matrices and analysis of drug action at the receptor G protein interface. The data are discussed in the context of the crystal structure of rhodopsin and additional biochemical information if required for the understanding of the spectroscopic results.

Kaon and Antikaon Production in Heavy Ion Collisions at 1.5 A GeV
(J. Phys. G 28 (2002) 2011)

Förster, A. for the KaoS Collaboration: I. Böttcher, A. Förster, **E. Grosse**, P. Koczon, B. Kohlmeyer, M. Menzel, **L. Naumann**, H. Oeschler, F. Pühlhofer, **W. Scheinast**, E. Schwab, P. Senger, Y. Shin, H. Ströbele, C. Sturm, F. Uhlig, W. Walus, **A. Wagner**

Abstract: At the Kaon Spectrometer KaoS at SIS, GSI the production of kaons and antikaons in heavy ion reactions at a beam energy of 1.5 AGeV has been measured for the collision systems Ni+Ni and Au+Au. The K^-/K^+ ratio is found to be constant for both systems and as a function of impact parameter but the slopes of K^+ and K^- spectra differ for all impact parameters. Furthermore the respective polar angle distributions are presented as a function of centrality.

Dependence of Energy Loss of Hard Jets on the Initial Thermodynamic State of Deconfined Matter at RHIC
(Phys. Rev. C 66 (2002) 014908)

Gallmeister, K., **B. Kämpfer**, O.P. Pavlenko

Abstract: The dependence of the radiative energy loss of hard partons (E>10 GeV) on the initial thermodynamic parameters is studied for deconfined matter to be expected at the Relativistic Heavy-Ion Collider (RHIC). We demonstrate that the specific QCD radiation pattern with a nonlinear dependence of the energy loss on the propagated distance leads to a strong increase of the energy loss with increasing initial entropy of deconfined matter supposing its lifetime is less than the average time to pass through the medium. This is in contrast to a parametrization with constant energy loss per unit length of propagation. For a sufficiently high initial temperature a two-regime behavior of the energy loss as a function of the initial parton momentum occurs. The angular structure of the energy loss of hard jets with respect to the initial temperature is also discussed for RHIC conditions.

Evidence for the Absence of Regularization Corrections to the Partial-Wave Renormalization Procedure in One-Loop Self-Energy Calculations in External Fields
(Phys. Rev. A 65 (2002) 042110)

Goidenko, I., G. Plunien, **S. Zschocke**, L. Labzowsky, G. Soff

Abstract: The equivalence of the covariant renormalization and the partial-wave renormalization (PWR) approaches is proven explicitly for the one-loop self-energy (SE) correction of a bound electron state in the presence of external perturbation potentials. No "spurious" correction terms to the noncovariant PWR scheme are generated for Coulomb-type screening potentials and for external magnetic fields. It is shown that in numerical calculations of the SE with Coulombic perturbation potential spurious terms result from an improper treatment of the unphysical high-energy contribution. A method for performing PWR utilizing the relativistic B-spline approach for construction of the Dirac spectrum in external magnetic fields is proposed. This method is applied for calculating QED corrections to the bound-electron g factor in H-like ions. Within a level of accuracy of about 0.1 % no spurious terms are generated in numerical calculations of the SE in magnetic fields.

THz radiation from free electron lasers and its potential for cell and tissue studies
(Phys. Med. Biol. 47 (2002) 3755)

Grosse, E.

Abstract: Free electron lasers (FELs) allow for the generation of electromagnetic radiation (EM) in a wide field of frequencies (respectively wavelengths) through the proper adjustment of the energy of an electron beam and the field configuration of a magnetic undulator passed by this beam. Terahertz (THz) radiation covers the region of the electromagnetic spectrum between approximately 0.3 and 30 THz and thus can be considered a continuation of the optical spectrum beyond the far infrared (IR). The very interesting results obtained from various studies of the interaction between IR radiation and biomolecules or tissue have stimulated increasing interest in the study of biological systems using THz radiation. This paper points out what role modern FELs can play in this research.

Search for mass-symmetric ternary fission in the reactions ^{14}N(53 AMeV) + ^{197}Au and ^{232}Th
(Nucl. Phys. A 712 (2002) 207)

Herbach C.-H., D. Hilscher, V.G. Tishchenko, **P. Gippner**, D.V. Kamanin, W. von Oertzen, H.-G. Ortlepp, Yu.E. Penionzhkevich, Yu.V. Pyatkov, G. Renz, **K.D. Schilling**, O.V. Strekalovsky, **W. Wagner**, V.E. Zhuchko

Abstract: Ternary fission of heavy hot composite systems with excitation energies of 1.5 - 2.5 MeV/amu has been studied in the reactions of ^{14}N(53 AMeV) with ^{197}Au and ^{232}Th. The ternary yields have been explored as a function of the charge Z_L of the lightest fragment: while Z_L increases from 6 to 25, the cross sections decrease from 5 to 0.08 mb for N + Au and from 15 to 0.8 mb for N + Th. The velocity vector $\vec{\nu}_L$ of the lightest fragment has been investigated in the rest frame of the other two heavier fragments. Two different components are observed: (i) an isotropic one with values of ν_L corresponding to the Coulomb repulsion from the combined heavier fragments before separation and, (ii) an anisotropic contribution with the lightest fragment emitted with lower ν_L perpendicular to the scission axis of the two heavier fragments. The latter component is distinguished from the isotropic one by an enhanced fraction of mass-symmetric ternary events and by up to 50 MeV lower total kinetic fragment energies. These features are indicative of a collinear stretched scission configuration, where the lightest fragment is positioned between the two heavier ones.

Proton and deuteron rapidity distributions and nuclear stopping in ^{96}Ru(^{96}Zr) + ^{96}Ru(^{96}Zr) collisions at 400 A MeV
(Phys. Rev. C 66 (2002) 034901)

Hong, B., Y.J. Kim, D.H. Kang, Y. Leifels, F. Rami, B. de Schauenburg, K.S. Sim, J.P. Alard, A. Andronic, V. Barret, Z. Basrak, N. Bastid, G. Berek, R.Čaplar, P. Crochet, A. Devismes, P. Dupieux, M. Dželalija, C. Finck, Z. Fodor, A. Gobbi, Yu. Grishkin, O.N. Hartmann, N. Herrmann, K.D. Hildenbrand, J. Kecskemeti, M. Kirejczyk, P. Koczon, M. Korolija, **R. Kotte**, T. Kress, R. Kutsche, A. Lebedev, X. Lopez, **W. Neubert**, D. Pelte, M. Petrovici, W. Reisdorf, D. Schüll, Z. Seres, B. Sikora, V. Simion, K. Siwek-Wilczyńska, V. Smolyankin, M.R. Stockmeier, G. Stoicea, P. Wagner, K. Wiśniewski, **D. Wohlfarth**, I. Yushmanov, A. Zhilin

Abstract: We present the centrality dependence of proton and deuteron rapidity distribution in Ru + Ru collisions at 400 A MeV. Data are compared with isospin quantum molecular dynamics (IQMD) calculations under various assumptions on the nucleon-nucleon cross section in the medium. The rapidity spectra of both particles can be reproduced by IQMD with a free nucleon-nucleon cross section for the most central collisions. The ratio of baryon rapidity distributions in isospin asymmetric collisions systems shows incomplete mixing and partial transparency of the projectile and target nuclei at this beam energy.

T = 0 and T = 1 States in the Odd-Odd N = Z Nucleus, $^{70}_{35}$Br$_{35}$
(Phys. Rev. C 65 (2002) 064307)

Jenkins, D.G., N.S. Kelsall, C.J. Lister, D.P. Balamuth, M.P. Carpenter, T.A. Sienko, S.M. Fischer, R.M. Clark, P. Fallon, A. Görgen, A.O. Macchiavelli, C.E. Svensson, R. Wadsworth, W. Reviol, D.G. Sarantites, G.C. Ball, J. Rikovska Stone, O. Juillet, P. Van Isacker, A.V. Afanasjev, **S. Frauendorf**

Abstract: Excited states in ^{70}Br were populated in the ^{40}Ca(^{32}S, pn) reaction at E_{beam} = 80-100 MeV and the ^{40}Ca(^{36}Ar, αpn) reaction at E_{beam} = 145 MeV. The resulting gamma decay was detected using the Gammasphere array triggered by a 30-element neutron detector. The cross-bombardment allowed the unambiguous assignment of levels to ^{70}Br, comprising a total of 32 states built both on the $J^\pi = 0^+$ ground state and a previously known $J^\pi = 9^+$ isomer, which is located at an excitation energy of 2293 keV by the observation of linking transitions. The structures are discussed within the context of the two-quasiparticle plus rotor model, the IBM-4 model and the cranked Nilsson-Strutinsky formalism. The nonobservation of a doublet of $J = 0, T = 1$ and $J = 1, T = 0$ states at low excitation in ^{70}Br is indicative that $T = 0$ proton-neutron pairing strength is weak in comparison to $T = 1$ pairing.

Beta Decay of ^{57}Zn
(EPJdirect A3 (2002) 1)

Jokinen, A., A. Nieminen, J. Äystö, R. Borcea, E. Caurier, P. Dendooven, M. Gierlik, M. Górska, H. Grawe, M. Hellström, M. Karny, Z. Janas, R. Kirchner, M. La Commara, G. Martinez-Pinedo, P. Mayet, H. Penttilä, A. Plochocki, M. Rejmund, E. Roeckl, M. Sawicka, C. Schlegel, K. Schmidt, **R. Schwengner**

Abstract: Beta-delayed proton decay of ^{57}Zn has been investigated at the GSI on-line isotope separator. The studied ^{57}Zn nuclei were produced in fusion evaporation reactions by using a 150 MeV ^{32}S beam on a ^{28}Si target. Beta-delayed protons were measured by a charged-particle telescope detector. The observed decay pattern was used to construct the level scheme of ^{57}Cu and to extract the beta feeding distribution. The experimental results are compared with shell-model calculations.

Dileptons and Photons from Central Heavy Ion Collisions at CERN-SPS
(Nucl. Phys. A 698 (2002) 424)

Kämpfer, B., K. Gallmeister, O.P. Pavlenko, C. Gale

Abstract: A unique parameterization of secondary (thermal) dilepton and photon yields in heavy-ion experiments at CERN-SPS is proposed. Adding those thermal yields to background contributions the spectral shapes of the CERES/NA45, NA38, NA50, HELIOS/3 and WA98 data from experiments with lead and sulfur beams can be well described.

ϕ Puzzle in Heavy-Ion Collisions at 2 AGeV: How Many K$^-$ from ϕ Decays?
(J. Phys. G 28 (2002) 2035)

Kämpfer, B., **R. Kotte**, C. Hartnack, J. Aichelin,

Abstract: The preliminary experimental data on ϕ production in the reaction Ni(1.93 AGeV) + Ni point to a puzzling high ϕ yield which can not be reproduced with present transport codes. We survey the experimental situation and present prospects for dedicated measurements of the ϕ multiplicities with the K^+K^- and e^+e^- channels at HADES and FOPI.

The Influence of the N = 50 Neutron Core on Dipole Excitations in ^{87}Rb
(Phys. Rev. C 65 (2002) 054315)

Käubler, L., K.D. Schilling, R. Schwengner, F. Dönau, E. Grosse, D. Belic, P. von Brentano, M. Bubner, C. Fransen, M. Grinberg, U. Kneissl, C. Kohstall, A. Linnemann, P. Matschinsky, A. Nord, N. Pietralla, H.H. Pitz, M. Scheck, F. Stedile, V. Werner

Abstract: Dipole excitations in the semimagic $N = 50$ nucleus ^{87}Rb were investigated at the Stuttgart Dynamitron facility using bremsstrahlung with an end-point energy of 4.0 MeV. The widths Γ or the reduced excitation probabilities $B(\Pi 1)\uparrow$ of 19 states were determined for the first time. The magnetic dipole excitations are well reproduced in the framework of the shell model, however, these calculations cannot describe the observed electric dipole excitations. The $1/2^+$ state at 3060 keV is proposed to be the weak coupling of an $f_{5/2}$ proton hole to the 3^- octupole vibrational state in the $N = 50$ core ^{88}Sr. The relatively strong $E1$ transition from that state to the ground state is explained as mainly the neutron $h_{11/2} \rightarrow g_{9/2}$ transition. The breakup of the $N = 50$ core and neutron excitations into the i$h_{11/2}$ shell are essential to describe electric dipole excitations, but neutron-core excitations do not play an important role for the structure of magnetic dipole excitations.

Polarization Observables in the Reaction $pn \rightarrow d\phi$
(Eur. Phys. J. A 14 (2002) 211)

Kaptari, L.P., **B. Kämpfer**

Abstract: The reaction $pn \rightarrow d\phi$ is studied within a covariant boson exchange model. The behavior of polarization observables being accessible in forthcoming experiments near threshold is predicted.

Testing Mean-Field Models Near the N = Z Line: γ-ray Spectroscopy of the T_z=$\frac{1}{2}$ Nucleus ^{73}Kr
(Phys. Rev. C 65 (2002) 044331)

Kelsall, N.S., S.M. Fischer, D.P. Balamuth, G.C. Ball, M.P. Carpenter, R.M. Clark, J. Durell, P. Fallon, S.J. Freeman, P.A. Hausladen, R.V.F. Janssens, D.G. Jenkins, M.J. Leddy, C.J. Lister, A.O. Macchiavelli, D.G. Sarantites, D.C. Schmidt, D. Seweryniak, C.E. Svensson, B.J. Varley, S. Vincent, R. Wadsworth, A.N. Wilson, A.V. Afanasjev, **S. Frauendorf**, I. Ragnarsson, R. Wyss

Abstract: Excited states in the $N = Z + 1$ nucleus ^{73}Kr have been investigated using the ^{40}Ca(^{36}Ar,2pn) and ^{40}Ca(^{40}Ca,α2pn) reactions at 145 and 160 MeV, respectively. γ rays were detected using the Gammasphere array and events were recorded in coincidence with charged-particle and neutron detectors. The three previously observed bands were extended to high spin, and a new unfavored positive-parity band has been observed. The alignment characteristics and decay properties of the bands are all consistent with large-deformation prolate rotation, with no clear evidence for oblate bands or shape coexistence. This is quite different from neighboring ^{72,74}Kr, indicating a strong shape-stabilizing role for the valence neutron. The experimental results are compared to extended total Routhian surface, cranked Nilsson Strutinsky, and cranked relativistic mean-field calculations. The results suggest that the paired calculations lack some important physics. Neutron-proton correlations may be the missing ingredient. There is also evidence for an unusual band crossing in the negative-parity bands, which may indicate the presence of $T = 0$ pairing correlations. At high spin all the models can reproduce the experimental data.

Dynamical Moment of Inertia and Quadrupole Vibrations in Rotating Nuclei
(Phys. Rev. C 65 (2002) 041307)

Nazmitdinov, R.G, **D. Almehed, F. Dönau**

Abstract: The contribution of quantum shape fluctuations to inertial properties of rotating nuclei has been analyzed within the self-consistent one-dimensional cranking oscillator model. It is numerically proven that for even-even nuclei the dynamical moment of inertia calculated in a mean field approximation in the rotating frame is equivalent to the Thouless-Valatin moment of inertia. If the contribution of the quantum fluctuations to the total energy is taken into account, the dynamical moment of inertia differs from the Thouless-Valatin value.

In-Beam PET Measurements of β^+ Radioactivity Induced by Proton Beams
(Phys. Med. Biol. 47 (2002) 21)

Parodi, K., W. Enghardt, T. Haberer

Abstract: Our first in-beam PET measurements of the β^+ activation induced by proton irradiation are presented. Monoenergetic proton beams in the energy and intensity range suited for the treatment of deep-seated tumours were delivered by the synchrotron of the Gesellschaft fuer Schwerionenforschung (GSI) at Darmstadt. They were stopped in PMMA blocks placed in the centre of the field of view of the positron camera that is installed in the heavy ion tumour treatment facility at GSI. The β^+ activity signal was found to be three times larger than that produced by carbon ions at the same range and applied physical dose. The reconstructed spatial β^+ activity distributions were analysed and compared with the production of positron emitters predicted by a calculation based on experimental cross-sections and on the proton flux given by the FLUKA Monte Carlo code. The shape of the depth-activity profiles was well reproduced by the model and the correlation with the proton range and the depth-dose distributions was carefully investigated. Despite the nontrivial range determination from the β^+ activity distribution in the proton case, our experimental investigation supports the feasibility of an in-situ proton therapy monitoring by means of in-beam PET, as already clinically implemented for the monitoring of carbon ion therapy at GSI Darmstadt.

Observation of a Doublet Band in the Nucleus ^{128}Pr
(Phys. Rev. C 65 (2002) 054324)

Petrache, C.M., G. Lo Bianco, D. Bazzacco, R. Menegazzo, M. Nespolo, G. de Angelis, N. Blasi, V.I. Dimitrov, **S. Frauendorf**, P. Semmes, J. Zhang

Abstract: The doubly odd nucleus 128Pr was studied via in-beam -ray spectroscopy using the 40Ca+92Mo reaction at 190 MeV. Five rotational bands were observed and assigned to configurations involving proton and neutron orbitals close to the Fermi level. The observed bands are discussed in the framework of the three-dimensional (3D) tilted axis cranking (TAC) model. Two of the negative-parity bands have almost degenerate energy levels, which suggests an interpretation in terms of the pseudospin doublet. It was impossible, however, to reproduce the observed small level spacing by either 3D TAC or two-quasiparticle-rotor model calculations.

From QCD Lattice Calculations to the Equation of State of Quark Matter
(Phys. Rev. D 66 (2002) 094003)

Peshier, A., **B. Kämpfer**, G. Soff

Abstract: We describe two-flavor QCD lattice data for the pressure at a nonzero temperature and vanishing chemical potential within a quasiparticle model. Relying only on thermodynamic consistency, the model is extended to nonzero chemical potential. The results agree with lattice calculations in the region of a small chemical potential.

β-Decay of ^{100}In
(Phys. Rev. C 66 (2002) 44319)

Plettner, C., L. Batist, J. Döring, A. Blazhev, H. Grawe, V. Belleguic, C.R. Bingham, R. Borcea, M. Gierlik, M. Górska, N. Harrington, Z. Janas, M. Karny, R. Kirchner, C. Mazzocchi, P. Munro, E. Roeckl, K. Schmidt, **R. Schwengner**

Abstract: The β decay of ^{100}In, the one proton hole and one neutron particle neighbor to ^{100}Sn, was investigated at the GSI on-line mass separator by using germanium detectors and a NaI total-absorption spectrometer. On the basis of $\beta\gamma\gamma$ coincidences, the ^{100}In decay scheme was established for the first time. The ground-state spin and parity for ^{100}In are discussed by investigating β feeding of levels in ^{100}Cd and delayed proton emission to ^{99}Ag. The half-life was remeasured and found to be 5.9(2) s. The Q_{EC} value was determined from the measured EC/β^+ ratio for the β-delayed protons to be 10.08(23) MeV. The main fraction of the β feeding was established to populate the region of 6 MeV excitation energy, which corresponds to a total Gamow-Teller (GT) strength of 3.9(9) and a centroid at 6.4 MeV. Large-scale shell-model calculations employing a realistic interaction are used to assign configurations to states in ^{100}In and ^{100}Cd. The GT β-decay strength distribution measured in the total absorption experiment is compared to shell-model predictions. The deduced overall hindrance of the GT strength agrees with the values predicted for the ^{100}Sn GT decay.

High-Spin Structure of the Spherical Nucleus ^{90}Y
(Phys. Rev. C 65 (2002) 044327)

Rainovski, G., **R. Schwengner, K.D. Schilling, A. Wagner**, A. Jungclaus, E. Galindo, O. Thelen, D.R. Napoli, C.A. Ur, G. de Angelis, M. Axiotis, A. Gadea, N. Marginean, T. Martinez, Th. Kröll

Abstract: High-spin states in ^{90}Y were populated in the ^{82}Se(^{11}B,3n) reaction at a beam energy of 37 MeV. γ rays were detected with the spectrometer GASP. The level scheme of ^{90}Y was extended up to $J^\pi = (18^+)$ at 9.6 MeV. Mean lifetimes of four levels were determined using the Doppler-shift-attenuation method. The structure of ^{90}Y was interpreted in terms of the shell model. The calculations were performed in the model space $\pi(0f_{5/2}, 1p_{3/2}, 1p_{1/2}, 0g_{9/2})$ $\nu(1p_{1/2},\ 0g_{9/2}, 1d_{5/2})$ and in an extended space including the $\nu(0g_{7/2})$ orbital also. The calculations in the extended model space reveal a correspondence between states in ^{90}Y and ^{89}Y. Moreover, a combination of the predicted states with $J^\pi \geq 14^{(+)}$ can be found that reproduces the large experimental B(M1) values of up to about 1 Weisskopf unit.

Tilted Dipole Bands in ^{123}Xe
(Phys. Rev. C 66 (2002) 014308)

Rainovski, G., D.L. Balabanski, **G. Roussev**, G. Lo Bianco, G. Falconi, N. Blasi, D. Bazzacco, G. de Angelis, D.R. Napoli, **F. Dönau, V.I. Dimitrov**

Abstract: High-spin states in ^{123}Xe were populated in the ^{110}Pd(^{18}O,5n) reaction at 75 MeV and gamma-ray coincidences were measured with the GASP spectrometer. A new rotational sequence of enhanced dipole transitions was established. This band, as well as a similar band in ^{124}Xe, may be described within the framework of the tilted axis cranking model as bands for which comparable amounts of angular momentum are generated by magnetic and collective rotation, respectively.

Shape Coexistence at High Spin in the N = Z + 2 Nucleus ^{70}Se
(J. Phys. G 28 (2002) 2617)

Rainovski, G., H. Schnare, R. Schwengner, C. Plettner, L. Käubler, F. Dönau, I. Ragnarsson, J. Eberth, T. Steinhardt, O. Thelen, M. Hausmann, A. Jungclaus, K.P. Lieb, A. Müller, G. de Angelis, A. Gadea, D.R. Napoli, A. Algora, D.G. Jenkins, R. Wadsworth, A. Wilson, W. Andrejtscheff, **V.I. Dimitrov**

Abstract: The nucleus ^{70}Se was studied using the ^{40}Ca(^{40}Ca, $2\alpha 2p$) reaction at a beam energy of 185 MeV. Gamma rays were measured with the EUROBALL III spectrometer. The known positive-parity bands have been extended and one new band of positive parity and two of negative parity have been identified. These bands are interpreted in terms of the cranked Nilsson-Strutinsky approach. Calculations suggest that the two negative-parity bands, which have the same signature, are both based on a configuration with two protons and three neutrons lifted from the fp shell to the $g_{9/2}$ orbital, but at different nuclear shapes. This represents a shape coexistence at high spin.

Radiotherapy for Chordomas and Low-Grade Chondrosacomas of the Skull Base with Carbon Ions
(Int. J. Radiation Oncology Biol. Phys. 53 (2002) 36)

Schulz-Ertner, D., T. Haberer, O. Jäkel, C. Thilmann, M. Krämer, **W. Enghardt**, G. Kraft, M. Wannenmacher, J. Debus

Abstract: Purpose: Compared to photon irradiation, carbon ions provide physical and biologic advantages that may be exploited in chordomas and chondrosarcomas.
Methods and Materials: Between August 1998 and December 2000, 37 patients with chordomas ($n = 24$) and chondrosarcomas ($n = 13$) were treated with carbon ion radiotherapy within a phase I/II trial. Tumor conformal application of carbon ion beams was realized by intensity-controlled raster scanning with pulse-to-pulse energy variation. Three-dimensional treatment planning included biologic plan optimization. The medium tumor dose was 60 GyE (GyE = Gy x relative biologic effectiveness).
Results: The mean follow-up was 13 month. The local control rate after 1 and 2 years was 96 % and 90 %, respectively. We observed 2 recurrences outside the gross tumor volume in patients with chordomas. Progression-free survival was 100 % for chondrosarcomas and 83 % for chordomas at 2 years. Partial remission after carbon therapy was observed in 6 patients. Treatment toxicity was mild.
Conclusion: These are the first data demonstrating the clinical feasibility, safety, and effectiveness of scanning beam delivery of ion beams in patients with skull base tumors. The preliminary results in patients with skull base chordomas and low-grade chondrosarcomas are encouraging, although the follow-up was too short to draw definite conclusions concerning outcome. In the absence of majo toxicity, dose escalation might be considered.

Magnetic and Collective Rotation in ^{79}Br
(Phys. Rev. C 65 (2002) 044326)

Schwengner, R., F. Dönau, T. Servene, H. Schnare, J. Reif, G. Winter, **L. Käubler, H. Prade**, S. Skoda, J. Eberth, H. G. Thomas, F. Becker, B. Fiedler, S. Freund, S. Kasemann, T. Steinhardt, O. Thelen, T. Härtlein, C. Ender, F. Köck, P. Reiter, D. Schwalm

Abstract: Excited states of the nucleus ^{79}Br were investigated via the reaction ^{76}Ge(^{7}Li, $4n$) at a beam energy of 35 MeV. Coincidence data of emitted γ rays were measured with an arrangement of six EUROBALL CLUSTER detectors. The $E2$ bands built on the $9/2^+$ and $3/2^-$ states were extended up to $J = 37/2$ at $E \approx 8.8$ MeV. The $M1$ band starting with a $15/2^-$ state at 2.6 MeV was observed up to $J = (29/2)$ at E = 6.4 MeV. Crossover $E2$ transitions within this band were observed for the first time. Mean lifetimes of 17 levels were deduced using the Doppler-shift-attenuation method. The $M1$ band can be described within the tilted-axis-cranking model on the basis of the tilted three-quasiparticle configuration $\pi(g_{9/2})\nu(g_{9/2})\nu(fp)$ which has a triaxial shape. This band appears as a mixed case including contributions of both magnetic and collective rotation.

Magnetic Rotation in ^{82}Rb and ^{84}Rb
(Phys. Rev. C 66 (2002) 024310)

Schwengner, R., G. Rainovski, H. Schnare, **A. Wagner, F. Dönau**, A. Jungclaus, M. Hausmann, O. Iordanov, K.P. Lieb, D.R. Napoli, G. de Angelis, M. Axiotis, N. Marginean, F. Brandolini, C. Rossi Alvarez

Abstract: High-spin states in ^{82}Rb and ^{84}Rb were populated in the reaction ^{11}B + ^{76}Ge at beam energies of 45 and 50 MeV. γ rays were detected with the spectrometer GASP. The level schemes of ^{82}Rb and ^{84}Rb were extended up to 6.0 and 7.4 MeV, respectively. Mean lifetimes of five levels in ^{82}Rb and eleven levels in ^{84}Rb were determined using the Doppler-shift-attenuation method. Regular magnetic dipole bands including strong $M1$ and weak $E2$ transitions observed in both nuclei show the characteristic features of magnetic rotation. These bands have been successfully described in the tilted-axis cranking model on the basis of the four-quasiparticle configuration $\pi(fp)\ \pi(g_{9/2}^2)\ \nu(g_{9/2})$. The calculations reproduce the band-like properties as well as absolute $B(M1)$ and $B(E2)$ transition strengths in both nuclei, which supports the concept of magnetic rotation. Excited states in ^{84}Rb were also interpreted in terms of the shell model using the model space $\pi(0f_{5/2}, 1p_{3/2}, 1p_{1/2}, 0g_{9/2})\ \nu(1p_{1/2}, 0g_{9/2})$. The predictions for low-lying states agree in general with the experiment. Moreover, calculated states with the main configuration $\pi(0f_{5/2}^{-2}1p_{3/2}^{-1}0g_{9/2}^2)\ \nu(0g_{9/2}^{-3})$ can be combined into $M1$ sequences which reproduce roughly the experimental transition strengths. However, these sequences do not show the features of magnetic rotation such as regular level spacings and $B(M1)$ values which decrease with increasing rotational frequency.

Charge-Exchange Reaction $pD \to n(pp)$ in the Bethe-Salpeter Approach
(Yad. Fiz. 65 (2002) 469)

Semikh, S.S., S.M. Dorkin, L.P. Kaptari, **B. Kämpfer**

Abstract: The deuteron charge - exchange reaction $pD \to n(pp)$ for the low values of momentum transfer and small excitation energies of final pp - pair is considered in the framework of Bethe-Salpeter approach. The method of calculation of the observables is developed for the case, when the pp-pair is in $^1S_0$-state. The methodical numerical calculations of the differential cross sections and tensor analysing powers are presented. The reaction under consideration is predicted to be a solid base for construction of the deuteron tensor polarimeter at high energies, and also to obtain some additional information about elementary nucleon-nucleon charge-exchange amplitude.

Structure of High-Spin States in ^{91}Sr and ^{92}Sr
(Phys. Rev. C 65 (2002) 034323)

Stefanova, E.A., M. Danchev, **R. Schwengner**, D.L. Balabanski, M.P. Carpenter, M. Djongolov, S.M. Fischer, D.J. Hartley, R.V.F. Janssens, W.F. Mueller, D. Nisius, W. Reviol, L.L. Riedinger, O. Zeidan

Abstract: The nuclei ^{91}Sr and ^{92}Sr were produced at high spin as fission fragments following the fusion reaction ^{36}S + ^{159}Tb at 165 MeV. γ rays were detected with the Gammasphere array. The level schemes of ^{91}Sr and ^{92}Sr were extended up to E $\approx$ 6 MeV and E $\approx$ 8 MeV, respectively. Level structures in ^{91}Sr and ^{92}Sr were interpreted in shell-model calculations performed in the configuration space $(0f_{5/2}, 1p_{3/2}, 1p_{1/2}, 0g_{9/2})$ for the protons and $(1p_{1/2}, 0g_{9/2}, 1d_{5/2})$ for the neutrons. Negative-parity states in the yrast sequences are described in these calculations by coupling 3^- proton excitations to the unpaired $1d_{5/2}$ neutrons. A possible reduction of the gap between the proton $1p_{3/2}$ and $1p_{1/2}$ orbitals in ^{92}Sr is discussed.

Kaon and Antikaon Production in Dense Nuclear Matter
(J. Phys. G 28 (2002) 1895)

C. Sturm for the KaoS Collaboration:, I. Böttcher, M. Debowski, A. Förster, **E. Grosse**, P. Koczon, B. Kohlmeyer, F. Laue, M. Mang, **L. Naumann**, H. Oeschler, F. Pühlhofer, E. Schwab, P. Senger, Y. Shin, J. Speer, H. Ströbele, C. Sturm, G. Surowka, F. Uhlig, **A. Wagner**

Abstract: The production and propagation of kaons and antikaons in relativistic heavy-ion collisions have been systematically investigated with the Kaon spectrometer at SIS/GSI. Experimental results on the K^+ and K^- yield and on the azimuthal emission pattern of K^+ mesons are presented. Within the framework of transport models the data can be explained assuming in-medium kaon-nucleon potentials.The comparison of K^+ production excitation functions obtained for Au + Au and C + C collisions with results of transport model calculations favours a soft nuclear equation-of-state.

Production of ω and ϕ Mesons in Near-Threshold πN Reactions: Baryon Resonances and the Okuba-Zweig-Iizuka Rule
(Phys. Rev. C 65 (2002) 065202)

Titov, I.A., **B. Kämpfer**, B.L. Reznik

Abstract: Results of a combined analysis are presented for the production of ω and ϕ mesons in πN reactions in the near-threshold region using a conventional "nonstrange" dynamics based on processes that are allowed by the nonideal ω-ϕ mixing. We show that the interferences of the t channel (meson exchange) and s, u channels (nucleon and nucleon-resonances) differ significantly for the ω and ϕ production amplitudes. This leads to a decrease of the relative yields, in comparison with the expectations based on a one-component amplitude with standard ω-ϕ mixing. We find a strong and nontrivial difference between observables in ω and ϕ production reactions caused by the different roles of the nucleon and nucleon-resonance amplitudes. A series of predictions for the experimental study of this effect is presented.

Quadrupole Moment of the 11^- Intruder Isomer in ^{196}Pb and Its Implications for the 16^- Shears Band Head
(Phys. Rev. Lett. 88 (2002) 102502)

Vyvey, K., S. Chmel, G. Neyens, H. Hubel, D.L. Balabanski, D. Borremans, N. Coulier, R. Coussement, G. Georgiev, N. Nenoff, S. Pancholi, D. Rossbach, **R. Schwengner**, S. Teughels, **S. Frauendorf**

Abstract: The quadrupole moment of the 11^- isomer in ^{196}Pb has been measured by the level mixing spectroscopy method. This state has a $\pi(3s_{1/2}^{-2}1h_{9/2}1i_{13/2})11^-$ configuration which is involved in most of the shears band heads in the Pb region. The first directly measured value of $Q_s(11^- =$ (-)3.41(66) b, coupled to the previously known quadrupole moment of the $\nu(1i_{13/2}^{-2}12^+$ isomer allows us to estimate the quadrupole moment of the 16^- shears band head as $Q_s(16^-) =$ -0.32(10) b. The experimental values are compared to tilted axis cranking calculations, giving insight into the validity of the additivity approach to couple quadrupole moments and on the amount of deformation in the shears bands.

Novel Features of the Fragment Mass Variance in Fission of Hot Nuclei
(Physics of Atomic Nuclei, Vol. 65, Nr.8 (2002) 1403)

Wagner, W., I.I. Gotchar, A.E. Gettinger, L.A. Litnevsky, H.-G. Ortlepp, D.V. Kamanin

Abstract: Basing on data obtained by the incomplete fusion reactions ^{7}Li (43 AMeV) + ^{232}Th and ^{14}N (34 AMeV) + ^{197}Au, the energy dependence of the variance of the fragment mass in fission of highly heated nuclei has been investigated for total excitation energies ranging from 50 up to 350 MeV. This dependence shows some unexpected features when the total excitation energy exceeds a value of about 70 MeV. After this value the steady increase of the variance expected from its temperature dependence changes to some kind of plateau between 100 and 200 MeV. Further on, at energies in excess of about 250 MeV, the variance is found to increase again sharply. In order to analyze this behaviour quantitatively, a dynamical stochastic model has been developed. The model employs the one-body dissipation mechanism and describes the decay of highly excited and rotating nuclei by fission and light particle evaporation. It satisfactory explains the measured prior-to-scission neutron multiplicities and the experimental mass variances up to an energy of about 250 MeV, but the stochastic treatment does not reveal any increase at higher excitation energies in contradiction with the data.

Production of ϕ Mesons in Subthreshold Heavy-Ion Collisions
(J. Phys. G 28 (2002) 2133)

Zétényi, M., **H.W. Barz**, Gy. Wolf, **B. Kämpfer**

Abstract: Within a BUU type transport model we study ϕ meson production in subthreshold Ni+Ni and Ru+Ru reactions. For the first time we included in our model the elementary reaction channels $\rho + N, \Delta \rightarrow \phi + N$, $\pi + N(1520) \rightarrow \phi + N$ and $\pi\rho \rightarrow \phi$. In spite of a substantial increase of the ϕ multiplicities by these channels our results stay significantly below the preliminary experimental data.

Evaluation of QCD sum rules for light vector mesons at finite density and temperature
(Eur. Phys. J. A 15 (2002) 529)

Zschocke, S., O.P. Pavlenko, **B. Kämpfer**

Abstract: QCD sum rules are evaluated at finite nucleon densities andtemperatures to determine the change of mass parameters for the lightest vector mesons ρ, ω and ϕ in a strongly interacting medium. For conditions relevant for the starting experiments at HADES we find that the in-medium mass shifts of the ρ and ω mesons are governed, within the Borel QCD sum rule approach, by the density and temperature dependence of the four-quark condensate. In particular, the variation of the strength of the density dependence of the four-quark condensate reflects directly the decreasing mass of the ρ meson and can lead to a change of the sign of the ω meson mass shift as a function of the density. In contrast, the in-medium mass of the ϕ meson is directly related to the chiral strange quark condensate which seems correspondingly accessible.

Renormalization of the Two-Photon Vacuum Polarization and the Self Energy Vacuum Polarization for a Tightly Bound Electron
(Eur. Phys. J. D 19 (2002) 147)

Zschocke, S., G. Plunien, G. Soff

Abstract: The renormalization method of Bogoljubov-Parasiuk-Hepp-Zimmermann (BPHZ) is used in order to derive the renormalized energy shift due to the gauge invariant Källén-Sabry diagram of the two-photon vacuum polarization (TPVP) as well as the self energy vacuum polarization S(VP)E beyond the Uehling approximation. It is outlined, that no outer renormalization is required for the two-photon vacuum polarization and that only the inner renormalization has to be accomplished. It is shown that the so-called nongauge invariant spurious term is absent for a wide class of vacuum polarization (VP) diagrams if one applies the widely used spherical expansion of bound and free-electron propagator. This simplifies significantly calculations in bound state quantum electrodynamis. As one result of our paper the use of the BPHZ-approach in bound state QED is established.

Proceedings and Reports

Afanasjev, A. V., **S. Frauendorf**, P. Ring
Rotating nuclei in the relativistic mean field theory: Microscopic nature of nuclear magnetism
Proceedings of the NATO Advanced Research Workshop on "The Nuclear Many-Body Problem 2001", Brijuni, Pula, Croatia, 2001, Eds. W. Nazarewicz and D. Vretenar, NATO Science Series II - Mathematics, Physics and Chemistry (Kluwer Academic Publishers) v. 53 (2002) 103 - 111

Altstadt, E., C. Beckert, H. Freiesleben, V. Galindo, **E. Grosse**, B. Naumann
Design of a photoneutron source for time-of-flight experiments at the radiation source ELBE
Proceedings of the International Workshop "Fast Neutron Physics" TU Dresden, Germany, September 5-7, 2002

Barz, H.W.
HBT radii for an opaque source at RHIC engines
Proc. Int Workshop XXX on Gross Properties of Nuclei and Nuclear Excitations on Ultrarelativistic Heavy Ion Collisions, Hirschegg, Austria, Jan. 13 - 19, 2002, p. 217

Cleymans, J., **B. Kämpfer**, S. Wheaton
Towards Strangeness Saturation in Central Heavy Ion Collisions at High Energies
16. International Conference on Ultrarelativistic Nucleus-Nucleus Collisions
Quark Matter 2002 (QM 2002), Nantes, France, July 18 - 24, 2002

Dekorsy, Th., **E. Grosse**, M. Helm, **W. Seidel, D. Wohlfarth**, A. Wolf, **R. Wünsch**
A Transport and Diagnostic System for the IR Beam of ELBE
24. FEL-Konferenz and User Workshop, Chicago, USA, Sept. 9 - 13, 2002, USA, Poster and Proceedings

Enghardt, W., K. Parodi, J. Pawelke, F. Pönisch, T. Haberer, M. Krämer, D. Schardt
Positronen Emissions Tomographie für die Qualitätssicherung bei der Schwerionentherapie
Deutsche Physikalische Gesellschaft, Abstracts der Frühjahrstagungen 2002,
http://www.dpg-tagungen.de/archive/2002

Enghardt, W., P. Crespo, F. Fiedler, K. Parodi, J. Pawelke, F. Pönisch, T. Haberer, C. Kausch, M. Krämer, D. Schardt
Positron emission tomography for quality assurance of carbon ion therapy
Book of Abstracts, XXXVI Meeting of the Particle Therapy Co-Operative Group, Catania, Italy, May 29 - 31, 2002

Fahmy, K., G. Furlinski, P. Gippner, E. Grosse, H. Piest, M. Szepan, W. Seidel, D. Wohlfarth, A. Wolf, **R. Wünsch**
Properties and the planned use of the intense THz radiation from ELBE at Dresden-Rossendorf
Poster and Proceedings Tera-Hertz Radiation in Biological Research, Investigation on Diagnostics, and Study on Potential Genotoxic Effects, Workshop Capri, Sept. 29 - Oct. 2, 2002, Italy

Gallmeister, K., **B. Kämpfer**, O.P. Pavlenko
Energy Loss of Quarks in Deconfined Matter at RHIC: Photon Tagged Jets, Single Electron and Dilepton Spectra from Open Charm
16. International Conference on Ultrarelativistic Nucleus-Nucleus Collisions,
Quark Matter 2002 (QM 2002), Nantes, France, July 18 - 24, 2002, nucl-th/0208006

Hietschold, V., T. Kittner, S. Appold, N. Abolmaali, **K. Parodi**, M. Laniado
MR perfusion measurement in contrast uptaking lesions: comparison of three correction levels
19. Annual Meeting of the European Society for Magnetic Resonance in Medicine and Biology, August 22 - 25, 2002, Cannes, France

Kamanin, D.V., V.S. Salamatin, **W. Wagner**, H. Freiesleben
The new Parameter for Separation of Binary Reaction Mechanisms in Heavy-Ion Collisions
Int. Symp. on Exotic Nuclei, Lake Baikal, Russia (2001), Conf. Proceed., Ed. Yu. E. Penionzhkevich, E. A. Cherpanov, World Scientific Pub. C. Pte. Ltd. (2002) p. 235

Kämpfer, B., J. Cleymans, **K. Gallmeister**, S. Wheaton
Centrality Dependence of Thermal Parameters in Heavy Ion Collisions at SPS and RHIC
30. International Workshop on Gross Properties of Nuclei and Nuclear Excitation, Hirschegg 2002, Jan. 13 - 19, 2002,(Eds.) M. Buballa et al., p. 158

Kämpfer, B., J. Cleymans, **K. Gallmeister**, S.M. Wheaton
Thermal Parameters in Heavy Ion Collisions at SPS and RHIC: Centrality Dependence
International Workshop on Quark and Hadron Dynamics, Budapest, Hungary, March 3 - 7, 2002, (Ed.) P. Levar, p. 213

Kämpfer, B., A. Peshier, G. Soff
Quasi-particle Model for Deconfined Matter
5. International Conference on Quark Confinement and the Hadron Spectrum
Gargnano, Brescia, Italy, Sept. 10 - 14, 2002, hep-ph/0212179

Kämpfer, B., A.I. Titov, B.L. Reznik
Baryon Resonance Dynamics in π N $\longrightarrow$ N V Reactions near Threshold
16. International Conference on Particles and Nuclei (PANIC 02),
Osaka, Japan, Sept. 30 - Okt. 4, 2002

Kitagawa, A., M. Endo, M. Hosaka, T. Kanai, M. Kanazawa, S. Koda, S. Minohara, T. Murakami, K. Noda, M. Suda, T. Tomitani, M. Torikoshi, E. Urakabe, S. Yamada, K. Yoshikawa, H. Mizuno, T. Nishio, M. Shinbo, Y. Futami, **J. Pawelke**, K. Hanawa, Y. Iseki, K. Sato, M. Mizota, M. Hirata, A. Komiyama
Radioactive Beam Project at HIMAC
Proceedings of the 2. Asian Particle Accelerator Conference, Beijing, China Sept. 17 - 21, 2001, 800-802
Report National Institute of Radiological Sciences, Chiba, Japan, HIMAC-044 (Dec 2001) 26 - 28

Kotte, R., B. Kämpfer
Acceptance and Count Rate Estimates for Experiments on Subthreshold Phi Meson Production in Central Collisions of C + C at 2 AGeV
Wiss. Tech. Ber. FZR-339 (2002)

Loos, M.J. de, C.A.J. van der Geer, S.B. van der Geer, A.F.G. van der Meer, D. Oepts, **R.Wünsch**
A 3D Particle Tracking Technique for FEL Start-Up and Saturation Effects
24. Int. Conf on Free Electron Lasers, Argonne (USA) Sept. 2002
Poster and Proceedings

Parodi, K., W. Enghardt, T. Haberer
The potential of in-beam PET for proton therapy monitoring: first experimental investigation
Verhandlungen der DPG, HK48.7, Physikertagung, Münster, March 11 - 15, 2002

Parodi, K., W. Enghardt, T. Haberer
Experimental investigation of the potential in-beam PET for proton therapy monitoring
DPG-Tagung, Leipzig, March 18 - 22, 2002

Parodi, K., W. Enghardt, T. Haberer
Experimental investigation of the potential in-beam PET for proton therapy monitoring
PTCOG XXXVI, Catania, Italy, Book of Abstracts (2002) 12, May 29 - 31, 2002

Parodi, K., W. Enghardt, T. Haberer
The potential of in-beam positron-emission-tomography for proton therapy monitoring: first phantom experiments
IEEE Nuclear Science Symposium Medical Imaging Conference NSS-MIC 2002, Norfolk, Virginia, USA, Conference Records, Nov. 10 - 16, 2002

Semikh, S.S., L.P. Kaptari, S.M. Dorkin, **B. Kämpfer**
Final State Interaction within the Bethe-Salpeter Approach in Charge Exchange PD $\rightarrow$ N(PP) Process
16. International Baldin Seminar on High-Energy Physics Problems:
Relativistic Nuclear Physics and Quantum Chromodynamics (ISHEPP 16),
Dubna, Russia, June 10 - 15, 2002, nucl-th/0209087

Spekl, K., D. Slonina, K. Brankovic, C. Hoinkis, **A. Panteleeva, J.Pawelke**, W. Dörr
Mikronukleus-Induktion in Keratinozyten und Fibroblasten nach Bestrahlung mit weichen Röntgenstrahlen
11. Symposium "Experimentelle Strahlentherapie und Klinische Strahlenbiologie" Dresden, Feb. 21 - 23, 2002
Exp. Strahlenther. Klin. Strahlenbio. **11** (2002) 135-139 (ISSN 1432-864X)

Tishchenko, V.G., C.-M. Herbach, D. Hilscher, H.-G. Ortlepp, **P. Gippner**, D.V. Kamanin, Yu.E. Penionzhkevich, **K.-D. Schilling, W. Wagner**
Ternary Decay of Hot Heavy Nuclei studied in the Reaction ^{40}Ar(36AMeV)+^{248}Cm
Internat. Symp. on Exotic Nuclei, Lake Baikal, Russia (2002), Conf. Proceed., ed. Yu. E. Penionzhkevich, E. A. Cherepanov, World Scientific E. Pte. Ltd.(2002) p. 167

Zschocke S., B. Kämpfer, O.P. Pavlenko, G. Wolf
Evaluation of QCD Sum Rules for HADES
40. International Winter Meeting on Nuclear Physics, Bormio, Italy, Jan. 21 - 26, 2002
(Eds.) I. Iori, A. Moroni, p. 102

Theses

Johann Arend (Hans) Piest
Exciting Polycyclic Aromatic Hydrocarbon Vibrations (Infrared absorption spectroscopy of astrophysically relevant jet-cooled neutral and cationic polycyclic aromatic hydrocarbons)
University of Nijmegen, Mai 2002

Olesya Savchuk
Combination of PMFTIRRAS mapping and SPR imaging technique for investigation of SAM formed from phosphonic acid
TU Dresden, November 2002

Talks at Conferences and other Institutes

Barz, H.W.
HBT Radii for an Opaque Source at RHIC Energies
Proc. Int. Workshop XXX on Gross Properties of Nuclei and Nuclear Excitations on Ultrarelativistic Heavy-Ion Collisions, Hirschegg, Austria, Jan. 13 - 19, 2002

Barz, H.W.
K^+, K^-, ϕ Mesons in Nuclear Matter
ANKE Collaboration Meeting, Jülich, April 10 - 12, 2002

Barz, H.W.
Kaon Production Analysed in the Rossendorf-Budapest BUU code
Antikaon-Workshop, Rossendorf, June 3 - 4, 2002

Dohrmann, F.
Electroproduction of Strangeness on Light Nuclei
Baryons 2002, 9th International Conference on the Structure of Baryons, Jefferson Laboratory, Newport News, USA, March 7, 2002

Dohrmann, F.
Electroproduction of Strangeness on Light Nuclei
Group Report at Nuclear Physics Spring Meeting of DPG (Germany), NNV (Netherlands) and BNN/SBP (Belgium), Münster, March 14, 2002

Dohrmann, F.
Elektroproduktion von Strangeness an leichten Kernen:
Gebundene Hyperon-Nukleon-Zustände und quasifreie Verteilungen
Institutsseminar, Institut für Kern- u. Teilchenphysik der TU Dresden, April 7, 2002

Dohrmann, F.
Hyperon-Nucleon Boundstates and Electroproduction of Strangeness on Light Nuclei
Invited seminar, INFN-LNF Frascati, Rom, Italy, May 2, 2002

Dohrmann, F.
Hyperon-Nucleon Boundstates and Electroproduction of Strangeness on Light Nuclei
Meson 2002, 7th International Workshop on Meson Production, Properties and Interaction, Cracow, Poland, May 25, 2002

Dohrmann, F.
Electroproduction of Strangness on Light Nuclei
Invited seminar, Bonn University, Institut für Strahlen- u. Kernphysik, July 4, 2002

Dohrmann, F.
The HADES Experiment at GSI: Status Report
Invited seminar, Workshop on Effective theories of strongly interacting matter, Manchester, UK, July 16, 2002

Dohrmann, F.
Electroproduction of Strangeness on Light Nuclei
Workshop International School of Nuclear Physics in Erice, Sicily, 24th course, Quarks in Hadrons and Nuclei, Sep. 17, 2002

Dohrmann, F.
Electroproduction of Strangeness on Light Nuclei
Kolloquium im Graduiertenkolleg II., Physikalisches Institut Giessen Universität, Nov. 21, 2002

Enghardt, W.
In-situ Therapy Monitoring by Mean of Positron Emission Tomography
Initial ENLIGHT Workshop, CERN, Genf, Switzerland, Feb. 12, 2002

Enghardt, W.
Positronen Emissions Tomographie für die Qualitätssicherung bei der Schwerionentherapie
Frühjahrstagung der DPG, Fachverband Strahlenphysik und Strahlenwirkung, Leipzig, March 19, 2002

Enghardt, W.
Positron Emission Tomography for Quality Assurance of Carbon Ion Therapy
PTCOG XXXVI, Catania, Italy, May 29, 2002

Enghardt, W.
Radiotherapie mit Photonen, Elektronen und schweren geladenen Teilchen
Lecture course, Fakultät Elektrotechnik der TU Dresden, June 27, 2002

Enghardt, W.
Beschleuniger in der Medizin
Heraeus-Ferienkurs für Physik, Dresden, Sep. 16 - 27, 2002

Enghardt, W.
Tumortherapie mit Ionenstrahlen
Physikalisches Kolloquium der Martin-Luther-Universität Halle, Wittenberg, Dec. 5, 2002

Fahmy, K.
FTIR- and Fluorescence-Spectroscopic Investigation of Drug Action on Signalling by a Prototypical G-Protein-Coupled Receptor
First international conference on biomedical spectroscopy, Cardiff, Great Britain, July 7 - 10, 2002

Fahmy, K.
FTIR-Spectroscopic Investigation of Protein Conformational Changes
and Drug Action in a G-Protein-Coupled Receptor
THz-Bridge Workshop, Capri, Italy, Sep. 29. - Oct. 2, 2002

Fahmy, K.
Uran-bindende Proteine: Gewässerreinigung mit biologischen Mitteln
Bruker-Anwender-Treffen, Ettlingen, Deutschland, Nov. 11, 2002

Frauendorf, S.
Quantum Mechanics II
Graduate course at University of Notre Dame,
Indiana, USA, spring 2002

Frauendorf, S.
Left-Handed Nuclei
International Conference on Frontiers of Nuclear Structure,
Berkeley, July 28 - August 2, 2002

Frauendorf, S.
Electricity and Magnetism
Undergraduate course at University of Notre Dame, Indiana, USA, fall 2002

Frauendorf, S.
Chirality of Nuclear Rotation
Third International Conference on Fission and Neutron-Rich Nuclei,
Sanibel Island, Florida, Nov. 3 - 9, 2002

Frauendorf, S.
Proton-Neutron Pair Correlations in N = Z Nuclei Nuclear
Physics Division, Argonne National Laboratory, USA, Dec. 16, 2002

Gippner, P.
The Radiation Source ELBE and the FEL Facilities
VIK Dubna, Flerov Laboratory of Nuclear Reactions, April 8, 2002

Kämpfer, B.
General Relativity
Lecture course, TU Dresden, Wintersemester 2001/2002

Kämpfer, B.
Centrality Dependence of Thermal Parameters in Heavy Ion Collisions at SPS and RHIC
30th International Workshop on Gross Properties of Nuclei and Nuclear Excitation:
Hirschegg 2002: Ultrarelativistic Heavy Ion Collisions, Hirschegg, Germany, Jan. 13 - 19, 2002

Kämpfer, B.
Evaluation of QCD Sum Rules for HADES
40th International Winter Meeting on Nuclear Physics, Bormio, Italy, Jan. 21 - 26, 2002

Kämpfer, B.
Thermal Parameters in Heavy Ion Collisions at SPS and RHIC: Centrality Dependence
International Workshop on Quark and Hadron Dynamics in Relativistic Heavy Ion Collisions, Budapest, Hungary, March 3 - 7, 2002

Kämpfer, B.
Isoscalar-Isovector Interference in πN Reactions
HADES collaboration meeting, Smolenice, April 11 - 14, 2002

Kämpfer, B.
QCD Sum Rules
Seminar, Universität Tübingen, April 25, 2002

Kämpfer, B.
Quasi-Particle Model of Baryon-Dense Plasma
Workshop Compressed Baryonic Matter, GSI Darmstadt, May 13 - 16, 2002

Kämpfer, B.
Energy Loss of Quarks in Deconfined Matter at RHIC: Photon-Tagged
Jets, Single Electron and Dilepton Spectra
Quark Matter 2002, Nantes, France, July 18 - 25, 2002

Kämpfer, B.
Quasiparticle Model for a Deconfined Baryon-Dense Plasma
Conference on "Quark Confinement and the Hadron Spectrum V",
Gargnano, Italy, Sep. 10 - 14, 2002

Kämpfer, B.
Baryon Resonance Dynamics on πN $\rightarrow$ NV Reactions near Threshold
PANIC 02, Osaka, Japan, Sep. 30 - Oct. 4, 2002

Kämpfer, B.
Unser Universum: Vergangenheit und Zukunft
Samstagsvorlesung, TU Dresden, Nov. 16, 2002

Kämpfer, B.
Gauge Field Theory
Lecture course, TU Dresden, Winter Semester 2002/03

Kanaki, K.
HADES Drift Chambers MDC III
Nuclear Physics Spring Meeting of DPG (Germany), NNV(Netherlands) and BNN/SBP (Belgium), Münster,

March 11 - 15, 2002

Kanaki, K.
Status of MDC Plane III Production at FZ-Rossendorf
XI HADES Collaboration Meeting, Smolenice, April 12, 2002

Kotte, R.
Status Report on the Outer Plastic Well
FOPI collaboration meeting, Darmstadt, March 21 - 22, 2002

Kotte, R.
Study of phi Meson Production in C + C at E = 2 AGeV
HADES collaboration meeting, Smolenice, April 11 - 14, 2002

Kotte, R.
Progress Report on FOPI's Phi Meson Analyses
FOPI collaboration meeting, Trakoscan, Croatia, Sep. 26 - 28, 2002

Möller, K.
The Rossendorf Dresden 40 MeV Electron Accelerator (ELBE radiation source) and its Experimental Program
FFLEEP Workshop, Trento, Dec. 4 - 7, 2002

Neubert, W.
Comparison of Radiation Transport Codes on Electromagnetic
Interactions and Neutron Production in the M*e*V Region
NEG user group meeting, Stoke-on-Trent, England, April 22 - 23, 2002

Panteleeva, A., S. Pieck, K. Spekl, H. Thiele
Biologische Wirksamkeit niederenergetischer Teilchen und Röntgenstrahlen
Seminar "Strahlenbiologie und Experimentelle Radioonkologie", TU Dresden, Klinik und Poliklinik für Strahlentherapie und Radioonkologie, Jan. 8, 2002

Panteleeva, A., S. Pieck, K. Spekl, H. Thiele
Klonogenes Zellüberleben und Chromosomenschaden bei Keratinozyten und Fibroblasten nach Bestrahlung mit 25 kV und 200 kV Röntgenstrahlen
Seminar "Strahlenbiologie und Experimentelle Radioonkologie", TU Dresden, Klinik und Poliklinik für Strahlentherapie und Radioonkologie, Jan. 8, 2002

Panteleeva, A.
Current status of preparation of RBE measurement at ELBE
Seminar TU Dresden, Institut für Strahlenschutzphysik, June 27, 2002

Parodi, K.
PET imaging for the Monitoring of Carbon Ion Therapy and Potential Application to Proton Therapy
University of Milano, Bicocca and TERA Foundation, Milano, Italy, Jan. 14, 2002

Parodi, K.
The Potential of In-Beam PET for Proton Therapy Monitoring: First Experimental Investigation
Frühjahrstagung der DPG, Fachverband Physik der Hadronen und Kerne, Münster, March 14, 2002

Parodi, K.
Experimental Investigation of the Potential of In-Beam PET for Proton Therapy Monitoring
Frühjahrstagung der DPG, Fachverband Strahlenphysik und Strahlenwirkung, Leipzig, March 19, 2002

Parodi, K.
Positron Emission Tomography for Quality Assurance of Carbon Ion Therapy
XXXVI Meeting of the Particle Therapy Co-Operation Group, Catania, Italy, May 29, 2002

Parodi, K.
Radiotherapy with Hadron Beams

20 lectures given at the University of Ferrara, Physics Dept., as complementary course to the course of Medical Physics Laboratory, June 3 - 13, 2002

Parodi, K.
The Application of Positron Emission Tomography (PET) to the Monitoring of Heavy Ion Therapy
Heraeus-Ferienkurs, TU Dresden, Sep. 20, 2002

Parodi, K.
The Application of Positron Emission Tomography (PET) to the Monitoring of Heavy Ion Therapy
Workshop "Imaging in Radiotherapy: Present and Future", ISS, Rome, Italy, Dec. 12, 2002

Pawelke, J.
Spurdetektoren, Szintillationsdetektoren, biologische Strahlenwirkung, Positronen-Emissions-Tomographie zur Kontrolle der Strahlentherapie mit schweren Ionen
Vorlesung "Experimentelle Methoden der Kern- und Teilchenphysik - Beschleuniger und Detektoren", TU Dresden, Institut für Kern- und Teilchenphysik, May 14, 2002

Pawelke, J.
Grundlagen der biologischen Strahlenschädigung
Heraeus-Ferienkurs, TU Dresden, Sep. 16 - 27, 2002

Pawelke, J.
In-Beam PET for Quality Assurance of Ion Therapy
National Institute of Radiological Sciences, Irradiation Group and Medical Physics Group at HIMAC, Chiba, Japan, August 2, 2002

Pawelke, J.
Positron Emission Tomography at the Research Center Rossendorf
National Cancer Center, Medical Physics Group, Kashiwa, Japan, August 8, 2002

Pawelke, J.
In-Beam PET for Quality Assurance of Carbon Ion Therapy
National Institute of Radiological Sciences, Research Center of Charged Particle Therapy, Chiba, Japan, August 9, 2002

Pönisch, F.
Streukorrektur in der Rekonstruktion von PET
Seminar, TU Dresden, Institut für Strahlenschutzphysik, May 23, 2002

Pönisch, F.
Rekonstruktion und Streukorrektur von PET-Daten bei der Schwerionentherapie
Heraeus-Ferienkurs, TU Dresden, Sep. 20, 2002

Scheinast, W.
Production of Kaons and Antikaons in Proton-Nucleus Collisions near Threshold
Nuclear Physics Spring Meeting of DPG (Germany), NNV(Netherlands) and BNN/SBP (Belgium), Münster, March 14, 2002

Scheinast, W.
Production of Kaons and Antikaons in Proton-Nucleus Collisions near Threshold
Workshop Meson 2002, Krakow, Poland, May 24 - 28, 2002

Schilling, K.D.
Nuclear Spectroscopy Investigations at the Radiation Source ELBE
VIK Dubna, Flerov Laboratory of Nuclear Reactions, April 8, 2002

Schilling, K.D.
Nuclear Physics Experiments of the New ELBE Accelerator in Rossendorf,
17th International Nuclear Physics Divisional Conference of the European Physical Society:
Nuclear Physics in Astrophysic, Debrecen, Hungary, Sep. 30 - Oct. 4, 2002

Schwengner, R.
Magnetic and Collective Rotation in ^{79}Br
Nuclear Physics Spring Meeting of DPG (Germany), NNV(Netherlands) and BNN/SBP (Belgium), Münster, March 11 - 15, 2002

Seidel, W.
Study of Heavy-Metal Complexes with Thermo-Optical Methods at CLIO
CLIO-Applications & Perspectives - Workshop, Orsay, France, Feb. 28, 2002

Wagner, A.
Der Coulomb-Aufbruch von 8-B und das solare Neutrino-Problem
Seminar TU Dresden, Institut für Kern- und Teilchenphysik, Febr. 5, 2002

Zschocke, S.
Evaluation of QCD Sum Rules for Light Vector Mesons at Finite Density and Temperature
Nuclear Physics Spring Meeting of DPG (Germany), NNV(Netherlands) and BNN/SBP (Belgium), Münster, March 11 - 15, 2002

Zschocke, S.
Evaluation of QCD Sum Rules for Light Vector Mesons at Finite Density and Temperature
Joint Institute for Nuclear Research, Dubna, Russia, Sep. 16, 2002

Talks at Rossendorf

Barz, H.W.
Fundamentals of the Statistical Model for Calculations of Nuclear Cross Sections
FZ Rossendorf, July 23, 2002

Enghardt, W.
Schwerionen-Tumortherapie
Lehrerfortbildung im FZ Rossendorf, Jan. 16, 2002

Enghardt, W.
Krebstherapie mit Schwerionen
Tag der offenen Tür, FZ Rossendorf, Sep. 14, 2002

Fahmy, K.
Systeme und Methoden der IR-Biospektroskopie
FZ Rossendorf, June 2002

Frauendorf, S.
Relativistic Mean Field Calculations for Superheavy Nuclei
FZ Rossendorf, July, 14, 2002

Pawelke, J.
Erzeugung quasi-monochromatischer Röntgenstrahlung für zellbiologische Experimente durch Elektronen-Channeling an ELBE
ELBE Machine Advisory Committee, FZ Rossendorf, March 25, 2002

Schwengner, R.
Stand der Vorbereitung kernphysikalischer Experimente an ELBE
ELBE Machine Advisory Committee

FZ Rossendorf, March 25, 2002

Seidel, W.
The FEL-Project at Rossendorf
FZ Rossendorf, Jan. 24, 2002 (Evaluierungskommission Hochfeldlabor)

Seidel, W.
Infrarotstrahlführung vom Resonator bis zu den Nutzerlaboren für U27
FZ Rossendorf, Elbe-Palaver, March 21, 2002

Seidel, W.
FEL (U27) und IR-Beamline, Konzept in den optischen Laboren
ELBE Machine Advisory Committee, March 25, 2002

Seidel, W.
The FELs at Rossendorf
FZ Rossendorf, April 22, 2002 (Studentengruppe Uni Göteborg)

Seidel, W.
The FEL-Project at Rossendorf
FZ Rossendorf, Sept. 06, 2002

Seidel, W.
Wie funktioniert ein Freie-Elektronen-Laser?
FZ Rossendorf, Tag der offenen Tür, Sept. 14, 2002

Talks of Visitors

Angelis de, G., Laboratori Nazionali di Legnaro (LNL), Italy:
The activities of the LNL as a multidisciplinary lab involved in nuclear physics, gravitation, basic quantum mechanics, solid state physics and applications shall be illustrated, August 7, 2002

Baer, M., K. John, MPI Physik Komplexer Systeme, Dresden
Struktur und Funktion von Lipiden in biologischen Membranen, Sept. 2002

Barth, A.,Universität Frankfurt/Main:
Swinging proteins - Was Schwingungen über die Funktion einer biologischen Nanopumpe verraten, May 27, 2002

Bernhard, C., Max-Planck-Institut FKF-Stuttgart:
Far-infrared ellipsometry using a synchrotron light source - some results on cuprate high Tc superconductors and related materials, Oct. 14, 2002

Cassing, W., Universität Gießen:
Anti-Kaon-Erzeugung in Proton-Kern-Stößen (Resultate aus dem Gießen-Code), June 3, 2002

Chatterjee, M.L., DRAGON Group TRIUMF, Vancouver, Canada:
Nuclear astrophysics experiments at TRIUMF, Oct. 23, 2002

Chatterjee, M.L., DRAGON Group TRIUMF, Vancouver, Canada:
Lecture series on nuclear physics, Nov. - Dec., 2002

Dathe, M., Forschungszentrum für molekulare Pharmakologie, Berlin:
Membrane-active peptides: the role of structural properties for membrane-disturbing and membrane-penetrating activity, Oct. 21, 2002

Erhard, M., Universität Würzburg, Experimentelle Physik II:
Untersuchung zur Terminierung von ZnSE(001)-und CdTe(001)-Oberflächen mittels Streuung langsamer Ionen, Dec. 11, 2002

Ferrari, A., CERN-SL Genf, Switzerland:
An introduction to FLUKA physics models and applications, August 29, 2002

Frauendorf, S., University of Notre Dame, USA:
Prediction of superheavy elements by the relativistic mean field theory, July 8, 2002

Gerlich, D., Technische Universität Chemnitz:
CO_2 laser induced evaporation from a nanoparticle, June 3, 2002

Hartnack, C., SUBATECH Nantes, France:
Kaon-Erzeugung in Proton-Kern-Stößen (Resultate aus dem Nantes-Code), June 3, 2002

Heyne, K., Max-Born-Institut, Berlin
Ultrafast coherent nuclear motions in h-bonds in acetic acid dimers, Sept. 2002

Junghans, A.R., University Washington, USA:
A new determination of the astrophysical s-factor for the ^{7}Be(p,γ)^{8}B reaction, Oct. 28, 2002

Kapusta, M., Soltan Institute for Nuclear Studies, Otwock-Swierk, Poland:
characterization of Hamamatsu S8550 avalanche photodiode arrays for high resolution scintillator matrices, May 7, 2002

Kraft, G., GSI Darmstadt:
Eine Anwendung nuklearer Methoden: Tumortherapie mit Schwerionen, March 1, 2002

Lieb, K.P., Universität Göttingen:
Photonen-Kernstrukturuntersuchungen und Materialbearbeitung, March 1, 2002

Morawetz, K., Max-Planck-Institut für Physik komplexer Systeme Dresden:
Giant resonances in asymmetric nuclei, May 27, 2002

Munshi-Golam, M., Institut für Theoretische Physik, Universität Gießen:
Hadronic correlation function and quark number susceptibility at high temperature, June 18, 2002

Piest, H., University of Nijmegen, Rijnhuizen, The Netherlands:
Linear and non-linear IR spectroscopy of astrophysically relevant species using a FEL, Jan. 4, 2002

Pietralla, N., Universität Köln:
Nuclear physics with a free electron laser, Feb. 1, 2002

Pramatarova, L., Bulgarian Academy of Sciences, Sofia, Bulgaria:
Development of an in vitro system for the study of biomineralization induced by Radiation, July 23, 2002

Reichelt, U., TU Dresden:
CR39-Festkörper-Spurdetektoren - Eigenschaften und Modellierung der Spurentwicklung, Jan. 14, 2002

Ritter, H.G., LBL Berkeley, USA:
Recreating the big bang with nuclear collisions at RHIC, Nov. 19, 2002

Satink, R.G. FOM-institute for Plasma Physics, Rijnhuizen, The Netherlands:
Dynamics of vibrationally excited, weakly bound complexes, Oct. 25, 2002

Savchuk, O., TU Dresden:
Application of surface plasmon resonance imaging and polarization modulation FTIRRAS mapping techniques for investigation of self-assembled monolayers formed from phosphonic acid on patterned surface, May 24, 2002

Semikh, S., JINR Dubna, Russia:
Polarization obervables in pD reactions within the Bethe-Salpeter approach, Nov. 27, 2002

Senger, P., GSI Darmstadt:
Seltsame Teilchen in dichter Kernmaterie, March 1, 20002

Sibirtsev, A., Forschungszentrum Jülich:
Strangeness-Erzeugung in Hadronen-Stößen, June 3, 2002

Stachel, J., Universität Heidelberg:
Dileptonen und chirale Symmetrie in relativistischen Schwerionenstößen, March 01, 20002

Strekalovsky, O., JINR Dubna, Russia:
Dubna Electron Synchrotron (DELSY) - a project of a new SR Source at JINR, Dec. 2, 2002

Uhd-Jepsen, P., Physikalische Fakultät der Universität Freiburg:
Far-infrared spectroscopy of biologically important molecules: What can we learn?, June 17, 2002

Wolf, Gy., KFKI Budapest, Hungary:
Vector mesons in hadronic matter, Dec. 13, 2002

Wolski, D., Soltan Institute for Nuclear Studies, Otwock-Swierk, Poland:
Comparative tests of preamplifiers for Hamamatsu APD arrays, May 7, 2002

Zetenyi, M., KFKI Budapest, Hungary:
ϕ meson production in p+A collisions - effect of in medium ϕ broadening, June 25, 2002

Meetings organized by the IKH

Topic	Period	Number of Participants
Workshop Antikaon-Workshop	June 03-04, 2002	20
Workshop Topical Meeting at FZ Rossendorf	June 10-11, 2002	40

Personnel

Personnel of the Institute for Nuclear and Hadron Physics

Director: Prof. Dr. E. Grosse[1]

Scientific Personnel

Dr. H.W. Barz
Dr. D.V. Dimitrov
Dr. F. Dönau
Dr. F. Dohrmann
Dr. W. Enghardt
Dr. K. Fahmy
Dr. S. Frauendorf
Dr. P. Gippner
Prof. Dr. B. Kämpfer
Dr. L. Käubler
Prof. Dr. H. Közle
Dr. R. Kotte
Dr. S.N. Mallion
Dr. K. Möller
Dr. H. Müller
Dr. L. Naumann
Dr. W. Neubert
Dr. J. Pawelke
Dr. J.A. Piest
Dr. H. Rotter
Dr. K.D. Schilling
Dr. M. Schlett
Dr. R. Schwengner
Dr. M. Sczepan
Dr. J. Seibert
Dr. W. Seidel
Dr. H. Sharma
Dr. A. Wagner
Dr. W. Wagner
D. Wohlfarth
Dr. R. Wünsch
Dr. S. Zschocke

PhD Students

P. Crespo
P. Evtushenko
F. Fiedler
G. Furlinski
K. Kanaki
N. Lehmann
B. Mukherjee
A. Panteleeva
K. Parodi
F. Pönisch
U. Reichelt
G. Rusev
A. Sadowski
W. Scheinast

Technical Personnel

H. Angermann
U. Baumann
J.U. Berlin
M. Boeck
M. Böse
R. Förster
D. Hachenberger
K. Heidel
L. Heinrich
R.R. Hensel
K.H. Hermann
M. Hoff
J. Hutsch
M. Langer
E. Leßmann
M. Paul
J. Philipp
B. Rimarzig
C. Schneidereit
W. Schulze
M. Sobiella
A. Wagner (II)
U. Wolf

[1]also TU Dresden

Guest Scientists

Almehed, Daniel	Department of Physics, UMIST, Manchester, UK
Angelis, de Giacomo	INFN, Legnaro, Italy
Botvina, Alexandre S.	Institute for Nuclear Research, Moscow, Russia
Bunzarov, Ivan	Institute for Nuclear Research and Nuclear Energy, Sofia, Bulgaria
Chankova-Bunzarova, Nedialka	Institute for Nuclear Research and Nuclear Energy, Sofia, Bulgaria
Chatterjee, Mohan Lal	DRAGON Group TRIUMF, Vancouver, Canada
Ferrari, Alfredo	CERN-SL, Genf, Switzerland
Junghans, Arnd Rudolf	University of Washington, Center for Experimental Nuclear Physics and Astrophysics, Seattle, USA
Kaptari, Leonid P.	JINR Dubna, Russia
Kapusta, Maciek	Soltan Institute for Nuclear Studies, Department of Electronics, Otwock-Swierk, Poland
Kosev, Krasimir Milchev	Razgrad, Bulgaria
Kostov, Latchesar Kroumov	Institute for Nuclear Research and Nuclear Energy, Sofia, Bulgaria
Nazmitdinov, Rashid	VIK Dubna, Russia
Pavlenko, Oleg P.	Institute for Theoretical Physics, Kiev, Ukraine
Pietralla, Norbert A.	Institute for Nuclear Physics, University Cologne, Germany
Pramatarova, Liliana	Institute of Solid State Physics, Bulgarian Academy of Science, Sofia, Bulgaria
Savchuk, Olesya	Chernivtsi, Ukraine
Semik, Serguei	JINR Dubna, Russia
Wolf, György	KFKI, RMKI, Budapest, Hungary